III-V Semiconductor Nanocavitieson Silicon-On-Insulator Waveguide : Laser Emission, Switching and Optical Memory

Alexandre Bazin

UNIVERSITE PARIS 7 - DENIS DIDEROT

THÈSE

Pour l'obtention du grade de
Docteur de l'Université Paris 7
UFR de Physique

Présentée par

Alexandre Bazin

III-V Semiconductor Nanocavities on Silicon-On-Insulator Waveguide : Laser Emission, Switching and Optical Memory

Date de soutenance: 24 Juillet 2013

Devant le jury composé de:

JURY

Jean-Michel GERARD	CEA-Grenoble/INAC	Rapporteur
Thomas KRAUSS	University of York, Royaume-Uni	Rapporteur
Christian SEASSAL	Institut des Nanotechnologies de Lyon-CNRS,	Examinateur
Alfredo DE ROSSI	Thales Research & Technology	Examinateur
Dries VAN THOURHOUT	Ghent University, Belgique	Membre Invité
Crina COJOCARU	Universitat Politecnica de Catalunya, Espagne	Membre Invité
Rama RAJ	Laboratoire de Photonique et de Nanostructures-CNRS	Directrice de thèse
Fabrice RAINERI	Laboratoire de Photonique et de Nanostructures-CNRS	Directeur de thèse

Résumé en français

La photonique sur silicium constitue une plateforme idéale pour transmettre et distribuer des signaux optiques au sein d'une puce et sur de longues distances sans pertes excessives. L'intégration de semiconducteurs III-Vsur des circuits photonique en silicium est un projet excitant mais ambitieux, que nous avons mené en combinant le meilleur de l'optoélectronique des semiconducteurs III-V et des technologies photonique en siliicium-sur-isolant (SOI en anglais). Afin de pouvoir remplacer les interconnexions metalliques existantes par des interconnexion optiques, nous nous sommes efforcés d'utiliser les objets ayant les dimensions les plus petites et consommant les plus petites énergies comme peuvent l'être les nanocavités en Cristaux Photoniques incorporant des matériaux actifs en III-V.

Cette thèse visait à conceptualiser, fabriquer et étudier expérimentalement des structures hybrides III-V/circuit photonique SOI, où une couche de III-V, reportée par collage adhésif à quelques centaines de nm du silicium, est gravée en une cavité optique de type cristal photonique « nanobeam » et résonante autour de 1.5 μm. Les principaux résultats de ce travail sont les démonstration 1) d'une efficacité de couplage entre la cavité et le guide d'onde SOI facilement ajustable, pouvant excéder 90% lorsque les conditions d'accord de phase sont remplies, 2) de l'émission laser en régime continue avec des puits quantiques via la passivation des surfaces, et 3) d'une mémoire optique de durée supérieure à 2s avec des énergies de commutations ultra-faibles (0.4 fJ). Nous présentons aussi un modèle pour fabriquer des cavités « nanobeam » de facteurs Q très élevés, encapsulées dans un matériau bas indice.

Abstract

Silicon photonics constitutes an ideal platform for conveying and routing optical signals, within a chip, and this, over mm long distances with very low losses. The integration of III-V semiconductors onto silicon-on-insulator (SOI) photonic circuits is an exciting but challenging task, which we took-up by combining the best of both III-V optoelectronic and Silicon photonic technologies. In order to be able to use optical interconnects as a replacement technology of current metallic interconnects, we strove for the smallest footprint and lowest energy consuming objects which can be Photonic Crystal nanocavities embedding III-V active material.

This thesis aimed at designing, fabricating and studying experimentally hybrid III-V/SOI Photonic Circuit structures, where a III-V layer, bonded adhesively at a few 100's of nm from silicon, is patterned into a "nanobeam" cavity of optical resonance around 1.5 μm. The main achievements of this work are the demonstration of 1) an easily adjustable coupling efficiency between the cavity and the SOI waveguide, which can exceed 90% when the phase-matching condition are fulfilled, 2) the continuous wave laser emission with quantum well materials through surface passivation, and 3) an optical memory lasting more than 2 s with ultra-low switching energy (0.4 fJ). We also present in detail the fully analytical model to fabricate high-Q factor nanobeam cavities encapsulated in a low-index material.

Remerciements

Je tiens tout d'abord à remercier Messieurs Thomas KRAUSS et Jean-Michel GERARD qui m'ont fait l'honneur d'accepter d'être les rapporteurs de ce travail de thèse. Je remercie tout aussi chaleureusement Crina COJOCARU, Alfredo DE ROSSI, Christian SEASSAL et Dries VAN THOURHOUT pour avoir accepté de faire partie de mon jury de thèse. J'adresse un remerciement à Dries VAN THOURHOUT pour les nombreux commentaires qu'il a fait sur ce manuscrit, bien utiles à l'heure des dernières corrections.

Je tiens à exprimer toute ma gratitude à Rama RAJ et Fabrice RAINERI pour m'avoir confié ce très beau sujet de thèse. Travailler avec eux a été une expérience incroyable dont je resterai nostalgique encore longtemps. Depuis les premières heures à "maniper" sur la table optique jusqu'à la rédaction de ce manuscrit de thèse et des articles, en passant par les heures en salle blanche, j'ai pris énormément de plaisir à les cotoyer durant ces quatres années. Ensemble, dans leur bureau où ils ont eu la bienveillance de m'accueuillir, nous avons beaucoup ri, discuté, débattu avec acharnement et parfois souffert aussi. Je sais aussi que j'ai pu leur mener la vie dure, parfois, et je m'en excuse. J'espère que nous pourrons encore savourer quelques bonnes bouteilles de vins comme nous l'avons fait chaque année au Salon des Vignerons indépendants! Pour ces quatres formidables années, merci.

J'ai eu la chance d'arriver dans l'équipe à un moment exceptionnel et excitant où bien des résultats attendus se sont concrétisés. Cela a été possible avant tout grâce à Yacine HALIOUA qui m'a précédé avec sa thèse sur l'intégration III-V sur Silicium et dont j'ai pris la suite directe. Je me rends compte aujourd'hui de l'importante quantité de travail qu'il lui a fallu pour mener à bien ce projet qui partait de peu de choses sinon de l'enthousiasme commun. Je remercie aussi Paul MONNIER et Tim KARLE qui ont complété cette équipe aussi bien par leurs savoirs scientifiques que par leur chaleur humaine. J'ai beaucoup appris avec Paul et je dois avouer que sans sa rigueur, sa méthodologie et son aide précieuse au laboratoire, cette thèse aurait perdu une bonne centaine des meilleures pages!

L'équipe a périodiquement changé au gré des stages, thèses et post-docs. Je remercie les post-docs Frédéric BORDAS et Vito ROPPO pour leurs conseils et nos discussions. Je souhaite une bonne continuation à Guillaume CROSNIER pour la fin de sa thèse dont j'espère qu'elle sera aussi fructueuse et épanouissante qu'elle l'a été pour moi. Enfin, merci à Daniel CHASTANET, Moustafa ABDEL HAFIZ, et à Neeti NEETI pour tout leur travail et leurs bonnes humeurs durant leurs stages respectifs. En particulier, merci à Daniel pour toute son aide sur les

expériences de bistabilité optique. Je souhaite ici adresser une pensée à Neeti qui nous a quitté trop tôt et dont le souvenir, sa gentillesse, son apparente joie de vivre, cohabitent en moi avec la tristesse, le regret et l'incompréhension.

Les années passées au Laboratoire de Photonique et de Nanostructure ont été pour moi des années riches en enseignements et rencontres. Elles ont commencé durant mon stage dans l'équipe d'Alexios BEVERATOS et d'Isabelle ROBERT. Merci à Alexios pour son enthousiasme exigeant lors de mes premières expériences avec les nanolasers! Cette période fut aussi marquée par mon séjour dans le bureau de Robert KUSZELEWICZ et de Sylvain BARBAY dont les jeux de mots, les plaisanteries et les nombreuses discussions autour de la machine à café ont souvent eut raison de mon stress! Merci à eux!

Comme bien des thèses en nanosciences, la fabrication de nos structures doit beaucoup à beaucoup de gens qui maintiennent dans la salle blanche du LPN un savoir-faire et une excellence dont il faut se réjouir, tant qu'ils existent. Je ne peux pas les citer tous mais je tiens maintenant à remercier quelques uns de ceux-la. Merci donc à Xavier LAFOSSE pour ses nombreux dépôts diélectriques ainsi que pour la réalisation des couches de MgF_2 qui me tenaient à coeur, et ce, malgré son emploi du temps chargé! Merci à Luc LE GRATIET pour m'avoir formé au polissage de substrat de Silicium et à l'utilisation de la polisseuse. Je remercie aussi Rémy BRAIVE et Isabelle SAGNES pour avoir pris le temps de réaliser la gravure lithographique pour nombre de mes échantillons. Merci à David CHOUTEAU et Olivia MAUGUIN pour tout le travail d'installation et de calibration lors de l'arrivée de la première presse pour nos collages. Merci à Grégoire BEAUDOUIN et Isabelle SAGNES pour l'ensemble de leur travail sur le bati de croissance MOCVD. Merci à Gilles PATRIARCHE pour ses mesures au microscope électronique à transmission. Je remercie aussi Stéphane GUILET pour m'avoir formé à la gravure sèche et pour ces éclaircissements sur les procédés de gravure plasma. Je remercie enfin Laurent COURAUD pour ses dépôts métalliques et nos discussions durant les longs trajets de bus.

Je remercie l'ensemble des membres du projet européen HISTORIC. Merci également à Pauline MECHET dont les visites ont été des moments très agréables. Je lui souhaite aussi une bonne fin de thèse à l'Université de Ghent.

Je remercie également les membres du service informatique : Mehdi IDOUHAMD, Alain PEAN, Eric LECOMPTE, Olivier ORIA et Lorenzo BERNARDI. Un merci spécial à Lorenzo pour toute son aide pour les simulations numériques sur le cluster. Merci aussi à Joelle GUITTON, Marina FERREIRA et Agnes ROUX pour leur aide précieuse à la réalisation des taches administratives les plus diverses, et ce malgré mes constants retards et oublis.

En dehors de mes directeurs de thèse, quelques personnes ont aussi permis à ce manuscrit de s'améliorer. Je tiens donc à remercier Sylvain BARBAY pour sa relecture de la première partie du chapitre 4 et ses conseils. Mes remerciements vont aussi à Vito ROPPO pour m'avoir signalé quelques erreurs dans les équation du chapitre 5, et à Pauline MECHET pour m'avoir fait remarquer des erreurs dans la partie fabrication de ce manuscrit et pour ses conseils pour les corriger.

Merci aussi à Samir HADDADI pour nos nombreuses discussions autour du design de cavités ou d'implantation de code Python pour réaliser nos masques de gravure, mais aussi pour les

bonnes rigolades quand nous en avions besoin. Je n'oublie pas Philippe HAMEL, Foued SELMI, Ramzi BENCHAMEKH, Viktor TSVIRKUN, Gregory LECLERT ou encore Hugo SALMON et d'autres qui me pardonneront de les oublier mais qui ont aussi eu un rôle important dans ces indispensables moments de détentes.

Durant ces quatres années, j'ai eu la chance de pouvoir compter sur des amis qui ont su me ramener un peu à la vie sociale quand il le fallait et qui ont eu la gentillesse de supporter mes complaintes régulières. Je pense à mes supers colocataires Vincent et Loren (et sa soeur Géraldine!) dont le soutien et les conseils m'ont été précieux. Je pense aussi aux amis de toujours: Nicolas, Fanny, Benjamin, Julien, Laure, Marie, Sylvain, Julien, Gabrielle, Kevin, Nathalie, Léonor, Victor, Emilie, Raph', Wolf',... et aux amis des cours de Japonais: Laura, Léa, Hanan, Arnaud, ... ainsi qu'à l'ensemble du CSPSE Escrime que j'ai lâchement abandonné après mon premier mois de thèse... Merçi à vous tous!

Enfin, j'adresse un très grand merçi à mon père (le seul vrai Docteur Bazin!), à *mi querida* Flor et à mon frère Jean-Baptiste.

Contents

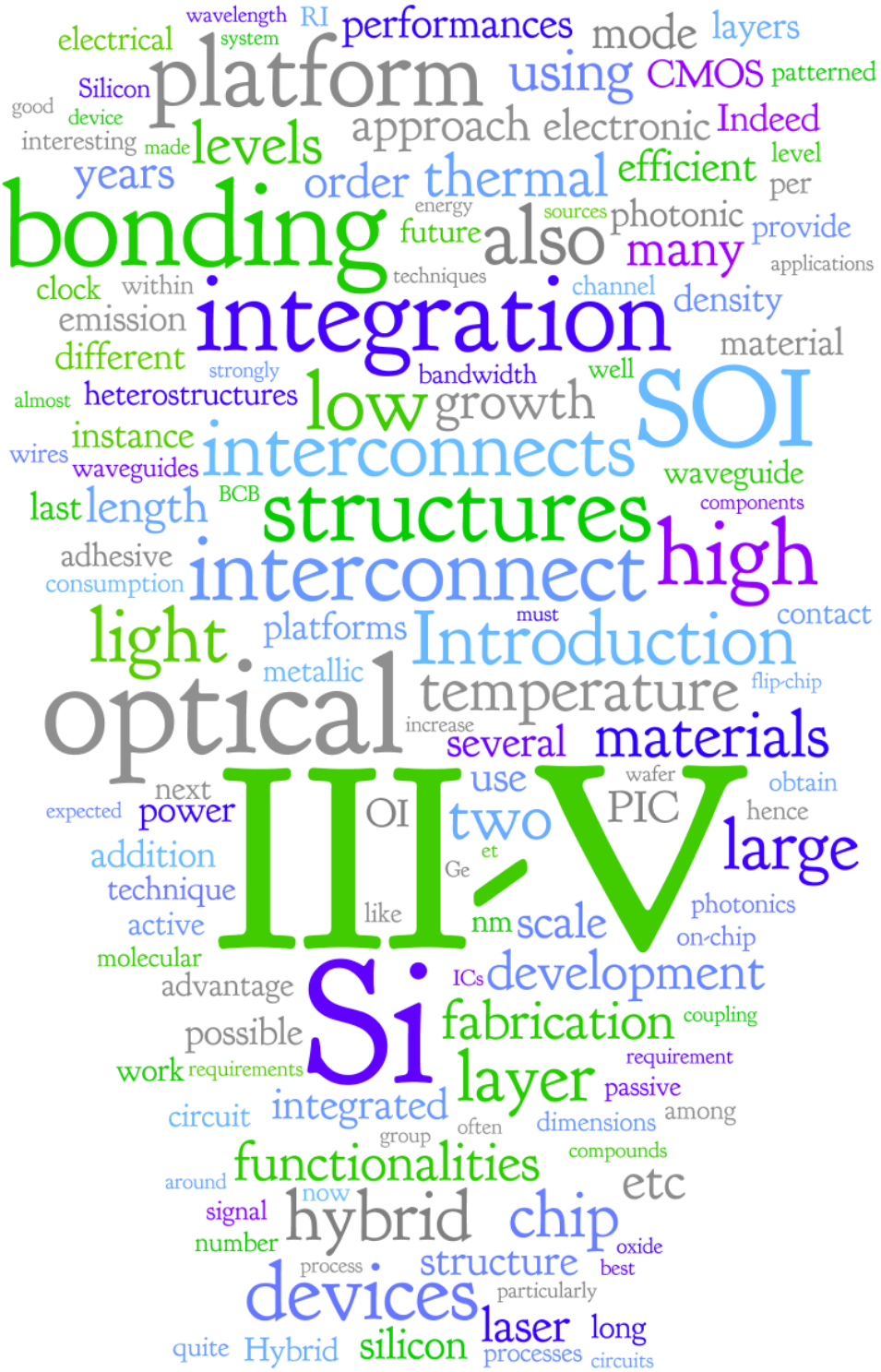
wavelength
RI
performances
mode
layers
electrical
system
platform
using
CMOS
patterned
Silicon
good
device
approach
electronic
Indeed
interesting
made
levels
level
years
order
thermal
efficient
per
bonding
energy
sources
photonic
provide
future
also
many
applications
techniques
clock
within
channel
density
integration
emission
material
different
strongly
bandwidth
well
SOI
almost
heterostructures
low
growth
instance
interconnects
wires
waveguides
waveguide
components
last
length
BCB
structures
high
adhesive
interconnect
consumption
contact
must
light
platforms
Introduction
metallic
flip-chip
optical
temperature
increase
several
materials
wafer
obtain
use
next
III-V
PIC
expected
power
OI
two
hence
large
addition
et
Ge
technique
photonics
like
active
nm
scale
on-chip
molecular
development
ICs
advantage
Si
fabrication
coupling
possible
requirement
work
requirements
layer
passive
integrated
among
circuit
often
dimensions
group
compounds
functionalities
etc
around
now
signal
hybrid
chip
number
oxide
process
structure
best
devices
particularly
laser
long
quite
Hybrid
silicon
processes
circuits

Chapter 1

Introduction

1.1 General motivations of the PhD

The motivations of this PhD have to be sought in the general context of development of optical interconnects (OI) at a chip level.

1.1.1 Context: the interconnect bottleneck

The continuous scaling down of the dimensions of micro-electronic components, initiated more than 50 years ago with the invention of the integrated circuits (IC), has since followed with accuracy the empirical Moore's law which predicts that the number of transistors per chip will double approximately every 2 years [1]. This exponential trend has made possible to obtain in 2012 the commercialisation of CPU with half-pitch dimensions as low as 22 nm! Although this figure is already expected to be outperformed by future generations of chips, the last decade has brought to light major concerns for the future down-scaling processes and particularly in the case of interconnects.

In the latest available edition (2011) of the *International Technology Roadmap for Semiconductors*[1] (ITRS) [2], the purpose of an interconnect is defined as follows:

> *The function of an* ***interconnect*** *or wiring system is to distribute clock and other signals and to provide power/ground, to and among, the various circuit/system functions on a chip.*

[1] http://www.itrs.net/

In Complementary Metal Oxide Semiconductor (CMOS) ICs, several levels of interconnects exist among which the *global interconnect* levels [3] which are dedicated to long distance communications, linking blocks of interconnects of lower levels, bringing them power, ground and clock. The down-scaling of the chip features has brought about serious problems regarding the future performances of these particular levels. Hence, the ITRS report also adds:

> *The fundamental development requirement for interconnect is to meet the* ***high-bandwidth low-power*** *signaling needs without introducing performance bottlenecks as scaling continues.*

This last remark points out the so-called *interconnect bottleneck* which is irremediably getting closer as the dimensions of on-chip interconnects get smaller. Indeed, as the cross-sectional area of the wires, usually made of copper embedded in a low-k dielectric, gets of the order of the mean free path of carriers ($\approx$ 40 nm in copper [4]), the resistivity of the wires increases dramatically, affecting in the same way the RC time constant per unit length of the interconnect.

Moreover, because the RC time constant is also proportional to the squared length of the interconnect, the achievable length of the interconnect is severely limited by the clock frequency under which the system is desired to be operated, thus limiting the available bandwidth [3, 5]. Figure 1.1 shows two graphs plotted by Miller [5] representing respectively the projected evolutions (ITRS data) of the on- and the off-chip clock rates (left graph) and interconnect channel number (right graph) for the next decade. The increase of the needed clock rates and the channel number represents a real challenge for future applications.

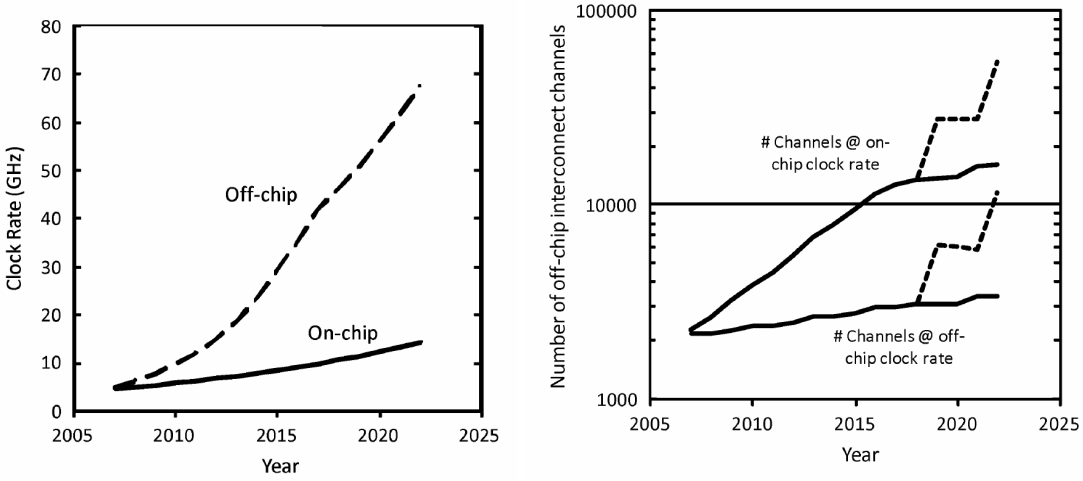

Figure 1.1: *Left: Projections of the on-chip and off-chip clock rates evolution in the next decade. Right: same for the interconnect channel number. From [5].*

In addition, the flow of electrons in these small wires produces through *Joule effect* a higher amount of heat that has to be evacuated through the poorly thermal conducting low-k dielectric. This obviously increases the power consumption of the devices because more power has to be injected to perform the desired functionalities but also an increased amount of power is needed to cool down and regulate the chip temperature. Nowadays, the environmental impact of such increase in the power consumption of chips, specially in datacom/computercom applications, can be huge and cannot be tolerated any longer.

For all these reasons, the "classic" metallic interconnects will, in all probability, fail to deliver the future requirements of high bandwidth and lower power consumption expected in many applications. Several alternative solutions are regularly evaluated by the ITRS interconnect working group such as Carbon Nanotubes (CNT) [6] or Graphene Nanoribbons (GNR) [7]. However, an increased attention is now being devoted to the use of OI in order to replace part of the electronic global interconnect levels.

1.1.2 Optical interconnects

Over the last 30 years, the fast development of optical communication, which accompanied the growth of internet, has allowed with amazing success to respond to the ever growing demand of bandwidth for high data rate signal transmission over very long distances. This was achieved by using optical fibres of extremely low optical losses ($\approx$ 0.3 dB/km at 1.55 μm for single-mode fibres) and also through massive investment in electro-optical technology.

In 1984, long before the observation of the interconnect bottleneck in ICs, the seminal paper of Goodman et al. [8] suggested the replacement of some levels of electronic interconnects by other using optics for Very Large Scale Integration (VLSI) systems. Indeed, the possibility that light offers to avoid the resistive losses of metallic wires was very promising. Soon after, Miller [9] boldly suggested that optical interconnections should be generalised to all interconnections except for very local chip interconnections. In the last 25 years, this assertion has however been qualified and many publications, among which [3, 5, 10, 11, 12, 13, 14] (including papers by Miller et al. and other references cited within these papers), have discussed the benefits of each type of interconnects as a function of many parameters (interconnect length, energy, footprint, etc) and related issues that must be tackled to increase the ICs performances. As an example, it was shown that, for a given set of interconnect width and running frequency, the best choice of interconnect technology in terms of maximum maximum flux density depends strongly on the interconnect length [3, 15]. Indeed, below a certain length of communication (the *partition length*), the use of OI is not justified with respect to electronic ones. While this

length was several 10's of metres long 20 years ago, it has now decreased below a few millimetres in the case of μ-metres large wires carrying only one channel of information at 20 GHz and, as was emphasized by Beausoleil et al. [3], below 100 μm for interconnects supporting 30 channels (see illustration of this in fig. 1.2). Such performances are possible by taking advantage of the unique property of OIs able to support many optical signals in a single interconnect through wavelength multiplexing. Because the partition lengths have largely decreased, OIs are expected to provide efficient solutions for off-chip interconnects, i.e. between $\approx$ cm^2 chips, e.g. for making processors communicate in a multi-core architecture, as well as for on-chip global interconnects. As can be expected by looking at fig. 1.1, the requirement in terms of energy per bit, density and bandwidth are not the same depending on the targeted application. As we will see, the work presented in this manuscript is more oriented towards on-chip optical global interconnects. Note that a review of the different requirements for on- and off-chip optical interconnects can be found in [5].

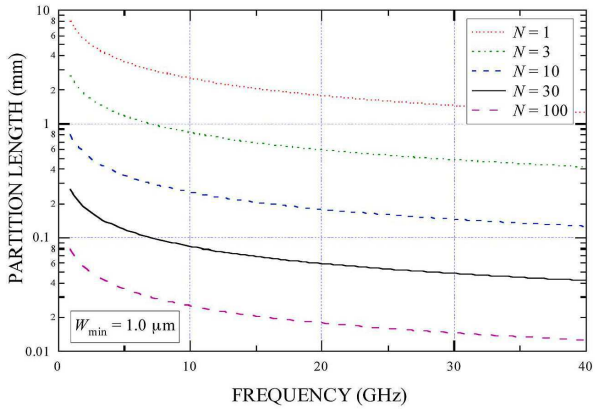

Figure 1.2: *Partition length for a wire/waveguide width W_{min}=1.0 μm. N is to the number of optical channels supported by the wire waveguide. From [3].*

In order to build a full OI system, several elements must be provided. An OI is constituted of:

- a *transmitter circuit* inputting the electrical signal into an optical output device.
- an optical output device, either a *laser source* and/or a *modulator* coding the optical signal.
- an *optical channel*, either a waveguide or simply free-space.
- a *photodetector* connected to a receiver circuit.
- a *receiver circuit* converting back the optical signal in readable electric signal.

Such a system will be competitive with electronic interconnects only if it fulfils several requirements [5, 14], among which:

- the fabrication compatibility with the silicon electronics and CMOS fabrication processes.
- a very low energy consumption per bit below a few 10's of fJ per bit.
- a high integration density (10^4-10^5 of devices per mm^2 corresponding to devices footprint $<$100 μm^2).
- a high bandwidth capacity ($>$ 10 GHz).
- a low cost[2].

We can also add another requirement which is not often discussed in OIs literature: a low thermal sensitivity. Indeed, it is often required that the devices work at room temperature and over a large span of temperature, usually up to 50-70 °C. This issue is quite problematic as the operation of many semiconductor optical components is strongly dependant on temperature. Of course, many implementations of OI can be provided and eventually depend on the targeted application, on the architecture of the chip at lower levels, etc. In this work, we did not address the whole OI design and fabrication which is a huge task, but we chose to tackle the issues, not-less ambitious, directed towards the integration of a light source within a chip and the development of integrated functionalities.

Our project takes advantage of two well mastered platforms for photonics: the silicon (Si) photonics and the III-V photonics.

1.2 Background

1.2.1 Si and III-V Photonics

In photonics, the challenges which we face today swirls around providing together the necessary *active* and *passive* functionalities fully integrated into a chip. These functionalities are, among others, light emission (laser), filtering, wavelength routing ((de)multiplexing), detection or switching. Because all of these functionalities have to comply with ultra-compactness and low-loss circuitry while maintaining low cost production in CMOS fabs, few materials can pretend to fit in. Besides it is very unlikely that a single material will be able to provide all of them at once with the desired performances previously cited.

For passive functionalities and particularly for waveguiding, several options are still under

[2]This last requirement is quite difficult to evaluate, as the cost usually diminishes with the production quantity and the investments pursued in order to develop new processing technologies.

exploration, e.g. using silicon nitride (SiN) [16, 17] or aluminium nitride (AlN)-On-Insulator [18] structures. However, Silicon-On-Insulator (SOI) is indubitably the most mature platform at the moment for passive photonic due to decades of investment in silicon (Si) μ-electronics industry. Indeed, because mass production lines with silicon-based material already exists, SOI possesses the advantages of low cost, high yield and high reliability. Optically, Si is transparent in the infrared range above 1.11 μm and hence enable light transmission in the telecom windows around 1.3 μm (O band) and 1.55 μm (C band). In order to confine light efficiently, SOI structures [19, 20] also benefits from the high refractive index (RI) of Si (≈ 3.46) combined with its natural oxide, SiO_2, of low RI (≈ 1.45). In the last decade, the demonstration of extremely compact SOI waveguides (a few hundreds of nm wide and high) with very small curvature radius (a few μm) have been achieved [20] (see fig. 1.3). In addition, the optical losses attained for straight waveguides are now typically of only 2-3 dB/cm.

These properties make the SOI platform almost "ideal" for developing integrated photonic circuits (PIC) at a large scale in the years to come. However, silicon suffers from one major drawback: its indirect electronic band-gap which impedes almost all radiative recombinations of carriers and therefore makes it unsuitable for efficient light emission. In addition, crystalline Si is a centro-symmetric structure, which forbids, at least in bulk material, to observe (and use) second-order non-linear effect, such as second-harmonic generation (SHG) or optical parametric generation (OPG). Many works have targeted to develop Si-based laser sources like, for example, studies using Raman effect [21] or strongly Erbium (Er) doped Si layers [22]. However, they reveal very inefficient and power consuming solutions to be considered at the moment for large scale applications.

Therefore the SOI platform is the best existing platform for immediate industrial realisations of *passive* functionalities in PIC.

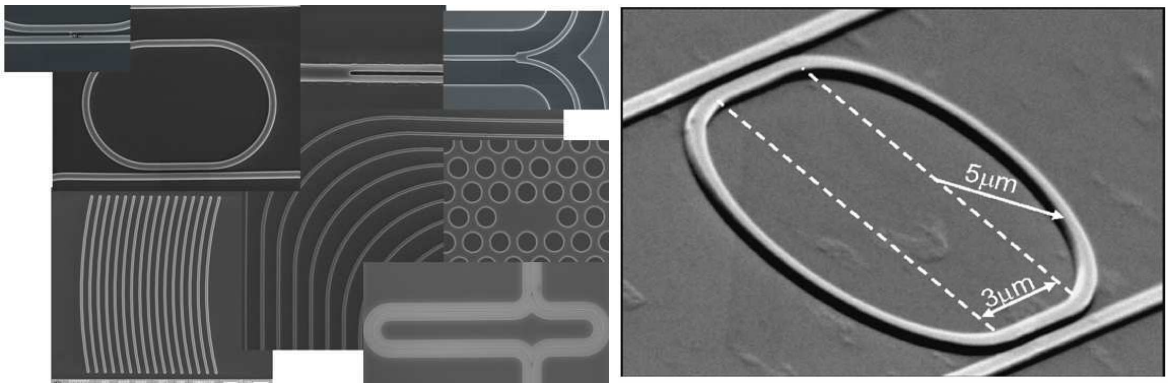

Figure 1.3: *Left: Examples of SOI photonic structures. From the IMEC (Belgium) website. Right: 5. Racetrack resonator in 220nm-thick SOI. From [20]*

If we seek out for efficient light sources, III-V semiconductors are the best available choice. Since the first demonstration of coherent emission in Gallium Arsenide (GaAs) [23] which almost followed the invention of the laser in 1960, III-V compounds have been extensively used as light emission source and had a leading part in the development of the so-called *optoelectronic* domain. These compounds are formed with a combination of atoms of group III and V of the periodic table. They can be grown, layer by layer, by different epitaxial methods (Molecular Beam Epitaxy, Metal-Organic Chemical Vapour Deposition (MOCVD), etc), into binary compounds (InP, GaAs, GaN, AlAs, etc), ternary ones (InGaAs, GaAsP, InGaP, etc), quaternary ones (InGaAsP, AlGaAsP, etc) or even quinary ones (GaInNAsSb, etc).

Their most interesting feature is that most of them possess a direct electronic band-gap which allows to achieve efficient light generation when an electrical current is injected into them. By playing on the different atom's relative concentrations, the band-gap energy of these compounds can be largely shifted to obtain light emission in a wide range of wavelength. Hence, using the great variety of possible III-V alloys, it is possible to tailor almost at will their emission wavelength from UV to infrared.

Furthermore, the development of the III-V growth processes enabled the fabrication of heterostructures containing Quantum Wells (QW) or Quantum Dots (QD) in order to engineer the carrier confinement and tailor the electronic density of states in 2 or 3 dimensions (see fig. 1.4 & 1.5). Consequently, the luminescence due to radiative carrier recombinations within these structures is also widely tunable. In addition, internal quantum efficiency found in optimised structures can be extremely high (≈ 100 %) which is an asset for building low-power consumption devices.

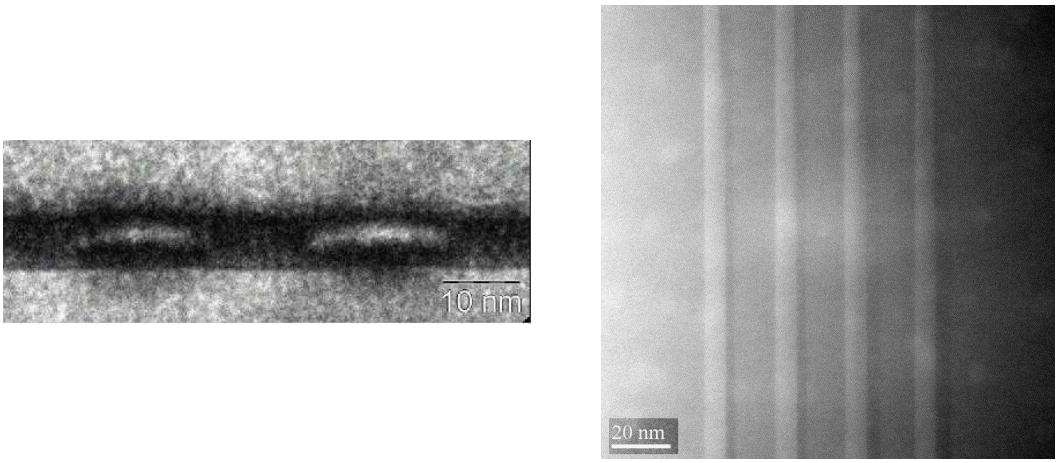

Figure 1.4: *Transmission Electron Microscopy (TEM) cross-section pictures of III-V heterostructures (from LPN): on left, 2 InAs QDs; on right, 4 InGaAsP/InGaAs QWs.*

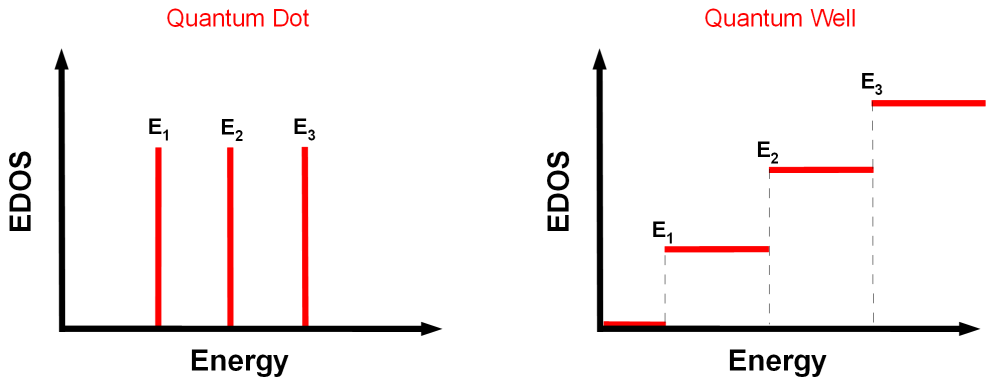

Figure 1.5: *Schematics of the typical Electronic Density Of States (EDOS) for QDs and QWs heterostructures.*

Many III-V optoelectronic devices like the popular Vertical Cavity Surface Emitting Laser (VCSEL) are nowadays produced on a very large scale. Other attractive and prominent optoelectronic devices using III-V materials including laser/detectors from visible to THz frequencies, modulators, amplifiers were developed thanks to the telecom advent.

However, contrarily to Si, they are not as well suited for guiding the light in ultra small waveguides because of the absence of a natural oxide (which would provide the necessary index contrast) and because of a much less mature processing technology, particularly at the micro/nanoscale levels.

The properties of III-V structures makes them the natural choice for building the *active* functionalities necessary in future PICs.

An important benefit for the use of III-V materials in PIC is their good optical compatibility with Si as their RI are quite high ($\gtrsim 3$) so that the RI contrast with Si is small. So, a promising idea will be to develop a Silicon photonic platform, enhanced with integrated III-V based optical active devices, which combines the very best of both worlds. This silicon/III-V photonics platform will minimise costs and maximise performances, hence opening up the field of large scale photonic integration.

Yet, such integration has been facing major issues: the strong lattice mismatch as well as the large difference of thermal expansion coefficients between Si and many III-V alloys. For instance, the lattice mismatch between Si substrates and Indium Phosphide (InP) is 8%, and the thermal expansion coefficients are, respectively, 2.6 $\times 10^{-6}$ $^{\circ}C^{-1}$ and 4.6 $\times 10^{-6}$ $^{\circ}C^{-1}$. Consequently, the direct epitaxial growth of III-V on Si leads to high dislocation density at the interfaces, preventing the growth of thin (< 500 nm) defect-free layers. Monolithic integration of III-V on Si PIC faces several other challenges such as the controlled growth on SOI patterned with a photonic

circuit and the decrease of the growth temperature ($\lesssim$ 650 °C) for CMOS fabrication process compatibility[3].

In the next part, we briefly present the different strategies adopted, up to now, with the view of integrating III-V devices on SOI PIC, and afterwards present the state of the art in hybrid structures.

1.2.2 Hybrid III-V /SOI platforms

The development of hybrid platforms has followed many different paths in order to fabricate PIC combining III-V and Si. In the next paragraphs, we summarize and discuss the most interesting ones.

More detailed reviews of these solutions can be found, for instance, in [25, 26, 27].

1.2.2.1 Flip-Chip approach

The most straightforward integration strategy is to bond the III-V devices, hence fabricated before the bonding, directly on top of Silicon circuits. This so-called *flip-chip* method of integration [28, 29, 30] puts into contact the III-V devices with the CMOS circuitry through conductive solder bumps. These bumps play several roles in the flip-chipped structures, enabling electrical contact of the device with the CMOS circuit, helping the heat spreading into the chip, impeding parasitic electrical current between the two levels, etc. Despite the robustness of the technique in terms of fabrication, it possesses inherent inconvenience for large scale integration. For instance, the bump size are usually several 10's of μm long which excludes high density integration (see fig. 1.6). The precision of the alignment procedure during the bonding is also quite low and offsets much higher than 1 μm are common. In addition, each III-V die, potentially containing arrays of devices dedicated to one specific functionality (sources, detectors, modulators, etc), must be aligned precisely and bonded individually on the CMOS chip. This could also be a rather slow process hence costly for large scale integration. Finally, the coupling efficiency between the III-V device (like a VCSEL) and the Si waveguide circuitry underneath can be problematic.

[3] A too high temperature applied on finished ICs can lead to high diffusion of dopants near metallic contact and impact strongly the circuit performances. The *thermal budget* of the chip fabrication accounts for such diffusion processes taking places during all the high-temperature steps and must remain as low as possible for the integration to be a viable strategy [24].

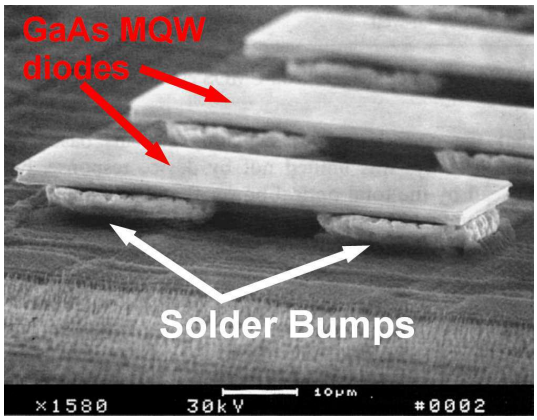

Figure 1.6: *Scanning Electron Microscope (SEM) pictures of GaAs Multiple Quantum Wells (MQW) diodes after flip-chip bonding and substrate removal. From [31].*

Because the flip-chip technique does not provide an ideal platform for large scale integration, a great deal of attention is now focused into the development of a unique hybrid platform where the III-V would be in the vicinity of the Si circuitry.

1.2.2.2 Direct III-V growth

In the last 25 years, many studies were devoted to monolithically integrate active material like III-V heterostructures but also Germanium (Ge) on Si substrates. The direct growth of III-V material above Si can be distinguished into two kinds: one aims at growing bulk material (but also stacks of bi-dimensional layers such as quantum wells), while the other aims at directly growing 3D nanostructured objects such as nanowires, pillars or quantum dots. Concerning the latter kind of growth, it is the subject of intensive work by many groups worldwide. Recently, the group of C. Chang-Hasnain at Berkeley University (USA) has demonstrated room-temperature optically pumped laser operation with GaAs/InGaAs nanopillars grown by MOCVD above silicon and emitting around 950 nm [32], hence outside the transparency window of silicon. One of the issues with this growth technique is it makes use of peculiar Si substrates, with non-conventional crystallographic orientation ((111) instead of (001)). Moreover, the control of the emission wavelength of such optical structures is fixed ones-and-for-all during the growth, by the pillar size and the concentration of Indium atoms, and no solutions to fix separately the emission wavelength of each nanolaser has come yet. In my humble opinion, such issues and others (homogeneity, yield efficiency of the fabrication, etc) are still strongly hindering further industrial applications.

The strategies to grow III-V bi-dimensional heterostructures are extremely diverse, but most of them rely on depositing/growing a buffer layer between the Si and the III-V which will absorb or distribute the strains between the two materials in order to limit the formation of

dislocations. For instance, III-V heterostructures were grown above thick relaxed III-V layers ($\approx$ 1-10 μm) [33] but also above "virtual substrate" of Ge/Si (or graded GeSi layers) [34, 35, 36]. Other thinner buffers ($\approx$10-100 nm) made of dielectric materials (Gd_2O_3 [37], $SrTiO_3$ [38]) gave interesting results in term of obtained dislocation densities and III-V emission intensities but these techniques are not yet mature for large scale integration. Finally, let's cite the Epitaxial Lateral OverGrowth (ELOG) technique, where the III-V growth occurs inside a dielectric window or trench (SiO_2, Si_3N_4) which prevents the propagation of the dislocations [39, 40, 41, 42]. Despite many years of work, the monolithic approach struggles to reach the requirements in term of growth quality, thickness of the heterostructures above Si and thermal budget to be, at the moment, of practical interest for large scale integration.

As an aside, it is worth mentioning here that monolithic integration of Germanium (Ge), which has an indirect electronic band-gap but can be highly doped and/or strained in order to distort the bands and foster the radiative recombinations, is also subject to intensive research. Lasing in Ge-on-Si structures has recently been demonstrated [43, 44] but is not yet efficient enough to be interesting for immediate integration. In addition, the growth of Ge needs a relax step at 650 °C which would significantly increase the thermal budget of the interconnects fabrication based on this approach. Nevertheless, more research effort will probably provide better performances. However, Ge photodetectors directly grown on Si are often considered as one of the best solution to convert optical data into electronic signals [45, 46, 47, 48].

1.2.2.3 Heterogeneous integration approaches

The best road towards highly functional complex PIC's is to heterogeneously integrate active InP-based components onto passive SOI circuits. The heterogeneous approaches make use of different bonding techniques of the III-V epitaxial layers on the Si layers. Many bonding processes have been developed over years, most of them using an intermediate layer between the III-V and the Si to achieve the hybrid structure. The main techniques of bonding for fabricating III-V/Si hybrid structures are:

- *wafer fusion* bonding [49, 50, 51].
- *metal* bonding [52, 53, 54].
- *molecular* bonding [55, 56, 57, 58].
- *adhesive* bonding [59, 60, 61, 62].

Let's cut short the discussion by putting aside the bonding through a metallic layer (or an eutectic alloy such as Au-GaAs [52]) which can be used to fabricate, at moderately high temperature (300 °C), nanostructured hybrid III-V laser on Si [53, 54]. Despite the advantage for electrical contacting and heat spreading brought by the metallic layer, its presence is problematic to optically couple the Si PIC to the III-V layer, as the metallic layer is highly absorbing.

Wafer fusion [50] is a technique where the III-V and Si materials are put in direct contact with each other (without the presence of any intermediate layer), so that strong chemical bonds are created between the two materials at their interface. The process requires a precise alignment of the crystallographic axis of the 2 wafers, as well as a thorough cleaning(s) of both surfaces. Besides, it is realised at relatively high temperatures (often around 650 °C). While this approach continues giving interesting results for GaAs/Si heterogeneous structures (see for instance recent publications by the group of Y. Arakawa [51, 63]), the wafer fusion is less compliant with III-V materials showing larger thermal expansion coefficient differences with that of silicon, like InP-based materials. Indeed, when the temperature is decreased from $\approx$ 650 °C to room temperature, dislocations appear, propagating and forming cracks on the bonded sample.

Nowadays, it is the *molecular* and the *adhesive bonding* techniques which are giving the most promising results. The next subsections are dedicated to the presentation of the two important platforms which emerged from the use of these bonding approaches. Both platforms enable to obtain integrated light sources, i.e. lasers, but differ substantially in their optical hybridisation schemes. The first scheme is a fully hybrid approach were the optical mode of interest lies in both the Si and the III-V. The second scheme is an evanescent coupling approach where the two layers (III-V and Si) support distinct modes (a guided mode in the Si and often a cavity mode in the III-V), separated by a low-index layer.

The development of these platforms is driven by the possibility, contrarily to the flip-chip approach, to process in parallel a very large number of devices directly on top of the Si IC. Moreover, this sort of 3D integration is also an opportunity for the conception of optical functionalities with enhanced performances by exploiting each material for what it is good at. Note that a review of these two platforms can be found in [27].

1.2.2.3.a Hybrid Silicon Evanescent Mode platform

The Hybrid Silicon Evanescent Mode platform [64] results from the work of the Bowers group (UCSB, USA), and further collaborations with Intel. III-V/Si hybrid structures are obtained through a particular molecular bonding technique. This technique is based on the surface preparation of the wafers with a thorough cleaning and an oxidation using an O_2 plasma to obtain a

thin (5 nm) oxide layer. The two surfaces are then put in contact while applying a pressure of a few MPa at 300 °C for 12 hours [57]. It is during the latter step that strong covalent bonds are created between the silicon oxide and the two materials.

In 2006, Fang et al. [65] demonstrated a hybrid III-V/Silicon electrically pumped laser diode. Figure 1.7 shows the cross-sectional scheme of the structure, with the mode distribution superimposed, and the corresponding SEM pictures of the fabricated structure. The III-V heterostructure contains AlGaInAs quantum wells sandwiched between doped regions for electrical contact. The SOI level is patterned into Si waveguides 2.5 μm-wide and 0.76 μm-high. In these devices, the control of the electromagnetic field is achieved through the only control of the Si waveguide mode whose distribution is mainly concentrated in the silicon core while the evanescent tail of the field overlaps with the III-V active material bonded on top. One advantage of this technology is the low constraint on the alignment of the III-V on the SOI level. In the end, the laser cavity is 860 μm-long. However, from a design point of view, the field overlap with the QWs is quite low, typically a few percent. Due to the distribution of the mode within the Si and the III-V, it is not possible to localise the light in tiny structures with this approach. Because the size of the structures is at least 500 μm^2, they are not ideal for dense on-chip integration.

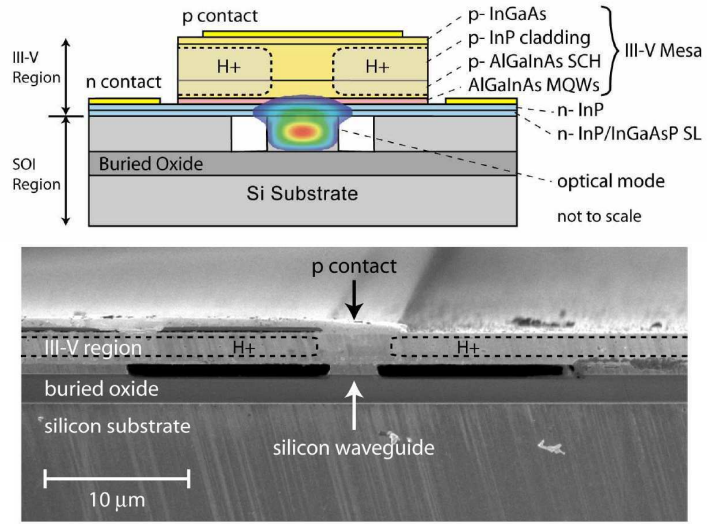

Figure 1.7: *Top: Cross-sectional scheme of the Hybrid Silicon Evanescent Mode structure. Bottom: SEM picture of the corresponding fabricated structure. From [65].*

In the next subsection is described the platform used in our work which is the only current alternative platform for the realisation of hybrid III-V/Si devices. Many features related to the use of this platform (design, fabrication, coupling, etc) will be further described all along the manuscript.

1.2.2.3.b Hybrid Evanescently-Coupled Modes platform

The Hybrid Evanescently-Coupled Modes platform was first demonstrated by the Photonic Research Group of Ghent University (Belgium). Unlike the platform developed by Bowers and co-workers, the optical structures made within this platform are constituted of two very distinct patterned levels, the III-V and the SOI, separated by a low-RI layer. The SOI waveguide mode and the III-V, patterned into, for instance, a cavity, are evanescently coupled to each other, i.e. each supported mode is weakly perturbed by the presence of the other level. An illustration of this type of structure is shown in figure 1.8 where an electrically pumped microdisk laser [66] is integrated above a SOI single mode waveguide (of typical dimensions 300-600nm-wide and 220nm-high) [67, 68] .

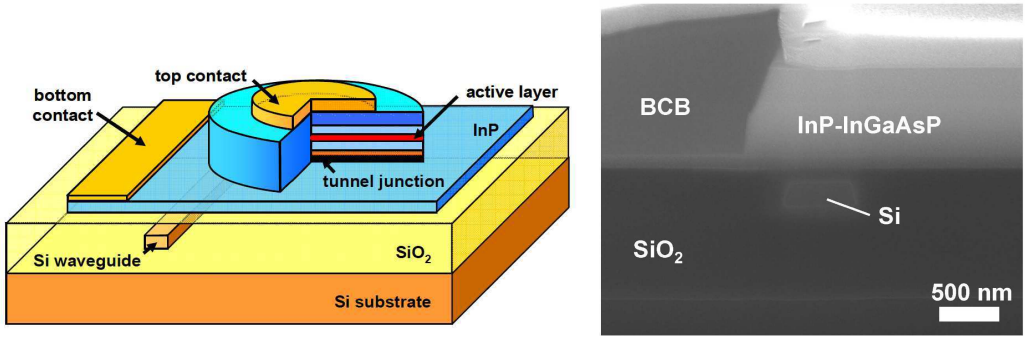

Figure 1.8: *Left: Scheme of the electrically pumped InP-based microdisk laser integrated with a nanophotonic SOI waveguide. Right: SEM picture of the structure. From [68].*

The fabrication of these structures relies, here, on adhesive bonding using the planarising polymer Di-Vinyl-Siloxane-Benzo-Cyclo-Butene (DVS-BCB) [59] as an intermediate low-RI layer, which is a rapid and convenient alternative to molecular wafer bonding. Sensitivity to particles, roughness and contamination is significantly relaxed using adhesive bonding. Bonding to patterned substrates is generally more challenging than to bare wafers, as the polymer conformity varies with the local pattern density of the underlying waveguides. BCB is a particularly good candidate as it possesses useful planarising properties. This adhesive bonding has also the advantage to be done at low temperature, around 300 °C. At this temperature, the liquid BCB, spun on the SOI before bonding, polymerise into a glass-like material of low RI ($\approx$ 1.5) and transparent in the infrared range. Hence, it is possible to obtain, simultaneously, a good optical confinement of each level and an efficient optical coupling between the two modes. Note that a disadvantage of BCB is its low thermal conductivity which makes, the thermal spreading from III-V less efficient. However, an efficient thermal management can be realised either *actively* by thermo-optic tuning [69, 70, 71] or *passively* by optimising the III-V surrounding materials, as

it is presented in detail in this thesis.

Note that, if, for some reason, BCB is not suitable for the heterogeneous integration of photonic components, silica-on-silica molecular wafer bonding can also be used to assemble the 2 levels as it is regularly done at LETI (France) [72, 73]. However, in this approach, the surface cleanliness is extremely stringent for the bonding yield efficiency.

In conclusion, the adhesive bonding approach allows to bond a wide variety of materials in order to mix and match different functionalities into a PIC.

Yet, the hybrid structures integrating microdisks cavities do not take full advantage of the ultimate optical confinement brought by the recent development of nanophotonics. Indeed, the light-matter interaction strength can be pushed to its limit by the use of ultra-small cavities with very long photon lifetime. Our approach is to bring the existing hybrid platform completely into the nanophotonic domain by using its most emblematic structures, the Photonic Crystal (PhC) nanocavities.

1.2.3 PhC-based Active Devices

As we will detail further along this manuscript, Photonic Crystals are optical structures based on strong and periodic variations of the refractive index with pattern pitches of only a few hundreds of nanometres, for the case of wavelengths ranging from 1 to 2 μm. They enable a unique control of the light propagation and, moreover, of the light confinement at the wavelength scale by using so-called "defects" in the periodic pattern. PhCs nanocavities allow to confine the electromagnetic field within tiny volumes V, below $(\lambda/n)^3$, close to the diffraction limit, with quality factors Q up to 10^9 (i.e. photon lifetime above 10's of ns). In addition, the spontaneous emission rate of emitters placed in such structures can be enhanced or inhibited proportionally to the ratio Q/V which can be extremely high. Hence, it is expected that they will be fundamental building blocks of ultra-low power consumption and high bandwidth PICs [74]. In practice, most of the recent demonstrations of functionalities made with PhCs have been done with bi-dimensional structures consisting in subwavelength-thick suspended III-V membrane, with one (or more) array(s) of holes etched within (a SEM picture of a suspended PhC membrane is represented in figure 1.9). As we will see in chapter 3, their fabrication is a challenging task, particularly within III-V semiconductors, and continues to be improved with the development of nanostructuration technologies.

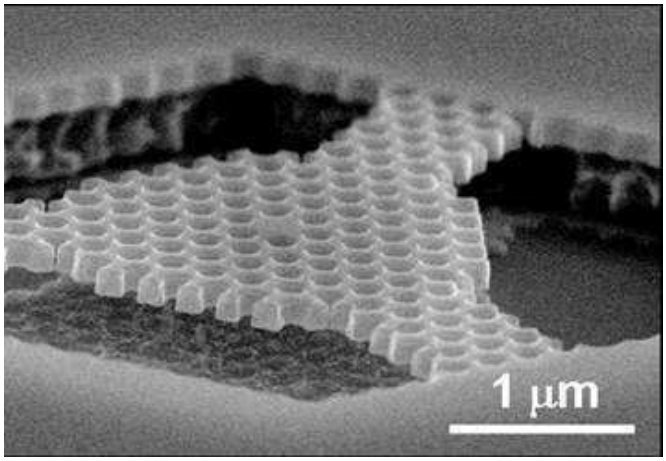

Figure 1.9: *SEM picture of a GaAs PhC microcavity etched on a 180 nm-thick membrane.*

Therefore, several groups worldwide (S. Noda's lab at Kyoto University (Japan), J. Vuckovic's group at Stanford University (USA), M. Notomi's and S. Matsuo's groups at NTT labs (Japan), M. Loncar's group at Harvard University (USA), O. Painter's group at Caltech (USA), T. Krauss's group at the University of St Andrews, A. De Rossi and co-workers at Thales Research Technologies (France), ...) have devoted considerable effort to render PhC structures usable in PIC by demonstrating highly efficient functionalities which take advantage of the exceptional optical confinement properties of PhC nanocavities as well as the strong light-matter interaction. The ambition is many fold: cavity QED and/or opto-mechanical effects, low-threshold PhC lasers, high speed modulation for application in high speed communications, non-linear physics...

Even though the demonstrations are impressive, the road to applications is still long. As an example, up to my knowledge, few system experimentÃ¨[75, 76, 77] has been performed on PhC non-linear devices (high bit-rate with BER measurements). After years of intense research, important issues remain indeed, some technological :

⇒ control over the operation wavelength;

⇒ reproducibility;

⇒ heat management;

and some fundamental:

⇒ optical coupling of the PhC nanocavity;

⇒ understanding in detail of the light-matter interaction for optimised performances.

1.3 Specific aims of the PhD

1.3.1 Toward Si Integrated Nanophotonics Devices with Photonic Crystals

The approach of the present work is to show the high potential of a PIC which integrates active III-V PhC-based devices above a passive SOI circuitry. The broad foundation for this work had been laid through a PhD work[4] shared between the Photonic Research Group at Ghent University and the Laboratory for Photonics and Nanostructures (LPN). It was within this work that the first hybrid III-V PhC /SOI samples were fabricated through the BCB bonding technique [79], mastered and improved. Many aspects were enlightened in order to couple efficiently the two optical levels constituted of a III-V PhC evanescently coupled to an underlying SOI waveguide. For example, effort was devoted to solve the issue of the alignment between the III-V etched pattern and the SOI waveguide. This work eventually resulted in a alignment precision below 30nm, as it is illustrated in figure 1.10 [62].

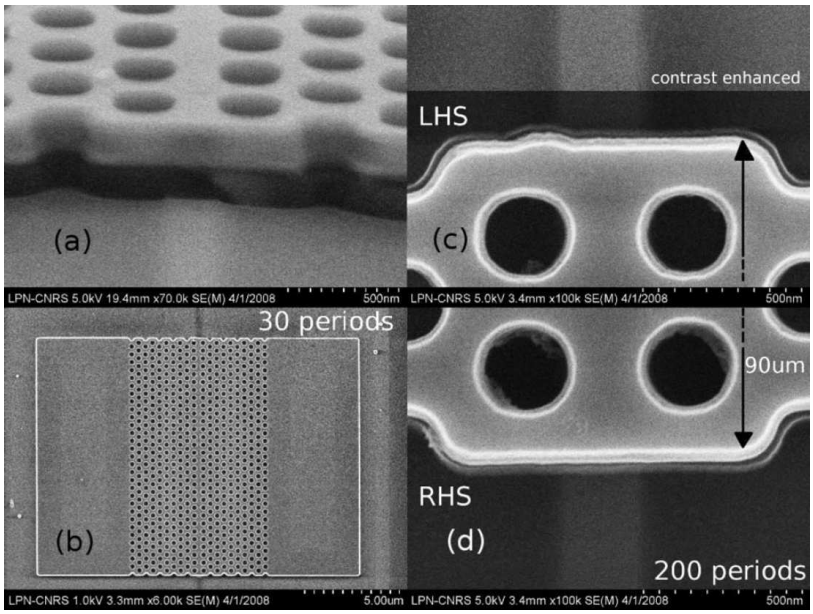

Figure 1.10: *SEM pictures of a hybrid III-V/SOI structures into which an InP-based membrane has been etched with a PhC defect waveguide. a) SEM angled view of the end of the sample showing the patterned InP layer on top of the etched intermediate BCB layer, the Si guide is barely visible to the SEM, here we see a slightly lighter region, b) full InP mesa containing etched* $\approx$ *13 µm short PhC, c) LHS of longer guide with enhanced contrast to display alignment with underlying waveguide, d) RHS of waveguide, which is* $\approx$ *90 µm further along the waveguide. From [62].*

[4] Yacine Halioua, "*Study of hybrid III-V/Si photonic crystal lasers*," 2011 [78].

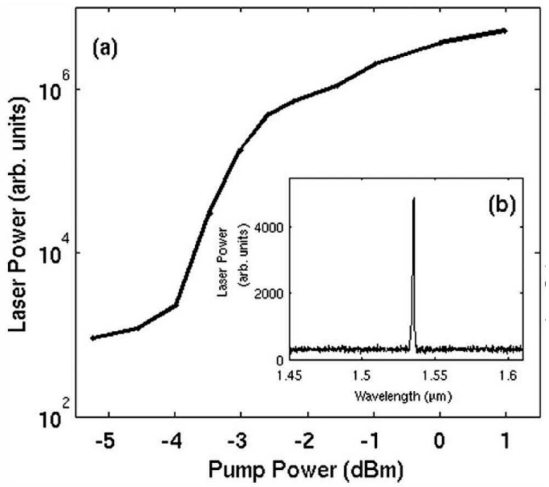

Figure 1.11: *Laser emission power, from the structure showed in 1.10, collected through the SOI waveguide as a function of the optical pump power in log-log scale. From [62].*

In these samples, laser operation was observed at room temperature due to the enhanced light-matter interaction provided by the low group velocity mode of the PhC defect waveguide (see SEM image) with the 4 InGaAsP/InGaAs quantum wells [79] (see fig. 1.11).

The more recent work in the context of my thesis focused on trying to fulfil the requirements expected from integrated optical source for OI applications through the fabrication within the hybrid platform of PhC nanocavities, instead of slow-mode PhC waveguide, which embed III-V active material. PhC nanocavities are indeed outstanding objects that will certainly prove to be in the future one of the best solutions for large scale photonic integration. At the beginning of this PhD, very crucial aspects had yet to be solved and the underlying physics had yet to be unravelled. In order to integrate the nanolasers into a photonic circuits, we aimed at fabricating and operating in the CW regime a waveguide-coupled PhC nanolaser which should have low power consumption, low footprint ($< 50\ \mu m^2$), a potential for being used as a switch with switching times of the order of picoseconds or tens of picoseconds requiring only femto-joules switching energies. As the reader will see, most of these requirements can be achieved in our platform.

1.3.2 Multi-tasks work: modelling, fabrication, experimental characterisation

It is well known that optoelectronic research studies requires to carry out a versatile work which includes:

- design aspects, from the beginning concept(s) (which often answers basic questions, e.g. "how to interface photonic crystal?", "how to integrate III-V on SOI?", etc) to the numerical simulations.

- fabrication aspects (which materials? which processes? what are the critical processes to master? etc).

- experimental aspects (what are the wavelengths of interest? what is the required sensitivity for the detection? how to detect fast phenomena? etc).

Moreover, in order to be efficient, continuous feedbacks resulting from all these different aspects (experimental $\longrightarrow$ fabrication, design $\longrightarrow$ experimental, etc) are part of tedious but necessary procedures to unambiguously determine the origin of the observed effects. During the last 4 years, I had the chance to be involved in all 3 aspects.

This multi-task work was achieved with the remarkable facilities and resources of LPN. While the numerical simulations (electromagnetic, thermal, etc) benefits from a 20 processors computer cluster, the fabrication of the samples are almost entirely done in the LPN ($\approx$1000 m^2) clean-room (see pictures below), which is a great advantage in terms of control of the sample quality and its fabrication reproducibility.

From the experimental point view, the lab work also benefits from the large number of apparatus of many kind (detectors of various speed and sensitivity, optics, mounts, mechanical actuators, laser sources, electronic signal processing systems, etc) which are required to investigate the many properties of our hybrid samples and which we brought,little by little, onto the optical table(s).

1.3.3 Participation to national and international scientific projects

This work gave me the opportunity to participate in one national (French) project and three more international (European) scientific projects which I list here after.

- FP7 European Project "HISTORIC" 2008-2011 (Website)
- French ANR Jeunes Chercheurs "PROWOC" 2009-2012
- FP7 European Project "COPERNICUS" 2010-2013 (Website)
- FP7 European Project "PHOXTROT" 2012-2016 (Website)

Together with the PROWOC [5] French project which funded most of my PhD (three first years), the European project HISTORIC targeted to the integration of large number of active devices (microdisks, PhCs) within the hybrid platform as well as integrate all-optical flip-flops and gates with these devices. This project was a collaboration between the IMEC/Ghent University (Belgium), the Technical University of Eindhoven (TUE, Netherlands), the Zurich IBM Research Laboratory (Swiss) and LPN (France). Most of the result presented here were done within these two projects.

In the European project COPERNICUS, regrouping researchers from 5 academic laboratories and 2 industrial partners, one of the major aim was to obtain low-power and high speed AOGs (all-optical gates). Within this project, we investigated switching processes based on the non-linear change in the refractive index induced by photo-excited carriers; this change shifts the resonance of a PhC cavity which may thus be used for switching purposes. In order to achieve fast AOGs, the recombination rate is manipulated in InP-based materials in order to drastically reduce the carrier lifetime while preserving the quality of the III-V PhCs. This is done by growing InGaAs QWs directly at the PhC surface which decrease the carrier lifetime by more than a factor 10. Note that this project is an on-going project which has already allowed the demonstration of fast switching at high repetition rate (> 10 GHz) with low energies. These samples are also potential candidates for efficient power limiters and for wavelength conversion operations. Recently, error free 20 GHz wavelength conversion using sub milliwatt peak powers was obtained in CMOS compatible systems (system measurements were done at the "Foton"

[5] InP **P**hotonic c**R**ystal **O**n silicon **W**ire hybrid **O**ptical integrated **C**ircuits

CNRS laboratory(France)). However, the results on these samples will not be presented in this manuscript but have already been partially presented in international conferences and will be found soon in publications.

Finally, the PhoxTroT[6] project, started in october 2012, is an extension of my work and regroup a large number of industrial partners who are harnessing the integration of optical links for computer interconnect (at very different scales). Our contribution will be the design of electrically pumped nanolaser in hybrid III-V/SOI structures where the PhC is etched directly into the SOI waveguide below the contacted III-V material, hence in a slightly different approach than the one this manuscript focused. This project, which funded the last year of my PhD, is still at an early stage but has already enabled the design of optimised SOI PhC cavities similar to the ones designed for the present work.

1.4 Organisation of the Manuscript

This manuscript is organised in 6 chapters, including this introductory chapter.

The Chapter 2 is devoted to the specific study of the Photonic Crystal (PhC) pattern etched in the InP-based membrane. The prominent properties of PhCs are introduced and an analytical design of high quality factor PhC Wire Cavities, fully encapsulated in low-RI surrounding materials and compatible with a very efficient optical coupling, is presented. The proposed cavity design is first numerically studied and is then used to fabricate real structures above Si substrates. Optical experiment are realised in order to compare their features with theoretical ones.

In chapter 3, the fabrication processes of our hybrid III-V/SOI structures, combining III-V PhC cavities above SOI waveguides, is described in detail. Our most recent progress in the fabrication are also presented, including the use of SiO_2 and MgF_2 to encapsulate the PhC cavities.

The Chapter 4 is dedicated to the laser emission in the hybrid structure. A nanolaser model specific to the use of QWs is developed and analysed numerically. Emphasis is directed towards the impact of spontaneous emission factor β, quality factor Q and non-radiative carrier lifetime τ_{NR}. The experimental characterisations with a micro-photoluminescence experimental set-up are shown. The two subsequent parts tackle issues relative to the continuous-wave operation of the laser: the heat sinking and the carrier surface recombinations. Both are major factors which enabled the continuous wave (CW) operating regime of our PhC lasers.

In Chapter 5, we investigate the optical coupling between the PhC cavity and the SOI waveguide. In addition to the theoretical analysis of the coupling by using the Temporal Coupled

[6]Photonics for High-Performance, Low-Cost and Low-Energy Data Centers and High Performance Computing Systems: Terabit/s Optical Interconnect Technologies for On-Board, Board-to-Board and Rack-to-Rack data links

Mode Theory, we developed an experimental procedure to measure the coupling efficiency from the light-in-light-out characteristics of the laser and from transmission measurements performed on the hybrid systems. We demonstrate coupling efficiencies above 90% as well as the possibility of fine tuning on the coupling through simple geometrical modifications of the system.

Chapter 6 starts by discussing the condition necessary to obtain optical bistability in the PhC laser injected by an external detuned laser. Following these theoretical and numerical analyses, we performed experiments demonstrating the viability of hybrid PhC laser/SOI in order to build an optical memory. Indeed, all-optical switching between stable system states of the laser emission is observed. Once the system is switched, it remains in the same state for duration above 2s. In addition, we also demonstrate that the switch can be obtained with ultra-low energies (sub-fJ !).

Finally, we will conclude and give some perspectives for future work.

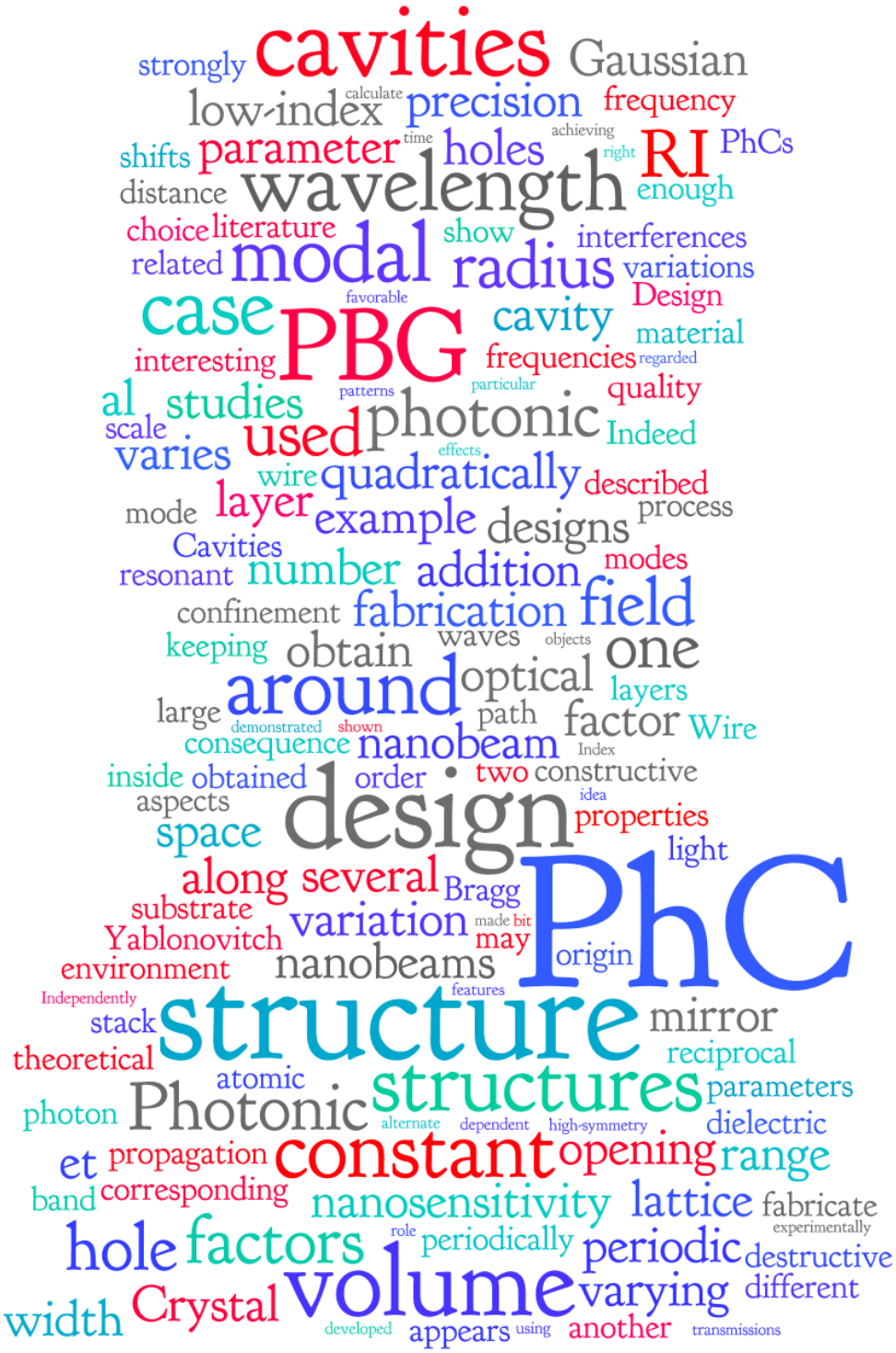
cavities
strongly
Gaussian
low-index
calculate
precision
frequency
achieving
shifts
parameter
time
holes
right
RI
PhCs
distance
wavelength
enough
choice
literature
show
interferences
related
modal
radius
variations
favorable
case
PBG
cavity
Design
material
interesting
frequencies
regarded
patterns
particular
quality
al
studies
photonic
scale
used
Indeed
varies
effects
wire
quadratically
described
mode
layer
example
designs
process
Cavities
resonant
number
addition
modes
confinement
fabrication
field
keeping
obtain
waves
objects
one
around
optical
layers
large
demonstrated
shown
path
factor
Wire
consequence
nanobeam
Index
inside
obtained
order
two
constructive
aspects
idea
design
space
properties
light
along
several
Bragg
PhC
substrate
variation
made
bit
Yablonovitch
may
origin
environment
nanobeams
features
Independently
structure
mirror
stack
theoretical
reciprocal
atomic
structures
parameters
photon
Photonic
alternate
dependent
high-symmetry
dielectric
et
propagation
constant
opening
range
band
corresponding
nanosensitivity
lattice
fabricate
experimentally
hole
factors
role
periodically
periodic
destructive
volume
varying
different
width
Crystal
developed
appears
using
another
transmissions

Chapter 2

Design of Photonic Crystal Wire Cavities on low-index substrate

This chapter is dedicated to the theoretical and experimental studies I carried out on PhCs Wire Cavities on low-index substrate. As explained before, these nanocavities constitute one of the two principal elements of the hybrid structure considered in my PhD.

We start with some generalities on PhCs which will give the basis to the reader the wherewithal to follow the work achieved on the wire cavities. The path undertaken to obtain high-Q wire cavities, naturally suited for the optical evanescent coupling scheme with a waveguide, is then exposed. Finally, results on numerical and experimental investigations are shown.

2.1 Principle and generalities on Photonic Crystals

Here, I will highlight the concept of photonic band gap (PBG) and some important properties of PhCs.

2.1.1 Important optical properties of PhC: PBG and slow-light

A Photonic Crystal is a structure where the Refractive Index (RI) n varies periodically *and* strongly at the wavelength scale in one, two or three dimensions of the space (see example in figure 2.1). When the parameters of these structures are properly chosen, it is possible to obtain an opening of a photonic band gap (PBG) which is a range of frequencies in which the propagation of light in the considered direction(s) is forbidden. These structures are the photonic analogue of atomic lattices, where the spatially varying dielectric constant ($\varepsilon = n^2$) plays the role of the atomic potential. The expression "Photonic Crystal" was popularised by Eli Yablonovitch[1]

[1] An interesting commentary by Yablonovitch on the origin of this appellation and the physical cases where he uses it can be found in "Photonic Crystals: What's in a Name?", in the march 2007 issue of Optics & Photonics

after the separate publications by himself [81] and by Sajeev John [82] of articles relating the opening of a PBG in two- and three-dimensional periodic structures. Their idea was to design and fabricate a structure enabling the tailoring of the electromagnetic environment of an emitter in order to suppress or accelerate the spontaneous emission [83].

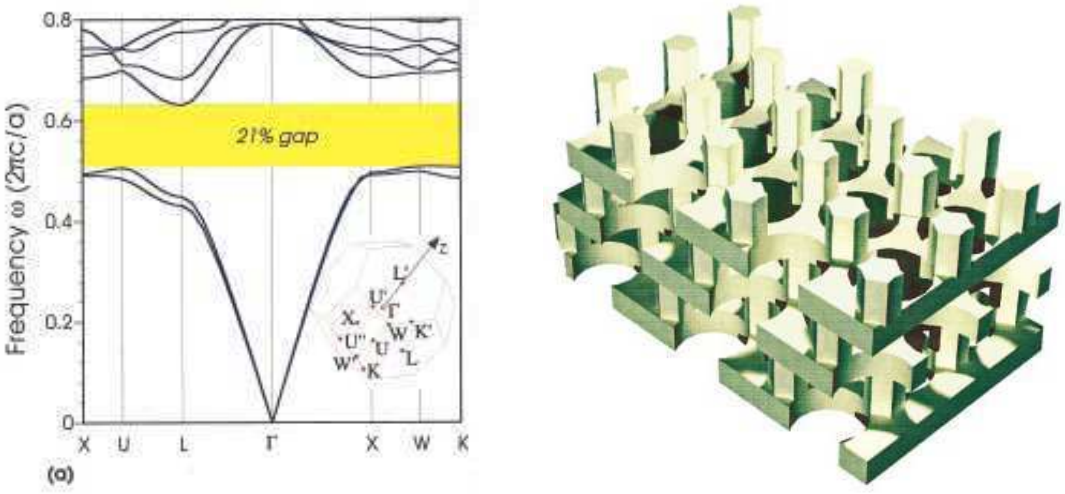

Figure 2.1: *Band Structure (left) of a 3D Photonic Crystal and its corresponding schematic representation (right) from [84]. The band structure is a plot of the optical frequency of the eigen modes as a function of their corresponding wavevector along a determined path in the reciprocal space. Usually, this path links several high-symmetry points of the reciprocal space (Γ, X, K,...). Here, a PBG, represented in yellow, appears in all the directions.*

The origin of the PBG is due to constructive and destructive interferences inside the wavelength scale periodic structure. The most simple example of this mechanism is the well known Bragg mirror which is a stack of layers where the RI varies periodically. When the number of alternate layers is large enough, the successive reflections and transmissions of the optical waves inside the structures impact the overall propagation of light by constructive and destructive interferences between the reflected and transmitted waves. Depending on the layer thicknesses and the RI at stake, the reflectivity of the stack can be close to 1, but only for a specific range of wavelength. A usual design of such a mirror is the quarter-wave mirror where each optical layer thickness corresponds to one quarter of the central wavelength of the range. This effect is identical to the opening of a PBG described earlier. Keeping in mind the definition of PhC given by Yablonovitch[80], we see that if the RI variations in the Bragg mirrors is high enough, they may be referred to 1D-PhCs.

PhC's optical properties are mostly determined by their photonic band structure, i.e. the diagram giving the optical mode frequencies ω as a function of the wavevector $\mathbf{k}$ [85] (see for example fig.2.1). The band structure depends obviously on the PhCs opto-geometrical parame-

News [80].

ters, such as their lattice configuration or the RI of their constituting materials.

The photonic band diagram can be calculated by solving the eigen-values of the equation for the electric field deduced from the Maxwell's equations and the application of the Bloch's theorem [86]. Indeed, the photonic band structure is simply obtained by representing the dispersion relation $\omega(k)$ in the first Brillouin zone associated to the PhC's lattice. For a given frequency, when the wavevectors are purely real, propagative modes are obtained and plotted on the band structure. When the wavevectors have a non zero imaginary part, the corresponding modes exponentially decay as they propagate in the PhC. These modes are not represented on the photonic band diagram. When this type of modes are obtained for a range of frequencies along the whole Brillouin zone, we have a full photonic band gap. if they are obtained in only certain directions of the PhC, we deal with partial photonic band gap. Generally, the calculation of the photonic band diagram is not analytical. Different numerical methods, such as the Plane Wave Expansion (PWE) (e.g. MIT Photonic Band Gap program) or the Finite Difference Time Domain method (FDTD) (Meep, Lumerical) were developed in order to calculate it efficiently. Each method has of course its assets and drawbacks whose full descriptions fall outside the scope of this manuscript. FDTD was preferentially used during this work. More details on this method are given in Section 2.1.4.

The appeal of PhCs comes from the fact that, by choosing their parameters properly, the photonic band diagram may be engineered almost at will. It is then possible to obtain PBGs which can be used, for example, to confine light within line-defect waveguides or point-defect cavities, the latter being discussed a bit further.

PhCs have also been the object of great interest due to the possibility of slowing down the propagation of light at particular frequencies and thus of substantially enhancing light-matter interactions. Indeed, at some particular frequencies, the photonic band diagram can show bands flattening when the wavevector value and direction correspond to the high symmetry points of the first Brillouin Zone. At these "band-edge" frequencies, the group velocity $v_g = \frac{\partial \omega}{\partial k}$ goes to zero attesting for an increase of the optical density of states. The so-called "Slow-Light" effects in PhC have been studied in a great variety of systems [87, 88, 89, 90]. One interesting application is the time-domain light processing using PhCs to build compact delay-lines [91] or again the demonstration of optical switches [92]. The enhancement of the optical density of states at the photonic band-edges has also been used to obtain laser emission [79, 93, 94, 95] in III-V semiconductor PhC.

In the following section, we will focus on the optical properties of 2D PhC and more particularly on planar PhCs

2.1.2 Planar PhC

Accordingly to what was previously described, 2D PhCs should enable a very good control of light propagation within 2 dimensions of space which could be very useful to build a planar optical circuitry. To consider the structure as purely 2D, the typical dimension in the direction normal to the plane of periodicity must be much greater than the typical dimensions of the periodic lattice. This is very difficult to achieve in practice for PhCs operating at wavelength in the visible or in the infrared. To circumvent the problem of the third direction, and prevent light from leaking out the structure in this direction, most of the 2D PhCs are made within a single mode step index optical waveguide [96]. They often consist in a periodic arrangement of cylindrical holes or rods etched in a semiconductor slab (high RI) surrounded by a low RI material such as air or silica. The air-bridged membrane drilled with holes represented in fig. 2.2 is a typical example of planar PhCs. These structures associate the dispersive properties induced by the 2D periodic lattice to the confinement in the third direction by total internal reflection at the low/high RI materials waveguide interfaces.

Here lies the fundamental interest of this type of PhCs as they enable, in principle, the full 3D confinement of light. To satisfy the TIR condition, the modulus of the in-plane wavevector $k_{\parallel}$ of a propagative mode has to be greater than the wavevector modulus k_l of a mode propagating in the low-RI surrounding material which verifies the relation $\omega = cn_l k_l$. This last relation, when plotted in the photonic band diagram, is commonly referred as the "light line" of the medium of RI n_l.

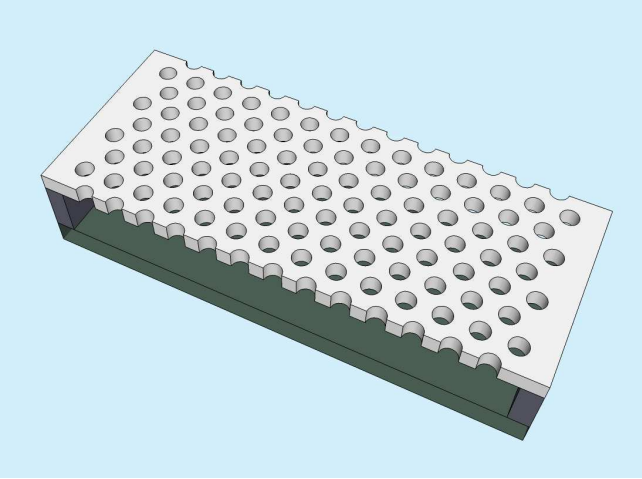

Figure 2.2: *Example of a bi-dimensional PhC etched in a suspended membrane.*

The graphic represented in figure 2.3 shows the photonic band structure of a 2D-PhC made of a triangular lattice of air holes drilled in an air-suspended semiconductor membrane. The band structure is plotted for the TE (magnetic field normal to the plane of periodicity) and TM

(electric field normal to the plane of periodicity) polarisations, the light line being delimited by the black line. Only the modes whose wavevector satisfies the condition for TIR are represented (mode below the light line), the other being hidden by the purple area.

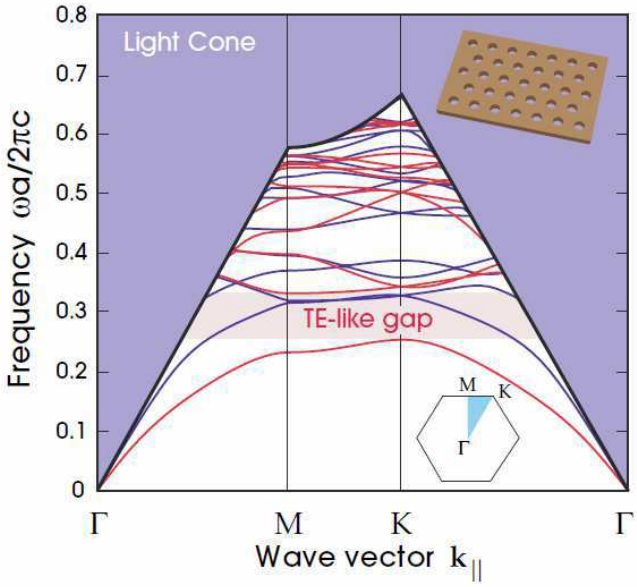

Figure 2.3: *Photonic Band Structure of a bi-dimensional photonic crystal composed of a triangular lattice of air holes etched in a dielectric slab. The violet zone corresponds to the radiative modes above the light line. The TE-like and TM-like modes are respectively plotted in red and blue. In this example, a photonic band-gap exists only for the TE-like modes. From [85].*

Let's note here that the presence of the light line has a major consequence on the design of PhC-based devices. Indeed, the modes lying above it are intrinsically lossy as, for these modes, the photonic grating partly diffracts the energy in these modes towards the continuum of radiative modes. For example, this explains the reason of the lossy nature of light propagation in planar PhCs made in low index contrast waveguides such as InP/InGaAsP/InP waveguides [97] as most of the modes lie above the light line. It also explains the choice of the community to focus its interest to PhCs made in high index contrast waveguides as the extent of modes below the light line is greater.

These planar PhC are certainly the most popular PhCs structures, as their fabrication relies on the technology used for the fabrication of most of integrated photonic devices. Despite beautiful studies with impressive amount of imaginative technological processing, the fabrication of 3D-PhC [98, 99, 100, 101] remains, in comparison with 2D-PhC fabrication, extremely challenging using the same type of technology. An example of such 3D-PhC fabricated structures can be appreciated in fig. 2.4, next to a 2D-PhC etched in a III-V membrane.

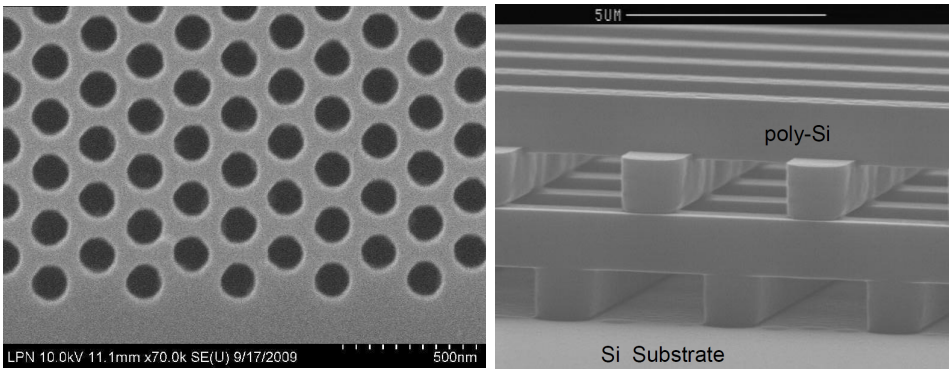

Figure 2.4: *Left: SEM top view of a planar 2D-PhC (triangular lattice of holes) made in a III-V membrane at LPN. Right: SEM image of 3D "woodpile" PhC made in polycrystalline-Si from [98].*

Tremendous progress has been made during the last fifteen years in the understanding of PhCs properties and myriad of new designs have been proposed to take advantage of the remarkable control of light propagation that 2D-PhCs allow. We can cite here waveguides of all sorts and shapes [102, 103], light beaming structures [104, 105], filters [106], but also, and in a large proportion, optical resonators.

2.1.3 PhC micro/nanocavities

Early on in the PhCs history [107], it appeared that PBGs could be used to build cavities trapping photons for very long time within ultra-small volumes, close to the diffraction limit. By creating a "defect" in the periodic pattern, like by locally removing or shifting holes in a 2D-PhC made of lattices of holes drilled in a slab, it is possible to create a cavity mode that can be represented in the dispersion profile $\omega(k)$ by a horizontal line inside the PBG (see fig.2.5). In real space, a cavity mode occupies a volume, called *modal volume*, that is mathematically defined as

$$V = \frac{\int d^3\mathbf{r}\varepsilon(\overrightarrow{r})|\ \mathbf{E}(\overrightarrow{r})\ |^2}{max(\varepsilon(\overrightarrow{r})|\ \mathbf{E}(\overrightarrow{r})\ |^2)} \tag{2.1}$$

where $\mathbf{E}$ is electric field vector and $\varepsilon = n^2$ the dielectric constant distribution of the structure. It is usually expressed in a $(\lambda_0/n)^3$ scale.

The minimal modal volume is determined by the diffraction limit[2] which gives a volume equal to $(\lambda_0/2n)^3$ where λ_0 is the cavity resonant wavelength and n is the RI of the material confining most of the field. If one wishes to design a PhC cavity built in a material with high RI ($n \sim 3$) and whose resonant wavelength is around 1.5 μm, then, supposing the optical mode is roughly

[2]In a $(\lambda_0/n)^3$ scale, the minimum modal volume is then equal to $1/8 = 0.125$.

isotropic, the minimum spatial extension that can be obtained will be close to 250nm, *below the μm-scale*, justifying the appellation of "nanocavity" .

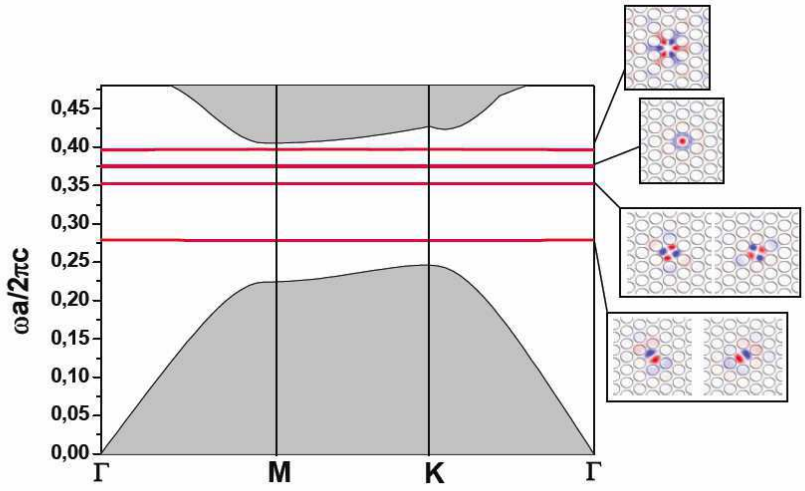

Figure 2.5: *Photonic Band Structure of H1 cavity (one hole removed in a triangular lattice of holes). Red lines correspond to the cavity modes. Spatial distribution of the H_z component of each mode is also shown. From [108].*

In addition, let's remark that the terminology "nano" used in association with PhCs also appears because the PBG's edges frequencies or any other features in the photonic bandstructure scales with the inverse of the lattice constant of the pattern [85], which is of the order of a few hundred nanometres in the case of resonant wavelengths in the telecom window. As a consequence, PhC are highly sensitive to geometrical parameter shifts. As an example, in this particular work, we will see that design of cavities with variations of holes diameters of 5 nm can induce a variation of the resonant wavelength as large as 10 nm. Regarding the fabrication of these objects, this nanosensitivity constitutes, obviously, a real challenge. Sophisticated fabrication techniques and material studies are needed to obtain PhCs structures of good quality. From another perspective, this nanosensitivity can be regarded as a way to easily modify the cavity properties (number of modes, confinement,...). Indeed, the great majority of studies on PhC cavities design shows very subtle shifts in the periodic patterns to create the desired effects. It is interesting to note that it often happens that theoretical studies reported in PhC literature do not take into account both of these nanosensitivity aspects, making the proposed PhC design, impossible to fabricate. As I will show a bit further, this is one of the aspects that we addressed during the design of our cavities.

The main properties of a PhC cavity are described by just a few physical constant: the modal volume V, the quality factor Q (related to the photon lifetime τ_{ph}) and the frequency of the mode

ω_0. In addition, in the case of a structure containing a medium with absorption or gain, another parameter has to be added: the field overlap Γ with the active material. Indeed, this parameter highlights the fact that the volume seen by the photon (V) may be very different from the volume seen by the carriers (V_a), impacting strongly the light-matter interaction intensity.

The field overlap Γ with the active material is simply defined as:

$$\Gamma = \frac{V_a}{V}$$

Finally, the quality factor Q is defined as the ratio of the energy stored in the cavity over the energy that is dissipated over one optical cycle. The most general definition is given by

$$Q = \omega \frac{\langle U \rangle}{\langle \frac{dU}{dt} \rangle} \tag{2.2}$$

where U is the energy inside the cavity and $\langle . \rangle$ denotes the time average over one cycle. Equivalently and more commonly found expression for Q where it is written as $\frac{\omega\tau}{2}$ where τ is the time constant of the field, equal to $2\tau_{ph}$. It is this last expression that we will use in this manuscript.

Increasing the Q factor of 2D PhC cavities while keeping their modal volume comparable to a cubic wavelength has been for 15 years one of the important goals of research in this domain. Nowadays, many designs are available to obtain Q factors higher than 10^6 [109, 110, 111, 112] with V comparable to $(\lambda/n)^3$. They all rely on the precise analysis of the losses of the cavities. In this type of structures, losses arise from in-plane and out-of-plane coupling to the outside world. The in-plane losses depend directly on the number of holes etched on the side of the cavity and can be in principle as low as wanted just by increasing this number. The out-of-plane losses come from the diffraction of light occurring at the interface of the defect cavity and the periodic mirrors. They often are the limiting losses in planar PhC cavities which explains the relatively low Q-factors obtained when no care is taken. The identification of their physical origin is thus of primary importance as it should provide a way of understanding the manner to reduce them. As a consequence, it is then convenient to write:

$$Q^{-1} = Q^{-1}_{in-plane} + Q^{-1}_{out-of-plane}$$

As we will discuss at greater length in chapter 4, PhC cavities are nanostructures exhibiting record values of the ratio Q/V. This is of primary importance for achieving very efficient non-linear devices, such as lasers or switches, as this ratio is directly proportional to the intra-cavity electromagnetic field intensity which usually drives the efficiency of the non-linear effects.

2.1.4 FDTD numerical simulations

The complex three dimensional structure of a PhC given by its dielectric constant distribution $\epsilon(\overrightarrow{r})$ makes it impossible to solve analytically the Maxwell's Equations that govern the electromagnetic field propagation.

Even though, several numerical methods have been developed to find the solutions, they all belong either to one of the two following categories: Frequency-Domain and Time-Domain methods. One of the first introduced method employed which belongs to the first category is the Plane-Wave Expansion method (PWE) and comes directly from the study of crystals in solid state physics. It consists of finding the eigenmode frequencies and wavevector states by decomposing the solutions on a plane-wave basis. This directly provides the values used to build the photonic band-structure of the system. Free programs like ***MIT Photonic Bands*** (**MPB**)[3] rely on this method. There exist of course other approaches like the Scattering Matrix Method (SMM) and these are just examples of the most used methods in the numerical study of PhCs. Eventually, the use of one or the other method depends on the type of system that is treated.

The second category of numerical calculations is the Time-Domain method. Among this category, Finite-Difference Time-Domain (FDTD)[113, 114] is a "brute force" method of solving Maxwell's Equations that relies on the direct calculus of the temporal evolution of an EM field input into the PhC. To do so, space and time are discretised [113] in order to solve equations by incrementing steps. The time-domain response of the system allows to retrieve many parameters, the first being, of course, resonant mode frequencies that are found by Fourier Transform (FT) the obtained temporal evolution of the field. Several FDTD programs are today available like ***Meep*** [4] developed at the MIT (USA) and that is distributed freely on internet under the GNU General Public License. For several years now, we have chosen to work with a commercial program called ***FDTD Solutions*** developed by *Lumerical*[5]. This tool presents major advantages compared to other free solutions: first, the 3D graphical interface is excellent and intuitive; secondly, it is possible to script all the simulations with a simple scripting language that allows to define all the parameters of the simulations and run loops to vary them. An excellent website supporting documentation with many examples is also a real help for the newcomer wanting to realize nanophotonic simulations. Finally, the program supports parallel calculations and was well suited for the simulations on our computer cluster. Our cluster is constituted of 5 nodes of 4 processors with 8Gb of RAM. Numerical parallelisation is a powerful method in order to reduce the simulation time, especially for large volume simulations.

In my work, FDTD was mainly used for two types of simulations: photonic band-structure calculations and calculations of PhC-based cavity modes (Q-factors, modal volumes V, field dis-

[3] http://ab-initio.mit.edu/wiki/index.php/MIT_Photonic_Bands
[4] http://ab-initio.mit.edu/wiki/index.php/Meep
[5] http://www.lumerical.com/

tributions).

To summarize, the simulation of a bi-dimensional PhC is organized in the following steps:

- set the geometry (pattern, dimensions) and materials (RI)
- input an excitation source, usually a fs-pulse, very wide spectrally, and determine its best position and polarisation to excite the modes.
- set a space discretisation step (always below $\lambda/(20n)$ in our case)
- set a simulation window
- set the boundary conditions (depending obviously on the type of simulation) and the possible symmetries
- set the type and number of monitor (RI or temporal monitor)
- set a simulation time (as long as we can bear)
- run the simulation
- retrieve the data

2.1.4.1 Photonic Band-Structure construction

3D FDTD was used to calculate the photonic band diagram of the structures we studied, a particular type of planar PhCs named 1D PhC wires. (Their description is given in the following section). 3D FDTD calculations are particularly suited for the treatment of planar PhC as they easily enable the taking into account of the periodicity of the lattice as well as the finite extension in the direction normal to the periodicity by imposing at the simulation space edges the right boundary conditions. For the calculation of the band structure, the simulation space coincides with the unit lattice cell in the plane of periodicity (see fig.2.6) and is δz long in the third direction with δz greater than the waveguide's thickness so that the evanescent tail of an eventual waveguided mode becomes negligible when it approaches the simulation border (typically δz=waveguide thickness+λ). These boundary conditions are taken to be as "Bloch periodic boundary conditions" along the direction where the wavevector is varied, meaning the following relation for the field amplitudes at the 2 simulation boundaries in this direction:

$$E(x_0 + a, y_0, z_0) = E(x_0, y_0, z_0)e^{-ika}$$

where a is the lattice constant in the considered direction and k the wavevector value of the modes for which we would like to know the frequency. In the direction normal to the plane of periodicity, the boundary conditions are set to "perfectly matched layers" which act as absorbing

layers which don't reflect any electromagnetic field, i.e. which mimic here an infinite half space made of the low RI material which surrounds the PhC.

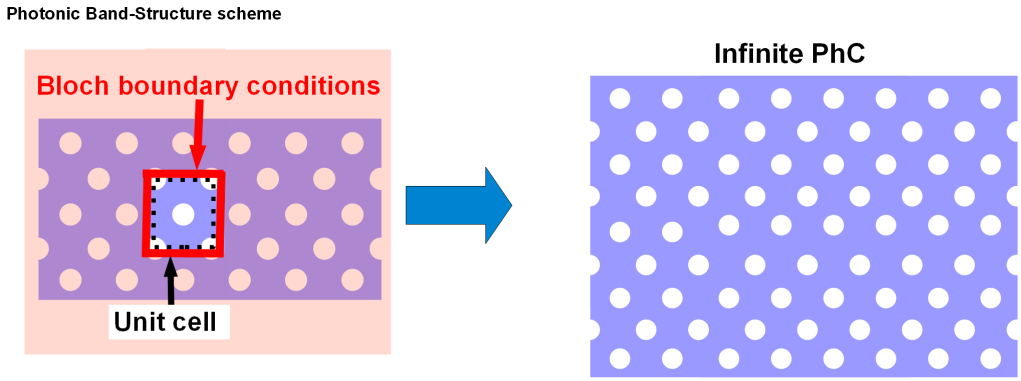

Figure 2.6: *3D FDTD simulation : Photonic Band Structure.*

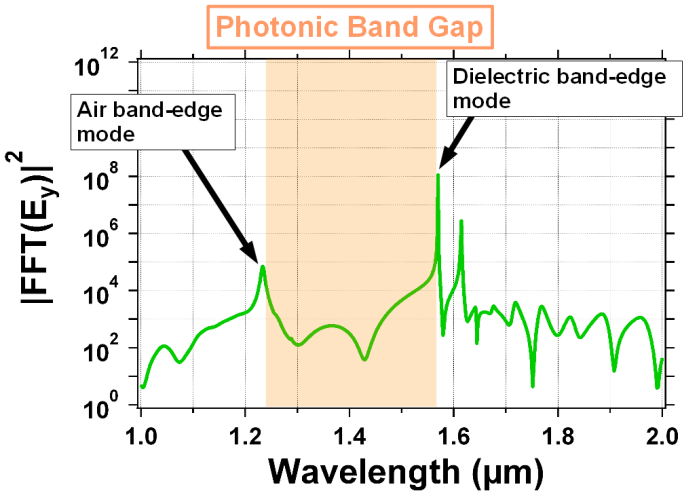

Figure 2.7: *Fourier Transform of the electric field recorded by a point monitor in a PhC wire unit cell with Bloch boundary conditions along the wire. Several modes appear including two band-edge modes delimiting the PBG.*

Before starting the simulation, 1 or several electric or magnetic dipole sources (possibly with an imposed phase-shift between each others) are well positioned in the simulation window by setting their time domain duration to few fs in order to obtain results within a large frequency range. Punctual detectors are placed within the PhC slab at different places in order to record the time domain evolution of the electric and magnetic fields components. A typical result of the FT of the E_y component squared is shown in fig.2.7. The peaks obtained in the spectrum corresponds to the PhC modes at the considered value of the wavevector. By recording the frequency of these mode and varying the wavevector value, it is then possible to obtain the

photonic band structure of the PhC under investigation.

2.1.4.2 Cavity simulation

3D FDTD was also used to simulate PhC-based cavities. The aim of the calculations was to determine the different resonant frequencies as well as the Q factor associated to each of these modes. Here, the simulation window is fixed to contain the whole structure with sufficient space around it to prevent any interaction with the boundary layers. The boundary conditions are set to perfectly matched layers. In order to save some simulation time, the simulation space may be reduced by adding symmetry planes but we must keep in mind that this choice also imposes the symmetry of the expected cavity modes. During the simulation, a dipole source positioned in the cavity launches a short excitation pulse (broad spectrally). The time decay of the electromagnetic field is monitored using a punctual monitor positioned in the cavity. An example of an obtained temporal evolution of the E_y component of the electric field in a PhC cavity is shown on figure 2.8. Here it can clearly be observed that the electric field decays in time very slowly attesting for the presence of high-Q cavity modes. The FT of the temporal trace of the field gives the frequencies of the different modes as can be seen in figure 2.8 if the simulation time is long enough to have a frequency resolution better than the cavity modes spectral spacing. However, the quality factor of the modes cannot be retrieved by inspecting the obtained spectrum as, in general, the simulation time is not long enough to have the sufficient spectral resolution to resolve the resonance peaks. Instead, the time domain trace is fitted using the *Harminv* [6] software[115] which decomposes any temporal signal in Fourier space as the product of sine function and a decaying exponential thereby allowing the identification of the resonant modes and their respective Q factors.

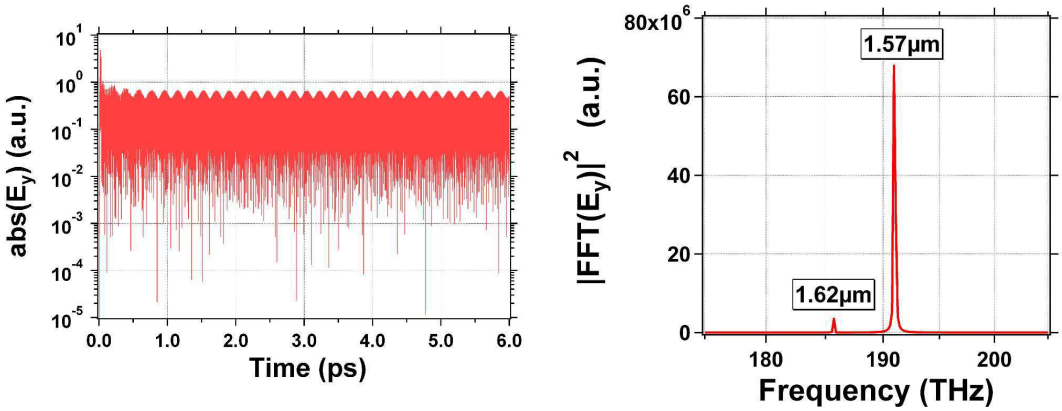

Figure 2.8: *3D FDTD simulation : Left) Example of the time trace (in log scale) of the field inside a PhC cavity. The flat aspect of the trace over 6 ps generally indicates the presence of one or more high-Q cavity mode. Right) Fourier transform of the E_y component showing two modes of a structure described in Section 2.2.3.*

[6] http://ab-initio.mit.edu/wiki/index.php/Harminv

2.2 Photonic Crystal Wire Cavities

After examining briefly some generalities of PhCs, I describe, in this section, the studies I carried out on PhC wire cavities. The optical properties of these resonators were theoretically and numerically analysed in order to set the correct geometrical parameters of the structures to fabricate such as they exhibit large quality factors. Unlike the vast majority of study on PhC cavities, the considered system is not made into an air-bridged semiconductor membrane but into a semiconductor slab either positioned on top of a low-RI material or fully surrounded by a low-RI material in order to be directly compatible with further integration on top of a SOI circuitry.

2.2.1 PhC Wire structure

PhC wires are the structures I privileged during my PhD work. They consist of "wire" waveguides drilled with a periodic array of holes as indicated by the schematics of fig. 2.9. Here, the waveguide dimensions are extremely compact in the transverse direction, typically 250 nm thick and 500 nm wide, which renders them single mode for the TE polarisation and which justifies the appellation of photonic wires. These structures combine the transverse confinement of light induced by TIR with the PBG resulting from the holes patterning. They are certainly the planar PhC structures which show the smallest footprints, an important asset to take into account while designing photonic devices.

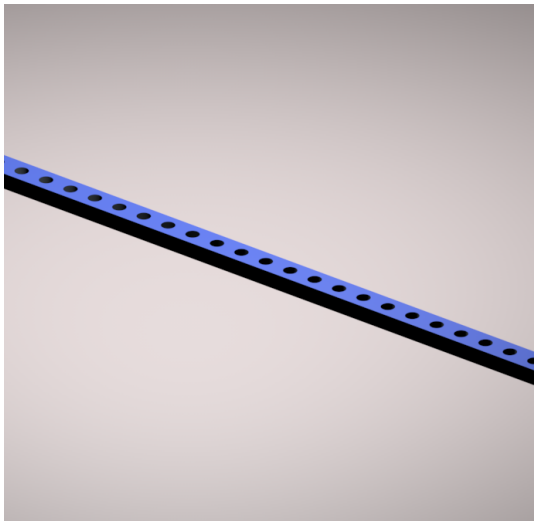

Figure 2.9: *3D scheme of PhC Wire.*

Photonic band diagrams for TE-polarisation for different perfectly periodic PhC wires are plotted in figure 2.10. The figure illustrates the transition from a simple non-patterned wire

waveguide to PhC wires with increased holes radii. We can see that the PBG opens up around the folding frequency of the wire waveguide mode at the edge of Brillouin zone and that its bandwidth increases while increasing the holes radius. It can also be seen that the band-edge frequencies shift toward higher frequencies when the holes radius is augmented.

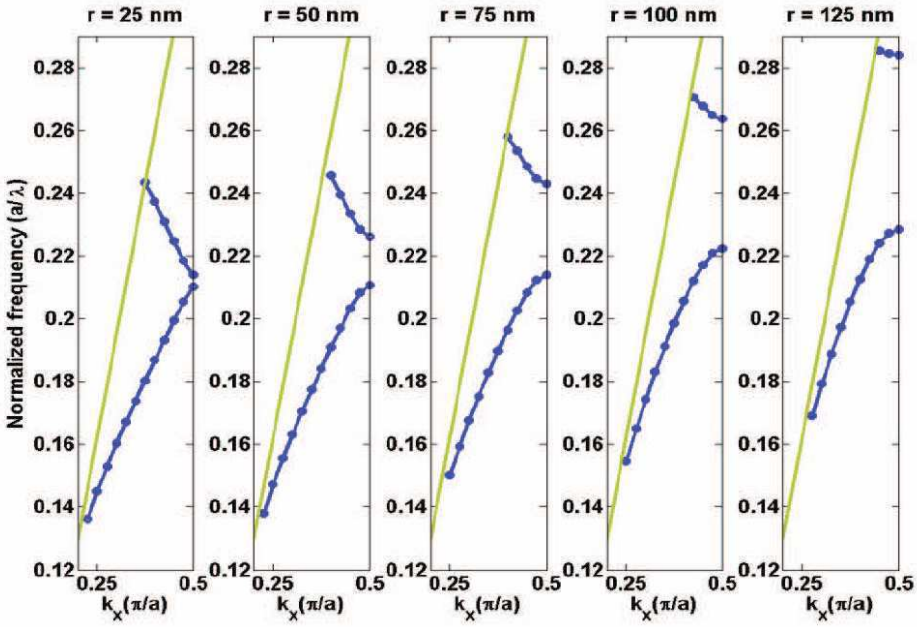

Figure 2.10: *Examples, from Y. Halioua PhD thesis [78], of Photonic Band Structures for PhC Wire of period a = 315 nm in a 505 nm large SOI wire for several hole radius. The PBG range is increased with the hole radius r.*

I represented in figure 2.11, the band structure of a typical InP-based PhC wire used in this work. Here, the PhC wire is positioned on top of a SiO_2 layer with the rest of the structure surrounded by air so that both the air and SiO_2 light lines have to be considered. We can see that the modes close to the 2 PBG edges are situated below both light lines meaning they are perfectly confined within the wire as they propagate. It is an important result as it somehow shows that this structure is suitable to make cavities as the PBG is partly below the light lines. The spatial distribution of the E_y component of the field at the 2 PBG edges frequencies are also represented in the figure showing that, for the valence band edge mode, the field is confined in the material between the holes, as for the conductance band edge mode, the field is mainly inside the air holes. These considerations may be important when one aims to optimise light matter interactions.

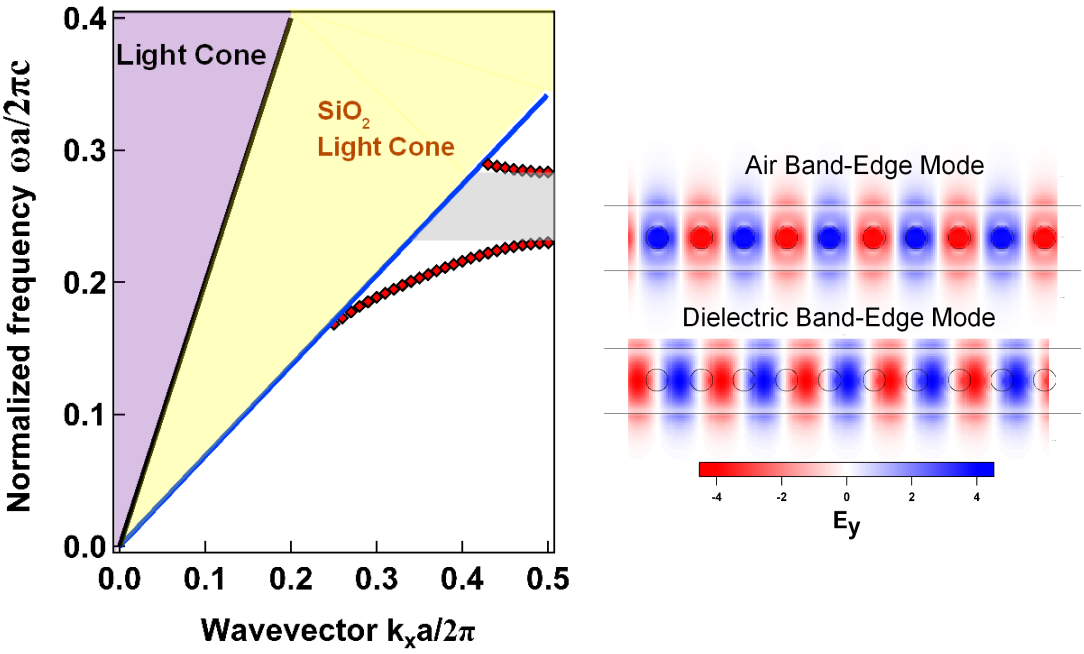

Figure 2.11: *Left: Photonic Band structure for the TE-like modes of a Photonic Crystal Wire of RI n= 3.35 on top of a SiO_2 layer and surrounded by a air (see scheme fig. 2.12). Right: E_y component spatial distribution for the two band-edge modes.*

The knowledge of the band structure was essential to move forward to the design of cavities using such PhCs. A PhC Wire cavity can be obtained by creating a "defect" in the periodicity of a PhC wire. A localised variation of the hole-to-hole distances or in the hole's radius is often used to create such defects. The simplest case of a wire cavity is a structure where two periodic lines of holes are separated by a distance L, each line of holes acting as a mirror for frequencies inside the PBG. Such a cavity, represented in fig. 2.12, is nothing else but a simple Fabry-Perot resonator. The first proposal and demonstration of a PhC wire cavity was achieved in 1997 by Foresi et al. [116]. They fabricated their structures within SOI wire waveguides and measured a Q factor of only 260 for cavity modes around 1.55 μm! This highlights that the design of high-Q cavities made in planar PhCs cannot be straightforwardly achieved after the calculations of the band structure.

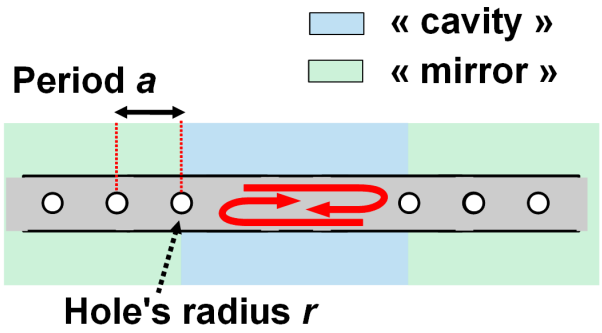

Figure 2.12: *Scheme of a defect-based PhC Wire Cavity.*

In what follows, I will describe the path undertaken during my PhD to design high-Q PhCs wire cavities. To start, the next section presents the first design of PhC Wire Cavities which have been integrated in our hybrid structures, the Tapered-Defect (TD) Wire Cavities [117]. It will be followed by the detailed description of a new design of high-Q (Q>500 000) PhC Wire Cavities.

2.2.2 Tapered-Defect Wire Cavities

2.2.2.1 Design

One of the interpretation of the diffraction losses at the defect cavity mirror interfaces is that these losses arise from the modal mismatch between the propagative mode in the defect part and the evanescent mode in the mirror formed by the lattice of holes [118, 119]. Indeed, Sauvan et al. [120], showed that the transverse distribution of the field propagating within a wire waveguide becomes more and more different to the evanescent field's transverse profile inside a periodic mirror formed by a single row of holes as the field's frequency falls farther and farther away from the valence band edge of the PBG. So, when the cavity mirrors are designed so that the resonant frequency is at the centre of the PBG, a large modal mismatch is expected resulting in important diffraction losses noted $\mathcal{L}(\omega)$. The associated mirror reflectivity in intensity writes simply:

$$R_{eff}(\omega) = (1 - \mathcal{L}(\omega))R_{PBG}(\omega)$$

where $R_{PBG}(\omega)$ is the mirror reflectivity if there were no diffraction losses.

A simple solution to decrease the mismatch would consist in using mirrors designed so that the cavity resonant frequency ω_{cav} falls in the PBG close to the valence band-edge. However, it

can be shown (see the evanescent decay factors of PhC Wire in fig. 2.20, directly related to the mirror strength) that, for these type of mirrors, $R_{PBG}(\omega_{cav})$ is much lower in comparison to that of a PhC Wire based mirror operated in the centre of the PBG containing the same number of holes. In order to increase R_{PBG}, the mirrors should contain a large number of holes which would extend considerably the footprint of the cavity. An other drawback is that these cavities exhibit quite large modal volumes as the penetration depth of the field of the mirror can be quite long which is not favourable to enhance light matter interaction.

So, to kill 2 birds with one stone, i.e. minimising $\mathcal{L}$ and maximising R_{PBG}, the mirror/cavity interfaces are engineered to adapt the wire waveguide propagative mode to the mirror's evanescent mode at the centre of the PhC PBG. This is achieved by including what is called a taper zone (see schematics on fig. 2.13) between the defect of the cavity and the periodic part of the mirrors where the radius of each hole and the hole-to-hole distance are varied. In [121], the authors used this method to fabricate Si-based PhC Wire Cavities with, at the time, a record high value of the measured Q factor of 58000. Note, the cavities were not made within an air suspended wire but in a wire on top a SiO_2 layer.

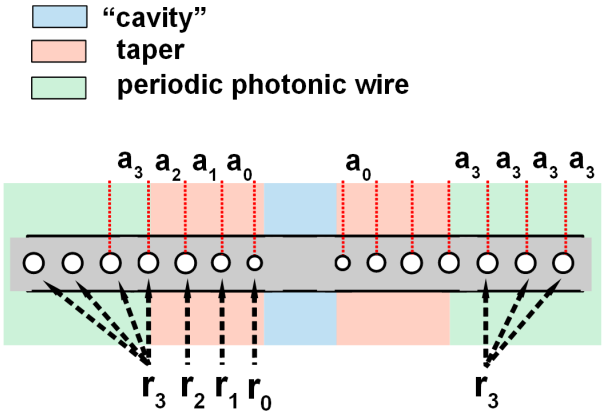

Figure 2.13: *Scheme of the center part of the tapered-defect cavity.*

This scheme was implemented in our team at LPN to design and fabricate InP-based Tapered-Defect (TD) PhC Wire Cavities, positioned on top of a SiO_2 layer, with modes of resonant wavelength close to 1.55 μm, Q factor values as high as possible, and modal volume V in the order of the $(\lambda/n)^3$. The taper zone contained three holes of reduced radii, as well as reduced "lattice constant", which values increased with their distance from the cavity centre. More detail on the opto-geometric parameters can be found in [122]. FDTD Simulations [78, 122] allowed to design cavities with Q in the order of a few 10000's (see fig. 2.14). The fabricated structures were lasers whose analysis of the light-in/light-out characteristics curve were used to retrieve the real Q factor which reach approximately 8000.

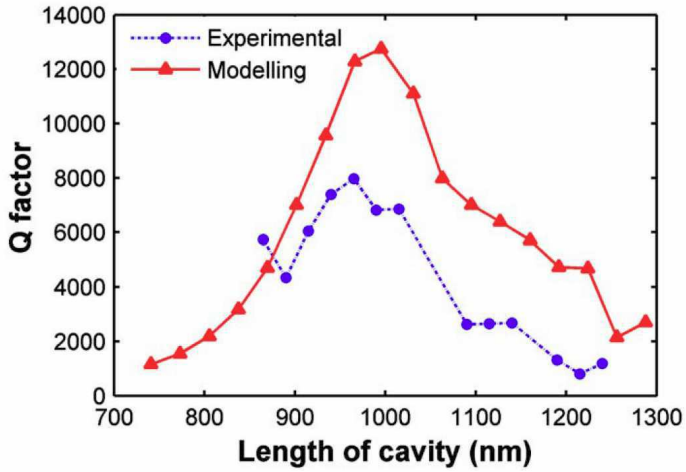

Figure 2.14: *Comparison with the theoretical and experimental Q factor as a function of the cavity length of TD PhC Wire Cavities[122].*

In order to improve these results, reflectivity calculations were performed using 3D FDTD. Two structures were studied: one with a perfectly periodic mirror and another with a tapered mirror, slightly different from the one discussed in [122]. The obtained mirror losses $(1 - R(\lambda))$ spectra are represented in figure 2.15. Like [120], we observed a significant decrease of the losses in the middle of the PBG of the tapered mirror compared to the regular non-tapered mirror. Indeed, we observed 10 dB of difference between the losses minima of the regular and the tapered mirrors.

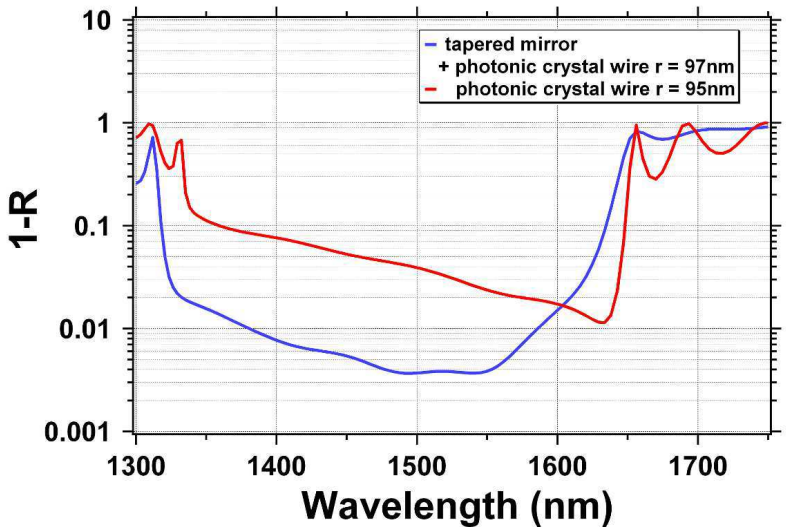

Figure 2.15: *Reflectivity simulations of PhC Wire mirrors with and without tapering. The number of holes is kept constant in both simulations. An improvement of 10 dB can be appreciated at the centre of the PBG.*

Figure 2.16 shows Q-factors extracted from 3D FDTD simulations performed on our TD PhC Wire Cavities as a function of the defect length[7] and are found to be always below 10^5. Besides, the dependence of Q on the wavelength is quite strong making the design poorly robust to fabrication uncertainties (RI, holes radius, III-V thickness, etc). One would indeed prefer to maintain the main characteristics of the cavity, particularly the Q factor, despite slight shifts in the structure geometry and regardless of the resonant wavelength. This behaviour is also reported by McCutcheon et al. [123] who were able to obtain theoretical Q-factors of 10^6 with modal volume below $(\lambda/n)^3$, with $\lambda \approx 600$ nm, in free-standing TD PhC Wire Cavity of SiN_x RI. In addition, despite the obvious room for improvement in our TD design, the TD approach seemed not at all straightforward with our intention to fully encapsulate the cavities in a low-index layer ($n \approx 1.4 - 1.5$) to improve the overall heat spreading of the device. Indeed, the lower RI contrast in encapsulated cavities will inevitably reduce the maximum achievable Q-factor.

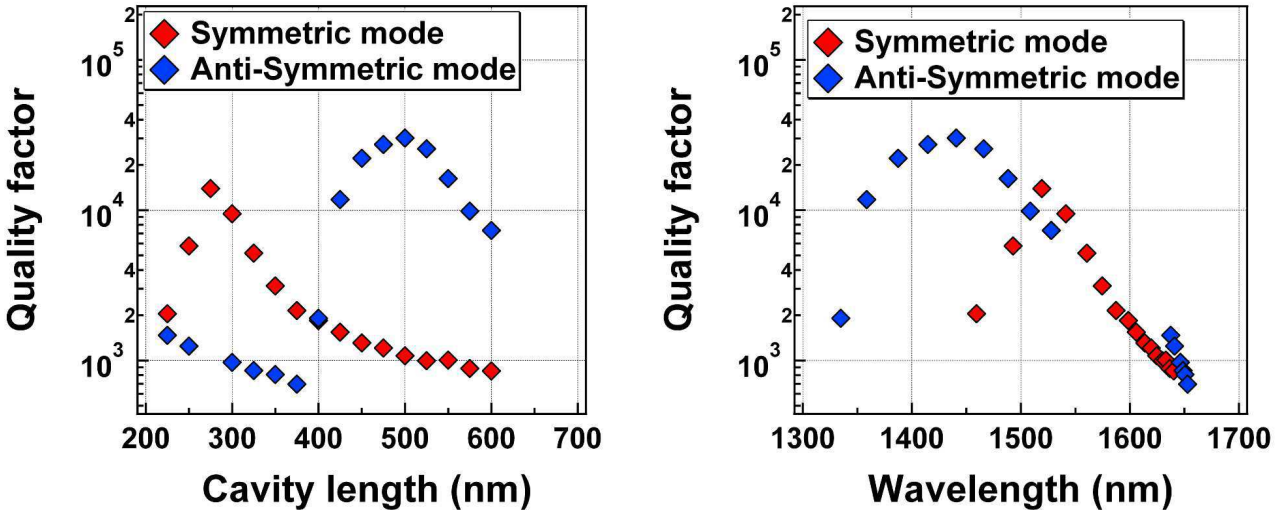

Figure 2.16: *Quality factors Q as a function of the cavity length L (top graph) and as a function of the resonant wavelength (bottom graph) for our design of TD PhC Wire Cavities.*

In the next part, we tackle a very different approach in order to obtain high-Q PhC Wire Cavities which is based on the *gentle confinement* [124] of the field through Gaussian apodisation.

[7] The cavity length is this designed is defined as the centre-to-centre hole distance between the two holes closer to the cavity center.

2.2.3 High-Q Apodised Wire Cavity

2.2.3.1 Principle

As we mentioned previously, the optical losses of cavities formed with planar PhC cavity arise from two contributions: the in-plane and the out-of-plane losses. While the in-plane losses can be usually suppressed by increasing the number of holes around the defect, the decrease of the out-plane losses requires a deeper understanding of their origin. More than a decade ago, it was emphasized by Srinivasan et al. [125] that the out-of-plane losses of a planar PhC cavity mode were dependent on its k-space distribution and particularly on the amount of k component that lied within the light cone of the surrounding material. In 2003, Akahane et al. [124] used a similar approach and proposed the concept of *gentle confinement* of the field. This concept intended to give a simple design rule for obtaining high-Q PhC cavity modes, with modal volumes in the order of $(\lambda/n)^3$. Their idea was to make the field decay at the cavity edges as "gentle" as possible in order to avoid the large increase of the momentum components within the light cone that usually appears in "regular" defect cavities . The schematics of figure 2.17, taken from [126], illustrates how, by making the field envelope Gaussian (also referred as Gaussian *apodisation*), the k-space component in the leaky region can be suppressed. Q-factor of such Gaussian apodised cavities were around 10^9 [126] which corresponds at 1.55 μm to photon lifetimes close to $1\mu s$!

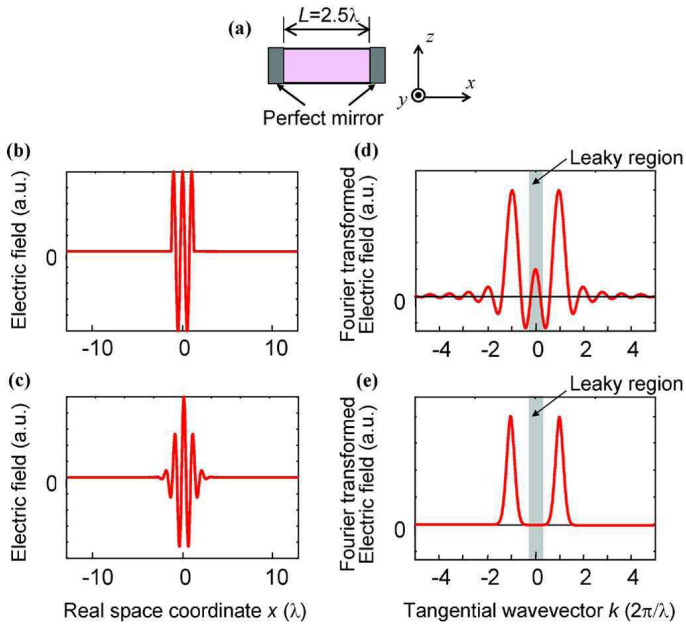

Figure 2.17: *Analysis of cavities with different in-plane confinement characteristics. (a) Simplified model of a cavity. Electric field profiles of cavities with (b) a rectangular envelope function, and (c) a Gaussian envelope function. (d) and (e): respective Fourier transform spectra of (b) and (c). From [126].*

In addition to the gentle confinement concept, the work of Tanaka et al. [126] shows a major interest in their way of implementation of the Gaussian apodisation which was entirely analytical. A large part of the rest of this chapter will be devoted to the analytical method we used to apodised the PhC Wire Cavities and to the demonstration of their high-Q.

2.2.3.2 Analytical method used for the design

In PhC literature, several works [111, 127, 128, 129] have shown that one dimensional PhC "wire-like" cavities could theoretically exhibit high-Q factors (above 10^6) up to 10^{10}. Although not explicitly stated at first, those designs used the concept of gentle confinement of the field as they always showed some form of gradation in the geometry of the structure (hole radius, periodicity, width) to ensure that the decay of the field along the structure varies quadratically with the distance to its center, i.e. that the field envelope profile is Gaussian. Ahn et al. [111] obtained Q factors up to 10^8 by increasing the width of the nanobeam quadratically with x, keeping the modal volume below $(\lambda/n_{Si})^3$. Quan et al. [112, 129] recently presented and discussed several designs of Gaussian mode profiles in Si nanobeam cavities. In the case of suspended nanobeams, they obtained Q factors greater than 10^9 with effective modal volumes V around $(\lambda/n_{Si})^3$ by varying quadratically the hole radius while keeping constant the hole-to-hole distance. In the less favorable case of nanobeams embedded in a low-index dielectric environment, they designed nanobeams with Q factors around 10^7 and experimentally demonstrated [129] Q factor around 500 000 with modal volume around $(\lambda/n_{Si})^3$. Independently and simultaneously, Kuramochi et al. [128] developed a similar approach that they applied to cavities etched in a silicon-on-insulator layer, achieving theoretical Q going from 2×10^8 to around 5×10^8 with modal volume V from approximately 0.65 to $1.0(\lambda/n_{Si})^3$. Experimentally, they fabricated cavities with Q factor up to 3.6×10^5.

We approached the problem differently and used a variation of the lattice constant of the structure to get a Gaussian attenuation of the field. The reason for this choice hinges on the necessity for an extreme precision of the hole positioning during the fabrication process, as this precision is directly related to the e-beam lithographic system precision which at LPN, today, is below 1 nm. On the other hand, we felt that designs using fine tuning of the hole radius, like made in [112, 129], could reveal much more difficult to control as the etching of the holes depends on various process steps such as the exposure dose, the time of development of the resist (very processor dependent), or even the etch rate of holes with different radius. The other choice of design [111] that consists of parabolically varying the nanobeam width is an interesting approach studied in the case of air-suspended membrane. Again, the necessary precision of etching for slowly varying the period seemed however more risky than the lattice constant variation appraoch that we finally choosed.

In consequence, we used an analytical method, adapted from the one in [126], to build a high-Q cavity based on a PhC Wire into which the lattice constant is subtly varied.

For frequencies contained in the PBG of a PhC wire, no propagating modes exist. If somehow we inject light in the PBG frequency range, the wavevector of the field will have a non-zero imaginary part q and the evanescent mode field will decay as e^{-qx}. To obtain a PhC wire cavity mode with a Gaussian profile, it is necessary then to vary q linearly with the distance x from the cavity centre so that the envelope will decay as e^{-Bx^2} where $q = Bx$. To do so, the analytical procedure to design the structure is based on the retrieval of the dependence of q on the lattice constant a. Basically, the value of q at a given frequency within the band gap depends directly on the distance of this frequency with respect to the band edges frequencies. As a change of the lattice constant induces modifications of the band structure, the value of q can thereby be tuned along the cavity.
Our calculations consist in:

(a) calculating q as function of the frequency for different values of the lattice constant

(b) calculating the modification induced by a change of the lattice constant on the band-structure

(c) finally calculating the variation of the lattice constant needed along the PhC to obtain a Gaussian field profile.

2.2.3.2.a Decay factor $q(f)$ inside the PBG of a PhC Wire

In this work, the calculation of $q(f)$ inside the PBG (outside the PBG $q(f)) = 0$) is done numerically with 3D FDTD by solving the propagation of a broadband pulse sent toward the PhC Wire (see fig. 2.18, left picture). At frequencies falling in the PBG, the field penetrates evanescently the periodic part of the wire (of lattice constant a) with a penetration length proportional to $1/q$. In order to monitor the decay at each frequency inside the PBG, the FDTD simulation window contains a linear monitor placed at the centre of the structure along the waveguide that performs a discrete temporal Fourier transform at each position x for each frequency.

Figure 2.18 (right) shows the spatial distribution of the calculated electric field intensity in log scale to perceive the effective variations of the field decay inside the PBG. The PBG is clearly noticeable as the field intensity is very low inside it (green zone). In the PBG, the field decay increases with the detuning to the band-edge modes and reaches its maximum around the middle of the PBG.

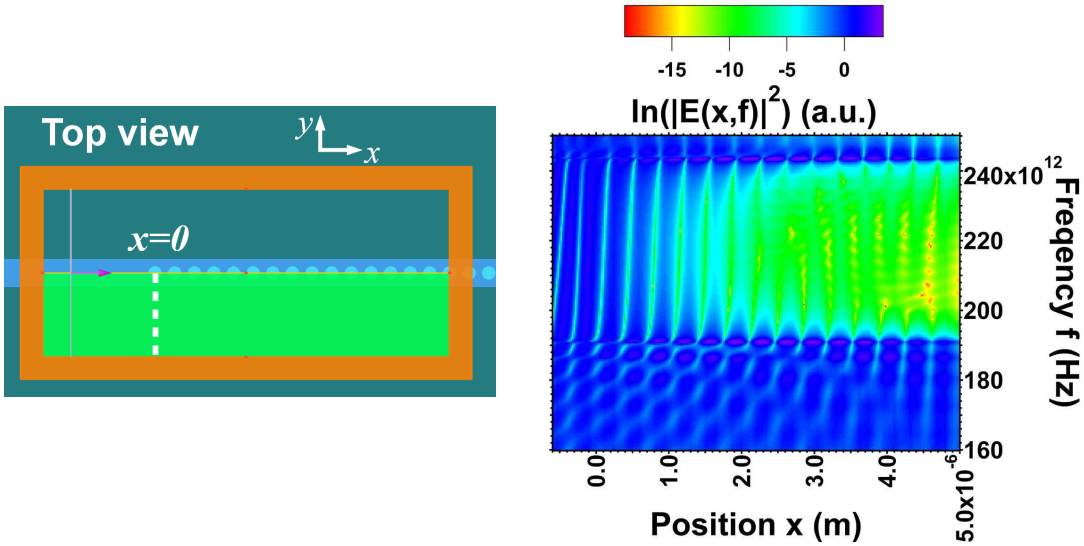

Figure 2.18: ***Left)*** *Top view of the FDTD simulated geometry. The guided-mode pulse is schematised by an arrow and the green zone indicates that we used symmetries to diminish the simulation time. A linear monitor that performs a Discrete Fourier Transform at each position and at the entered frequencies is placed in the centre of the structure along the waveguide. Notice that the first hole is placed at $x=0$.* ***Right)*** *Logarithm of the electric field intensity distribution along the linear monitor and in a frequency range across the PBG. Inside the PBG the decay of the field is fast. The period of the PhC wire is here $a=350$ nm and the hole radius $r=120$ nm.*

The values of $q(f)$ are obtained by fitting, for each frequency, the decay of the field (in the periodic part of the wire) with a function, which is a product of a cosine and a decaying exponential. Figure 2.19 shows an example of such fit for a PhC wire of period $a = 350$ nm. This procedure is repeated for all frequencies in the PBG and the result is plotted in fig. 2.20 for various period a.

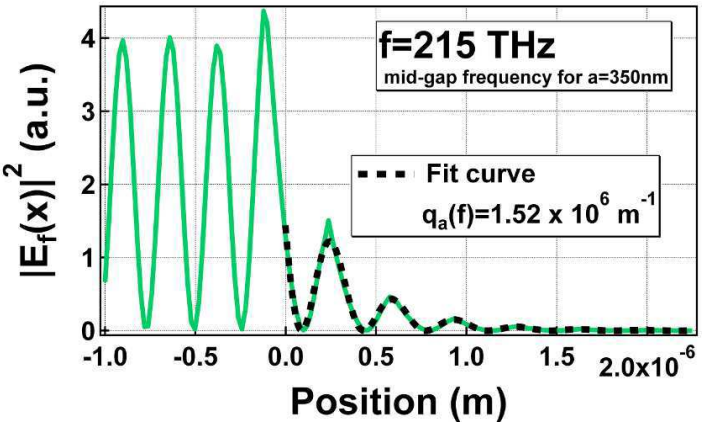

Figure 2.19: *Calculated electric field intensity energy distribution for the mid-photonic band gap frequency along the simulated structure showed in 2.20 with the period $a = 350$ nm.*

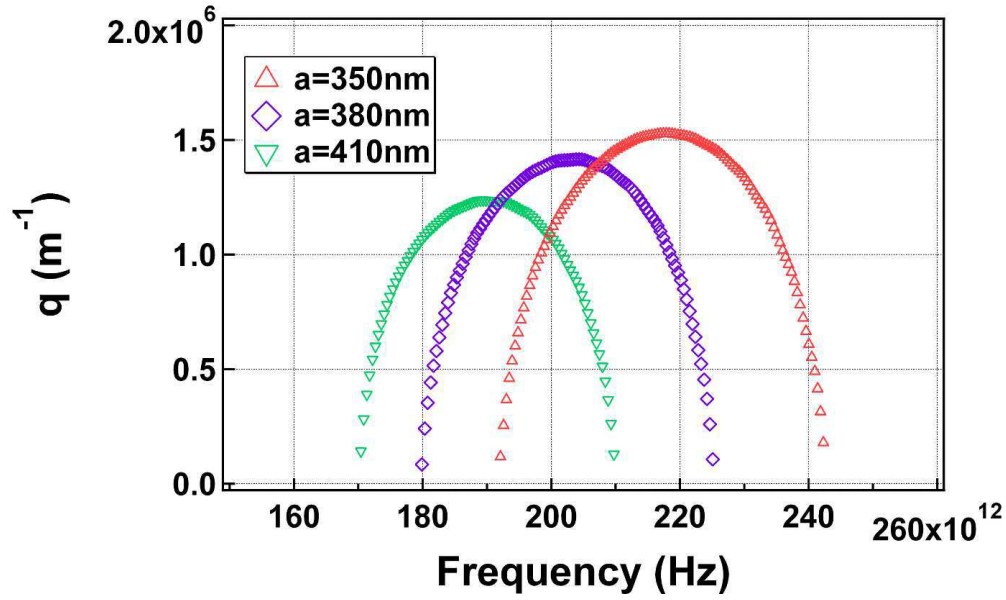

Figure 2.20: *Calculated imaginary part q of the evanescent field wavevector in the PBG of PhC Wires (285nm×505nm, n=3.35) with a radius fixed to 120 nm and with respective period a= 350 nm (red), 380 nm (purple) and 410 nm (green).*

For a given value of the period a, the dispersion relation $f(q_a)$ inside the gap can be approximated near the dielectric band-edge mode frequency by a parabolic function

$$f = f_a^{cut} + A_a {q_a}^2 \tag{2.3}$$

or, in a more suitable way to investigate the decay factor q_a,

$$q_a(f) = \sqrt{\frac{f - f_a^{cut}}{A_a}} \tag{2.4}$$

where A_a is a parameter slightly dependent on the period a and where the cut-off frequency f_a^{cut} of the dielectric band-edge mode can be expressed, in the period range of interest, as

$$f_a^{cut} = \frac{K}{a} + \tilde{f} \tag{2.5}$$

with $\tilde{f}$ is a constant that we express as a function of a period a_0 and its associated cut-off frequency $f_{a_0}^{cut}$. Figure 2.21 shows the calculated cut-off frequencies for the two band-edge modes of PhC wires as a function of the inverse of the period a. A linear fit gives $K = 4.82 \times 10^4$ THz.nm and $\tilde{f} = 53.5$ THz.

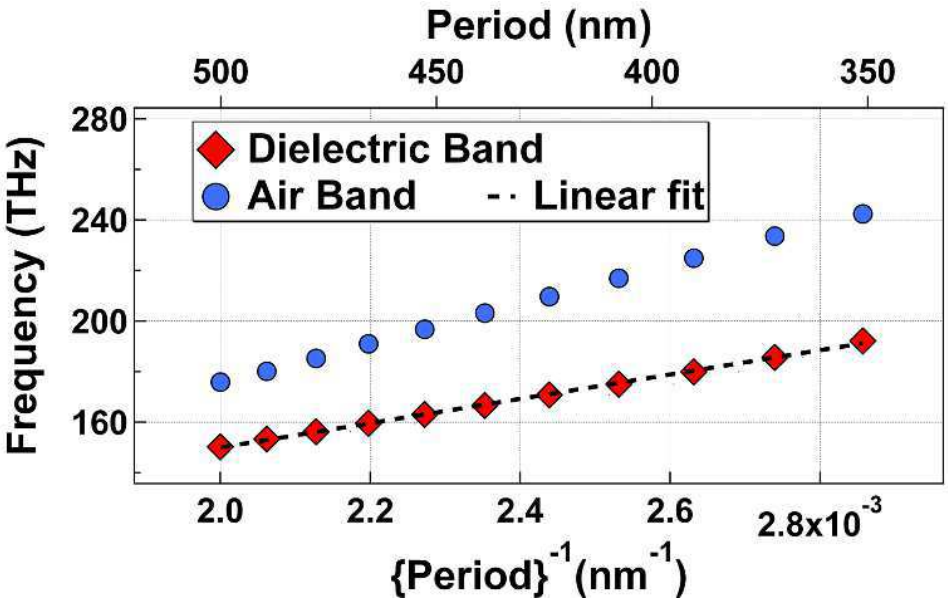

Figure 2.21: *Cut-off frequencies of the band-edge mode of a PhC wire as a function of the inverse of the period a. The dependence is linear and the fit gives* $f^{cut}(a) = \frac{4.82 \times 10^7}{a} + 53.5 \times 10^{12}$ *(with a in metres) for a* $285 \times 505nm$ *InP-based PhC of index* 3.35 *and for a hole radius* $r = 120nm$.

Using (2.5), we can rewrite eq. (2.4) in the following form

$$q_a(f) = \sqrt{\frac{f - K\left(\frac{1}{a} - \frac{1}{a_0}\right) - f_{a_0}^{cut}}{A_a}} \tag{2.6}$$

The parameter A_a is finally obtained by fitting the curves of fig. 2.20 with the expression (2.4) near the dielectric band-edge mode frequency. The fitting accuracy of expression (2.4) may vary with the accuracy on the obtained q_a values and with the range of frequency that the fit explores. The latter dependence is the most critical in this procedure. Ideally, the choice of the frequency range for the fit should be correlated to the expected displacement of the frequency cut that is going to be applied, in order to obtain the Gaussian profile. For the moment, let's just remark that the value of A_a is subject to a non-negligible error bar.

The variation of A_a as a function of a is linear and can be written:

$$A_a(a) = A_0 + \alpha(a - a_0) \tag{2.7}$$

Figure 2.22 shows the value A_a obtained and a linear fit of A_a as a function of a giving A_0=5.8±0.1 $Hz.m^2$ and α=0.024±3 $\times 10^{-3}$ GHz.m.

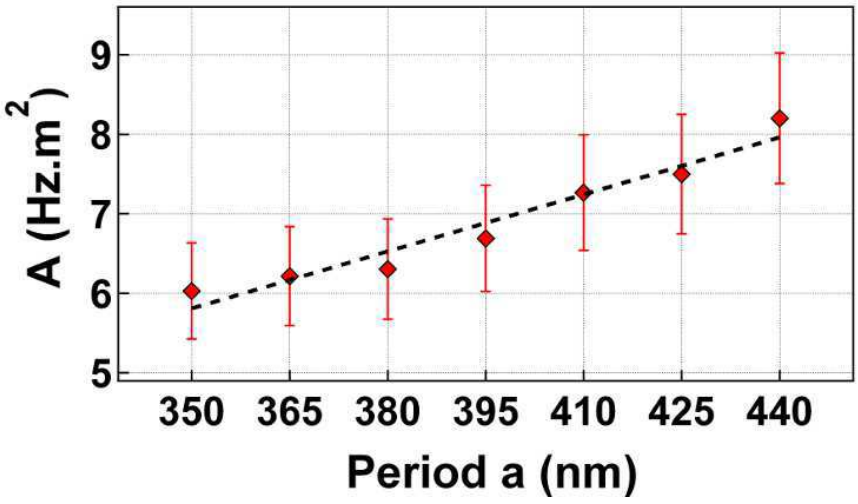

Figure 2.22: *Parameter A as a fonction of the period a of the PhC Wire. The linear fit gives* A_0*=5.8±0.1 Hz.m*^{2} *and* α*=0.024±3* $\times 10^{-3}$ *GHz.m.*

Now that we have explored the dependence of the losses within the PBG of PhC Wire as a function of the frequency and as a function of the period a, we have all the information to create a PhC Wire Cavity of Gaussian profile mode by calculating the variations of $a(x)$ along the cavity.

2.2.3.2.b Continuous function $a(x)$ to obtain a Gaussian profile

Suppose that from $x = 0$, we start to vary the lattice constant of the structure by parts so that $a = a(x)$ as depicted in fig. 2.23 to obtain a linear increase of q with x such as

$$q(x) = Bx \tag{2.8}$$

with B a constant in m^{-2}. The hole-to-hole distance at the centre of the cavity is fixed to a_0 such as the cavity frequency f_{cav} is at the arbitrary cut-off frequency $f_{a_0}^{cut}$ [8].

[8] As we will see, this is an approximation. As pointed out by Quan et al.[112], a perturbative calculations would show that the cavity resonance asymptotically approaches the band-edge frequency depending on the number of modulated lattice constant used to apodise the cavity, with respect to the extension length of the field.

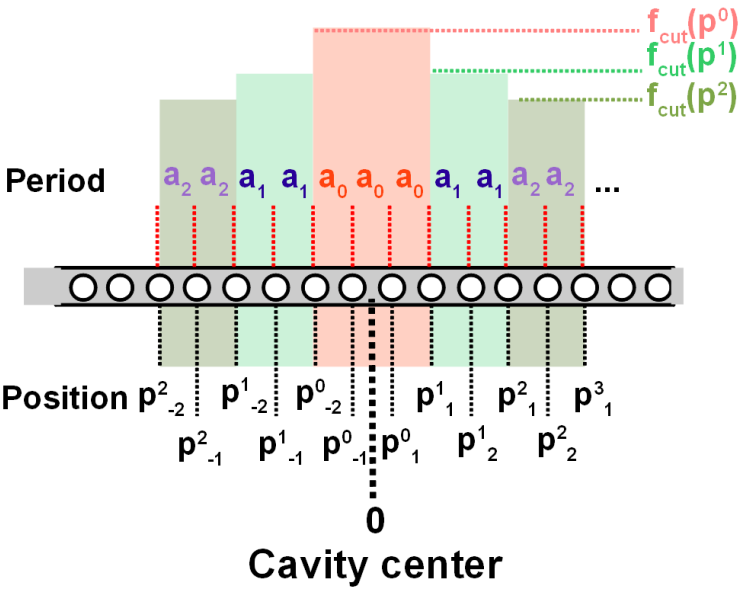

Figure 2.23: *Scheme of the center part of the apodized cavity.*

The expression (2.6) applied at $f = f_{cav}$ gives the general expression of $q(a(x))$ of the field for such modulated structure:

$$q(f_{cav}, x) = \sqrt{\frac{K\left(\frac{1}{a_0} - \frac{1}{a(x)}\right)}{A_{a(x)}}} \tag{2.9}$$

Equalizing eq. (2.8) and (2.9) we obtain after some manipulation the following equation:

$$\alpha B^2 x^2 a(x)^2 + \left(\tilde{A}_0 B^2 x^2 - \frac{K}{a_0}\right) a(x) + K = 0 \tag{2.10}$$

where $\tilde{A}_0 = A_0 - \alpha a_0$ to simplify a bit the writing.

- If $\alpha = 0$, the solution of eq. (2.10) is simply given by

$$a(x) = \frac{a_0}{1 - \frac{A_0 B^2 a_0}{K} x^2} \tag{2.11}$$

- If $\alpha \neq 0$, equation (2.10) is a quadratic equation in a of determinant:

$$\Delta(x) = \left(\tilde{A}_0 B^2 x^2 - \frac{K}{a_0}\right)^2 - 4\alpha B^2 x^2 K \tag{2.12}$$

$$= \tilde{A}_0^2 B^4 x^4 - 2B^2 K \left(\frac{\tilde{A}_0}{a_0} + 2\alpha\right) x^2 + \frac{K^2}{a_0^2} \tag{2.13}$$

In order to determine the number of solutions of eq. (2.10) we must again solve an equation of the fourth degree in x which can be solved, in two times, by first solving a quadratic equation of unknown $X = x^2$. Then we get:

$$\Delta(X) = \tilde{A}_0^2 B^4 X^2 - 2B^2 K \left(\frac{\tilde{A}_0}{a_0} + 2\alpha \right) X + \frac{K^2}{a_0^2} \tag{2.14}$$

with a new determinant δ_X which is:

$$\begin{aligned} \delta_X &= 4B^4 K^2 \left(\frac{\tilde{A}_0}{a_0} + 2\alpha \right)^2 - 4\tilde{A}_0^2 B^4 \frac{K^2}{a_0^2} && (2.15) \\ &= 16 B^4 K^2 \alpha \left(\frac{\tilde{A}_0}{a_0} + \alpha \right) \qquad > 0 && (2.16) \end{aligned}$$

This means eq. (2.14) has two solutions X_+ and X_- that are:

$$X_\pm = \frac{K}{\tilde{A}_0^2 B^2} \left(\left(\frac{\tilde{A}_0}{a_0} + 2\alpha \right) \pm 2\sqrt{\alpha \left(\frac{\tilde{A}_0}{a_0} + \alpha \right)} \right) \tag{2.17}$$

Both solutions are positive so we can rewrite the determinant Δ as function of x

$$\Delta(x) = (x - \sqrt{X_+})(x + \sqrt{X_+})(x - (\sqrt{X_-})(x + \sqrt{X_-}) \tag{2.18}$$

The quadratic equation in $a(x)$ has solutions when $x \in \left]0, \sqrt{X_-}\right[$ and when $x \in \left]\sqrt{X_+}, +\infty\right[$. There is a range of value of x between $\sqrt{X_-}$ and $\sqrt{X_+}$ where there is no solution for $a(x)$. As we start from $x = 0$, the values of $a(x)$ will be determined as a function of x values in the range $]0, \sqrt{X_-}[$.

Again two solutions a_+ and a_- of eq. (2.10) are possible. Because $a_+ \to +\infty$ when $\alpha \to 0$, we only keep $a_-(x)$ as a valid solution.

$$\boxed{a_- = \frac{-\left(\tilde{A}_0 B^2 x^2 - \frac{K}{a_0} \right) - \sqrt{\left(\tilde{A}_0 B^2 x^2 - \frac{K}{a_0} \right)^2 - 4\alpha B^2 x^2 K}}{2\alpha B^2 x^2}} \tag{2.19}$$

Equation (2.19) is the most general solution in our approach.

Figures 2.24, 2.25 and 2.26 show examples of the calculated "ideal" variations of the lattice constant a (top graph), the decay factor q (middle graph) and the field envelope (bottom graph) as a function of the position x for three values of the constant α. These variations are, of course, unrealistic since to obtain them it would be necessary to vary continuously the "period" of the PhC with x .

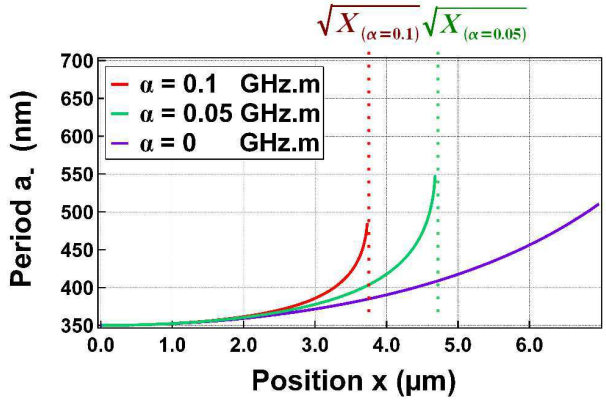

Figure 2.24: *Hole-to-hole distance as a function of the distance x to the cavity center for three different values of coefficient α.*

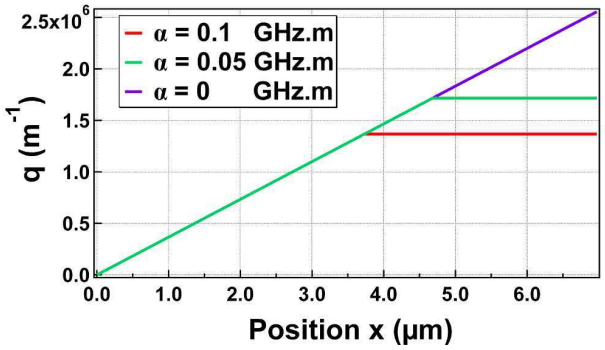

Figure 2.25: *Decay factor q as a function of the distance x to the cavity centre for three different values of coefficient α.*

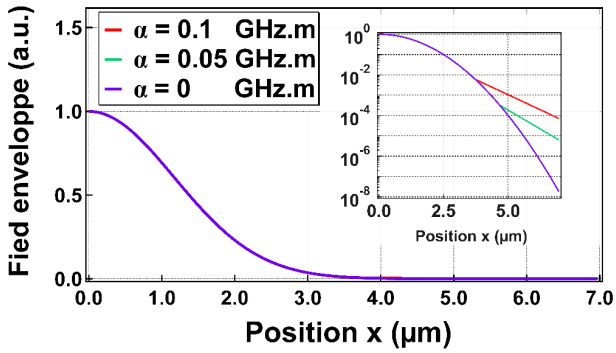

Figure 2.26: *Ideal field envelope as a function of the distance x to the cavity centre for three different values of coefficient α.*

As we expect, the period a increases with x, this, more abruptly when α is augmented. The range of values of a is also more restricted when α is higher. Because $a(x)$ diverge at $\sqrt{X_-}$, the range where it is possible to vary the lattice constant is also limited to $\sqrt{X_-}$. In practical, in such situation, the lattice constant remains constant before $\sqrt{X_-}$. This has a noticeable effect on the variations of q: close to 0, q varies proportionally with x as expected but close to $\sqrt{X_-}$, the value of q is clamped to a constant value, which means that the decay of the field is from that position purely exponential and not Gaussian anymore. These "ideal" field envelopes are plotted in the inset of fig.2.26 where the red and the green curves become straight lines for x > $\sqrt{X_-}$.

However, even with a large value for α=0.1 GHz.m, the field envelopes we found are almost identical. Hence, in the following, we will simply neglect the effect of α and use expression (2.11) for $a(x)$.

Up to now we have considered continuous variation of a and q, even though $a(x)$ varies by step in a real structure. The variation of q induced by this discretisation can differs significantly of the one obtained in a continuously varying model. The challenge of the actual construction of the apodised PhC Wire Cavities is to get the value of q as close as possible to the "ideal" case.

We will now describe and explain the hole positioning method chosen in this work.

2.2.3.2.c Construction method

Similarly to the construction designs presented by Noda's group [126], the centre (x=0) of our structure is positioned between two holes (see fig. 2.23). In this configuration the maximum of the field intensity is located at x=0, between the holes. Note that it is also possible to build an apodised structure centred on a hole with similar characteristics. Thus, our choice is arbitrary. Because the structure is symmetric in the x direction, we describe only the x>0 space region.

The first "block" of central period a_0 is chosen to be 3 periods long, i.e. the two first holes position are:

$$\begin{aligned} p_1^0 &= \frac{1}{2}a_0 \\ p_2^0 &= \frac{3}{2}a_0 \end{aligned}$$

As illustrated in fig. 2.23, we choose to arrange the next holes by blocks of 2 periods. It would have been possible to define blocks of only 1 period long but this would have led, for the same target field envelope, to smaller shifts Δa, especially for the firsts blocks. Instead, we kept in mind that we wanted to actually fabricate these structures; so, we tried to keep the shifts higher than the e-beam maximal resolution which, at present in LPN, is 0.5 nm. In the very latest results of this thesis, it appeared that implementation of 1 period long blocks could improve significantly the obtained Q-factors of the cavities with large spatial extensions. However, this optimisation will not be addressed in this manuscript as the Q factors obtained with 2 blocks are high enough for the purpose of this PhD. Let's add that blocks longer than 2 periods would have

decreased the accuracy of the linearisation of $q(x)$, i.e. the accuracy on the Gaussian apodisation of the field described above.

We call "1^{st} hole" of the block, the hole in the middle of the block. The position of the two holes (indexed by k) of the i^{th} block are then expressed as

$$\begin{aligned} p_k^i &= \frac{3}{2}a_0 + 2\sum_{j=1}^{i-1} a_j + k * a_i \\ &= \tilde{C}_i + k * a_i \end{aligned}$$

where $a_i = a(p_1^i)$ and $\tilde{C}_i = \sum_{j=0}^{i-1}(2a_j) - \frac{1}{2}a_0$.

Hole positioning: strategy n°1

The simplest strategy to shift the period is described in figure 2.27. After placing the second hole (the last hole of the first block), we extract from the ideal variation of $a(x)$ at position p_2^0 , deduce the new period a_1 which will lead to a new value for q, following the established linearisation illustrated in fig. 2.25. With this period, we can place the two holes composing the second block and then repeat the procedure to extract the third period a_2 and again to position the holes of the third block. This algorithm is equivalent to considering that the decay factor q_i for the i^{th} block is equal to its value at the beginning of the block.

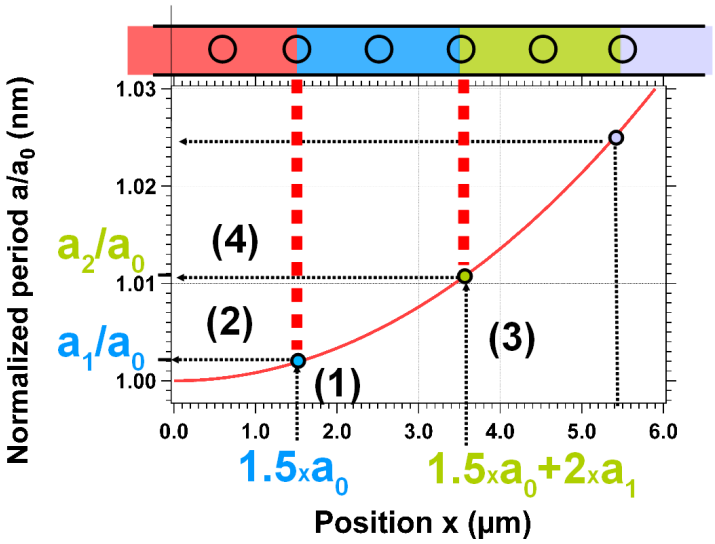

Figure 2.27: *Scheme I for Gaussian apodisation: straightforward case where we start from the last hole position of the first block* ***(1)*** *and deduce the period* a_1 ***(2)***. *After positioning the two holes of the second block, we repeat the procedure (****(3)*** *and* ***(4)****).*

.

This strategy was not implemented in the case of apodised structures made with 2 "periods" long blocks but gave good results in the case of blocks of length of 1 "period". Again, this case

will be eluded in this work, but constitutes in the end a simplified case of the method presented here.

Hole positioning: strategy n°2

Another possible strategy is the one described in figure 2.28 where the goal is to obtain blocks of decay factors q_i that are taken in the middle of the block. This is not straightforward anymore as it implies finding simultaneously the middle position of the block, which is conveniently placed here at the position p_1^i of the first hole, with its associated lattice constant a_i. Mathematically, this means we need to solve eq. (2.11) at $x = p_1^i$, which writes:

$$a(p_1^i) = \frac{a_0}{1 - \frac{\tilde{A}_0 B^2 a_0}{K}(p_1^i)^2} \tag{2.20}$$

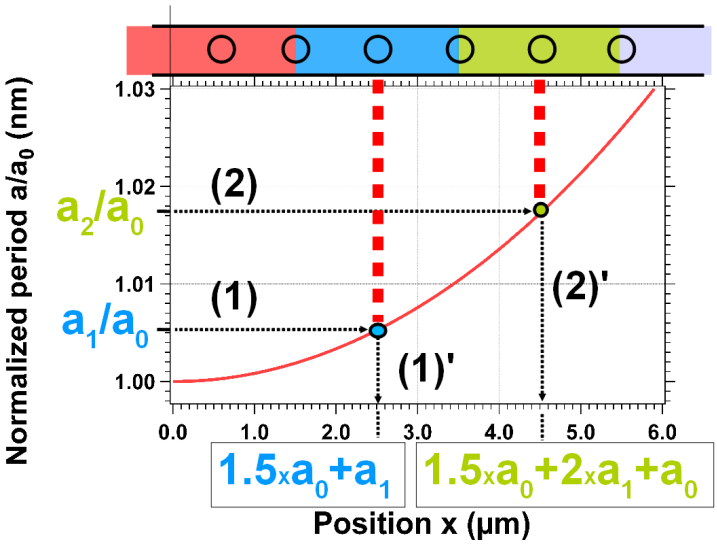

Figure 2.28: *Scheme II for Gaussian apodisation: we fix the decay factor value exactly in the middle of each block. We must simultaneously find* a_i ***(1)*** *and* p_1^i ***(1)'*** *by solving* (2.20).

.

The solving of equation (2.20) requires that we solve a cubic equation in a_i. To simplify the calculus, we assume that $\frac{\tilde{A}_0 B^2 a_0}{K}(p_1^i)^2 \ll 1$, then

$$a_i = a_0 \left\{ 1 + \frac{\tilde{A}_0 B^2 a_0}{K} \tilde{C}_i + {a_i}^2 \right\} \tag{2.21}$$

$$= a_0 \left\{ 1 + \frac{\tilde{A}_0 B^2 a_0}{K} (\tilde{C}_i^2 + 2\tilde{C}_i a_i + {a_i}^2) \right\} \tag{2.22}$$

which can be rewritten as the following quadratic equation:

$$a_i{}^2 + a_i \left(2\tilde{C}_i - \frac{K}{\tilde{A}_0 B^2 a_0{}^2} \right) + \left(\tilde{C}_i^2 + \frac{K}{\tilde{A}_0 B^2 a_0} \right) = 0 \tag{2.23}$$

The solutions of this quadratic equation are:

$$a_i^{\pm} = \frac{-\left(2\tilde{C}_i - \frac{K}{\tilde{A}_0 B^2 a_0{}^2} \right) \pm \sqrt{\left(2\tilde{C}_i - \frac{K}{\tilde{A}_0 B^2 a_0{}^2} \right)^2 - 4\left(\left(\tilde{C}_i\right)^2 + \frac{K}{\tilde{A}_0 B^2} \right)}}{2} \tag{2.24}$$

$$= \frac{-\left(2\tilde{C}_i - F\right) \pm \sqrt{4\tilde{C}_i F + F\left(F - 4a_0\right)}}{2} \tag{2.25}$$

where $F = \dfrac{K}{a_0{}^2 \tilde{A}_0 B^2}$. The acceptable solution for our model is a_i^- since the a_i^+ solution is much higher than a_0, even for the first block.

Figures 2.29 illustrates the hole-to-hole distances and field profile envelopes for continuous and discrete variations of $a(x)$. In the continuous case, we see that the approximation made to pass from eq. (2.11) to eq. (2.22) is good, as it only slightly decreases the variations of a with x and leads in both cases to an almost identical ideal field profile envelope. Within the same approximation, with eq. (2.25), we also iteratively computed and plotted the case of a PhC with discrete variations of the lattice constant a. From these variations of a_i, we calculate the field envelope by taking q=$q(a_i)$=$constant(i)$ for each block (see fig. 2.29) in order to have an idea of the effect of the discretisation on the targeted Gaussian envelope. In this case, we show that the discretised envelope has a spatial extension slightly higher than in the continuous case. This is the result of the propagation in the first block which is "decayless" at the resonance frequency, i.e. q=0, and hence participates to shift the starting point of the envelope decrease. We will see in section 2.2.3.4 that this discrepency is however not a problem as the increase of the spatial extension is linear as a function of the targeted one.

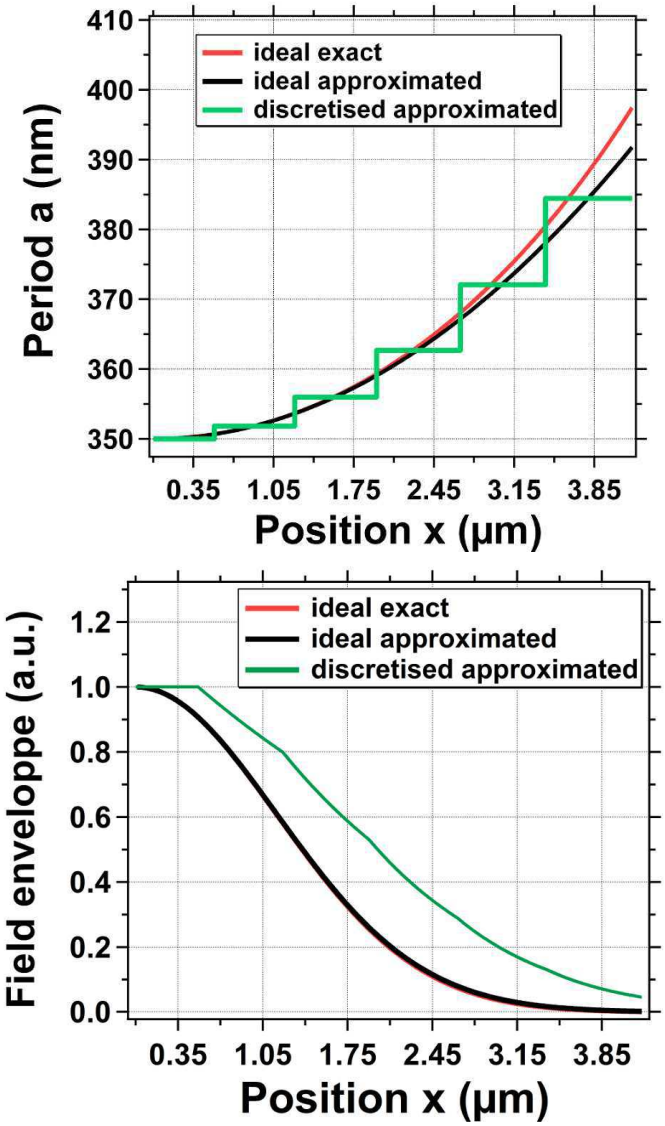

Figure 2.29: *Hole-to-hole distances a (top graph) and their corresponding field envelope profiles (bottom graph) as a function of the position x from the cavity centre for the three considered cases.*

The apodised structure is divided in a zone where the lattice constant varies and a zone where it remains constant (periodic structure). For a given spatial extension, we chose a constant number of blocks of varying lattice constant (here, 6 blocks, i.e. 12 holes starting from the centre), and a periodic block of 11 more holes. Note that, in this work, we kept the length of the two zones constant for the sake of simplicity. However, as we will illustrate, the best solution would be to adapt the length of the apodisation zone to the desired spatial extension of the cavity mode.

In the next section, we present the results of the 3D FDTD simulations we performed on cavities build with the Gaussian apodisation procedure.

2.2.3.3 Typical mode distribution calculated with 3D FDTD

The cavity is assumed to have a refractive index $n = 3.35$ which is the average RI of the InP ($n = 3.17$) slab embedding InGaAsP/InGaAs quantum wells. The cavity environment, including the holes, is made of SiO_2 ($n = 1.46$). The wire is 505 nm wide and 285 nm high. The height of the wire is kept under $(\lambda/3.35)^3$ in order to kept the cavity monomode in the transverse direction and its precise value is just the actual thickness of the III-V material we use experimentally. The width was chosen by equalising the effective index of the wire and the one of a Silicon-On-Insulator wire in order to favour the evanescent optical coupling (see chapter 5 for more detail on this point). The central period a_0 is 350 nm and the constant hole radius r is 120 nm. The parameter B equals 3×10^{11} m^{-1}, α is neglected, A_0 is taken to be 5.8 $Hz.m^2$ and K=4.82×10^7 $Hz.m$.

Figures 2.30 shows the electric field intensities for the 4 first modes of the cavity.

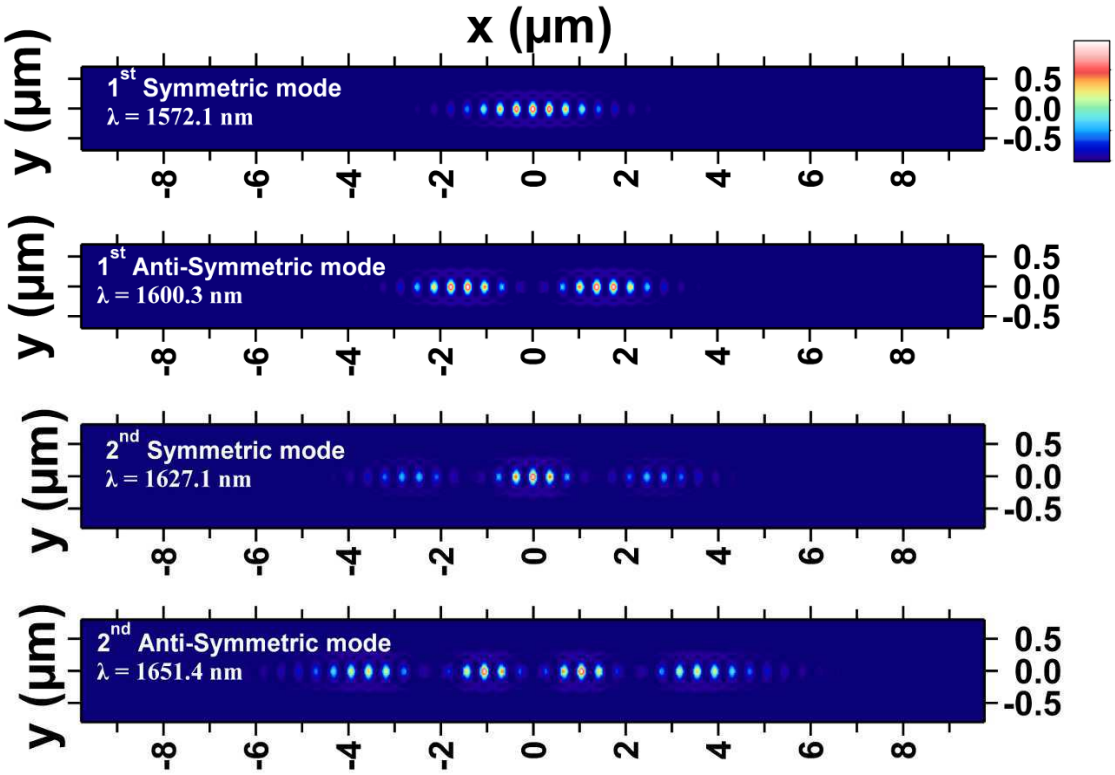

Figure 2.30: *Electric field intensities of the first 4 modes of a PhC Wire Cavity designed with Gaussian apodisation of the field.*

Note that the electric field intensities are confined in the high index material, between the holes, which was expected since we built them from dielectric band-edge modes. Like in the simulations of the TD PhC wire cavities, we distinguish the modes of the cavity by their wavelength and their symmetry with respect to the plane perpendicular to the wire and passing through the cavity centre ($x = 0$).

The first symmetric mode has a resonance at the wavelength λ=1572.0 nm. The quality factor Q obtained by harmonic inversion gives $Q \approx 955\ 000$, which is more than one order of magnitude greater than that of the TD PhC wire cavities. The first anti-symmetric mode has a higher resonance wavelength λ=1600.3 nm and a Q-factor around 350 000. Then, the second symmetric and anti-symmetric modes have respectively resonance wavelengths equal to 1627.1nm and 1651.4nm but their quality factors, respectively 85 000 and 6900, are much smaller than for the first modes. The reason for this is that those mode do not originate from the central block band-edge mode but from some other lateral block band-edge mode which can propagate back and forth between the blocks, like in a FP cavity. These modes are then closer to the TD PhC wire cavity modes we studied initially. Their field profile envelopes are not Gaussian as their intensity distribution extend above the Gaussian apodisation distance which, in this case, is 4.5 μm. In addition, the approximation made in the model ($\frac{\tilde{A}_0 B^2 a_0}{K}(p_1^i)^2 \ll 1$, values of A and K, etc) can also partly account for these shorter photon lifetimes. Higher Q-factors can be obtained for the second order modes by extending the apodisation over a greater length by adding more blocks, keeping in mind that it is necessary to keep the band-edge mode of the new blocks far enough from the cavity mode. However, for most applications, we are interested in achieving perfect single mode operation. In reality, we obtain most of the time two high-Q modes with a free-spectral range (FSR) determined by the width of the mode along the wire. We will see that this is not detrimental for QW nanolasers.

2.2.3.4 Impact of the cavity-field envelope on the losses

In order to modify the spatial extension of the field along the x direction, it is more convenient to replace the parameter B by Full-Width Half Maximum (FWHM) parameter which is defined through the following relation:

$$FWHM = 2\sqrt{\frac{ln(2)}{B}} \tag{2.26}$$

Figures 2.31, 2.32 and 2.33 show the E_y field profiles along the wire ($y = 0$) of the first symmetric mode of the cavities of FWHM equal to 2.1, 3.0 and 4.2 μm and their Fourier transforms. The wavelength are found to be respectively λ= 1588.1 nm, λ=1572.1 nm and λ= 1564.8 nm and the Q-factor respectively 37 000, 910 000 and 240 000.

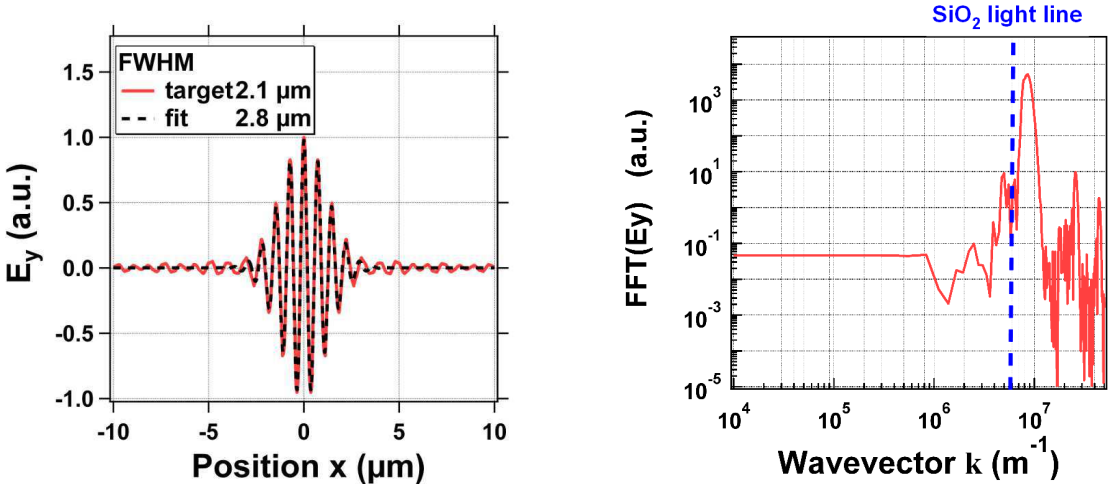

Figure 2.31: *E_y field profile along the wire (y=0) and the associated FT of the first symmetric mode of a cavity of FWHM equal to 2.1 µm. Fit (dashed line) with a Gaussian-cosinus product function is also plotted.*

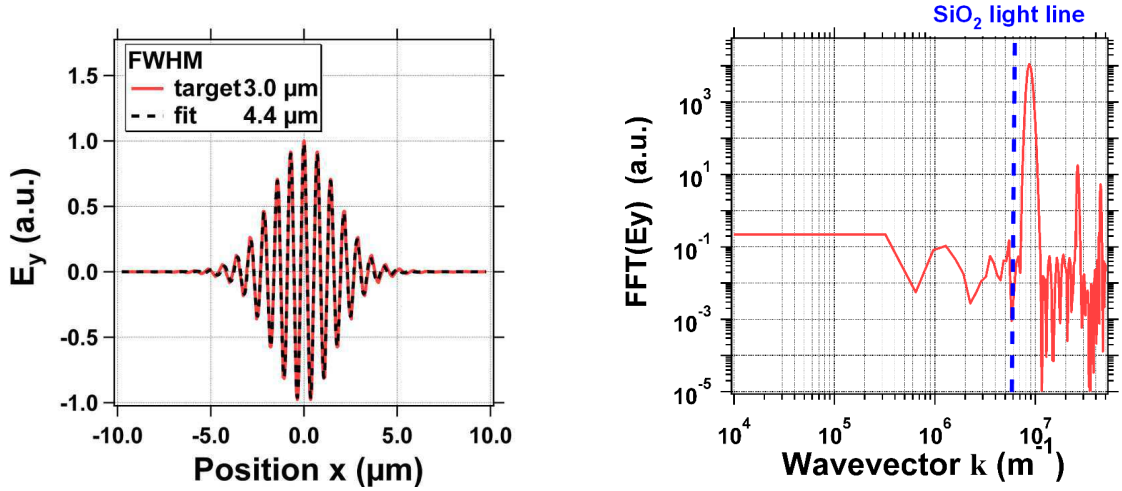

Figure 2.32: *E_y field profile along the wire (y=0) and the associated FT of the first symmetric mode of a cavity of FWHM equal to 3.0 µm. Fit (dashed line) with a Gaussian-cosinus product function is also plotted.*

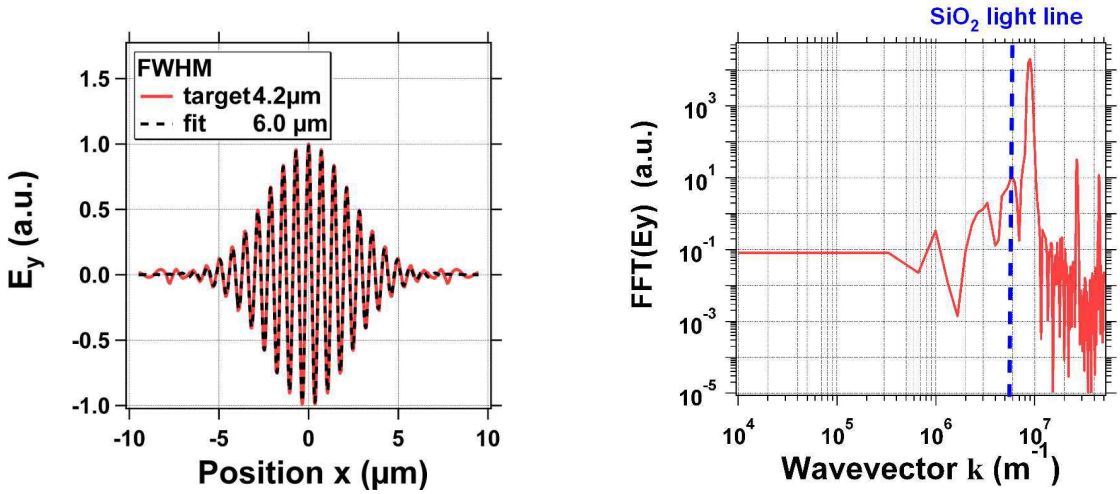

Figure 2.33: *E_y field profile along the wire (y=0) and the associated FT of the first symmetric mode of a cavity of FWHM equal to 4.2 µm. Fit (dashed line) with a Gaussian-cosinus product function is also plotted.*

As expected, the field profiles (red traces) follows almost perfectly a Gaussian envelope. The most direct way to test the reality of this claim is to fit the profiles by the product of a Gaussian and a cosine functions. We used the usual Levenberg-Marquardt algorithm to fit the profiles. The fitted curves (dashed lines) follow accurately the calculated profiles in the region where most of the field is confined.

The effective FWHM of the fields extracted from the fits are compared in fig. 2.34 with those which were targeted. In the range of FHWM that was tested, we found that the values obtained from the fits are always higher than the FWHM targeted values, as expected from fig. 2.29. Although the differences between the two values, targeted and effective, increase when increasing the target FWHM, we observe that this increase is perfectly linear in our FWHM range. Hence, it is possible to improve our model, by adding such relation mathematically. Note also, that it is very likely that the levels of accuracy on the values of A or K obtained by fit can also partly explain these differences.

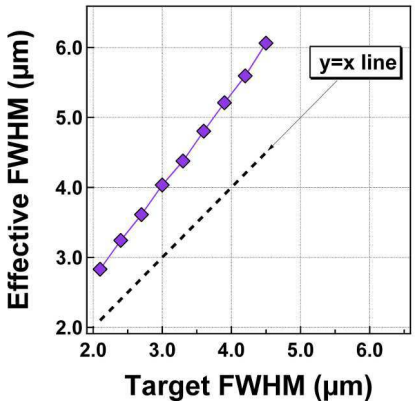

Figure 2.34: *Effective FWHM obtained with 3D FDTD as a function of the target FWHM. The dashed line indicates the y=x limit.*

In the case of the FWHM equal to 2.1 μm and 4.2 μm, the Gaussian-cosinus function fit cannot account for the remaining oscillations of the field that are observed but are correlated with a decrease of the Q-factors compared to the FWHM equal to 3.0 μm

Figure 2.35 shows the Q-factors (red markers) obtained when we vary the FWHM. Although it appears that the extension of the field is easily controllable by directly changing the FWHM parameter, the Q-factor varies between 10^3 to more than 10^6. The high-Q (above 500000) are obtained for a particular range of FWHM, between 2.5 and 3.5 μm. Below 2.5 μm, the Q-factor quickly decreases when the FWHM is decreased, while, above 3.5 μm, we observe a shallower decrease. As we are going to show, these behaviours are mainly due to an unoptimized number of chosen blocks of apodisation.

Before that, it is interesting to compare the evolution of the Q-factor with the FWHM to the amount of the spatial Fourier Transform of the field that is contained in the leaky region, i.e. the region of the reciprocal space within the light cone of the surrounding medium defined by $k < 2\pi n_{SiO_2}/\lambda$ (here $k = 5.8\ \mu m^{-1}$). This can be firstly appreciated by looking at figures 2.31, 2.32 and 2.33. We can can clearly see that, as expected, the field distribution peaks at a wavevector close to π/a_0 ($k = 9\ \mu m^{-1}$) and that the amount of the field within the light cone is greater for a FWHM = 2.1 μm than for a FWHM = 4.2 μm. The amount of the field within the light cone is estimated for different FWHMs by calculating the integral ξ along the x direction within the light cone of the FT of the field. The result is plotted in figure 2.35 (green markers) in the same range in y-axis than that of the Q factor. We observe that, for most of the cases, a diminishing

of ξ corresponds to an increase of Q of the same order of magnitude showing that the "smart confinement" of the field is at the origin of the boosting of the Q factor (some inconsistent values are probably due to the FT resolution or to the 1D analysis of the field distribution instead of a full 2D calculation). Moreover, the increase of ξ that can be observed from both sides of the highest Q value is another proof that something is wrong in this apodisation process.

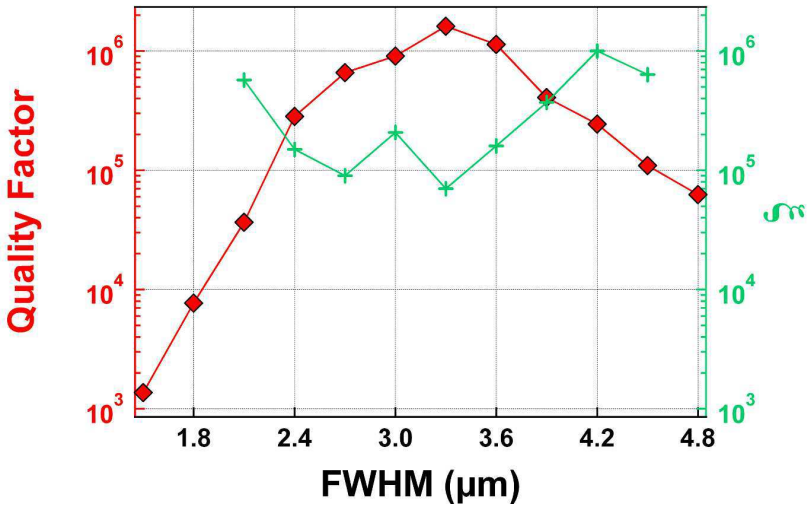

Figure 2.35: *Evolution of the quality factor Q and the integral ξ of the first symmetric mode as a function of the FWHM. Central period is taken as 350 nm with hole radius of 120 nm.*

2.2.3.5 Impact of the length of the apodisation zone

Because we fixed a constant number of blocks (6), some issues in the confinement can appear, depending on the FWHM.

Firstly, the number of apodisation blocks limits the length of the zone where the field should vary with a Gaussian envelope. Thus, if the number of blocks of the Gaussian apodisation is too small, the length of the apodised zone becomes shorter than the expected extension of the cavity mode and, of course, a decrease of the Q factor should arise. Indeed, as we can see in figures 2.26 when the lattice constant is fixed, the field profile stops to be Gaussian to exponentially decay with the distance, resulting in an increased amount of the field distribution in the leaky region. Secondly, the strength of the mirror formed by the periodic part of the structure is completely determined by fixing both the FWHM and the number of blocks. This means, if the FWHM and the number of blocks are not chosen properly, the periodic part of the structure could reflect

poorly light which could lead to an increase of the in-plane losses. Optimally, the FHWM and the number of blocks should be fixed such as the lattice constant a_i of the periodic part of the cavity corresponds to the maximum achievable q. As indicated by figure 2.20, this happens when $a_i = a_i^{max}$ for which $f_{a_0}^{cut}$ falls right in the middle of the PBG of the PhC defined by the lattice constant a_i^{max}.

Another issue, that we did not tackle during the calculations of $a_i(x)$, is the case when the variation of the lattice constant becomes so large that the cut-off frequency associated with the last lattice constant exceeds the range where f^{cut} and q can be approximated with a parabolic function (relation (2.3)). This happens when $a_i > a_i^{max}$ as beyond this lattice constant, q starts to decrease which will obviously impact the field profile envelope.

Figure 2.36 illustrates this particular point for three cavities of FWHM respectively 2.1, 3.0 and 4.2 μm and of central period fixed to 350 nm. In this figure, we plot the frequencies of the two band-edges mode as a function of the inverse of the lattice constant. Here, the mid-gap frequency that limits the validity of eq. (2.3) is reached when the lattice constant goes beyond 410 nm. As it is shown in the figure, this leads to a flaw in the design which is partially responsible for the rather low Q (37000) obtained for a FWHM equal to 2.1 μm. Indeed, in this case, the lattice constant goes up to 487 nm, much above 410 nm. One can also notice tha the lattice constant increases so much (above $\approx$ 455 nm) that the air-band-edge mode frequency goes below the cavity frequency. This is of course terrible for the confinement of the cavity mode as it creates a channel of losses through which light can directly couple and escape. After realising this point, one can understand better the origin of the field oscillations far from the cavity centre seen in fig. 2.31.

Table 2.1 reports the evolution of the Q factor of the mode of FWHM= 2.1 μm when we try to correct this issue by decreasing the number of block. We observe that when the apodisation is stopped just before reaching 455 nm (5 blocks instead of 6), the Q factor passes right away from 37000 to 165000. While with 4 blocks the Q factor is approximately the same, it start to decrease again when we decrease more the number of blocks, despite the supposedly better implementation of the apodisation design. We guess that, here, we fall in the problem previously described that is the length of the apodised zone (2.34 μm) becomes too short to confine a cavity mode of effective FWHM of 2.8 μm (see fig. 2.34).

Finally, it is important to keep in mind that for small FWHM, the shifts in the decay factors have to be very large over a small range of blocks to follow the ideal variation calculated previously.

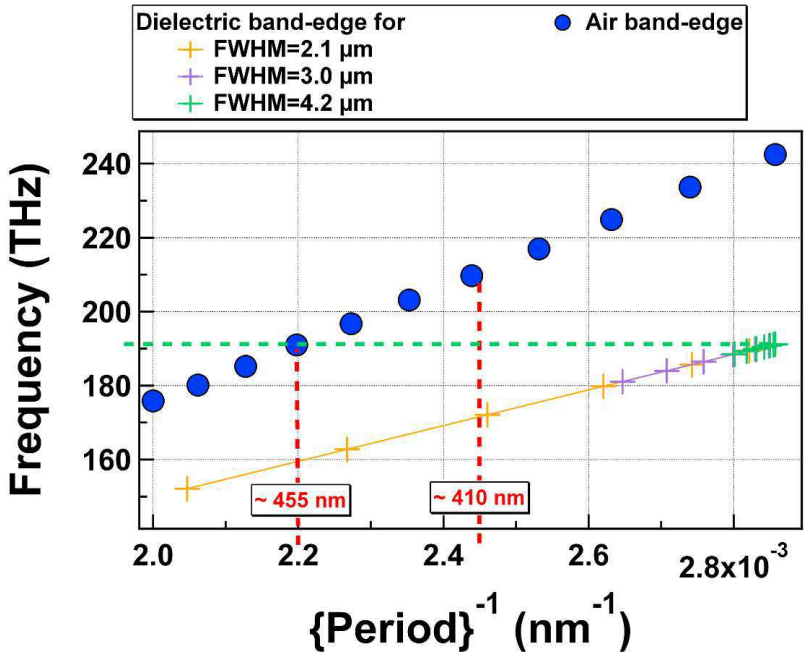

Figure 2.36: *Evolution of the cut-off frequencies inside the apodised cavities of FWHM 2.1, 3.0 and 4.2 µm as a function of the inverse of the period a of each block. The evolution of the the air band-edge mode frequency is also plotted. The horizontal dashed line indicates* $f_{a_0}^{cut}$ *and vertical dashed lines the values of* $1/a$ *for which* $f_{a_0}^{cut}$ *is right at the centre of the PBG and at the air band-edge.*

FWHM	2.1 μm	2.1 μm	2.1 μm	2.1 μm	2.1 μm
Number of blocks	2	3	4	5	6
Position of first periodic hole	1.60 μm	2.34 μm	3.13 μm	3.98 μm	4.09 μm
Q-factor	29 000	127 000	161 000	165 000	37 000
$(max(a))^{-1}$ $(\times 10^{-3} nm^{-1})$	2.74	2.62	2.46	2.27	2.05

Table 2.1: *Q-factor vs number of apodisation blocks.*

2.2.3.6 Impact of the number of periodic holes on the Q factor

Here, we assume that we work with a cavity of FWHM giving a high Q cavity, i.e. between 2.5 and 3.5 μm. The total length of these cavities is around 16 μm long. One can wonder how many numbers of holes in the periodic zone is necessary to keep a high Q. Therefore we simulate a cavity of FWHM equal to 3 μm whose number of periodic holes varies between 5 and 15, 11 being

the number of holes we used in afterwards fabricated samples. Figure 2.37 shows the resulting Q factors for the two first symmetric modes in the order defined previously.

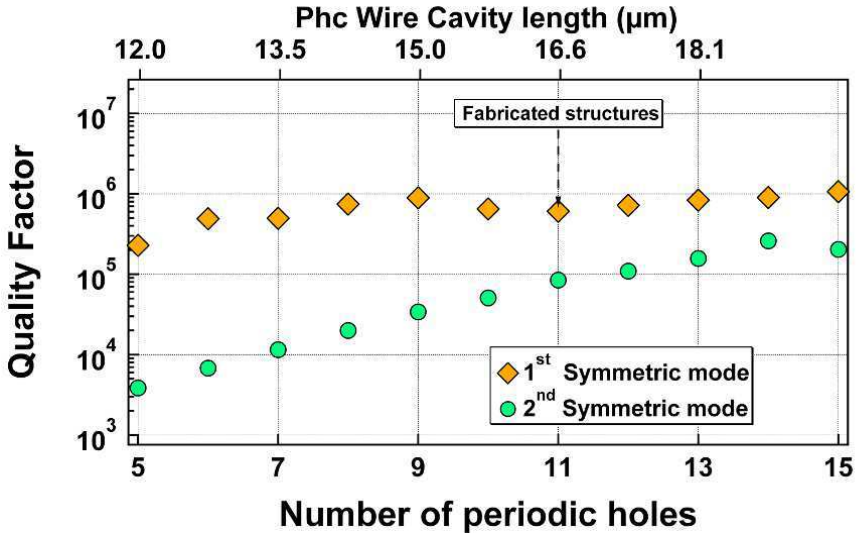

Figure 2.37: *Quality factor Q of the first two symmetric modes as a function of the number of periodic holes (bottom axis) and the total PhC Wire length (top axis). The parameters of the simulation are a_0=350 nm, r= 120 nm and a targeted FWHM=3.0 µm. The arrow indicates the number of holes that were in the fabricated sample.*

For the first symmetric mode, which is the main mode of interest in this work, we can see that the increase of the holes number from 11 to 15 keeps the Q factor unchanged. However, when this number goes below 6, the Q begins to decrease significantly, from $Q \approx 10^6$ to $Q \approx 200000$ for 5 holes. Differently the Q factor of the higher order modes are more sensitive to this holes number. We plot as an example, the Q factor of the second symmetric mode as a function of the holes number. This could have been expected by looking at its intensity profile, more extended than the 1^{st} symmetric mode. For the laser application targeted in this work, it can be useful to set a number of holes in the periodic part to avoid mode competition which may lead to instabilities of the laser emission.

2.2.3.7 Wavelength dependence on the FWHM

Figure 2.38 shows the wavelength variations of the two first symmetric modes when the FWHM of the first symmetric mode is varied. It is striking that the 1^{st} symmetric mode wavelength can be very different from the dielectric band-edge wavelength of the central block, which is here

close to 1567 nm. As we pointed out earlier, this has been studied in more details in [112] and references therein through a perturbative calculation. Moreover, the spectral separation between these modes decreases for increasing FWHM. We conclude that the Free Spectral Range (FSR), i.e. the spacing between two successive modes, follows the same behaviour so that it is possible to push away the 1^{st} anti-symmetric mode from the 1^{st} symmetric mode to obtain for example single mode laser emission.

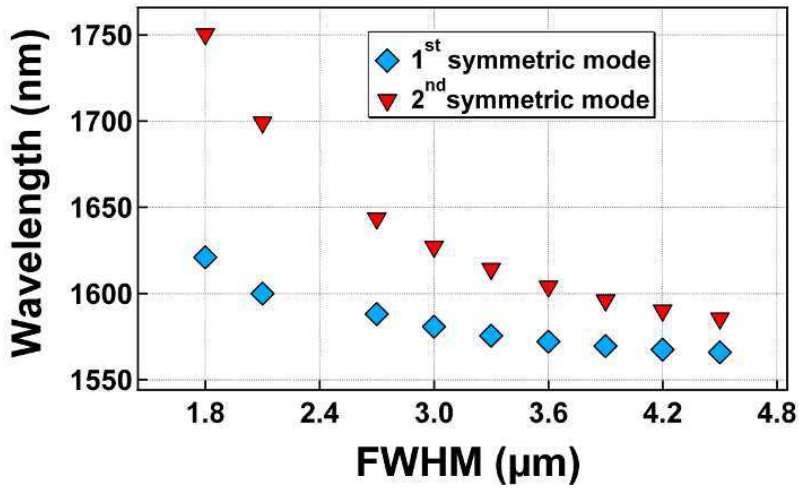

Figure 2.38: *Evolution of the wavelength of the 2 first symmetric modes as a function of the FWHM. Central period is taken again equal to 350 nm and the hole radius to 120 nm.*

2.2.3.8 Modal volume dependence on the FWHM

Figure 2.39 shows the modal volume V of the first symmetric mode when the FWHM is varied. We observe that V varies linearly with the FWHM. The obtained values are ranging from 0.5 to $1.25(\lambda/n_{Si})^3$, which are typical values found in literature for high-Q cavities [112].

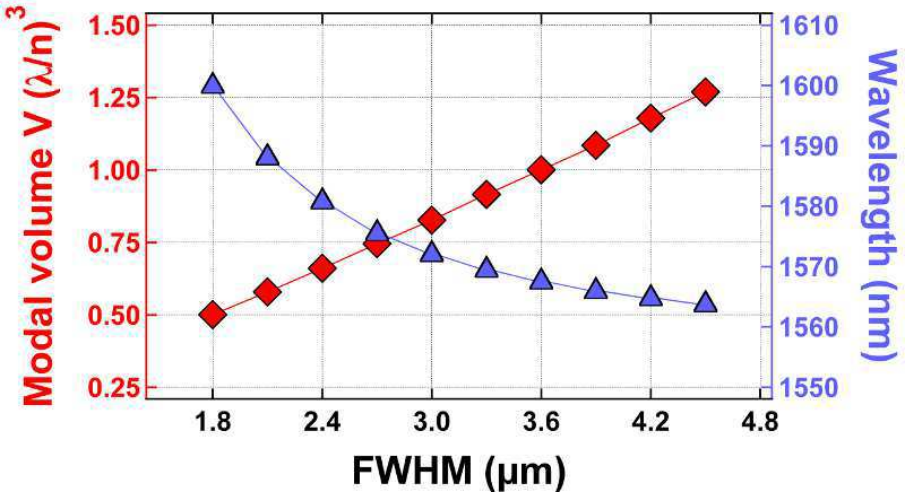

Figure 2.39: *Evolution of the modal volume V and wavelength of the first symmetric mode as a function of the FWHM. Central period is taken again equal to 350 nm and the hole radius to 120 nm.*

Until now, we have shown designs of apodised PhC Wire Cavities with a fixed central period a_0 and radius r. In the good conditions, we obtain Q-factors above 10^6. Now, we are about to present a major advantage of this design: its excellent tunability.

2.2.3.9 Impact of the central period and hole radius on the Q factor Tunability

Contrarily to what has been reported on PhC Wire Cavities based on tapered defect mirror [122, 123], the apodised design allows to vary the wavelength from 1400 to 1600 nm while keeping their impressive confinement properties.

Figures 2.40 and 2.41 illustrate this point by plotting the Q and wavelength when the central period a_0 of an apodised cavity is varied from 310 to 360 nm. In this range, the mode wavelength increases linearly when the central period is increased with a slope $d\lambda/da_0 \approx 4$ nm/nm. The Q remains practically the same in all cases, specially for the first symmetric mode. The left graph of fig. 2.41 clearly proves the perfect tunability in the range 1400-1600 nm by showing that the high Q-factors are maintained whatever the wavelength is.

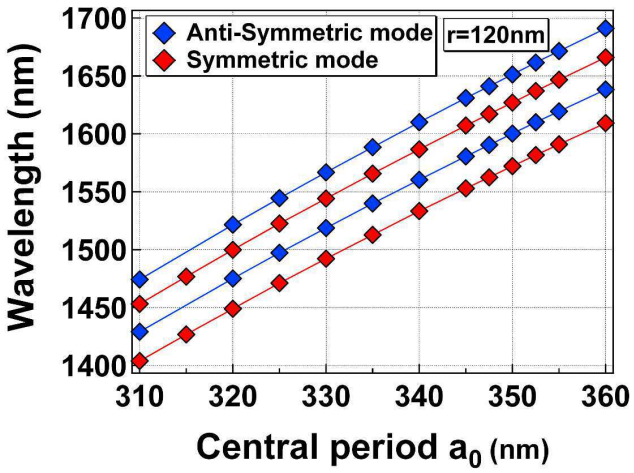

Figure 2.40: *Variations of the resonant wavelengths with the central period a_0 extracted from FDTD simulations. The four first modes are found for a PhC Wire Cavity with a constant hole radius equal to 120 nm and a FWHM equal to 3.0 μm.*

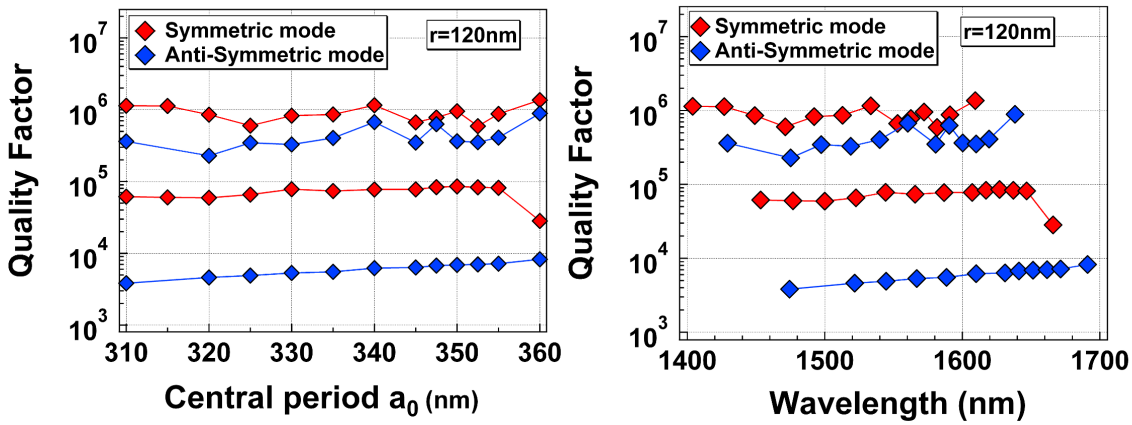

Figure 2.41: *Variations of the quality factor with the central period a_0 (left graph) and with the resonant wavelength explored by tuning the central period (right graph) extracted from FDTD simulations. The four first modes are found for a PhC Wire Cavity with a constant hole radius equal to 120 nm and a FWHM equal to 3.0 μm.*

Figures 2.42 and 2.43 show the Q and wavelength of several cavities of different hole radius r, with a central period set to 350 nm and a FWHM to 3.0 μm. Here, the wavelength decreases when the radius is increased with a slope $d\lambda/dr \approx -3.5$ nm/nm, in the radius range from 110 to 130 nm. Again, the plot of Q as a function of the wavelength shows that the high Q can be maintained despite the variations of wavelength, here going from 1530 to 1605 nm.

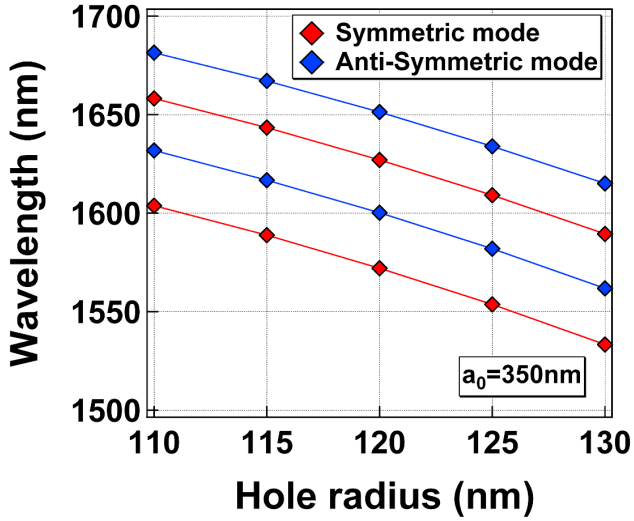

Figure 2.42: *Variations of the resonant wavelengths with the hole's radius r extracted from FDTD simulations. The four first modes are found for a PhC Wire Cavity with a constant central period* a_0 *= 350 nm and a FWHM equal to 3.0 µm.*

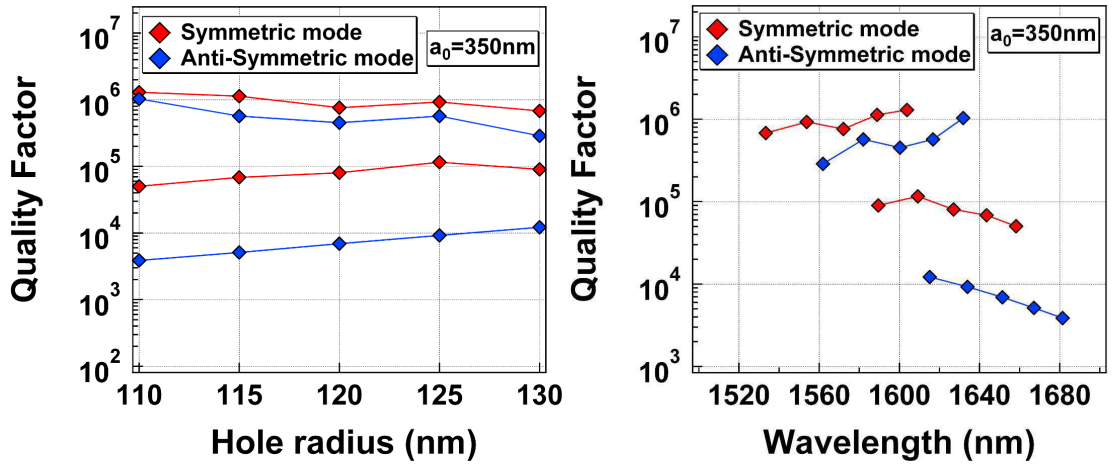

Figure 2.43: *Variations of the quality factor with the hole's radius r (left graph) and as a function of the resonant wavelength explored by tuning the radius of the holes (right graph). The four first modes are found for a PhC Wire Cavity with a constant central period* a_0 *= 350 nm and a FWHM equal to 3.0 µm.*

These results also show that our design will be pretty robust to errors of fabrication, which affect the real dimensions of the fabricated structures. As we will highlight in the next chapter, the precision on the lattice constant writing is defined by the electron beam lithographic system and is sub-nanometric in our case. However, the width of the wire and the hole's radius may differ more largely ($\approx$ 5-30 nm) from the intended ones, depending on the etching process. The fact that the cavities conserve their confinement properties for a large range of r is very important in

this design. Besides, the variations of the nominal wavelength due to the fabrication can easily be calibrated to correct the nominal radius and wire width values.

2.2.3.10 Spectral characterisation of fabricated samples

In this last section, we describe the spectral distribution of the fabricated apodised cavities as a function of the size of the different parameters such as the central period a_0 or the radius r. We fabricated the cavities, fully encapsulated in SiO_2, in an InP-based membrane containing strained InGaAsP/InGaAsP quantum wells. More details on the processing to obtain such cavities are given in the next chapter.

For the experimental characterisation, we benefit here from the *active material* embedded in the cavities which are optically pumped in a micro-photoluminescence set-up (described in chapter 4). The light escaping the cavity is collected and analysed in a spectrometre.

The sample examined here is a sample used to calibrate our fabrication process and test our design by varying many parameters. In this sample, we decided to vary the central period a_0, the radius r and the width W of the wire. Note that the two latter values are the nominal ones written in the lithographic mask ("GDS" file) but are generally shifted from the obtained values due to the etching process.

Figures 2.44-2.46 show a portion of the spectral measurement campaign results. We indicate on each graph the symmetry of each mode, found by assuming that the lower wavelength mode is symmetric with respect to the plane passing by x=0 and perpendicular to the x-axis. In fig. 2.44, the resonant wavelengths of each cavity are plotted as a function of the central period. They vary perfectly linearly with a positive slope $d\lambda/da_0 \approx 3.1$ nm/nm, in agreement with the simulations (4 nm/nm). The FSR is around 25 nm for all cavities, also very close to the one found in simulation. The variation of the λ's with r (fig. 2.45) present a negative slope $d\lambda/dr \approx$ -3.8 nm/nm, to compare with -3.5 nm/nm given by simulations. Finally, we also plotted in fig. 2.46 the variations as a function of the wire width W and found a slope $d\lambda/dW$ of 1.25 nm/nm.

Concerning the values of the wavelength, we can focus on the first symmetric mode. For a_0 = 350 nm, r= 120 nm and W = 505 nm, we find the mode at 1496 nm so $\approx$ 75 nm below the expected value (1571 nm). This discrepancy is mainly due to the effective dimensions of the holes and the wire width. For instance, if we suppose that each facet of the structure is over-etched by 10nm, the real hole's radii will be increased by 10 nm and the width of the wire will be decreased by 10*2=20 nm. Therefore, the total shift of the mode $\delta\lambda$ will then be 1.25*(-20)+(-3.8)*10=-72 nm, which is close to the one we found with this sample! In addition to the etching consideration, note that the value of the RI of our III-V slab is not precisely known. If the real average RI of the slab is shifted by only $+1 \times 10^{-2}$, a shift of +4 nm is expected.

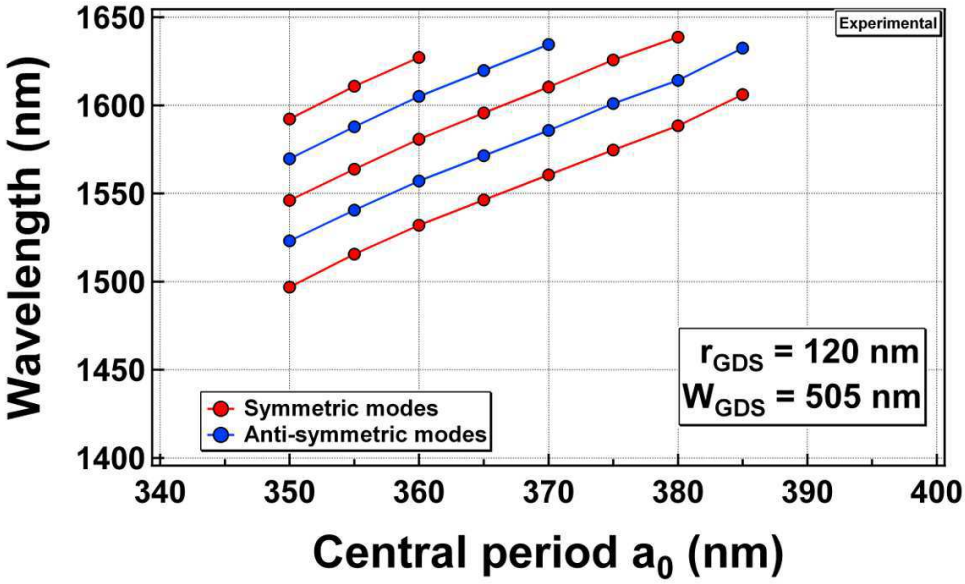

Figure 2.44: *Experimental spectral distribution of the modes of apodised PhC Wire Cavities as a function of the central period* a_0.

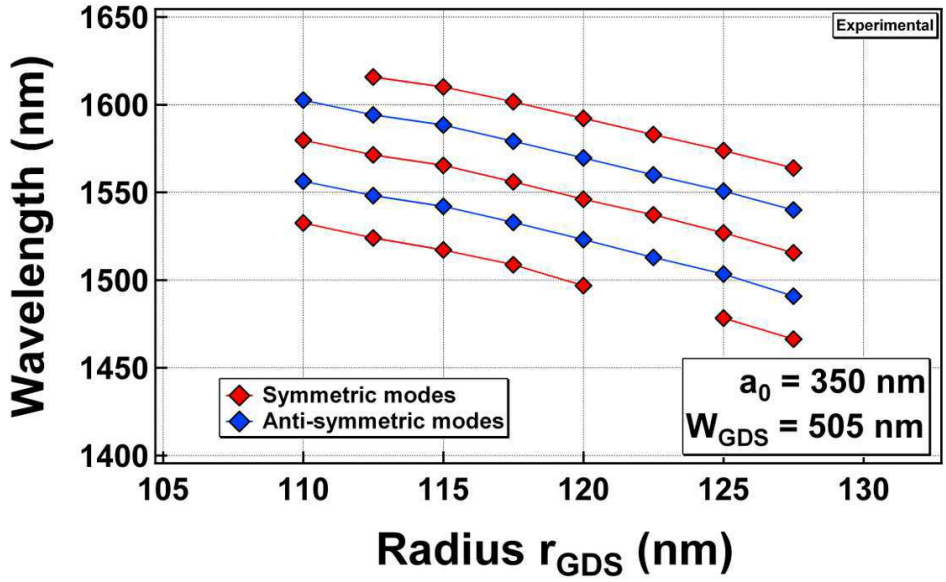

Figure 2.45: *Experimental spectral distribution of the modes of apodised PhC Wire Cavities as a function of the nominal radius* r.

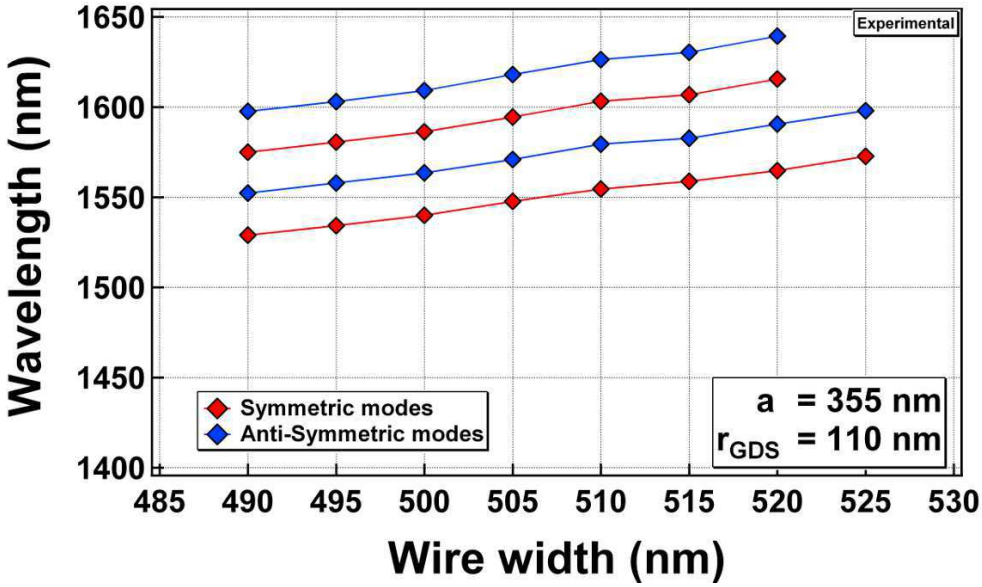

Figure 2.46: *Experimental spectral distribution of the modes of apodised PhC Wire Cavities as a function of the nominal wire width W.*

All this uncertainties in the fabricated system can however be calibrated easily and corrected. Because λ varies linearly with a_0, r and W, once the different slopes of the wavelength variations known, it is trivial to shift these parameters in order to tune the cavity wavelength to the desired position, for instance, at the maximum of the gain in the case of laser applications.

As a prelude to the next chapter, dedicated to the fabrication of the hybrid structures, let's add that, in this work, it was necessary to regularly process calibration samples, in order to adapt the process to the unavoidable variations that can appear with time in any of the many steps necessary to build a cavity. For example, depending on the state of the etching chamber (cleanliness, pressure, temperature, ...), a given etching recipe can result in very different structures.

Finally, we limit here the characterisation of the fabricated sample to their very basic spectral properties as it is quite challenging to measure the quality factor of the cavities embedding an active material (quantum wells in this work). However, we will see in chapter 3 and 4 that the analysis of the laser emission characteristics can provide good estimations of the actual Q of our fabricated apodised cavities.

2.3 Conclusion

After briefly reviewing the fundamental properties of photonic crystals, we dedicated this chapter to the design of PhC cavities of high quality factor and modal volume of the order of $(\lambda/n)^3$. This study focused on PhC cavities formed in a wire which are, by consequence, naturally suited

for the coupling with an adjacent wire waveguide and whose footprints are usually below 20 μm^2. Two designs of PhC Wire Cavities, one already known and one original, were presented.

The first one is formed by two carefully tailored Bragg-mirrors embedded in the photonic wire [122, 123] that we refer as "Tapered-Defect" (TD) cavities. Despite previous demonstration of very high-Q's [123], the strong sensitivity, regarding the Q factor, of this sort of PhC wire cavity on its geometrical dimensions, particularly the holes diameter, make their fabrication challenging and the design poorly robust to slight variations during the processing.

The second design is based on the concept of *gentle confinement* [124]. We provided a fully analytical method to position the holes in the photonic wire to obtain cavity modes with Gaussian profiles which results in high Q factors above 10^6 and modal volume close to $(\lambda/n)^3$. By contrast with the TD cavities, we demonstrated the good robustness of their Q factor with variations of the main cavity parameters. Beside, the strong light confinement is achieved in structures fully encapsulated in a material of refractive index close to 1.5. Excellent tunability of the resonant modes was also demonstrated numerically and experimentally, both behaviour in good agreement.

This cavities also present a major advantage in comparison with TD cavities when it comes to the evanescent coupling with a SOI waveguide: their k-space distribution is centred in π/a_0 which makes the phase matching between the cavity and the guided mode extremely easy to tune. This particularity will be demonstrated and discussed in detail in chapter 5.


fig.3.18
Cl2/H2
2□m-wide
obtained
et
sample
PhC
enough
future
processed
conventional
presence
moment
step
III-V
visible
wire
required
low
despite
aligned
processes
shows
bonding
border
design
Figure
look
higher
ICP-RIE
layers
breaking
Si
deposited
achieved
using
waveguides
results
layer
Despite
ICP
previous
arise
stress
environment
chamber
place
sidewalls
cell
membrane
cracks
optical
mostly
neither
optimisations
silicon
see
quality
removed
improve
structures
hard-mask
done
excellent
thermal
close
zone
use
hybrid
cavities
exposed
Moreover
next
surface
includes
angles
SiN
MgF2
pictures
without
lower
chemistry
indeed
bottom
worth
possible
HSQ
limited
al
partly
feature
etched
relaxations
generation
striking
chemically
RI
closely
optimisation
pattern
conductivity
mechanical
encapsulation
significantly
bulk
Indeed
also
taken
structure
slightly
O2
give
sinking
applications
thin
flow
SiO2
easier
deposition
protected
impediment
defines
process
SOI
corresponding
chapter
handle
keeping
cladding
measured
heat
cavity
around
promising
fabrication
e-beam
good
thick
region
eventually
less
resist
trenches
etching
material
keeps
dense
least
trench
IBAD

Chapter 3

Fabrication of Hybrid III-V Photonic Crystal on SOI circuit

In the previous chapter, we showed how to design high-Q PhC Wire Cavities which are photonic structures naturally suited for the evanescent optical coupling with a waveguide. We concretize such a coupling by fabricating hybrid structures constituted, from one part, of a *passive* Silicon-On-Insulator (SOI) level and, from another part, of a III-V *active* level.

In what follows, we present the entire fabrication processes of the hybrid structure, from the SOI fabrication to the etching of the III-V PhCs passing through the bonding of the two material layers. We will address the main issues that were tackled at LPN during the last 5 years from the emergence of the III-V PhC /SOI circuit project to its latest technological developments.

Apart from the fabrication of the SOI circuit done through the *ePIXfab* European network, the complete fabrication of our samples is achieved at LPN. LPN has a large clean-room of $\approx$1000m² (700m² (class 100/1000)+ 300m² epitaxy(class 1000/10000)+ 150m² (technical areas)) belonging to the *Renatech* French national nanofabrication network providing all the necessary tools for the fabrication research and development in micro- and nano- technology. Within this facility, we have been able to continuously progress in the fabrication process of the hybrid structure.

3.1 Interfacing Photonic Crystals with the outside world

As it was introduced in chapter 1, the extraction (insertion) of light from (into) PhCs cavities was for a long-time a major drawback to their use in real applications, as, in practice, only a small amount of the light stored in these nanocavities is efficiently collected into useful signals. Indeed, even though PhCs cavities exhibit the most remarkable features for the enhancement of light matter interaction, devices based on the use of these structures do not hold their promises in terms of overall power efficiencies because of this problem of interfacing with the outside world. In the case of a cavity made in a 2D-PhC slab, the light is generally coupled out from the

structure either by diffraction and coupling to the radiative modes or by using a neighbouring waveguide.

The first mechanism involves usually complex out-of-plane radiation patterns which are generally not suited for surface operation. Quite recently, interesting work [130, 131, 132, 133] on how to optimise the beaming of the out-of-plane emission has been achieved, but these studies aim at goals very different from the in-plane integration in a photonic circuit.

The use of a waveguide neighbouring the PhC cavity to couple light in and out was implemented over the last decade in many different ways. Many studies [134, 135, 136, 137] have used waveguides designed directly inside the PhC slab, such as the one formed by a missing row of holes in a triangular lattice of holes (so-called "W1" PhC), to either side- or butt-couple a PhC cavity. In some designs, the PhC waveguide can then be coupled to a simple step-index wire waveguide [138, 139, 140] possessing generally better performances in term of footprint and losses than W-*like* PhC waveguides. In order to build a photonic integrated circuit, this scheme of interfacing PhCs where PhC-based elements are coupled to each other in the same level has been investigated by many groups in passive materials like SOI [135, 136] or active ones like III-V semiconductors [141, 142]. However, the use of an active material for waveguiding purposes remains a real problem due to the absorption. To overcome this problem it is possible to use an all III-V semiconductor based approach as for telecom devices, making use of epitaxial regrowth to separate the active regions where the lasers are made from the passive ones where light propagates without being absorbed. This was successfully achieved with InP-based PhC crystals lasers in [141, 142]. The downside of this approach comes from the incompatibility of this process with the Silicon CMOS-based platform due to the high temperature ($\approx 600^{\circ}$C) reached during the regrowth step. Of course, further developments may overcome such a hurdle for the integration of these devices.

Another original approach of coupling was achieved in the Painter's group (Caltech) by coupling the PhC with a tapered optical fibre that is positioned close to the PhC surface [143]. This demonstration was followed by other studies [144, 145, 146] which allowed to observe several aspects of the light-matter interaction (CQED, bistability) in PhC cavities. This technique, obviously limited to the coupling to one isolated element, presents also limitations in terms of coupling efficiency due to the large difference in RI between the optical fibre and the III-V semiconductor and the imprecise control of the of the fibre-cavity distance. Indeed, in order to obtain sufficiently large coupling, the fibre is often simply stuck to the PhC surface. This can result in unwanted modification of the optical properties of the PhC structure.

Our approach is different from what was previously proposed and relies on the heterogeneous integration of III-V semiconductor active PhCs with a SOI passive waveguides circuitry. Here, the passive and the active functionalities are spatially separated in 2 optical levels and coupled by evanescent wave coupling. As already mentioned and will be demonstrated in this manuscript, these structures enable a very efficient interfacing of active nanophotonic elements densely integrated in a circuit as well as the direct compatibility with CMOS electronics.

3.2 Hybrid III-V/SOI structure

Let's briefly introduce the components that constitute the hybrid structure schematised in figure 3.1. A Silicon-On-Insulator (SOI) waveguide circuitry forms the *passive level* of the structure whose role is to route the optical field in and out the PhC with single mode wire waveguides. Each waveguide is terminated by two grating couplers used to inject and collect light with a cleaved optical fibre. Around the SOI waveguide, we find the bonding layer of BCB (the "adhesive") that forms, with an additional SiO_2 layer, the low-RI bottom cladding of the III-V PhC. This layer thickness is usually below 500nm to allow an efficient evanescent coupling between the SOI waveguide and the PhC. The *active level* is made of III-V material, usually containing quantum wells (QW) which can emit light around $1.55\mu m$. Finally, our latest generation of structures contains a low-RI top cladding which improves their thermal behaviour.

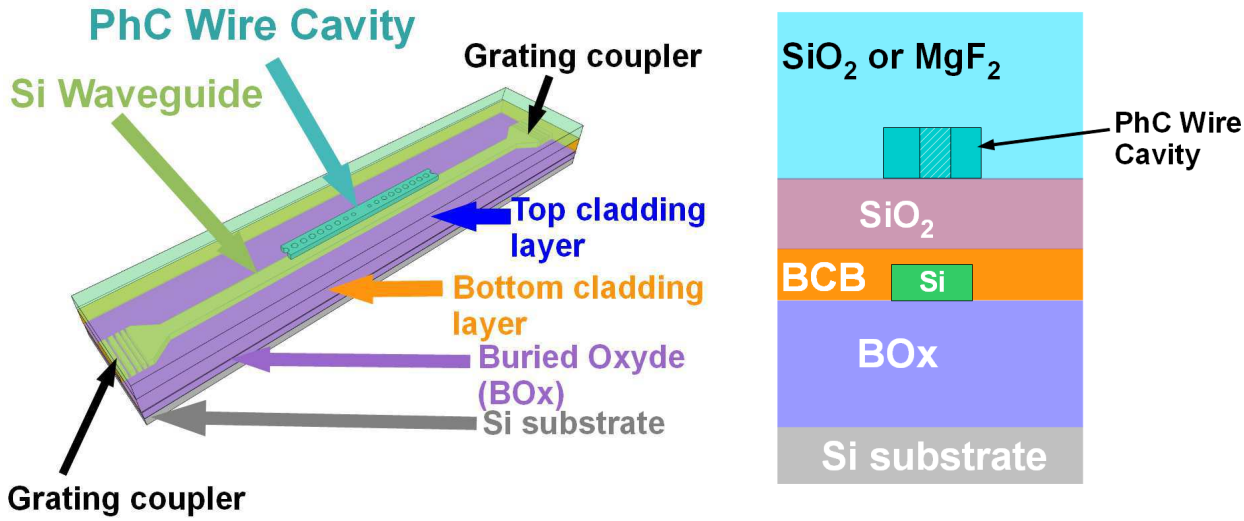

Figure 3.1: *Scheme of the hybrid III-V/SOI structure.*

3.2.1 Passive level: SOI circuit

3.2.1.1 Design

The lower level of the hybrid structure (see fig. 3.1) is formed by the *Silicon-On-Insulator* level which consists of a thin Si patterned layer on top of a SiO_2 rear cladding layer. Both materials are transparent at the telecom wavelengths of $1.3\mu m$ and $1.55\mu m$. Tight light confinement is ensured thanks to the high RI contrast between the Si ($n_{Si} = 3.46$) and the oxide ($n_{Si0_2} = 1.45$). The SiO_2 layer also referred as the Buried Oxide layer (BOx) is $2\mu m$ thick to prevent optical leakage from the waveguide core into the Si substrate (below the BOx). The 220nm Si layer is patterned into ridges with lateral sizes below 600nm to obtain single mode waveguides for transverse electric (TE) polarization[1] [20].

[1] In TE polarisation the electric field is perpendicular to the waveguide sidewall, parallel to the surface.

The SOI photonic circuit that we used contains waveguides of widths ranging from 250 nm to 550 nm in steps of 50 nm. Two kinds of waveguides were designed: straight waveguides and curved waveguides (see fig. 3.4). The waveguide losses are typically around 2.4 dB/cm originating from scattering due to imperfections in the fabrication of the waveguide.

Each waveguide is approximately 8 mm long. At 500 μm from their centre, the waveguides widen up to a width of 10 μm terminating on both sides by shallowly etched grating couplers [147, 148]. These grating couplers, shown in fig. 3.2, allow the coupling of light with a cleaved single-mode optical fibre (SMF) with an efficiency of $-5.1dB$ in a 40 nm wide spectral range[2] for the TE polarisation. We can note here that the use of such couplers allow a fairly low sensitivity on the fibre alignment with the grating [149].

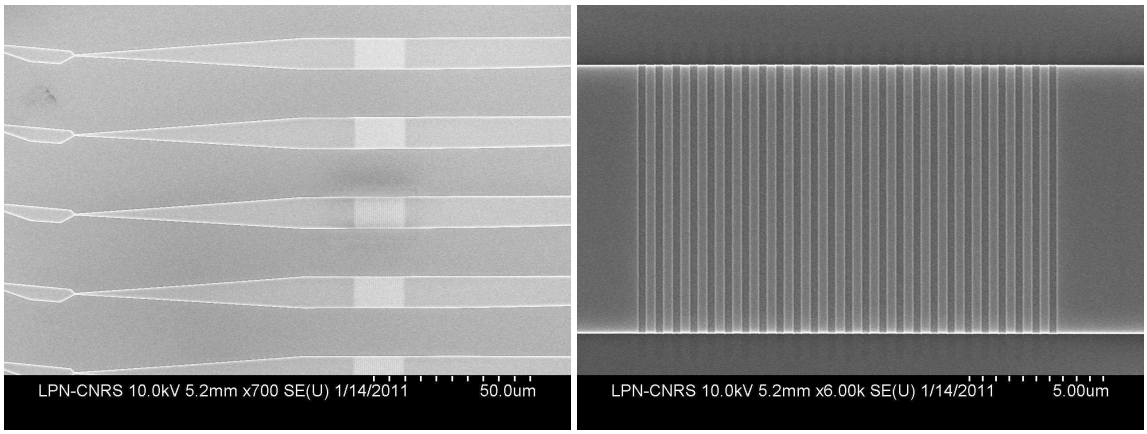

Figure 3.2: *SEM pictures of grating couplers at each side of the SOI waveguides.*

In addition to the photonic circuit itself, arrays of alignment markers are defined on both sides of the SOI and are used to perform aligned electron beam lithography. Each marker consists of a square-shaped 10x10 μm hole, defined in a 100x100 μm square pillar. The alignment issues will be discussed in more detail in Section 3.3.3.1.

3.2.1.2 Fabrication

After we have designed the important features of the SOI circuit, the SOI structures were ordered and processed through the **ePIXfab** [3] network. This network is dedicated to academic research. Several runs per year allow research groups to obtain affordable SOI samples processed in a CMOS line. Depending on the run, samples are processed either at IMEC (Louvain, Belgium) or at CEA-LETI (Grenoble, France).

The fabrication process to obtain SOI takes advantage of the SmartCut technique developed at LETI [150] ten years ago. In this technique (see fig. 3.3) a silicon wafer is firstly oxidized to create the thermal oxide layer and is then implanted with a high dose of hydrogen ions, forming in the Si substrate a uniform layer of weak lattice bonds between the Si atoms [151]. This wafer

[2] 1dB bandwidth
[3]

is then bonded to a clean silicon wafer. Thermal processing at 1000 °C splits the structure along the cleavage zone created by the ion implantation. In the end, the wafer is polished by *chemical mechanical polishing* (CMP) down to a 220 nm thick Si top layer.

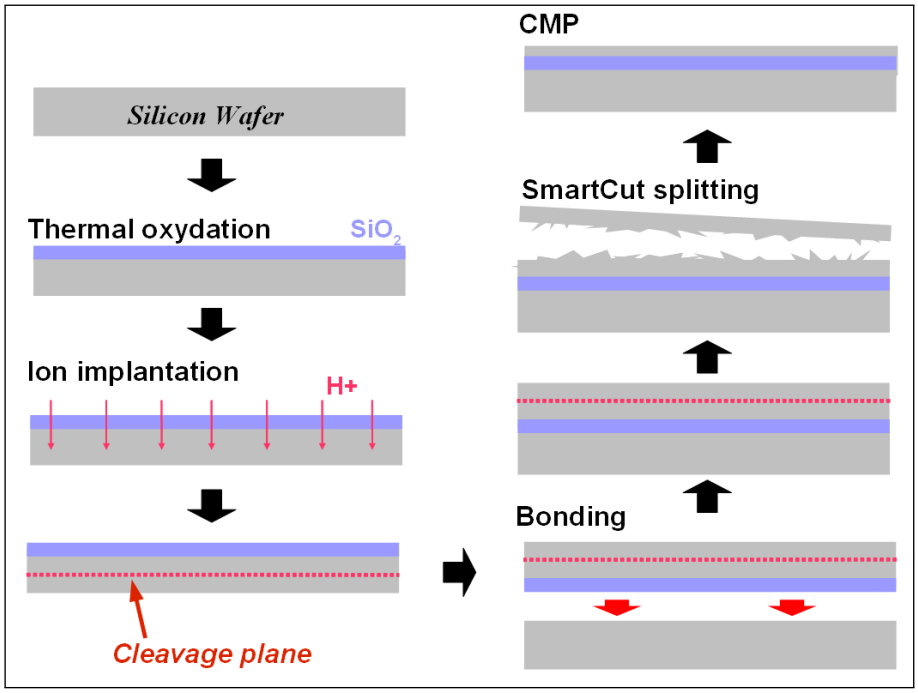

Figure 3.3: *Steps of SOI fabrication I*

The process to define the waveguide into the silicon slightly differs from one CMOS-line to the other (IMEC or LETI). Fig. 3.4 shows a scheme of the process flow followed for the fabrication of the SOI used in this work. Both fabrication lines rely on Deep UV lithography [152] followed by Reactive Ion Etch (RIE) dry etching [153]. The main difference in SOI process comes from the type of hardmask, deposited on top of the Si layer, into which the patterns are transfered in a first time. Indeed, the hardmask used in LETI is made of SiO_2 while IMEC prefers to use a Si_3N_4 layer. In both cases, a thin organic anti-reflective layer (BARC[4]) is coated on in order to limit reflection on the SOI structure of the UV light during deep UV lithography. A photoresist layer is coated above the BARC layer and, after a baking step, the sample is illuminated with 193nm UV light above the photonic circuit metallic mask pattern. The hardmask is then opened by RIE. Once the hard-mask is opened, the anti-reflective coating layer is etched using Br/F based chemistry. The silicon can then be etched through the hard-mask by RIE dry etching with a Cl_2/HBr gas mixture [153] leaving the designed Si circuit. In addition[5], the SOI wafers may

[4]Bottom Anti-Reflective Coatings.
[5]This last steps are not illustrated in Fig. 3.4.

also be covered by an oxide layer which is finally thinned down by CMP.

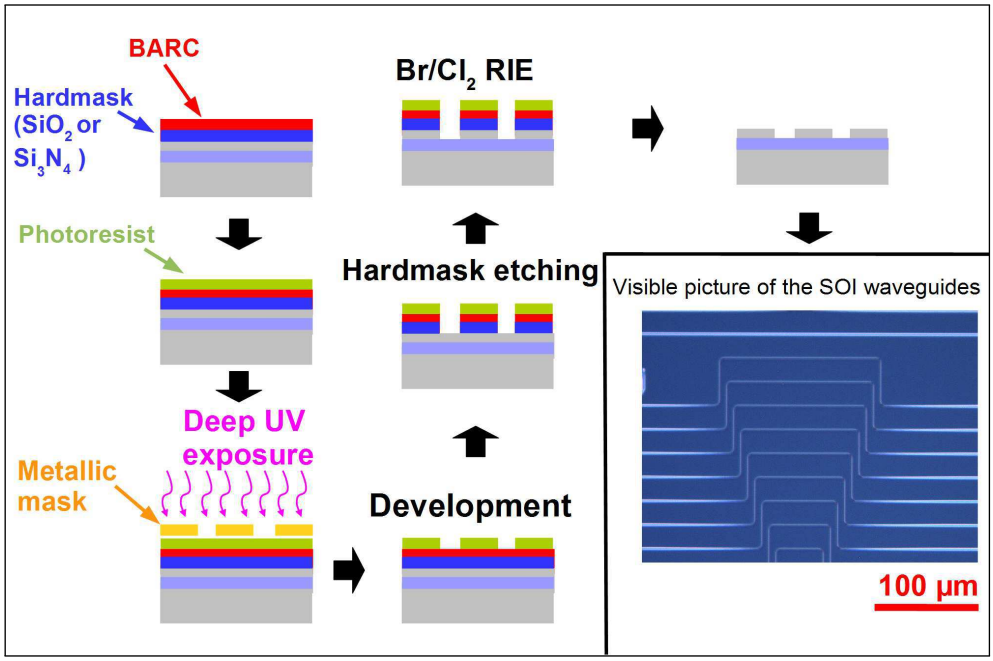

Figure 3.4: *Steps of SOI fabrication II with a microscope picture of a few curved waveguides.*

The next section is dedicated to the description of the active material level (material properties, PhC structure).

3.2.2 Active level: III-V Photonic Crystal

3.2.2.1 Quantum Wells material

A wide variety of materials can be bonded to build the top level of our a hybrid device, to allow mixing and matching of different functionalities. In our structures, we take advantage of the great versatility of III-V semiconductor materials. In terms of non-linear behaviour, bulk III-V semiconductors like Gallium Arsenide (GaAs) or Indium Phosphide (InP) are known to exhibit large non-linearities several order of magnitudes higher than in Silicon or in other materials commonly used for frequency up-conversion (KTP, $LiNbO_3$). These non-linearities can be further enhanced by tailoring the electronic band structures. Suitable alloys (InGaAs, InGaAsP, AlInGaAs,..) can be formed by engineering their composition. Furthermore, unlike silicon, III-V materials have a direct band-gap which is a major characteristic to make efficient stimulated emission sources. Thus, radiative transitions can be obtained at the desired wavelength, ranging from $0.2\mu m$ to $20\mu m$.

III-V materials also benefit from decades of growth experience. A large variety of III-V heterostructures can be grown from bulk stacks of different alloys all the way to quantum confined structures such as quantum wells, wires or dots. We observe that the gain material choice will

depends obviously on its characteristic but also on factors as the target application and the overall fabrication complexity. In the literature on III-V PhC lasers, one can commonly find the use of quantum dots layers [154, 155, 156, 157, 158] or other sophisticated heterostructures [159, 160], such as the buried-heterostructure (BH) [160].

Our choice was to go with membranes containing multiple quantum wells (MQW). Compared to QDs (which have a higher differential gain than QWs), the gain of QWs is much higher due to the higher carrier density obtained in the wells. MQW-based laser have also a higher saturation power leading to an effective maximum output power higher than for a laser making use of QDs. MQW also present the advantage of having a fast carrier capture rate (below 1 ps) into the wells compared to the capture rate into QDs, which varies from a few ps to a few 10's of ps depending on the dot structure and density. As a consequence, faster build up time of the laser can generally be achieved and higher modulation bandwidth is expected.

Most of the heterostructures used is this work were grown at LPN by Metalorganic Chemical Vapour Deposition (MOCVD). However, some optimised samples, grown by Molecular Beam Epitaxy (MBE), were also purchased at the 3-5 Lab (Marcoussis, France). I will hereafter describe the structure of the MOCVD samples whose growth pattern is comparable with the MBE ones. The active layer consists of an Indium-Phosphide-based membrane embedding 4 InGaAsP/InGaAs quantum wells positioned at the middle of the membrane and whose electronic resonance is around 1.53 μm. Figures 3.5 show the scheme of a typical grown heterostructure. Note that a 300 nm InGaAs etch stop layer is present to protect the membrane while the InP substrate is removed. The heterostructure of figure 3.5 is optimized for optical pumping at 1180 nm compared to previous samples pumped at 800 nm. Indeed, the InP layers, transparent at 1180 nm, are reduced to a minimum thickness to improve the total membrane optical absorption at 1180 nm. Then, the absorption takes place mainly in the InGaAsP barriers and a little bit in the InGaAs wells. The total membrane thickness is approximately 285 nm, close to $\lambda/(2\tilde{n}_m)$ (where $\tilde{n}_m$ is the average refractive index of the membrane) to minimise the light emission of the QWs in the vertical direction.

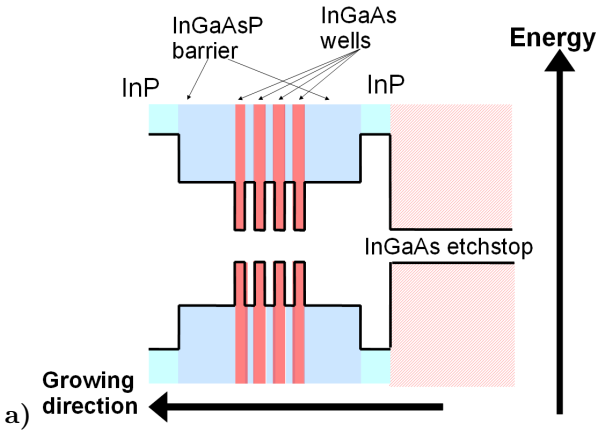

b)

Thickness (nm)	Structure	
24	InP	
79	InGaAsP	
15	InGaAsP	x4
8.5	InGaAs	x4
79	InGaAsP	
24	InP	
300	InGaAs	
650	Buffer InP	
	InP:S substrate	

Figure 3.5: *Scheme of an MOCVD III-V membrane containing 4 quantum wells InGaAsP/InGaAs.*

Fig. 3.6.a shows a Transmission Electron Microscopy (TEM) image of the heterostructure of our MOCVD grown sample. Fig. 3.6.b shows the typical photoluminescence of the active material. Here, the FWHM of the emission is larger than expected probably due to thickness fluctuations along the QWs.

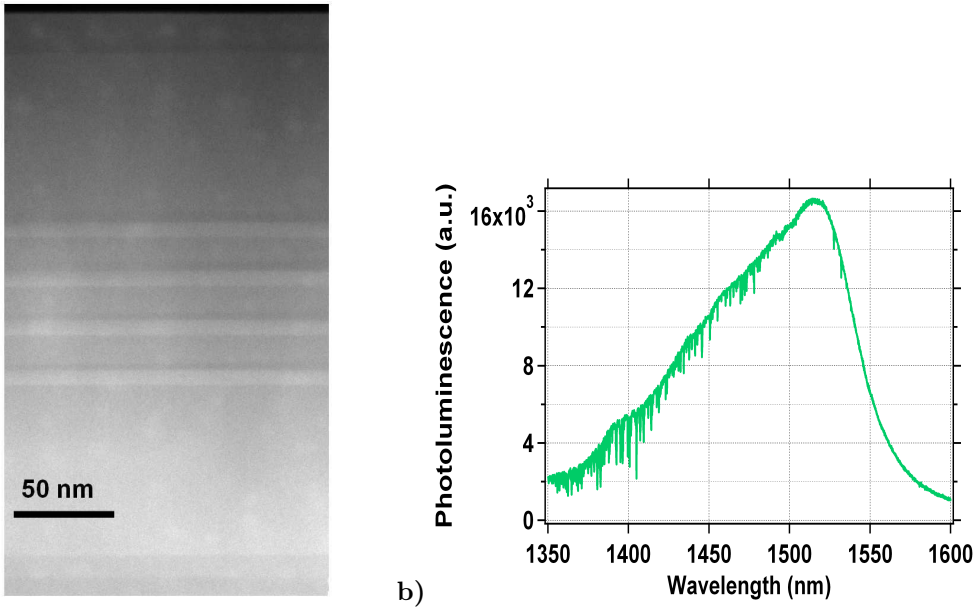

Figure 3.6: ***a)*** *TEM image of InP-based membrane containing 4 InGaAsP/InGaAs quantum wells.* ***b)*** *Photoluminescence*

3.2.2.2 Photonic Crystal Wire Cavity

The optical properties of the PhC Wire Cavity were detailed in chapter 2. The value of the geometrical features of the structures to be fabricated are fixed after the FDTD simulations, in order to obtain a high-Q cavity mode at 1.55 μm. The width of the wire is targeted at 505 nm and the hole radii to 120 nm. Typically, the structure contains 50 holes. For 2.8 μm targeted FWHM, the hole-to-hole distance is subtly varied along the cavity from 350 nm to 385 nm with steps which can be of the order of 1nm. Considering the necessary control over the hole-to-hole distance and extreme sensitivity of the resonant wavelength with the structure dimensions (1 nm change in the hole radius gives approximately 4 nm change in resonant wavelength), the patterning resolution is targeted at 1 nm which imposes the use of electron beam lithography. Moreover, as we will see in Section 3.3.3.1 and in Chapter 5, the precise definition of the geometrical features of the PhC Wire Cavity is also crucial to accurately control the optical coupling efficiency.

3.2.3 Bonding layer

The bonding layer refers to the intermediate layer between the III-V and the silicon. It is an important element in the hybrid structure as its characteristics may affect several properties of the system. The waveguide and the cavity were designed taking into account the presence of

this layer in order to get the best characteristic of each separate element after bonding.

From an electromagnetic point of view, the bonding layer has to ensure two conditions: first, be transparent at the aimed infrared window, around 1.55 μm and, secondly, be a low RI layer in order to ensure a tight optical confinement in the SOI waveguide and the PhC cavity. In practice, the bonding layer is constituted of two sub-layers: at the bottom, a polymer layer (n 1.54) allowing the adhesive bonding (see next section for fabrication details) and on top, an amorphous SiO_2 layer (n 1.46).

The presence of the silica layer, which may be only few nm thick, allows to reach a high yield efficiency, above 95 %, in the bonding process.

The polymer layer is a divinylsiloxane-benzocyclobutene (DVS-BCB) layer and can be made as thin as a few 10's of nanometres during fabrication [161]. The latest generations of hybrid structures in the course of my thesis were realised by pushing the BCB layer to its minimum thickness and adjusting the total bonding layer thickness with the SiO_2 layer, in order to maintain a desired distance between the Si and the active layer. Typically, the coating of BCB above the SOI circuitry is done to obtain a 300 nm thick layer which, because of its planarising power, results in only 80 nm on top of the 220 nm thick waveguide. Another major drawback led us to use this approach: the very poor heat sinking when using BCB. BCB has indeed a very low thermal conductivity around 0.29 $W.m^{-1}.K^{-1}$ compared to InP or Si. The optimisation of the heat sinking is the subject of an entire section of chapter 4.

Finally, in order to keep a good coupling efficiency, the bonding layer thickness should also be smaller than a few λ/n_b where n_b is the average optical refractive index of the layer.

3.2.4 Top cladding layer

In the early stage of this research, samples which were fabricated using BCB-bonding on SOI [62] or Si [122] did not include any top cladding. Like the bonding layer, the top cladding layer can affect significantly the properties of the PhC cavity. As shown in the previous chapter, special care has to be taken during the cavity design to prevent additional optical leakage out of the cavity. The cladding consists of a single low-n layer to keep the high index contrast with the cavity's semiconductors. Unless mentioned otherwise, the thickness of the cladding is always 1 μm above the cavity.

The main reason that motivated the full encapsulation of the cavity was the heat spreading from the cavity to its environment. Heat plays a complex role in the achievement of a laser working under *continuous wave* (CW) excitation. The Section 4.4 of the next chapter will give more details on the thermal issues in the hybrid structures as well as the improvements obtained in the heat management during this thesis.

Note here that two low-n materials were used and compared during this thesis: amorphous SiO_2 (n=1.45, $\kappa \sim$ 1-1.5 $W.m^{-1}.K^{-1}$) and then MgF_2 (n=1.38, $\kappa \sim 15$ $W.m^{-1}.K^{-1}$). The latter material possess a very low refractive index which is extremely useful when high refractive index contrast is needed, as a well as a thermal conductivity approximatively 10 times higher than that of SiO_2 .

3.3 Fabrication of the hybrid III-V/SOI circuit structure

The whole fabrication of our samples is done in the *clean-room* of LPN, taking advantage of almost/more than a decade of work on III-V photonic crystal fabrication. Unlike classical under-etched photonic crystal membrane, the hybrid structures fabrication relies on bonding an epitaxial III-V layer to SOI wafer. The main techniques of bonding were already presented in Section 1.2.2.3. We opted for adhesive bonding which was brought to our team in 2007 thanks to a collaboration with the Photonic Research Group in Ghent University (Belgium). This collaboration was extended to a shared PhD work (Yacine Halioua [78]) that allowed us to fully comprehend the bonding technique and even improve its yield efficiency to attain a near 100% efficiency.

Basically, the fabrication follows 4 steps:

- *Surface preparation*: the two layers (SOI / III-V) undergo several cleaning steps and coating to optimise bonding efficiency.
- *Bonding*: using adhesive bonding, the two levels are bonded together.
- *Patterning*: III-V is patterned into cavities aligned with the SOI waveguides.
- *Encapsulation*: The cavities are encapsulated in a low-n top cladding (mainly to overcome detrimental heating effects).

3.3.1 Surfaces preparation

The protecting resist on top of the SOI is firstly removed by a 5' ultrasonic cleaning step in an acetone bath followed by a isopropyl-alcohol (IPA) bath and a drying N_2 flow. Next, the SOI undergoes an 0_2 plasma clean to remove the possible remains of resist [6].

The III-V epitaxial layer is cleaned with the same procedure (ultrasound in acetone, IPA, N_2 drying). Then, we sputter on the InP surface to be bonded an amorphous silica layer. This additional step in the process flow of III-V/Si adhesive bonding was introduced at LPN after noticing that the BCB wetting was much better on silica than on an InP surface. As a consequence, an intermediate silica layer of only 20 nm drastically changes the yield efficiency of bonding. Furthermore, a much thicker silica layer is now used to help heat dissipation from the III-V cavity and is regarded also as a better way to precisely control the total bonding layer thickness.

Finally, the III-V substrate is cut into a $1cm^2$ die in order to match the size of the SOI circuit and especially to protect the grating couplers from potentially damaging further processing.

[6] It was also observed that it improves adhesion by creating native oxide layer on the Si.

3.3.2 Adhesive bonding using BCB

We start the process with a commercially available (*Dow Chemicals*) solution containing a partially polymerized divinylsiloxane-benzocyclobutene (BCB) oligomers mixed with its solvent, mesitylene. Beside its low optical loss property at 1.55 μm, the use of BCB is motivated by its excellent thermosetting and planarising power [162]. During polymerization, a very low amount of by-products is released preventing the formation of bubbles that could be trapped in the bonding layer and which fits our objective to obtain a flat III-V layer on top of a pre-patterned Si level. The degree of polymerization and the amount of mesitylene in the solution determine the final thickness of layer after spin-coating. Sub-micron thickness of BCB, below 100nm, can be achieved [59] by adding mesitylene to the 1μm-thick BCB solution (CYCLOTENE 3022-35, *Dow Chemicals*).

For our application, we use a BCB:mesitylene solution with 2:1.5 respective fractions. The solution is spin-coated on the SOI with a spinning speed of 5000 rpm and an initial acceleration of 2000 rpm/s. The SOI with BCB is then softly cured at 80°C for 15 min in order to outgas remaining solvent. Then, the III-V die is put in contact with the BCB and a 300°C hard bake step finishes the polymerisation of the BCB.

The adhesion obtained after the hard baking step is very dependant on how the III-V and the SOI dies are put in contact. During my PhD, the use of a mechanical press for the bonding greatly improved the flatness of the III-V surface and has become more reproducible than the previous method [62] which consisted in gently placing and pressing the III-V die by hand.

First, the SOI is heated up at 150°C which in turn fluidifies the BCB. The wetting of BCB with the silica layer is thus improved. An important step issue for achieving adhesive bonding is to remove to the utmost of the air bubbles trapped between the III-V and the SOI when the two dies are put in contact. Early in this work, this was (quite successfully) done before curing by firmly pressing and sliding the III-V die on the SOI at 150°C. However, the flatness of the surfaces which can be estimated by the number of rings in the diffraction pattern of visible light on the III-V surface (Fizeau fringes) was still very variable and operator-dependant. This drawback is suppressed with the use of a mechanical press. An oven in the press heats up the sample at 150°C before the press applies a pressure of 2000 N/cm^2 on the the sample. The temperature of the sample is then quickly elevated and maintained at 300°C for 3 hours in order to fully polymerise the BCB.

Lately, a high precision substrate bonder (*Süss MicroTech*) was acquired by the laboratory allowing to realize the bonding in a vacuum environment (see fig. 3.7). The sample done in this way showed the best flatness characteristic with a close to 100% bonding yield efficiency.

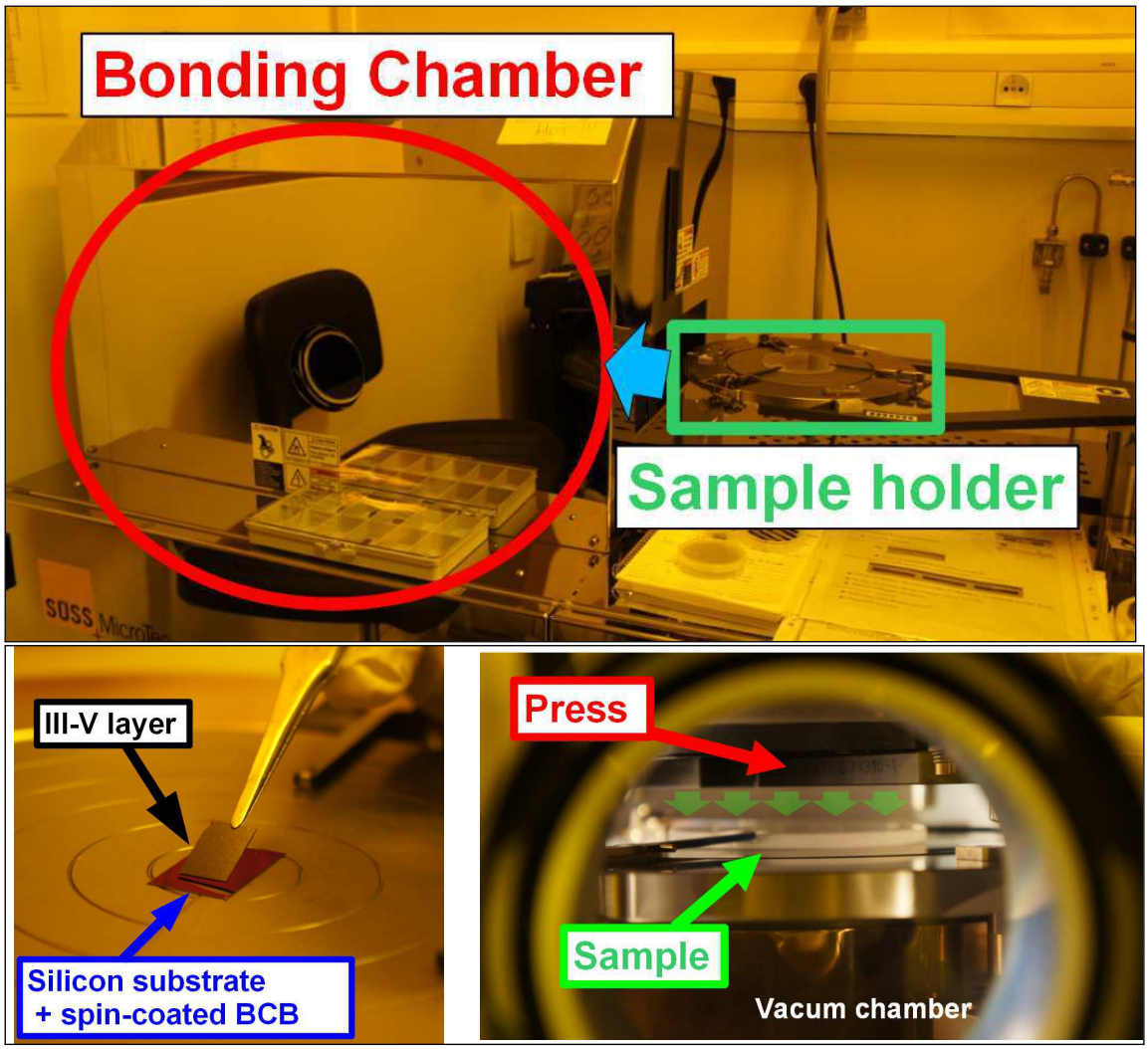

Figure 3.7: *Bonding process.*

3.3.2.1 Substrate removal

After bonding, the InP substrate is removed by wet etching [163] in an HCl solution for approximately 1 hour. This step is done in a highly ventilated isolated environment inside the clean room to prevent the exposure of the operator to highly toxic gas such as phosphine. The etching of the InP substrate ceases when the InGaAs etch stop is reached due to the high etching selectivity of HCl between these two materials. Figure 3.8 shows pictures of a III-V die bonded on an SOI before and after the substrate removal. H_2SO_4:H_2O_2:H_2O in the ratio 3:1:1 is finally used to remove the InGaAs etch stop layer.

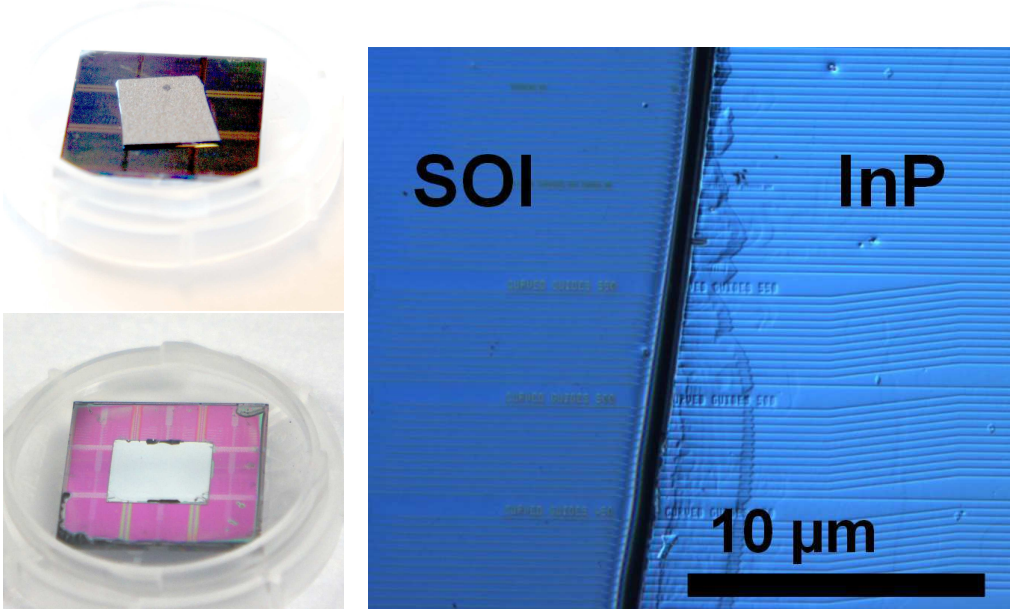

Figure 3.8: *Pictures of the III-V dice bonded on top of an SOI before (left-top) and after (left-bottom) the InP substrate removal. Right: microscope picture showing the border of the III-V layer (right side) on top of the SOI waveguides.*

3.3.2.2 Bonding layer thickness control accuracy

As it was described in Section 3.2.3, the bonding layer is constituted of a silica layer on top of the BCB layer. Unlike the thickness of the silica which is precisely known after deposition, the BCB thickness depends on the conditions of bonding. Up to now, the control of the bonding layer thickness has not been systematic. Clear quantitative figures of BCB homogeneity are still lacking. Focused Ion Beam cut done in collaboration with Ghent University, on III-V bonded on Si substrates with $1\mu m$-thick BCB showed large inhomogeneities in the BCB thickness (0.1-1.1μm) below the III-V. These inhomogeneities seem to follow the thickness gradient induced by a bad positioning of the III-V onto the SOI. However, experimentally, we note that the flatness of the BCB can be increased by targeting thinner BCB layer by increasing the mesitylene concentration in the BCB:mesitylene mixture. In addition, the use of the substrate bonder has also had a positive effect on the obtained flatness.

As a consequence, to limit the impact of potential inhomogeneities, the BCB thickness on SOI is reduced to approximatively 300 nm. When the pressure is applied on the heated sample, we think the BCB thickness reduce to a minimal value. The thickness of BCB above the 220 nm waveguide is assumed to be approximately 80 nm. Further investigation would give more insight on this point.

3.3.3 III-V patterning

In practice, the patterning is achieved following two main steps: firstly, the fabrication of an etching mask on top of the III-V layer, obviously aligned with the SOI level, and secondly, the etching of the III-V layer through the mask.

During my PhD, two types of masks were used: one is a silicon nitride (SiN) layer and the other is an electron-beam exposed Hydrogen Silses Quioxane (HSQ) layer. The definition of the PhCs pattern relies in both case on electron-beam (e-beam) lithography, but requires a single e-beam step when HSQ is used to define the whole pattern above the waveguides. Besides, this resist proves to be much more suitable to obtain sharp edges in the III-V PhC. For these reasons, I will now focus on the process using this resist to pattern our bonded layer.

3.3.3.1 Electron beam lithography

E-beam lithography is a lithographic technique of nanometre scale precision where a focused electron beam scans and writes a pattern on an electrosensitive resist. To do so, the electron beam is switched on and off during the scan over the sample. The resolution of this technique depends on several parameters, like the exposure dose, the e-beam spot size, the sample scanning method, and also the type of resist that is employed. Indeed, ultimately, it is the average length of the polymer chain in the exposed resist that sets the pattern resolution. During our studies, subnanometric resolution was successfully obtained using HSQ thanks to an optimisation of the pattern writing as well as to the latest upgrade of LPN's e-beam machine.

Despite its relatively long exposure time, this tool is perfectly matched with the academic research goals as it allows to define any desired design with no additional cost and in a quantity sufficiently large for research studies.

3.3.3.1.a Alignment markers opening

The e-beam lithography system is set to use the markers made in the SOI level to precisely define the reference frame of coordinates to use for the alignment of the exposed patterns on the III-V level to the SOI waveguides. Therefore, a preliminary step is to reveal the arrays of alignment markers that are masked by the bonded III-V layer on top of the SOI. To do so, trenches are opened around each line-arrays of markers by UV lithography. Figure 3.9 shows the process steps to obtained such trenches.

A layer of the AZ-9260 photoresist is spin-coated on the sample and then soft-baked on a hot plate at $110°C$ for 7'30". The sample is then exposed for 2' with a broadband (310-450 nm) mercury vapour ultraviolet (UV) exposure source (through a metallic slit/mask to define 500 μm trenches. The exposed photoresist is developed with a solution of $AZ-400K$:H_2O (1:4).

The membrane and the bonding layer are completely removed inside the trenches. Successive wet etch step with HCl and H_2SO_4:H_2O_2:H_2O are used to remove the InP layers and the InGaAsP/InGaAs quantum wells. The silica layer beneath the membrane is etched during 8' with an ammonium fluoride (AF) solution. The cured BCB is removed by RIE using sulphur hexafluoride/ oxygen (SF_6/O_2) plasma.

A good contrast in the e-beam detection of the markers is obtained by fully etching the $2\mu m$ thick BOx layer (AF, 25'). It is then the abruptness of the edges of the markers that ensures a correct measurement of the position of their centre.

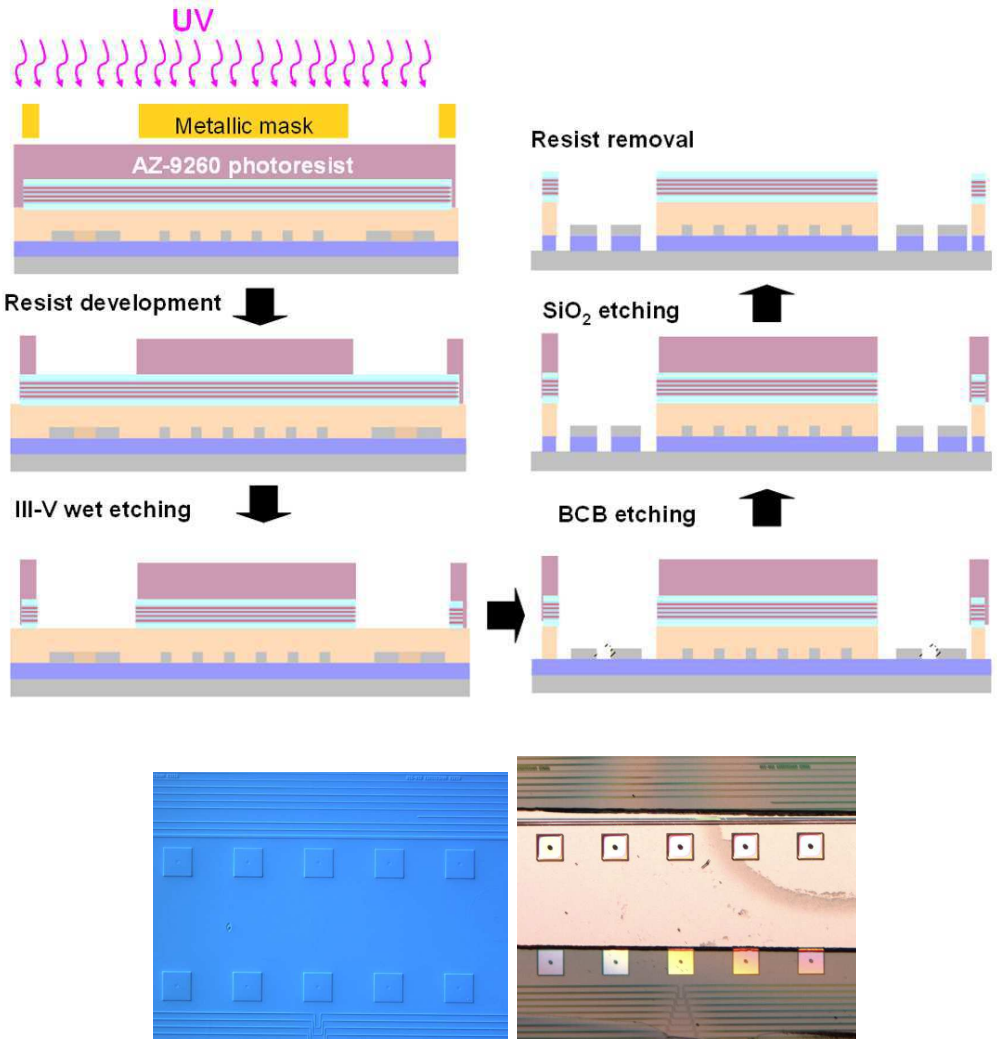

Figure 3.9: *Process flow of the alignment markers opening with, below, pictures of the markers underneath the III-V layer before and after the opening of the trenches around an array of markers.*

3.3.3.1.b Electrosensitive resist exposure

The effect of the e-beam exposure on the resist depends on the nature of the resist used which can be either of positive or negative tone. In the case of a negative resist, such as *HSQ* [164, 165], the exposed surface of the resist solidifies while the rest of it is removed afterwards in a developer solution, revealing the desired pattern.

The use of HSQ as spin-on glass for PhC patterning was achieved in 2004 by Assefa et al.[166]. This technique significantly simplifies the hard-mask fabrication, without compromising the optical quality of the structure, as a single e-beam step is enough to pattern the III-V PhC cavities above the waveguides. Indeed, the III-V that is not protected by the resist will be etched during the III-V dry etching. This is not the case in the alternative method of fabrication of the hard-mask which employs a positive resist, polymethyl-methacrylate (PMMA), spin-coated above a SiN layer. Indeed, in this scheme (see fig. 3.10), the exposed surface is only the one that surrounds the edge of the cavity (which includes the inside of the holes). Because, the e-beam writing with a high resolution can be very time consuming, the exposed surface around the cavity is limited to 2 μm-wide trenches, which eventually keeps the most of the III-V surface protected by the SiN hard-mask. The removal of this remaining III-V above the SOI circuit, with exception of the cavity, is necessary to prevent large optical losses due to absorption by the III-V active material. It can then be achieved using a second e-beam lithography step which defines a mask protecting the etched cavities while allowing the exposure of the rest of the III-V to a wet etching. To avoid these complications, we tested HSQ which turned out to also improve the quality of the fabricated structures. It is now part of the process of the latest generation of hybrid samples produced in this work. Figure 3.11 shows the process flow that is followed to fabricate the PhCs in the III-V layer bonded on the SOI.

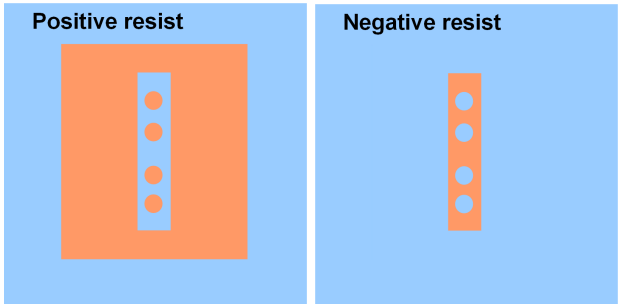

Figure 3.10: *Scheme of the exposure of the resist in the e-beam process depending on the tone of the resist. The exposed surface is put in orange.*

The HSQ resist (FOx-15, flowable oxide from Dow Corning) is spin-coated (v=4000 rpm, a=4000 rpm/s, 30") on top of the sample and baked for 30' at 150°C. The thickness of this layer is close to 450nm. The sample is then positioned inside a *Leica EBPG 5000+* e-beam writer system. The diameter of the electron beam is estimated to be around 6nm and the resolution of the e-beam is now down to 0.5nm. However, most of the fabricated cavities studied in this work were exposed with a resolution of 2.5 or 1.25nm.

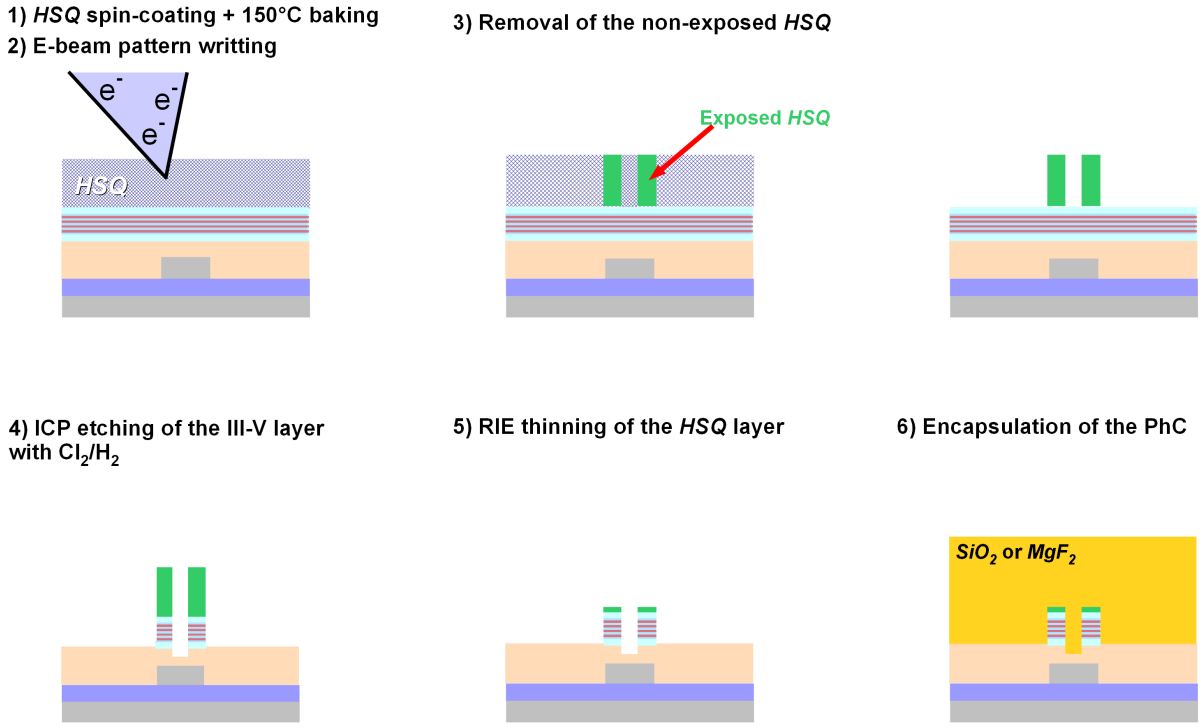

Figure 3.11: *Process flow of the PhC fabrication.*

The pattern to expose is generated into a GDS-II file using a python script with the IPKISS© library. Using objects predefined in the library, the patterns (holes, trenches, etc) are written as a combination of more or less complex polygons. The GDS-II is then converted into a procedure file that command the e-beam to expose only the zones that will not be etched subsequently. During my PhD, combined improvement in the resolution of the e-beam writer and in the understanding of some previous GDS-II design flaws helped to improve the overall pattern precision. One detected flaw was the faceting that appears on the GDS-II mask when the internal resolution of the IPKISS library was not set low enough. Figure 3.12 shows an example of this flaw on a hole shape and shows also its corrected shape when the meshing resolution was decreased down to 10pm. Thus, the meshing resolution does not limit the quality of the fabricated samples anymore.

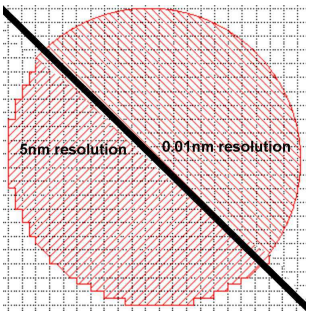

Figure 3.12: *Example of facetting due to a bad meshing of the GDS-II file.*

In order to obtain structures with sizes as close as possible to the originally intended ones, it may be necessary to correct the dimensions of the object in the GDS-II file by a correction term that depends on the overall process. For instance, transfer of the pattern from the HSQ mask to the III-V level often results in slight discrepancies in the sizes of the holes which can be measured later or deduced by an optical characterisation of the cavity's resonant wavelength. Then, the addition of a simple correction term allows to shift the resonances back to their expected position. Note that this discrepancy can be found on the dimensions but not in the positioning of the holes which is set by the subnanometric resolution of the writing grid. This is the reason why we designed our high-Q PhC wire cavities with holes of constant radius and where only the lattice constant is subtly varied.

The alignment procedure of the cavity patterns with the SOI circuit is done by a semi-automatic procedure. A centre position of the SOI circuit is defined by detecting at least 3 markers from the top and the bottom marker line-arrays etched in the SOI. In order to align the cavities with the waveguides, the GDS pattern contains, in addition to the PhCs, four markers included at the edges of the pattern. They define a centre that the e-beam writer identifies to be the one of the SOI level. Using this procedure, the e-beam can position all the elements forming the PhCs relatively to the waveguide with a high precision which was demonstrated to be better than 30 nm [62].

Finally, after exposure, the resist is developed for 3' in a AZ-400K:H_2O solution with a 1:4 ratio. Figure 3.13 shows a typical SEM picture of a hard-mask of a wire cavity made in HSQ.

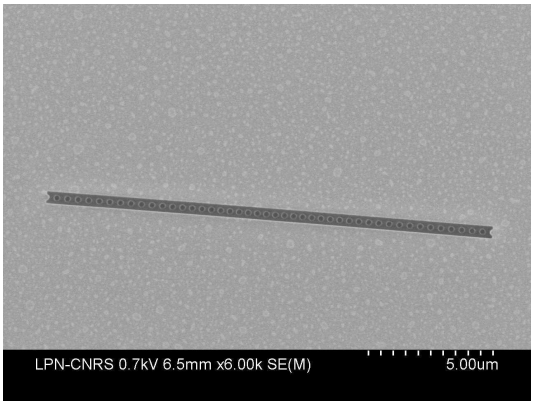

Figure 3.13: *SEM image of the HSQ hard-mask used for the fabrication of PhC Wire Cavities.*

The fabrication of an HSQ hard-mask proved to be much simpler and more reliable than the alternative SiN hard-mask transferred from a e-beam exposed PMMA mask. Indeed, the necessary RIE etching step to transfer the pattern into the SiN is never perfectly anisotropic and gives SiN sidewalls with significant roughness and imperfect verticality. These defects are in turn transferred and amplified during the III-V dry-etching. The sidewalls of HSQ observed after the development present a lower roughness and a higher verticality than that of our standard SiN masks.

3.3.3.2 III-V etching with Inductive Coupled Plasma

The pattern written in the hard-mask is transferred to the InP-based layer by a Inductive Coupled Plasma (ICP) dry-etching process with a Cl_2/H_2 gaseous source [167]. This etching process was developed at LPN for the deep-etching($>5\mu m$) of InGa(Al)As/InP heterostructures in order to obtain smooth and vertical sidewalls with no undercut.This high-aspect-ratio etching is possible because of the good anisotropy of the etching mechanism. Bouchoule et al. [168, 169] demonstrated that this anisotropic etching was due to the surface passivation of the sidewalls which are deposited with a thin silicon oxide layer during the etching using a Si cathode[7]. When applied to the etching of a thin InP-based membrane such as our ≈285nm-thick III-V layers, this process gave better results in terms of verticality of the PhC sidewalls compared to the previous ICP etching process using a Cl_2/BCl_3N_2 chemistry [172]. Figure 3.14 shows a SEM image of a PhC wire cavity after 2' of ICP etching, with the HSQ mask above it. As a comparison, an SEM picture of a cavity etched with Cl_2/BCl_3N_2 chemistry is given in figure 3.16. Although the good verticality of the structure can be assessed for the Cl_2/H_2 process, there remains some room for improvement in the optimisation of the etching conditions for the etching of the InGaAsP material composing the majority of our membranes.

[7]This has also been observed during ICP etching of GaAs using a chlorine-based plasma in presence of Si(cathode). It has been shown that an addition of 0_2 gas [170] or N_2 gas [171] could induce the deposition of SiO_2-like passivation layer on GaAs sidewalls.

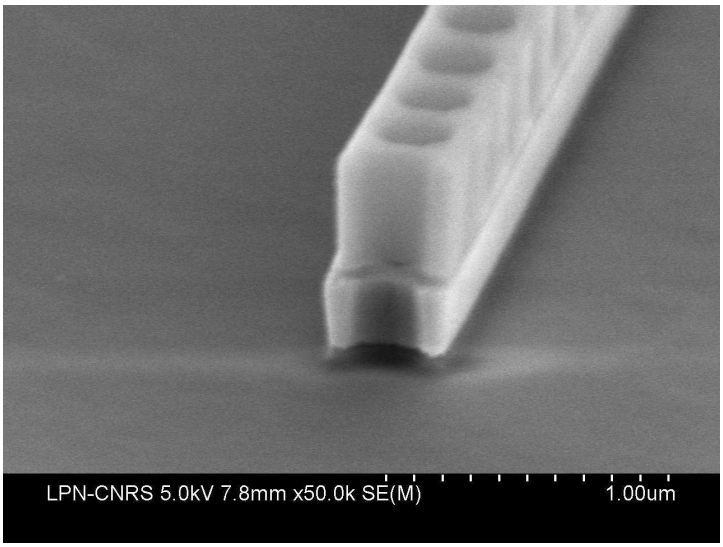

Figure 3.14: *SEM picture of an ICP-etched III-V PhC wire cavity before the thinning of the HSQ hard-mask. The verticality of the sidewalls appear to be quite good. Note that the SiO_2 is slightly etched (< 50 nm) during ICP.*

The hard-mask is then thinned for 10' with Reactive Ion Etching (RIE) using a $SF_6/O_2/CHF_3$ gas mixture. Special care has to be taken because of the simultaneous thinning-down of the SiO_2 layer of the bottom cladding. Indeed, if all the SiO_2 is removed, the BCB will be removed very quickly, exposing the Si waveguides to the plasma. Because this etching is not selective between HSQ and Si, this can potentially cause irreversible damage to the sample by etching the Si waveguides, particularly inside the PhC holes. The HSQ thickness ($\approx$ 450nm) is usually thicker than that of the SiO_2 layer (200-450 nm) and, despite the slightly faster etching rates of HSQ, it may be necessary to let a few tens of nm of the HSQ mask above the cavity. Because the exposed HSQ has similar optical properties as SiO_2, we did not notice any dramatic effect on the cavity behaviour. In the future, optimisation of the process with a thinner flowable oxide resist will probably overcome this hurdle.

Figure 3.15 shows several SEM views of PhC wire cavities above SOI waveguides. The excellent alignment of the two optical levels as well as the roundness of the PhC holes can be appreciated. Note on the lower right picture the SiO_2 bottom cladding is now much more etched than before RIE (fig.3.14).

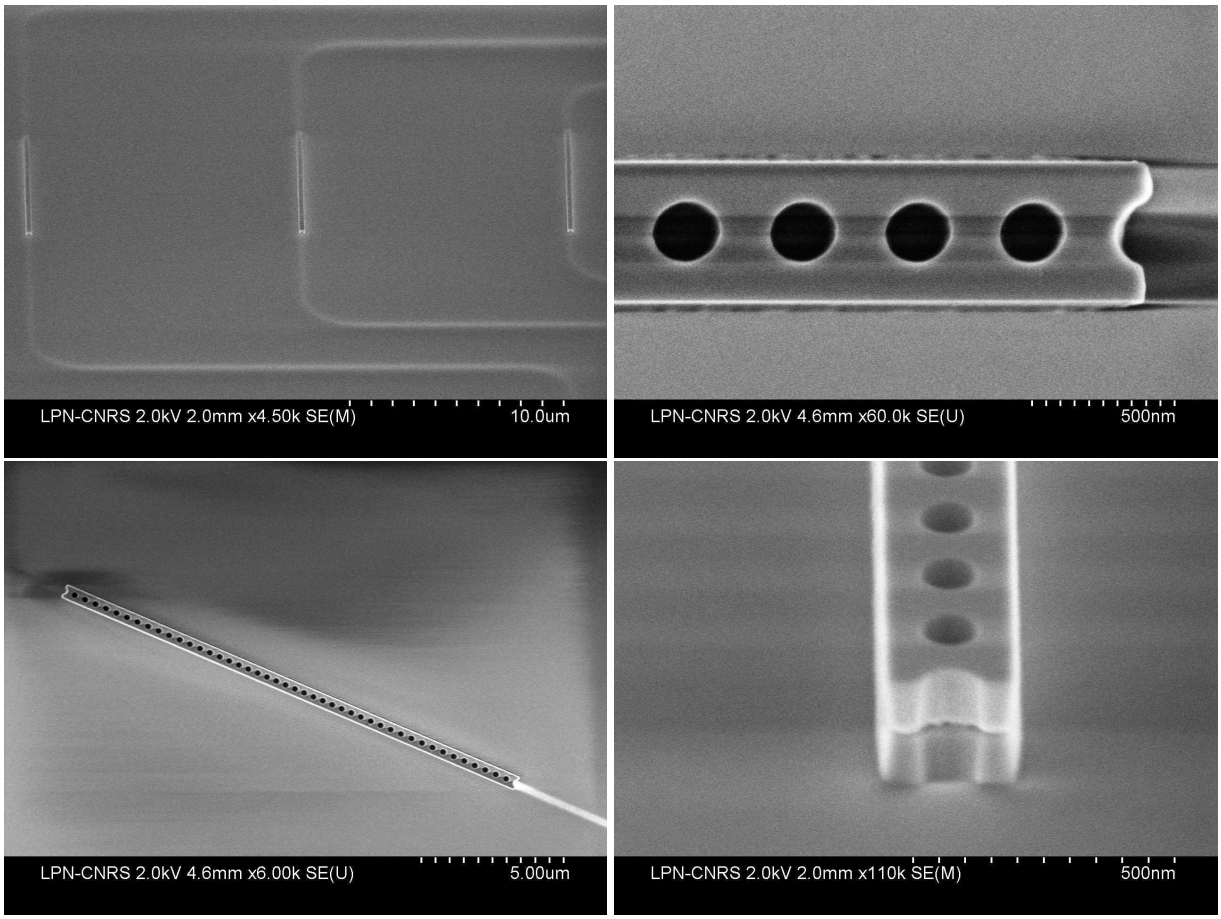

Figure 3.15: *SEM pictures of an ICP-etched III-V PhC wire cavity above a SOI circuit after the thinning of the HSQ hard-mask.*

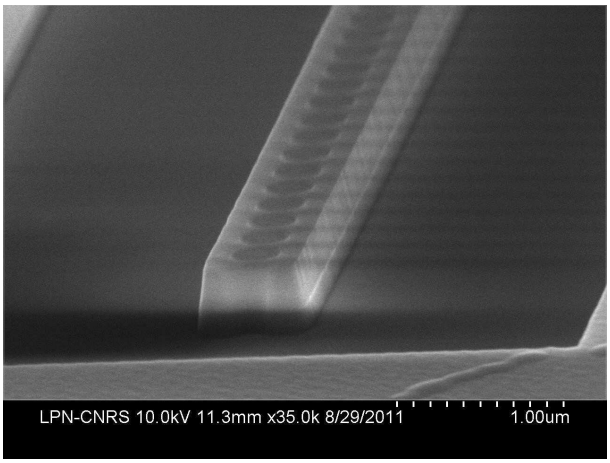

Figure 3.16: *SEM picture of an ICP-etched III-V PhC wire using Cl_2/BCl_3N_2 ICP instead of Cl_2/H_2.*

Once the cavities are etched, an additional step is added to the process flow in order to obtain CW lasing: surface passivation with a $(NH_4)2S$ solution. This step is described in the last part of the next chapter. After passivation, the cavities are encapsulated with a low-RI material.

3.3.4 Encapsulation

The design of the latest generation of hybrid PhC lasers/SOI structures includes a top cladding which is primarily meant to improve the heat sinking of the laser. The other reason is to protect the cavity from any polluting environment such as dust, oxidation, humidity. It is worth mentioning that such pollutants were never observed on the optical table environment but are likely to be found in real life. The challenge in this design lay in obtaining a Q factor of the cavity high enough, despite the lower RI contrast between the III-V and the hole material. As we saw in the previous chapter, Q-factors above one million can be achieved at least in theory.

Two encapsulation materials of low-RI were used : silicon dioxide and magnesium fluoride. The layer is $1\mu m$ thick above the cavity.

3.3.4.1 With SiO_2

The deposition of SiO_2 is done by RF Magnetron Sputtering in a Ar / O_2 plasma environment. In the chamber, the sample is placed in front of an amorphous SiO_2 cell, almost stoichiometric, and at a distance of 100 mm. An Argon plasma bombards the SiO_2 cell from which clusters of atoms are ejected and eventually deposited on the sample whose temperature is close to 80 °C. To improve the stoichiometry of the deposited SiO_x layer, i.e. to get x as close as possible to 2, an additional O_2 gas flow is present in the chamber. With this process, the deposition rate was equal to 1.2 Å/s so that the deposition was 2 hours and a half long. Figure 3.17 shows a picture of a processed III-V/SOI sample with a 1 μm-thick SiO_2 encapsulation layer.

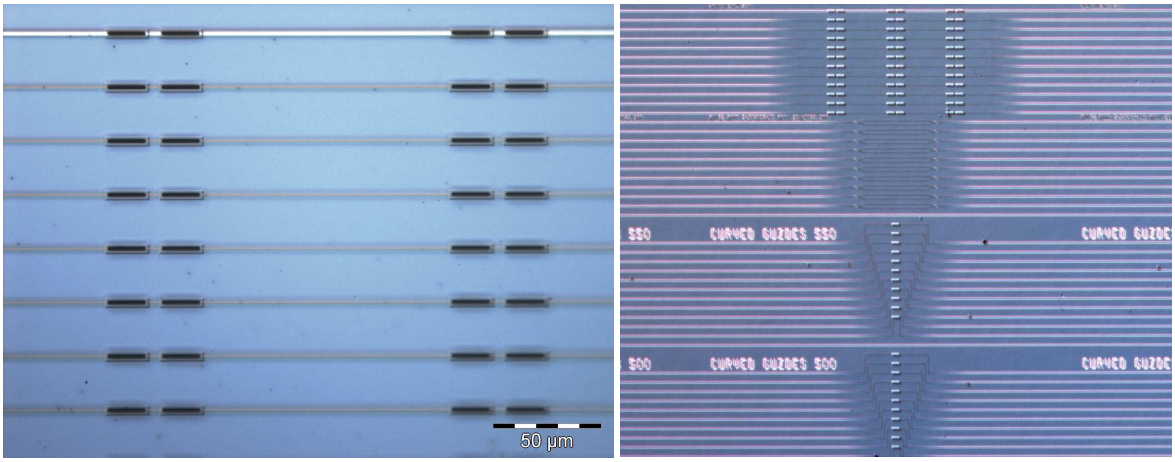

Figure 3.17: *Visible picture of a hybrid sample encapsulated in 1µm of SiO_2.*

3.3.4.2 With MgF_2

The MgF_2 layer is deposited by thermal evaporation in a Ion Beam Assisted Deposition (IBAD) chamber (although without the ion beam assistance here). The sample is radiatively heated at a temperature close to 150 °C. The MgF_2 is then heated and the deposition lasts around 30 min ($\approx$ 5 Å/s). Figure 3.18 shows pictures of a hybrid sample with PhC cavities aligned with SOI waveguides. A striking feature is the presence of many cracks visible on the sample but only on the region of the SOI where the bonding has taken place. These cracks are not visible when the MgF_2 is deposited on a bulk Si layer (see fig.3.19) which shows a dense layer with a measured RI n=1.38. The cracks in the hybrid sample arise from mechanical relaxations between the SiO_2 bottom cladding and the thick MgF_2 layer. If we look closely, each cavity of this sample is surrounded by a darker zone corresponding to the ICP-etched region. Indeed, this sample was processed using a SiN hard-mask which defines the PhC wire cavities and also a 2μm-wide trench around the cavities. During ICP, SiO_2 is partly etched which results in this visible trench. We observe that the cracks around the cavities originate mostly from the angles at the outer border of this etched zone, thus preventing the cavities from breaking. Here again, further optimisations of the process is required. It is highly probable that thinner layers will give less cracks without significantly reducing the heat sinking of the layer. Moreover, optimisation of the stress in the layer could be obtained as it is done in [173] with Ar^+-assisted IBAD.

Despite an excellent thermal behaviour and its very low RI, MgF_2 hardness constitutes an impediment. This material, indeed, can neither be chemically removed nor etched with conventional ICP-RIE processes which renders, at the moment, its use in our nanostructures quite limited. *A contrario*, SiO_2 is easier to handle despite its slightly higher RI and lower thermal conductivity. As we will see in the next chapter, MgF_2 provides outstanding thermal sinking, and is, if not promising, at least worth keeping in mind for future applications.

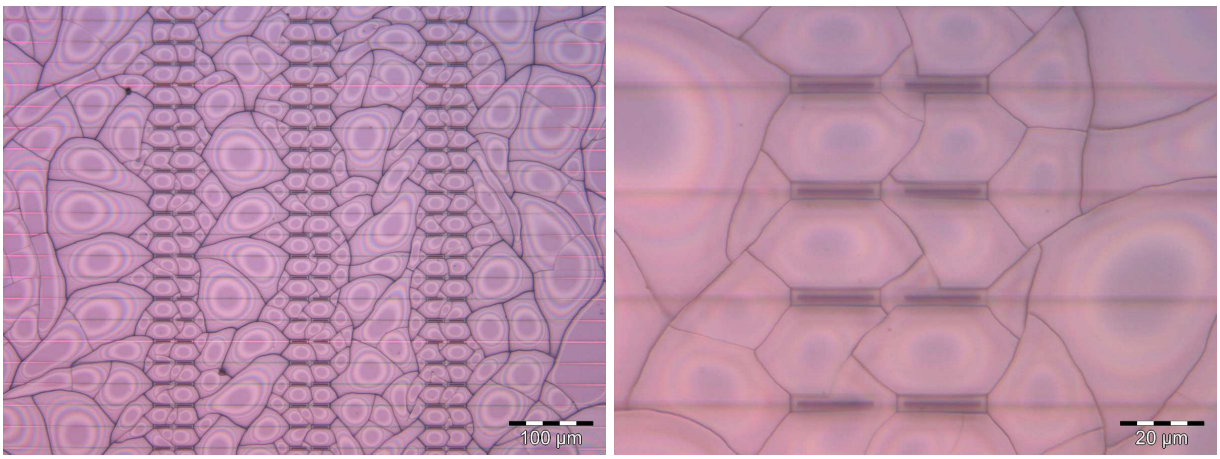

Figure 3.18: *Visible picture of a hybrid sample encapsulated in 1 µm of MgF_2. Above a certain thickness, mechanical relaxations produce many cracks in the top cladding. Here the cracks around the cavities originate mostly from the angles of the ICP-etched zone (see the trenches around the cavities) as this sample was process in the 2 e-beam-steps processed flow with a SiN hardmask.*

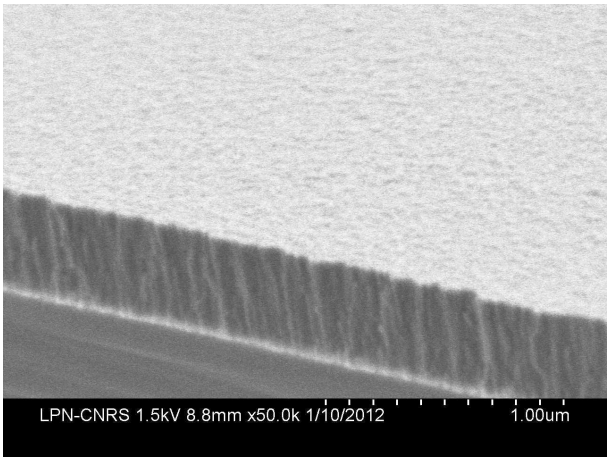

Figure 3.19: *SEM image of a MgF_2 layer deposited on a Si wafer. The resulting layer has a RI of 1.38 and looks dense enough to obtain the expected thermal properties ($\kappa \approx 14\ W.m^{-1}.K^{-1}$).*

3.4 Summary

In summary, this chapter reported on the fabrication of hybrid III-V PhC/SOI circuit structures. Many features have been implemented in the process flow in order to address the major issues of the final device. The bonding yield has been significantly increased by addition of a SiO_2 layer and is now close to 100%. The accuracy on the bonding thickness is now transferred from the BCB, thinned down by pressing, to the SiO_2 bottom cladding whose deposition can be controlled at a few nm scale. The definition of the PhC pattern is simplified to a single e-beam step and the III-V sidewalls are smoother and sharper than before. In addition, key processes such as passivation and encapsulation were introduced and we will show in the next chapter that they enable stable CW laser operation of our devices. Finally, the MgF_2 material, seldom used in infrared photonic application, is brought to the attention of the nanophotonic community.


pump
exhibit
given
high
photons
due
appear
particular
regime
First
increase
however
al
intensity
III-V
figure
understanding
bimolecular
Crystal
aspect
questioning
properties
lifetime
instance
part
particularity
demonstration
suppressing
powers
microcavity
expected
situated
function
stimulated
thesis
system
exposing
visible
higher
log-log
predicted
spontaneous
uncertainty
hand-in-hand
several
illusive
description
zone
exactly
accompanied
Bj
laser
incompatibilities
thus
plot
may
QDs
chapter
lasing
impact
i.e
light
close
fact
threshold
well
aiming
N2
equal
decrease
non-radiative
apparent
expect
questions
QWs
ork
curve
nonradiative
PhC
mode
mechanism
change
Lasing
values
g2
lifted
red
trace
measuring
behaviour
emitted
number
Cavity
seen
still
coherent
going
case
highlight
famous
recognize
set
interest
Wire
re-directing
equals
takes
emission
works
waveguide
four
slightly
hand
distinction
transition
rate
long
Photonic
different
experimental
characteristic
spectral
showing
definition
approaches
diminishes
containing
4.3.The
position
unambiguously
coherence
define
recombination
factor
detail
partly
power
interesting
et
□NR
operation
coupled
purity
lasers
quantum
refer
table
varies
effect

Chapter 4

Lasing with a III-V Photonic Crystal Wire Cavity coupled to a SOI waveguide

This chapter aims at describing the key features of the hybrid structure when laser emission is obtained inside a III-V PhC cavity evanescently coupled with a waveguide.

To begin with, the underlying physics of the laser emission taking place in our PhC nanocavity is discussed. A theoretical laser model, specific to the use of QWs as active material, is presented and compared with experimental results.

The second part is devoted to a study of the heat sinking in the hybrid structure and the ways to improve it.

Finally, we will present the work done on surface passivated PhC structures which enabled us to obtain stable CW laser emission.

4.1 Control of the spontaneous emission in PhC for laser applications

This chapter deals with laser emission in optically pumped PhC microcavities coupled to a single-mode waveguide. While the optical coupling between the waveguide and the laser will be analysed a little bit later, it is worthwhile to remark as an introduction to this chapter that PhC-cavity laser "on their own" are extraordinary objects capable of setting a new standard in the laser domain in terms of size, energy consumption and speed. Their most prominent properties originate from the unique coupling between the active material and the electromagnetic environment. Indeed, as we hinted in chapter 2 by solving numerically Maxwell's Equations, the spectral density of electromagnetic states $\rho(\omega)$ in a cavity is radically modified compared to an unstructured environment (i.e. without cavity). As a result, excited emitters loose the

possibility to radiatively relax into all (free-space) modes, but are now forced to a limited range of very specific permitted modes. Such control of the emission, and in particular the spontaneous emission, has been the motivation of many studies related to these structures[1].

One important effect resulting from this particular light-matter interaction in PhCs is the *Purcell* effect[174]. When an emitter is placed inside a cavity, acceleration[175, 176] or inhibition[2][175, 176, 177] of the spontaneous emission may occur depending on the overlap of the electromagnetic energy density with the emitter linewidth. In other words, the apparent radiative lifetime of an emitter placed for instance in a PhC can be quite different from the one of an emitter placed in a bulk material.

When an emitter is placed within a PhC cavity, its radiative lifetime is modified by a factor F_p, called Purcell factor, in such a way that:

$$\frac{1}{\tau_{rad}} = \frac{F_p}{\tau_{rad}^{bulk}} \tag{4.1}$$

where τ_{rad}^{bulk} is the radiative lifetime of the emitter placed in the bulk material. In the case of an emitter placed in a cavity, the Purcell factor F_p is given by:

$$F_p = \frac{3}{4\pi^2}\left(\frac{\lambda_c}{n}\right)^3 \frac{Q_p}{V} \tag{4.2}$$
$$\text{where} \qquad Q_p^{-1} = Q^{-1} + Q_{emitter}^{-1}$$

where V is the modal volume, n is the RI of the material surrounding the emitter and where λ_c is the emitted light wavelength. Q is the quality factor of the cavity (linked to the cavity photon lifetime τ_{ph}, see eq.(2.2)) and $Q_{emitter}$ is a quality factor related to the dephasing processes of the emitter. In QWs, the dephasing processes are characterised by a dephasing time T_2 which depends on the radiative lifetime of the emitter τ_{rad}^{bulk} and on the pure dephasing time T_2^* induced by interaction of the emitter with its environment (carrier-phonon coupling, electrostatic interactions...). $Q_{emitter}$ is given by:

$$\frac{1}{Q_{emitter}} = \frac{1}{\omega}\frac{1}{T_2} = \frac{1}{\omega}\left(\frac{1}{T_2^*} + \frac{1}{2\tau_{rad}^{bulk}}\right) \tag{4.3}$$

Relation (4.2) indicates that the Purcell factor can be larger than 1 only when V is of the order of or smaller than $(\lambda/n)^3$ (which is the case in PhC cavity) and when the sum $Q^{-1}+Q_{emitter}^{-1}$ is small enough. The latter condition depends obviously on τ_{ph} and T_2. For example, T_2 can be from few tens to 100 picoseconds [178] when QDs are used as the active material and when the structure is operated at cryogenic temperature (around 4K). In this case, the Purcell factor is often limited by the photon lifetime. F_p values higher than 20 were reported experimentally for

[1]The control of the spontaneous emission is part of one major research field named Cavity Quantum Electro Dynamics (CQED) which is studied in all kinds of systems but whose exposé would go much beyond the scope of this work.

[2]The suppression of the spontaneous emission is sometimes excluded from the appellation Purcell effect. Here, we extend this appellation to both inhibition and acceleration.

PhC cavities [178]. However, at room temperature, the Purcell Factor is completely determined by the dephasing time of the emitter which is of the order of few tens of fs [179] (much shorter than τ_{ph}). Hence, a rapid calculation gives F_p close to 1. In the case of QWs, the dephasing time is assumed to be of the order of 30 fs. Because the "Purcell" quality factor Q_p is in fact limited by the dephasing time at room temperature, the real contribution to the acceleration of the spontaneous emission is due to the wavelength-scale modal volume achievable in PhC cavity. In our system, the value of F_p is usually between 1 and 4.

The other important consequence of the control of spontaneous emission in PhC cavities is the modification of the value of the spontaneous emission factor β which is defined as the ratio of the photons emitted in the cavity mode over the total emitted photons. It can be expressed as:

$$\begin{aligned} \beta &= \frac{F_p}{F_p + \gamma} \\ &= \frac{\text{Photons emitted in the considered cavity mode}}{\text{Total of emitted photons}} \end{aligned} \tag{4.4}$$

where γ is defined as the ratio of the rate of spontaneous emission in all other modes over the rate of spontaneous emission if the emitters were in the bulk material.

Most of the time, in a laser, the amount of the spontaneous emission which is coupled into a considered laser mode is quite small. Generally, this is due to the fact that the emitter spectral linewidth is much broader than that of the cavity so that a significant part of the emission which is allowed to couple to the continuum of radiative modes, freely propagates outside the cavity. The other reason is that usual lasers have a large number of cavity modes and, in addition, only a small fraction of the light is emitted in the right directions which couple with the desired optical mode. β is in the range of 10^{-5}-10^{-4} for edge emitting lasers [180] and in the range of 10^{-5}-10^{-2} for VCSELs [181, 182]. From the expression (4.4), we see that β will tend towards 1 for large values of F_p, but maybe more interestingly, when γ goes to zero. This is where PhCs come into play as they enable the inhibition of spontaneous emission which is not coupled into the cavity mode thanks to their photonic band gap. As a result, for PhC lasers, β is expected to be orders of magnitude greater than in conventional lasers, and should even approach 1 for optimised structures. For instance, β was demonstrated to get close to 1 in planar microcavities containing a single emitter [183] as well as in PhC cavity lasers [155]. Moreover, as the PBG bandwidth can be larger than the emitter linewidth at room temperature, this holds even for lasers operated at room temperature which is the case for PhC nanolasers embedding InP-based QWs. One of the most striking point in these studies, is the potential decrease of the laser threshold due to the increase of the spontaneous emission factor β [184, 185]. In addition, a high value of β is also expected to increase the maximum modulation speed of the laser [158, 186] which is definitely an important figure of improvement.

As a consequence, the integration of PhCs lasers represents a disruptive approach in the way of building a Photonic Integrated Circuit as they can potentially be driven at very low pump

levels and enable ultrafast modulation speed. In order to achieve a PhC laser which makes full use of the control of the spontaneous emission and which also couples efficiently to a Si waveguide, we decided to use III-V-based active PhC Wire Cavity (described in chapter 2) which are also referred as PhC "nanobeam cavities". Recently, several groups -including mine- have demonstrated laser emission in this type of PhCs in the case of free-standing beams embedding either QWs [111, 187, 188] or QDs[189] and in the case of PhCs wire cavities in the heterogeneous platform [117, 122] embedding InGaAsP/InGaAs QWs.

The next section is dedicated to the rate equation model we use to describe the PhC nanocavity laser behaviour.

4.2 Laser model for quantum wells PhC laser

4.2.1 Rate equations

Rate equations are the time-dependent evolution equations for the carriers and for the photons in the laser. These equations are coupled to each other through the spontaneous emission and the stimulated absorption/emissions of photons. To describe a PhC cavity laser, we express the rate equations as a function of the photon number $s(t)$ contained in the modal volume V, as defined in section 2.1.3, and the carrier density $N(t)$ (in cm^{-3}) in the active material. V_a is the active volume participating in the laser emission. Basically, V_a is the volume of the active material which is spatially overlapped with the cavity mode and is given by:

$$V_a = \frac{\int d^3\mathbf{r}\boldsymbol{\Delta}(\overrightarrow{r})\varepsilon(\overrightarrow{r})|\,\mathbf{E}(\overrightarrow{r})\,|^2}{max(\varepsilon(\overrightarrow{r})|\,\mathbf{E}(\overrightarrow{r})\,|^2)} \tag{4.5}$$

where $\mathbf{E}(\overrightarrow{r})$ the electric field, ε is the space dependent dielectric constant and $\Delta(\overrightarrow{r})$ is equal to 1 in the active material and is equal to zero everywhere else. To be more complete, the impact of carrier diffusion should also be taken into account for the calculation of V_a as some carriers may diffuse in or out of the cavity region during their lifetime [190]. As regards the compactness of PhC lasers, the value of V_a is much smaller than in other type of lasers such as edge emitters, VCSELs or even microdisks lasers.

The general expression of the rate equations is given by [180]:

$$\frac{dN}{dt} = R_{inj} - R_{sp} - R_{NR} - R_{st} \tag{4.6}$$

$$\frac{ds}{dt} = -\frac{s}{\tau_{ph}} + V_a\,(\beta R_{sp} + R_{st}) \tag{4.7}$$

where τ_{ph} is the photon lifetime in the cavity and β is the spontaneous emission factor.

R_{inj}, R_{sp}, R_{NR} and R_{st} are, respectively, the rates of injected carrier density into the QWs, of spontaneous emission, of non-radiative recombination and of stimulated emission, all in $cm^{-3}.s^{-1}$. The injection rate R_{inj} corresponds to the effective injection rate into the fundamental level of the wells. Note that, in the optical pumping scheme considered here, only a part of the pump

power focused on the sample is absorbed by the material and only a fraction of the excited carriers are effectively captured by the wells. We will come back to this point further ahead, but it is useful to highlight that the injection rate R_{inj} does not take into account absorption or capture issues.

Figure 4.1 schematically describes the different processes which play a role in carrier recombination and photon emission.

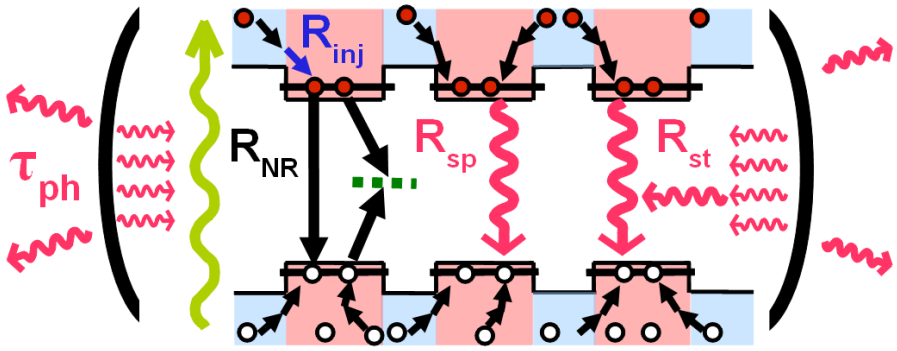

Figure 4.1: *Schematic of the model of the optically pumped PhC laser. The green arrow indicates the pump energy that injects free-carriers in the barriers. The red (white) dots represent the electron (holes) and the arrows indicate how they are captured into the wells, with a rate R_{inj}, before recombining through radiative (R_{sp}, R_{st}) or non-radiative (R_{NR}) recombination processes. The dynamics of the optical losses is determined by the photon lifetime τ_{ph} inside the cavity, schematised by the two brackets.*

In QWs, the spontaneous emission decay is carrier dependant so that R_{sp} writes:

$$R_{sp} = F_p B N^2 \tag{4.8}$$

where B is the bi-molecular recombination factor in cm^3/s and where we multiply the usual bimolecular recombination rate by the Purcell factor F_p which allows us to take into account the acceleration (or inhibition) of the spontaneous emission rate because QWs are placed in an optical cavity.

The two other rates in eq.(4.6) are given by:

$$R_{NR} = \frac{N}{\tau_{NR}} \tag{4.9}$$

$$R_{st} = G(N)s \tag{4.10}$$

where τ_{NR} is the non-radiative carrier lifetime in s and $G(N)$ is the net gain of the material in cm^{-3}/s. For QWs, it can be shown[191, 192, 193] that this gain can be approximated with a very good accuracy by

$$G(N) = G_0 \ln\left(\frac{N}{N_{tr}}\right) \tag{4.11}$$

where N_{tr} is the transparency carrier density. At $N = N_{tr}$, the stimulated emission compensates exactly the absorption and the material becomes transparent for photons at the operating wavelength. Above N_{tr} the gain is positive indicating that the material is amplifying the number of photons s, while for carrier densities below N_{tr}, we are in the absorption regime.

From the Einstein relations, linking the rate of spontaneous emission and the rates of stimulated absorption and emission, we have:

$$\beta R_{sp} = \frac{R_{st} n_{sp}}{s} \tag{4.12}$$

where n_{sp} is the *population inversion factor* expressed, in semiconductors, using the occupation probabilities of carriers in the valence band (f_1) and conduction band (f_2). The expression is given by[180]:

$$n_{sp} = \frac{f_2(1 - f_1)}{f_2 - f_1}$$

Generally n_{sp} depends on the carrier density which must be included in the Einstein relations. Because relation (4.12) must be verified for any carrier density, we can assume that n_{sp} can be written as:

$$n_{sp} = A' \frac{N^2}{\ln\left(\frac{N}{N_{tr}}\right)} \tag{4.13}$$

where A' is a constant to be determined. To do so, we remark that, inserting (4.13) in eq.(4.12), we obtain

$$G_0 = \frac{\beta F_p B}{A'} \tag{4.14}$$

The constant A' is fundamentally a material related parameter and does not depend on the optical mode density of the cavity. The method used to determine A' will not be described here as it relies on an iterative fitting procedure of experimental laser linewidth and intensity measurements as a function of the injection. Let's just say that we fitted these data with β/A' and converge to a value of $A' = 5 \times 10^{-36}$ cm^6. It is this value that we used in the rest of the analysis.

We see then that rate equations ((4.6) and (4.7)) in the case of a PhC laser embedding QWs as active material are finally

$$\frac{dN}{dt} = R_{inj} - F_p B N^2 - \frac{N}{\tau_{NR}} - \frac{\beta F_p B}{A'} \ln\left(\frac{N}{N_{tr}}\right) s \tag{4.15}$$

$$\frac{ds}{dt} = -\frac{s}{\tau_{ph}} + V_a \beta F_p B \left(N^2 + \frac{1}{A'} \ln\left(\frac{N}{N_{tr}}\right) s\right) \tag{4.16}$$

4.2.2 Laser stationary regime

The resolution of the rate equations (4.15) and (4.16) in the stationary regime $\left(\frac{d}{dt} = 0\right)$ enables to construct the laser emission characteristic curve which shows the number of photons inside the cavity s as a function of the carrier injection rate R_{inj} into the wells.

In the stationary regimes, eqs. (4.15) and (4.16) transform into

$$R_{inj}(N) = \left(F_p B N + \frac{1}{\tau_{NR}}\right) N + \frac{\beta F_p B}{A'} \ln\left(\frac{N}{N_{tr}}\right) s(N) \quad (4.17)$$

$$s(N) = \frac{V_a \beta F_p B N^2}{\frac{1}{\tau_{ph}} - \frac{V_a \beta F_p B}{A'} ln\left(\frac{N}{N_{tr}}\right)} \quad (4.18)$$

For a given carrier density N, we can therefore obtain the stationary solution linking $R_{inj}(N)$ and $s(N)$. Then, it is also possible to calculate the total output power of the cavity, given by $P_{out} = s \times \frac{h\nu}{\tau_{ph}}$, and the pump injection power given by $P_{inj} = R_{inj} \times V_a \hbar \omega_{pump}$ where we consider a quantum efficiency of 1, i.e. that the carriers generated by the absorption of the pump light at ω_{pump} are entirely captured by the wells.

Figures 4.2 shows examples of numerically calculated laser characteristic curves in linear and log-log scales, for a typical set of (assumed) parameters of our InP-based PhC lasers (see table 4.1) . These curves plot the photon number s (and P_{out}) as a function of the injection carrier rate R_{inj} (bottom axis) and equivalently as a function of the injection power P_{inj} in μW (top axis). Two regimes of emission are visible: one is the spontaneous emission regime when the stimulated emission is negligible and the other is the stimulated emission regime when it is the contrary. The transition from one regime to the other, clearly visible in the linear scale graph, occurs around the laser threshold injection power $(R_{inj})_{th}$. It is the well known behaviour of any lasers where a steep increase in the output is expected as their threshold is crossed. For low β factor, the laser threshold is reached when the gain compensates the optical losses (related to $1/\tau_{ph}$). In this "classical" picture of the threshold definition, $(R_{inj})_{th}$ writes:

$$(R_{inj})_{th} = \left(\frac{1}{\tau_{NR}} + F_p B N_{tr} e^{\frac{A'}{V_a \beta F_p B \tau_{ph}}}\right) N_{tr} e^{\frac{A'}{V_a \beta F_p B \tau_{ph}}} \quad (4.19)$$

where the stimulated emission is neglected at threshold. As we will see, this definition is even more ambiguous when β approaches 1. In log-log scale, the curve appears "S"-shaped, highlighting a third zone of interest within a small range of injection rates around the threshold. This smoothly varying curve is more commonly used in experiments as it allows to better observe the different regimes (spontaneous, transition, stimulated) than in the linear scale.

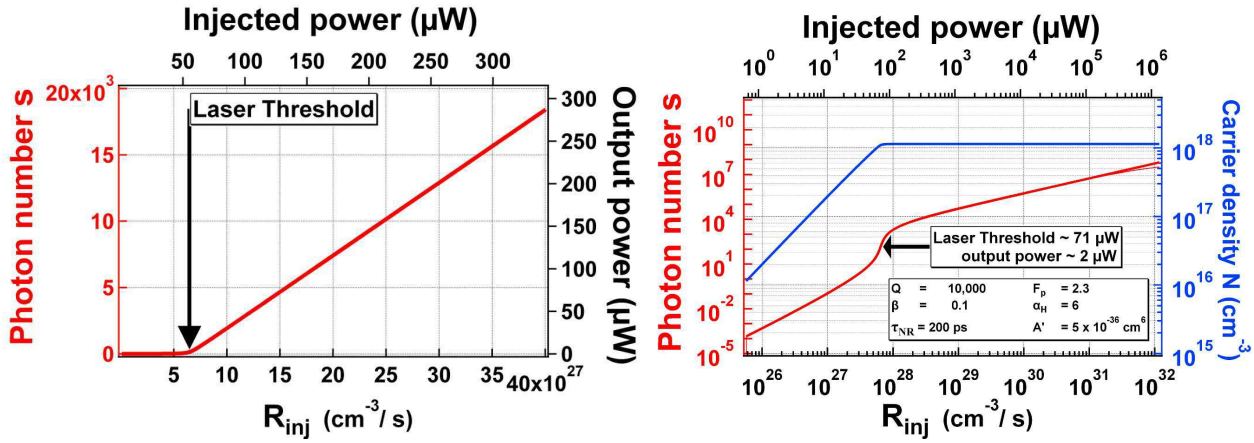

Figure 4.2: *Theoretical characteristic curves of a laser in linear and log scale. The carrier density N (in blue) is also plotted as a function of the injection.*

λ_{tr} =1550 nm	$A' = 5 \times 10^{-36}$ cm^6
$Q = 10000$	$\tau_{NR} = 200ps$
$\beta = 0.1$	F_p=2.3
$N_{tr} = 10^{18}\ cm^{-3}$	V_a=6.8 $\times 10^{-14}\ cm^3$
B= 3 $\times 10^{-10}\ cm^3/s$	$\alpha_H = 6$

Table 4.1: *Numerical parameters used in the steady-state resolution of the laser rate equations.*

We also plot in fig. 4.2 (right) the evolution of the carrier density as a function of the injection level. We observe that, obviously, N increases when the pump power increases. When N is equal to the transparency carrier density $N_{tr} = 10^{18}\ cm^{-3}$, the net gain $G(N_{tr})$ is equal to 0 and the cavity is transparent for light propagation. If the pump increase goes on, N increases until the injection rate reaches the threshold rate at which point the value of N becomes fixed at N_{th}. Note that, in fact, this is not perfectly accurate as the carrier density truly tends asymptotically to N_{th}. However, the variation above threshold are quite small and we will assume that $N = N_{th}$ above the threshold. This is the reason why, above threshold, the gain is clamped at a value $G(N_{th})$.

The calculated S-curve gives the order of magnitude of the encountered value for the absorbed threshold power which, for the values of table 4.1, is of 71 μW and is estimated to be in the range of a 1-100 μW in real fabricated objects. The total output power at threshold is here $2\mu W$ and can be further increased by increasing the pumping. Of course, in real devices, several effects limit the increase of the output power, like the spectral hole burning, the heating of the system or the structural damage. The maximum output power has not been measured in this work, but output powers of a few 10's of μW have been estimated to pass inside the Si waveguide.

The characteristic of the laser emission depends on many parameters. In what follows we investigate the modification of the S-curves as a function of 3 important parameters of the PhC nanolasers: the β factor and the non-radiative carrier lifetime τ_{NR} and the Q factor.

4.2.3 Main parameters impacting the laser threshold power

4.2.3.1 Impact of the spontaneous emission factor β

As it was stated in the first part of this chapter, the impact of the β factor is expected be important[185, 194] on the laser operation characteristics, and in particular on the laser threshold power.

The laser behaviour as a function of the β factor is illustrated in figure 4.3 where we plot the characteristic curves of a PhC laser for four values of β (0.01, 0.1, 0.9 and 1). To highlight the change due to re-directing of the spontaneous emission into the lasing mode, we set the non-radiative lifetime τ_{NR} to $1\mu s$ which is equivalent to suppressing the effect of the non-radiative recombination rate. The other parameters are the same as in table 4.1. In log-log scale, we observe that, when β is well below 1, the transition from the spontaneous emission to the stimulated emission regime is marked by a rapid jump in the emission intensity as a function of the pump power. On the other hand, as β takes larger values and approaches 1, the threshold power diminishes while the laser transition becomes smoother. Such behaviour was predicted in the case of microcavity lasers in several articles [184, 195, 196, 197] which analyse in detail the particular laser behaviour when β equals 1. Indeed, in the case of QDs emitters embedded in the microcavity, the laser emission intensity curve does not exhibit any apparent threshold when β=1 which led to refer them as "thresholdless lasers". This particularity has been and still is the object of intense research aiming at its experimental demonstration and at the understanding of its impact on the emitted photons properties. In a system containing QWs, the behaviour is slightly different as can be seen in figure 4.3. The increase of β is naturally accompanied by a decrease of the apparent threshold, i.e. for instance the inflexion point of the curve, but, in the case where β=1 (red trace), the spontaneous emission part of the curve merges with the transition zone which results in a two slopes curve. This distinction between the QWs and the QDs laser behaviour is due to the spontaneous emission mechanism which is a bimolecular process in QWs and whose rate varies as N^2, instead of as N in QDs. Then, the uncertainty on the "threshold" position that surrounds QDs laser with $\beta = 1$ can be considered as partly lifted in the case of QWs laser. This is only partially true. First, let's say that it is illusive to expect a full description of a laser behaviour from a single light-light curve. Despite the fact that lasers are also famous for their long coherence length (going hand-in-hand with the spectral purity of the emission), this aspect does not appear in such a characteristic curve. In the end, the questions are what are the light properties that we expect to use to unambiguously define the laser emission and how do we recognize the transition from spontaneous emission to laser emission, i.e. where exactly is the laser threshold situated. While Björk et al. [185] used a

so-called "quantum" definition of the threshold, where the number of photons in the lasing mode was equal to 1, other works [198, 199, 200] have focused their interest in the statistical property of the emission by measuring the second order correlation function $g^2(\tau)$ of the laser emission with high $\beta(>10^{-2})$ as a function of the pump power, showing that its value gets close to 1 (coherent light) for powers significantly higher than the visible "threshold", thus, exposing some incompatibilities between the definitions. While some additional insight remains to be given to the threshold definition, in this thesis, we shall not enter too deeply in this questioning, however puzzling and interesting it may be.

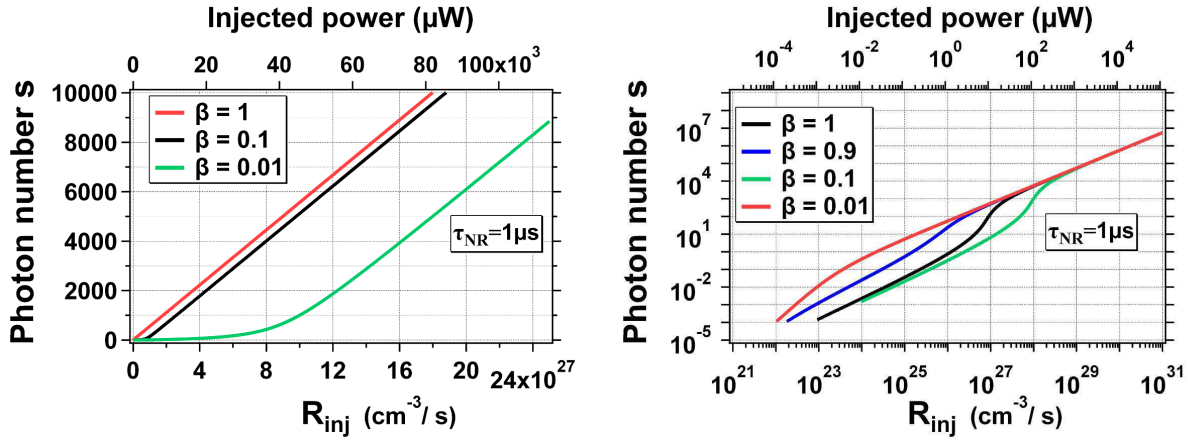

Figure 4.3: *S-curves of a PhC laser for three values of the spontaneous emission factor β, taking τ_{NR}=1μs and with the remaining parameters of table 4.1.*

In practice, we choose to read-out the laser threshold value in the laser characteristic curve by taking the injection level where the curvature sign changes, i.e. at the inflection point. As we will see, in our structures, we have found estimation of β between 5×10^{-2} and 0.3, depending on the structure property. For these values, experimentally, there is little discrepancy between the value given by the intersection with the x-axis of a linear fit of the light-light curve above threshold and the one given by the inflection point (the "apparent" threshold). We plotted in fig. 4.4 the latter values extracted from the calculated S-curves as a function of β. We used two different non-radiative carrier lifetimes τ_{NR}: 200ps and 1μs. When the non-radiative recombination can be neglected, the impact of the β factor on the apparent threshold (traces with markers) is quite important as the threshold is decreased by two orders of magnitude when β passes from 0.01 to 0.9. However, note that the variation of the threshold with β is flatter in the middle of that range, around 0.1 indicating that our typical PhC cavities will be weakly sensitive to a slight modification of β. Of course, if we can engineer the structures so that $\beta \to 1$, the apparent threshold will decrease considerably. However, here again, everything depends on the

laser threshold definition. While the limiting case $\beta = 1$ is problematic because of its blurry laser transition range, the case β=0.9 (blue trace) still presents an S-shape, although extremely smooth, with an apparent threshold which is still fairly clearly identifiable.

The dashed solid line in fig. 4.4 corresponds to the classical definition of the threshold given by the expression (4.19). These data show that the two threshold values differ significantly for β factors above 0.2 and that the apparent threshold can be much lower than that obtained from the approximation of eq.(4.19). We see then that when β is too high, it is not possible to neglect the stimulated emission which depends also on β due to the Einstein's relations. The discrepancy is lesser when non-radiative recombination comes into play (red markers trace). The decreasing of the apparent threshold when β gets close to 1 for τ_{NR}=200ps is strongly attenuated. For such values, the classical threshold gives approximately the same result as the inflection point values.

We see then that the impact of β on the laser threshold can potentially be very important if it were not for the reduction in non-radiative carrier lifetime in PhCs. Even in this case, the laser threshold changes very little with β, other dynamical analyses of the rate equation show that, at identical laser output power, the expected available modulation bandwidth of the PhC laser increases when β increases. This point will, however, not be treated in this manuscript and will be discussed in a future paper after further exploration as this point is very important for these nanolasers.

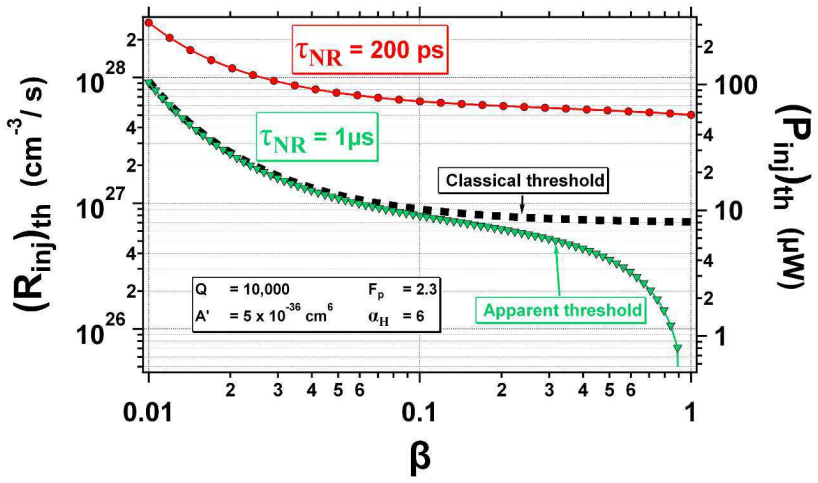

Figure 4.4: *Threshold carrier injection rate* $(R_{inj})_{th}$ *and power injection rate* $(P_{inj})_{th}$ *as a function of the* β *factor for* τ_{NR}*=200ps (red markers) and* τ_{NR}*=1µs (green markers). The solid dashed line is the classical threshold (eq.*(4.19)*) in the case* τ_{NR}*=1µs.*

In the next section, we will illustrate the impact of the non-radiative carrier lifetime on the laser and on its threshold value.

4.2.3.2 Impact of the non-radiative recombination rate

Non-radiative carrier recombinations have a major impact in the behaviour of our PhC laser. As this issue will be treated in more depth later (section 4.5), lets just note here that non radiative carrier recombination represents a problem encountered while working with semiconductor PhC lasers. The processing of these λ-scale structures induces irremediably the creation of defects at the etched interfaces where carriers efficiently recombine non radiatively. As the pattern dimensions can be well below the diffusion length of the carriers, the non radiative lifetime τ_{NR} is expected to be significantly shorter than in the bulk material. As it will be shown at the very end of this chapter (see fig. 4.33), measurements performed on InP-based pillars containing InGaAs QWs demonstrated a reduction of τ_{NR} from 1.5ns down to 200ps when the radius of the pillars is shrunk down to 200nm. Hence, the non-radiative carrier lifetime used to calculate the trace in fig. 4.2 was taken more realistically equal to 200ps.

Figures 4.5 show the S-curves for several spontaneous emission factors β and for 2 different non-radiative carrier lifetimes. These lifetimes are set to illustrate two realistic cases observed with our III-V PhC structures. While one lifetime is equal to 200ps, the other is taken to be 2.2ns which is possible to obtain by "passivating" the PhC sidewalls. This process is presented in detail in section 4.5. First, we can observe, by comparing the cases τ_{NR}=1μs, τ_{NR}=2.2ns and τ_{NR}=200ps, that the shape of the S-curves (for β=1, for example) is steeper around the threshold when τ_{NR} is small. Furthermore, when non-radiative recombination increases, the laser threshold naturally increases, as carriers participate less efficiently towards increasing the photon number in the cavity. For β values taken equal to 0.01 and 0.1, the laser threshold, when passing from 200ps to 2.2ns,decrease, respectively, by a factor of $\approx$2.5 and $\approx$ 5. While these reductions are not spectacular, non-radiative recombinations have a more dramatic effect on the laser behaviour as they create considerable heat in the structure. Because PhC wires in the hybrid structure are thermally isolated by the BCB bonding layer and also by the buried oxide layer of the SOI, heat spreading is fairly bad if it is not optimised carefully. Then, hot spots can arise in the structure, preventing sometimes the lasing effect and, even worse, inducing material damages. This is the reason why thermal optimisation is a major issue to which I devoted considerable attention (see section 4.4).

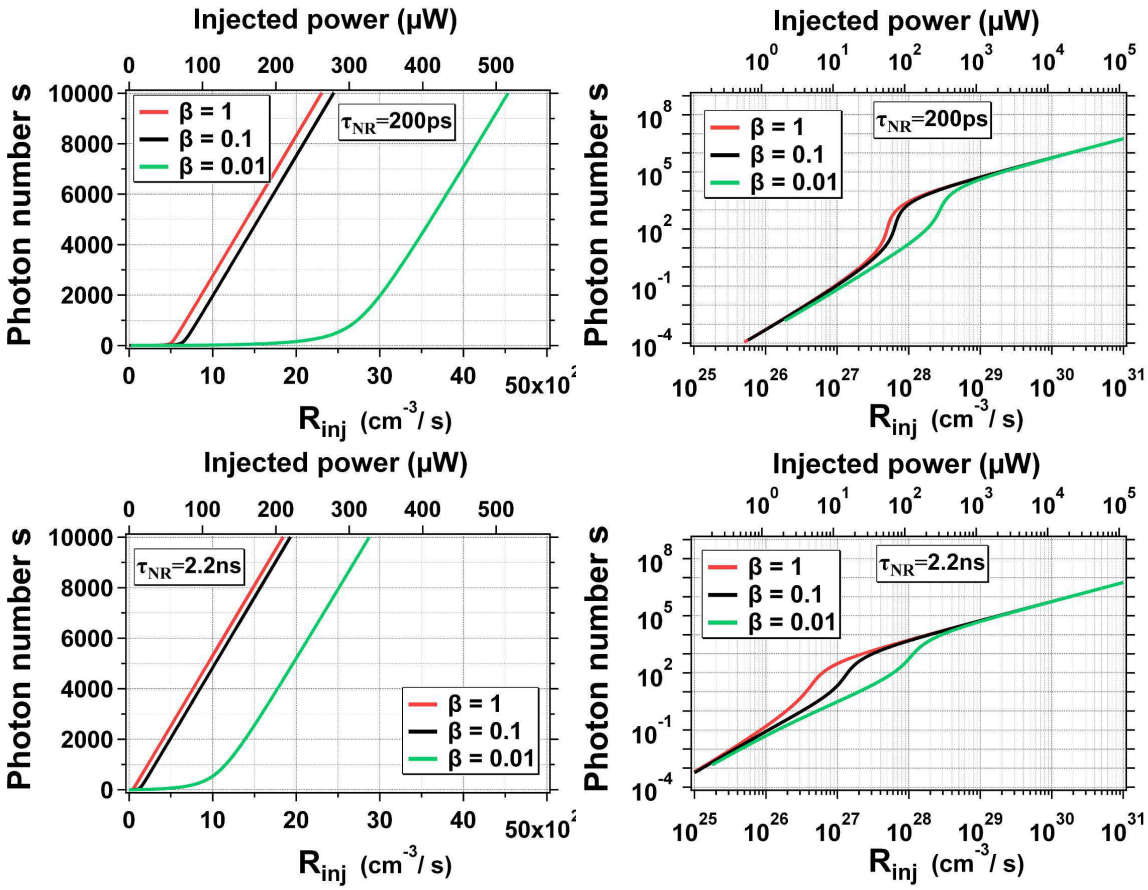

Figure 4.5: *S-curves of a PhC laser for three β factor values 0.01 (green), 0.1 (black) and 1 (red) in linear and log-log scale. Two values of τ_{NR} are considered 200ps (upper graphs) and 2.2ns (lower graphs). The rest of the parameters are again those of table 4.1.*

The attentive reader will have noticed that, up to now, the non-radiative carrier recombination process taken into account was that of carriers *inside* the wells. However, non-radiative carrier relaxation of the photoexcited carriers above the energy level of the well also unfortunately provides heat in the sample. If the carriers non-radiatively recombine before reaching the participating QW energy level, this will also decrease the quantum efficiency of the device and thus decrease the effective injection rate R_{inj}, which in turn will increase the effective injection power.

4.2.3.3 Impact of the Q-factor

The optical losses of the cavity are characterised by the photon lifetime τ_{ph}, directly proportional to the quality factor Q. On figure 4.6 is plotted the laser threshold as a function of the Q-

factor when β=0.1 and τ_{NR}=200ps. For high values of Q, we note that the threshold tends asymptotically towards a minimum value whose exact expression can be found in (4.20) by approximating the expression (4.19) when τ_{ph} tends towards $+\infty$.

$$(R_{inj})_{th} = \left(\frac{1}{\tau_{NR}} + F_p B N_{tr}\right) N_{tr} \tag{4.20}$$

This expression is, of course, valid only in the case where the apparent threshold is close to the classical threshold (see fig. 4.4). Here, the threshold is entirely determined by the material constants, i.e. the carrier density at transparency and the non-radiative carrier recombination lifetime.

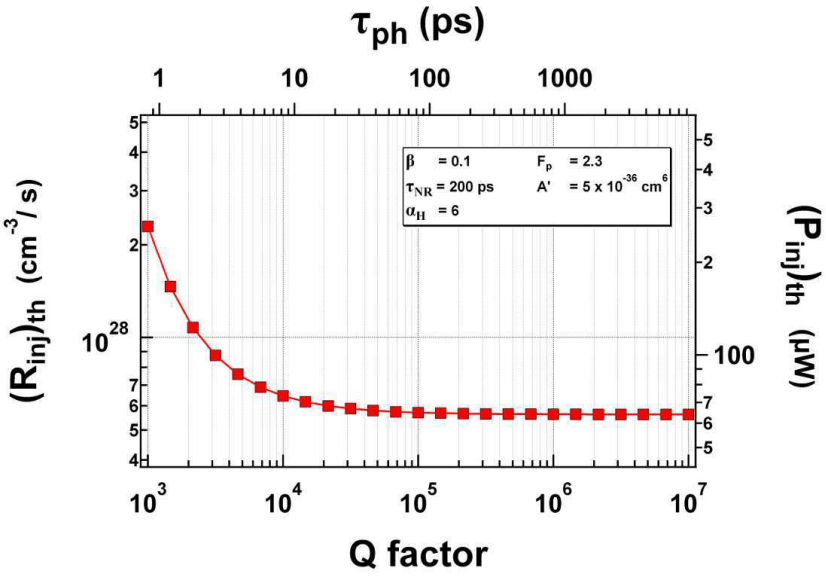

Figure 4.6: *Theoretical laser threshold versus the quality factor Q of the cavity.*

In the case of β equals 0.1, most of the laser threshold diminution obtained by increasing the Q factor takes place for Q's below 10^4. Moreover, for larger non-radiative lifetimes, the variation of the threshold power versus Q tends to be smoother. For this reason, using cavity exhibiting Q-factors above 10^4 will impact little the energy consumption of our PhC laser which embeds QWs.

Note that this is not in contradiction with the goal of chapter 2 which was to design high-Q cavities. Indeed, if the impact of the photon lifetime plays little role on the threshold value, it will not be the same for the dynamical behaviour of the laser, as very long photon lifetime will inevitably clamp the maximum modulation speed. Besides, as it will be shown in more detail later, the use of high-Q cavities potentially enables very efficient coupling to a supplementary channel of optical losses, such as a SOI waveguide positioned in the vicinity of the resonator,

without increasing the power consumption. Indeed, for example, if we could fabricate a PhC wire cavity laser with an intrinsic Q-factor of 10^5 (Q-factor at transparency without waveguide), the laser threshold would weakly increase by augmenting the overall losses by the coupling to a waveguide so that the total Q factor of the structure falls to 10^4. With these figures, more than 90% of the laser emission would be coupled to the waveguide. This is of course of primary importance in a real device. Furthermore, let's remark that the poor dependence of the laser threshold on Q actually renders difficult the experimental evaluation of the Q factor of the laser cavities as it is not directly measurable through the threshold power. The determination of Q is, indeed, a challenging task because of the presence of the active material. In this work, we usually quantify its value by fitting the entire experimental data set constituting of the S-curves with the steady-state model.

4.2.4 Emission wavelength and linewidth of the laser

Figure 4.7 shows the emission wavelength variation with the injection pump power corresponding to the PhC laser of S-curve plotted in fig. 4.2.

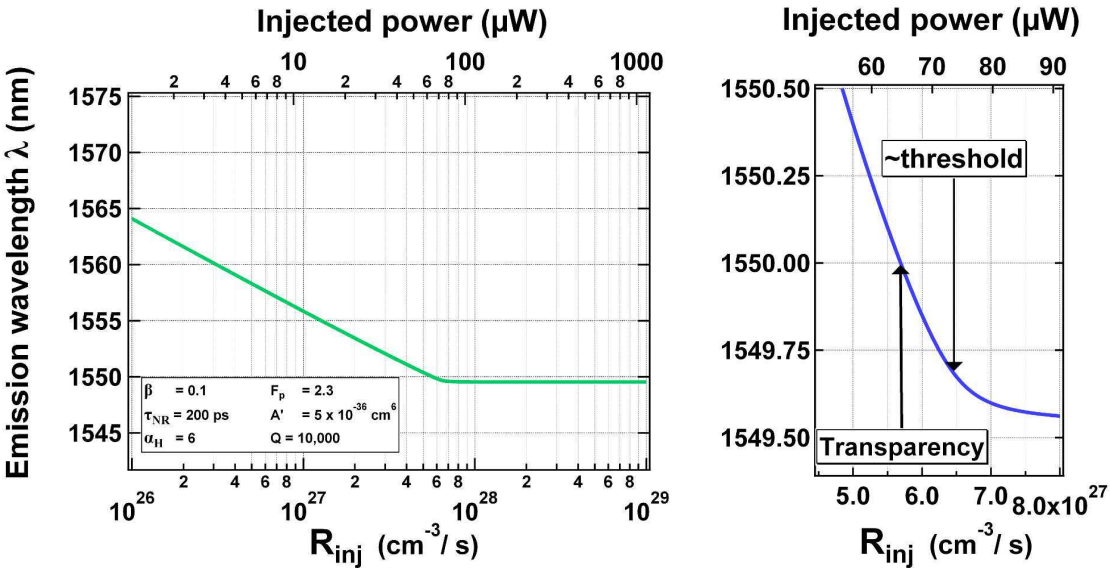

Figure 4.7: *Emission wavelength plotted as a function of the injection rate and power. The right graph shows the variations around the transparency and the threshold. Note that no thermal effect is taken into account here.*

We observe that the cavity shifts towards the blue, i.e. towards shorter wavelengths, as the number of carriers inside the cavity increases. Mathematically, the frequency of the cavity is expressed:

$$\begin{aligned} \omega &= \omega_{tr} + \frac{1}{2}\alpha_H G(N) \\ &= \omega_{tr} + \frac{1}{2}\alpha_H \frac{F_p \beta B V_a}{A'} \log\left(\frac{N}{N_{tr}}\right) \end{aligned} \tag{4.21}$$

where ω_{tr} is the cavity frequency at transparency. The right graph shows the resonance shift around the threshold. Note that, because there is a shift from the "cold" cavity resonance, i.e. at transparency, to the clamped cavity resonance above the threshold, it is not accurate to compare the latter wavelength with the simulated resonance which is computed for a cold cavity. This frequency shift from transparency toward the asymptotic value to which ω tends (or equivalently, λ) depends on N_{th} which strongly varies with τ_{NR}. However, this shift remains usually quite small, and in the plotted case using τ_{NR}=200ps, the wavelength shift from transparency is only 0.3nm at the apparent threshold and 0.46nm at twice the threshold. The best option would be to measure the cavity frequency exactly at transparency, but it is experimentally challenging to determine the transparency pump power. This is another reason why the quality factor Q of the cavity cannot be easily measured in a laser device.

The linewidth of the emission depends on the pumping level with respect to the laser threshold. As represented in figure 4.8, two regimes, one below and one above the threshold, come into play when the pump power is increased. Below threshold, the linewidth follows the famous *Schawlow-Townes* expression[180, 201] that we can simply write

$$\begin{aligned} \Delta\omega_{BT} &= \frac{V_a \beta R_{sp}}{S_{steady}} \\ &= \frac{1}{\tau_{ph}} - \frac{F_p \beta B V_a}{A'} \log\left(\frac{N}{N_{tr}}\right) \end{aligned} \tag{4.22}$$

where S_{steady} is the photon number in the cavity the steady-state regime.

Above threshold, the linewidth follows a modified *Schawlow-Townes* expression specific to semiconductor lasers. One characteristic of solid state semiconductor lasers is the variation of the material RI with the carrier density N. This leads to phase-amplitude coupling of the field described by Henry in [202]. Indeed, the amplitude and the phase of the laser couple to each other through the correlation between the gain variation and the RI variation when the carrier density varies. This is described by the already introduced *Henry* enhancement factor α_H which is defined by :

$$\alpha_H = \frac{\partial n'/\partial N}{\partial n''\partial N} \tag{4.23}$$

where n' and n'' are respectively the real and imaginary part of the RI. The values of the α_H-factor are typically in the range 3-10 for InGaAsP QW lasers.

The *Schawlow-Townes* relation is also decreased by a factor 2 due to the suppression to the phase-noise component that accompanies the passage to the threshold. In the end, the relation is modified by a factor $\frac{1}{2}(1+\alpha_H^2)$[180, 203] and it writes:

$$\Delta\omega_{AT} = \frac{1}{2}(1+\alpha_H^2)\,\Delta\omega_{BT} \tag{4.24}$$

The two relations are plotted in fig. 4.8 as a function of the carrier density and as a function of the carrier injection rate. Below threshold, the linewidth (blue trace) is simply the one of a cavity containing an absorbing material where the linewidth is principally related to the spontaneous decay of carriers. Above threshold, the enhanced linewidth (red trace) continues to decrease with the photon number inside the cavity. Hence, the higher the laser output power is, the narrower its linewidth will be. Unfortunately, the phase transition from one regime to the other is not easy to solve with our approach, but can be found, for example, in [204].

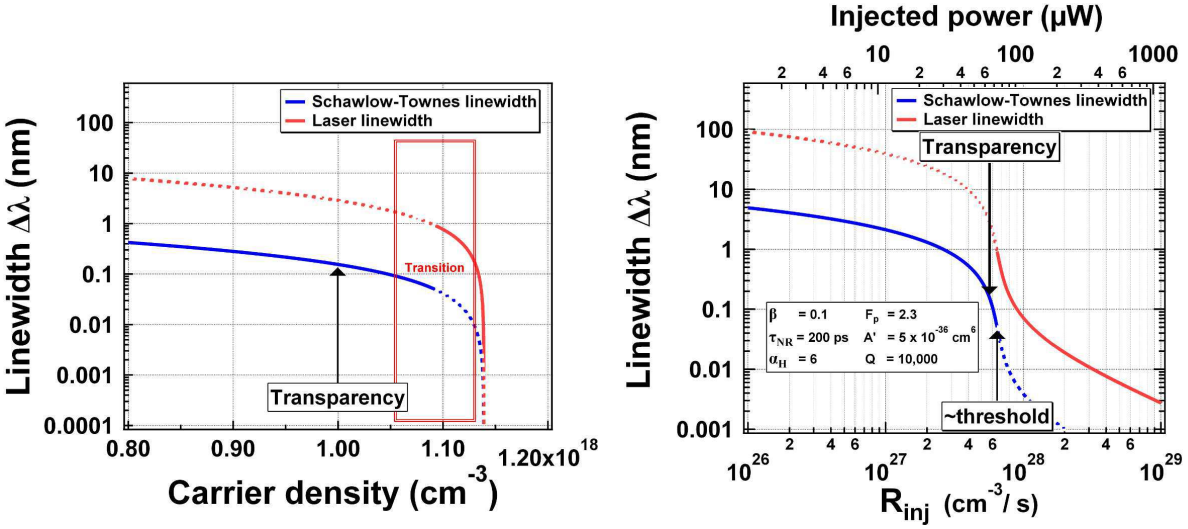

Figure 4.8: *Theoretical linewidth of the emission below and above threshold plotted as a function of the carrier density N (left graph) and of the injection (right graph). The red box in the left graph indicates the range of densities where the phase transition occurs from the amplified spontaneous emission regime to the laser regime.*

It is sometimes claimed in semiconductor PhC laser literature that the laser linewidth is directly related to Q. This is of course very wrong as the linewidth of the laser varies with several contributions and the first one being the pumping power. Often, estimations of the Q factor are given by measuring the emission linewidth at threshold. Again, this can lead to extremely false values and the only way to directly measure the Q-factor is to probe the cavity exactly at transparency. However, as mentioned above, it is quite tricky to evaluate exactly the pump power necessary to reach the transparency.

To conclude, as we will see in the next section, the measurements of our PhC laser linewidth is limited by the measurement apparatus. Our spectral resolution equals 0.06nm which usually hinders the accurate measurement of the laser phase transition.

4.3 Laser Characterisation

4.3.1 Micro-Photoluminescence set-up modified for grating coupler/optical fibre coupling

Figure 4.9 shows a picture of our Micro-Photoluminescence (μ-PL) set-up. The pump beam path is indicated in blue while the path of the light emitted above the PhC cavity surface is in red.

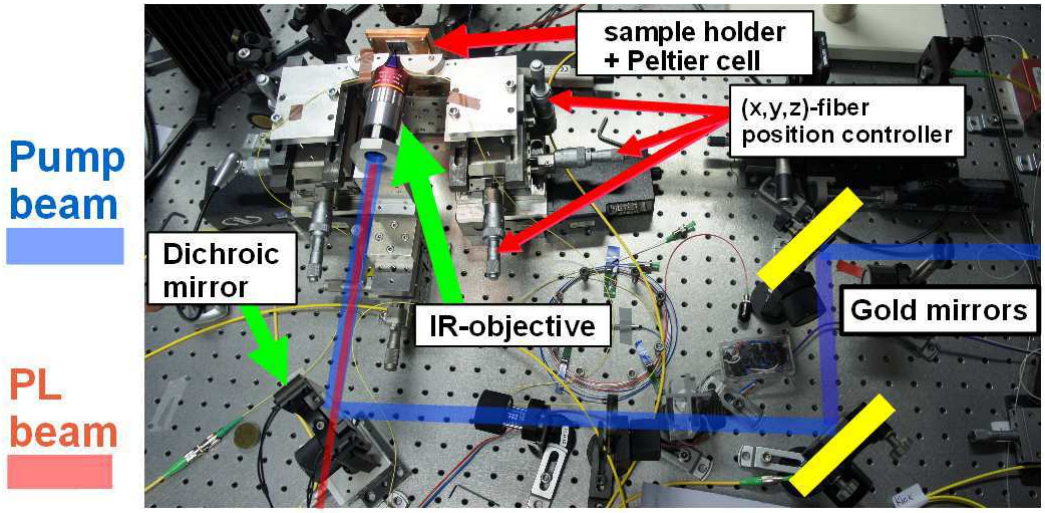

Figure 4.9: *Photography of the μ-PL set-up. The sample is surface pumped by a Laser Diode emitting at 800nm or at 1180 nm (indicated by a the blue beam). The pump is focused on the sample by a microscope objective (*Mitutoyo, f=200mm, N.A.=0.26*) which collects the retro-reflected part of PL (red beam). The PL is separated from the pump using a dichroic mirror and is then sent to a spectrometer.*

The PhC cavity is optically surface pumped by an external laser diode (LD) emitting light with energy above the barrier gap energy. The photons are absorbed by the material creating pairs of electron-holes that relax non-radiatively (*thermalisation process*) down to the quantum wells, thus feeding the QWs with carriers. As is depicted in the set-up scheme of fig.4.10, the pump beam is sent on to a dichroc mirror and reflected toward the sample. A Mitutoyo Infrared Objective (*f=200mm, N.A.=0.26*) is placed in front of the pump beam, focusing the pump on the cavity down to a spot size around $20 - 30\mu m^2$.

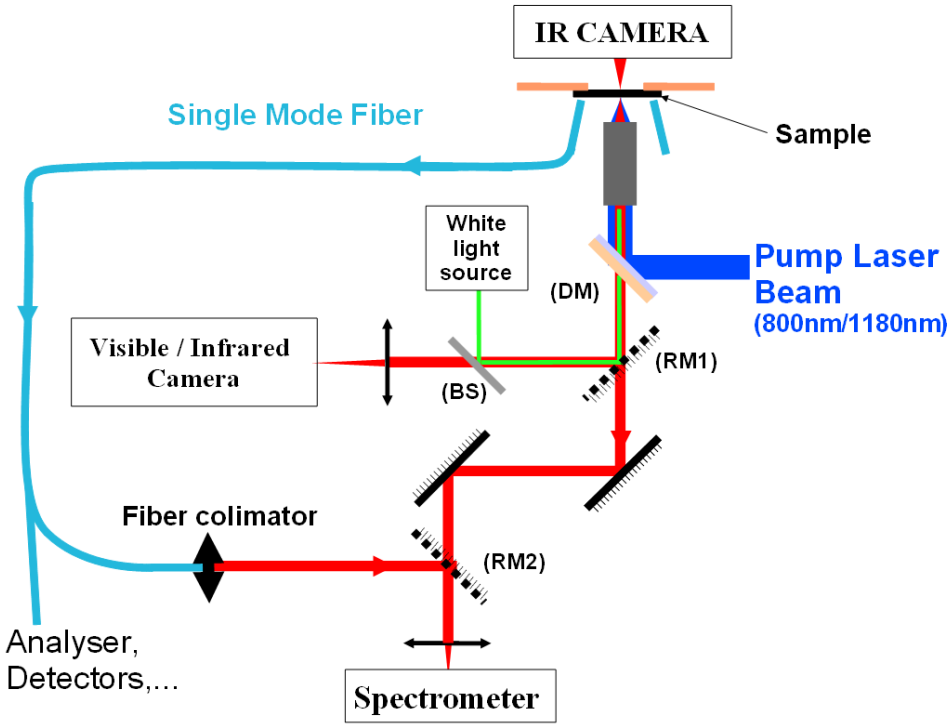

Figure 4.10: *μ-PL schematic setup. The sample is surface pumped by a Laser Diode emitting at 800nm or at 1180 nm.*

As can be seen on figure 4.11, the set-up is modified to be able to collect and inject light into the waveguide with optical fibres through the grating couplers made in the SOI. The sample is fixed with silver conductive lacquer on a copper holder. The latter is bonded to a Peltier cell, which sets the temperature of the sample substrate. The holder position is controlled in the x-, y- and z-directions by 3 mechanical actuators.

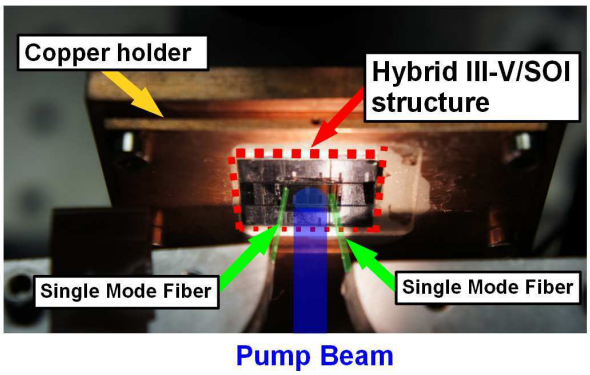

Figure 4.11: *Close-up photography of the holder with a III-V/SOI hybrid structure. SMF-28 placed at both sides of the sample, above grating couplers, allow light to be coupled in the SOI waveguide.*

For studying hybrid III-V/SOI samples, the working distance, i.e. the relative distance between the sample and the objective output, is limited by the presence of the coupling fibres above the grating couplers. As a result, it is not possible to take advantage of the high numerical aperture (> 0.9) objectives which give smaller spot size but which, unfortunately, also have smaller working distances.

4.3.1.1 Choice of the pump

Optical pumping is carried out using LDs emitting either at 800nm or at 1180nm. The choice of the LD has to take into account two issues: the absorption of the active layer for each wavelength and the heating of the sample due to thermalisation of pumped carriers into the wells. The final choice is based on a trade-off between the overall absorption of the III-V layer, that depends on the thickness of the active material compared with the InP cladding, and the induced heating of the sample. The heat E^H that is created through phonon-assisted relaxation of carriers can be written

$$\begin{aligned} E^H &= E_\lambda - E_{QW} \\ &= E_\lambda - E^B_{gap} + (E^B_{gap} - E_{QW}) \end{aligned}$$

where the energy brought by the pump is $E_\lambda[eV] = 1.24/\lambda[\mu m]$, E_{QW} is the energy level of the main radiative transition inside the QW which is close to 0.8 eV and E^B_{gap} is the gap energy of the barriers which is around 1.03 eV. Thus,

$$E^H_{800nm} = \frac{1.24}{0.8} - 0.8 = 750\text{meV}$$
$$E^H_{1180nm} = \frac{1.24}{1.18} - 0.8 = 250\text{meV} << E^H_{800nm}$$

In practice, even if the 1.18 μm LD has a much lower thermal contribution than the 800 nm LD, the limited available output power of the LDs ($\approx$ 20 mW before the microscope objective) combined with the lower absorption[3] of the 1180nm light as compared to the 800nm ligth (α_{800nm} $\approx$30% > α_{1180nm} $\approx$10%) renders the choice less obvious. The absorption of the pump at each of the LD wavelengths depends on each material forming the III-V heterostructure, in particular the barrier (InP+InGaAsP) composition. For instance, InP is transparent at 1180 nm but isn't at 800 nm. With our epitaxied samples, the absorption of the pump is always higher at 800 nm than at 1180nm as all of the III-V alloys (InP, InGaAsp, InGaAs) contribute to the absorption. To be able to work comfortably with the 1180nm LD, the InGaAsP barrier layer thicknesses were increased and the transparent InP layer decreased, keeping the same total thickness of the slab. A typical example of optimized epitaxy, where the InP layers constitutes less than 20% of the slab, was given in the previous chapter (fig.3.5).

4.3.1.2 Pump modulation

LDs can be electrically driven to obtain optical rectangular pulses of duration down to 10ns every 100ns, i.e. with a duty cycle of 10%. In order to prevent heat accumulation, the repetition rate is usually below 500kHz and the duty cycle around a few percent. Our laser diodes are mounted in 14 pins butterfly cases that are positioned in an ILX Lightwave laser diode mount equipped with an internal bias-T which enables the direct modulation of the output power with an arbitrary waveform generator from Agilent. When modulated, the rise and fall times of our LDs is limited to $\approx$ 5ns. This can be a problem when one wants to measure the emission spectrum around the laser threshold. Indeed, the spectrum is an average measurement of the emission by a cooled array of detectors over a certain exposure time. Depending on the pumping level, the emission intensity and wavelength might, more or less, vary due to the change of the pump intensity during the rise/fall time. This leads sometimes to artificial asymmetric spectrum broadening. However, this can be solved by increasing the pump pulse duration compared with the rise/fall times.

4.3.1.3 Sample Imaging

The imaging of the sample is used to coarsely position either the pump beam on top of the cavity or the single-mode fibres above the grating couplers. The sample can be imaged in reflection or in transmission depending on the camera (visible or IR) used .

In reflection, a white light source is sent on the sample using a removable mirror (RM1). The reflected light coming back from the microscope objective passes through a beam-splitter and

[3] i.e. the average absorption of the active layer

a lens in order to be focused onto a visible camera or on an IR camera. The "surface" image usually monitors a zone of approximately $300\times300\mu m^2$ around the cavity centre as can be seen on fig.4.12.

Because the major part of the sample is made of Si, the sample is imaged in transmission in the IR where this material is transparent. A mechanical arm is used to move the camera behind the sample. Fig. 4.12 shows IR pictures of a lasing cavity and of the grating couplers. The intensity of light exiting through the grating couplers is in this case much higher than the intensity imaged at the surface. Of course, these observations cannot be used to properly estimate the coupling efficiency between the cavity and the waveguide as the measured intensities depends on many parameters like the emission diagrams of the PhC and the gratings, the transmissions of the waveguide and the gratings or the numerical aperture of the objective. However, this is often a good start to roughly estimate the coupling efficiencies and to compare them in structures on the same sample having different geometries.

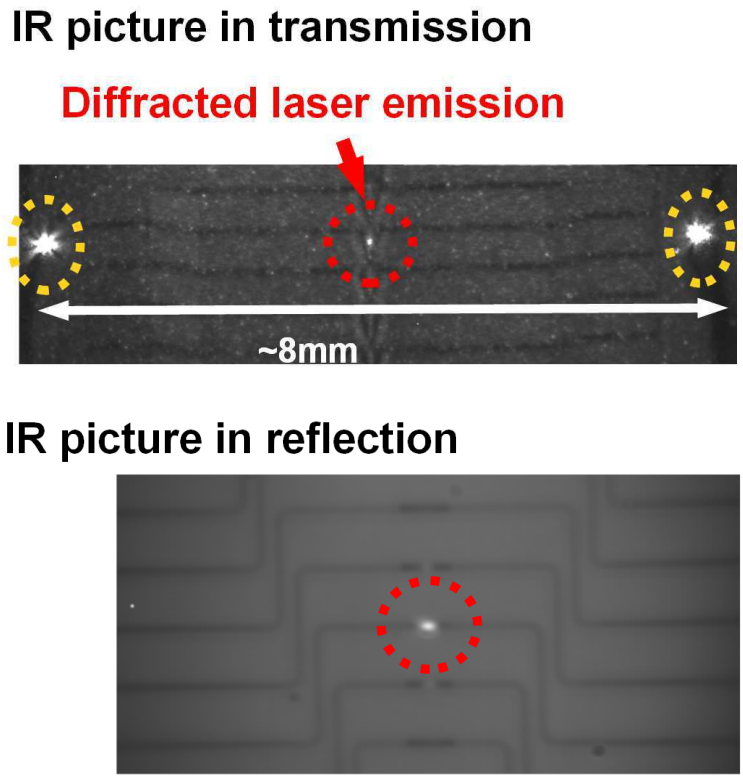

Figure 4.12: *Top picture: Panorama of IR pictures taken in transmission of a hybrid structure with a PhC wire cavity laser coupled to a SOI waveguide. The very bright spots at the end of each waveguide are the light diffracted by the grating couplers and attest for a good coupling efficiency. In comparaison, the collection, with our microscope objective of N.A.=0.26, of the laser light diffracted by the holes is much weaker. Bottom picture: IR image taken in reflection.*

4.3.1.4 Surface Collection

The PL is partly coupled to the continuum of radiative modes above the light line either by diffraction or by scattering due, for example, to surface roughness in the structure. The collection of the light is made through the microscope objective used to pump the material. The emission around $1.5\mu m$ then goes through the same optical path as the pump beam but is now transmitted by the dichroic mirror. The light is then sent towards a spectrometer, and measured by a cooled InGaAs detectors array of quantum efficiency η close to 70%. The spectral resolution with this spectrometer is around 0.06 nm.

4.3.1.5 Single Mode Fibre coupling with the SOI level

The remaining part of the PL is evanescently coupled with the waveguide as it will be described in the next chapter. The 220nm-thick SOI waveguide is single-mode in the TE polarisation when its width is below 700 nm. The propagating losses inside the waveguide are around 2-3 dB/cm [20, 205] for a waveguide width of 500 nm. The improvement of the SOI processing now enables to obtain the same order of losses with waveguide of width below 500 nm. Besides, slight variations in the fabrication can occur but the losses measured are always below 5 dB/cm. These losses must, of course, be taken into account to precisely quantify the light levels right under the cavity to retrieve, for example, the total power of laser emission coupled into the waveguide or to evaluate some light powers injected into the cavity as it is the case when we want to trigger some non-linear effects (see next chapter on optical bistabilty).

Light is then diffracted by the grating couplers [149] and coupled with cleaved single-mode fibres (SMF-28). The fibres are positioned with three mechanical actuators in the x-, y- and z-directions and one rotation stage to set the correct angles of fibres with respect to the sample. They can be positioned above the grating couplers with quite good alignment tolerances (losses $\approx$ 0.5 dB for 1 μm offset from optimal position) and with an angle with the sample surface around 10° to obtain the maximum coupling efficiency which is around 30% at the best. Remark, that further improvement in the coupling efficiency of SOI grating couplers has been achieved [206] in Ghent University reaching experimental coupling efficiency close to 70% over a 3 dB bandwidth of 80 nm.

4.3.1.6 Automation of the laser characterisation

The laser characterisation requires the measurement of the emission power over a wide dynamic range as we want to record the transition from spontaneous emission to stimulated emission to plot the S-shaped light-light curve. Thus we decided to use the spectrometer to detect the laser emission and the threshold because of:

- Its ability to give full spectral information
- Its ability to cover a very large dynamic power range as the exposure times can be varied by more than 6 orders of magnitude.

In addition, we decided to fully automatise the set-up in order to save measurement time and to increase repeatability. Combining fast automatic acquisition of the full spectra at different exposure times to the automatic variation of the pump power and to the automatic numerical fitting of the emitted power leads to :

- Instant access to the log-log S-shape response of emitted power versus the pump power
- Instant access to the variation of laser linewidth versus the pump power
- Instant access to Side Mode Suppression Ratio (SMSR) information

This automation is computer-controlled via a Python script. The Python routine controls the power of the pump beam via the calibrated rotation of a neutral density filter. For each incident power value, the routine registers spectra for several exposure times of the IR detectors array inside the spectrometer. The dynamic power range of the measurement is constantly reset in order to best match the detectors array response and to thus save measurement time. Consequently, several spectra are stored at each measurement step. Then all the spectra are sorted and numerically fitted by an IGOR PRO[4] script external to the Python script.

IGOR PRO is a commercial program for scientific data processing, like the other well-known program ORIGIN, which keeps all the loaded data in a single experiment file. One major advantage of IGOR PRO is that its scripting interface allows to develop home made scripts for the data processing. This is particularly useful in the day-to-day work to avoid as much as possible the repetitive tasks as simple as loading, fitting and plotting "by hand", but program those steps in scripts.

In this work, a script was written to extract the S-curves as well as the linewidth and emission wavelength variations with the pump level. It loads, fits the emission spectra with Lorentzian functions, and finally plots the results with an indication of the estimated threshold power.

In conclusion, this fully automated set-up allows several important improvements in the laser characterisation as it reduces the experiment time, thus reducing the risk of damaging or of misalignment of the pump beam (due to mechanical drifting, temperature, etc). With this set-up, it is then possible to characterise more lasers in the same amount of laboratory time. This is important in our case as we can process hundreds of different nanolasers on a single chip. The measurements are also more reliable as they are not investigator-dependent but are based on previous precise calibrations. Let's add that this set-up can be used to characterise any microcavity laser emitting in the same range of wavelengths.

4.3.1.7 Pump power considerations

In the following, we will express the pumping power either in terms of the external pump power P_{ext} or in terms of the absorbed pump power P_{abs}. They are related to each other by the following relation:

$$P_{abs} = \alpha_{\lambda} \sigma_S P_{ext} \tag{4.25}$$

[4] http://www.wavemetrics.com

α_λ is the absorption coefficient of the material at a given pump wavelength λ, σ_S is the surface overlap between the focused beam (of diameter $\approx$ 5-6 μm) and the PhC surface. This overlap is illustrated in figure 4.13. Typical value of σ_λ are between 7 and 10%. Considering an absorption α_λ of 10% and a σ_S of 10%, we see that 1 mW of external pump power focused on the sample corresponds to only 10 μW of absorbed pump power P_{abs}. Because we assume a quantum efficiency of 1, the totality of P_{abs} contributes to the previously defined pump injection power P_{inj}, i.e. $P_{abs} = P_{inj}$.

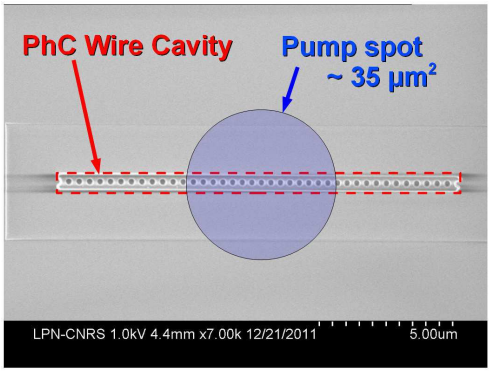

Figure 4.13: *SEM image of a PhC Wire Cavity with a superimposed spot of diameter equal to the waist of the focused pump beam.*

4.3.2 Characterisation measurements

4.3.2.1 Typical results

In this section, we present typical experimental data from the characterisation of PhC Wire Cavities coupled to a SOI photonic circuit.

Before going further in the description of the observed laser emission, it is worth to remark that the design parameters of the Gaussian apodised PhC wire cavity are usually adjusted to obtain single-mode frequency operation. In all what follows, the studied laser mode is always the lower wavelength mode, i.e. the first symmetric mode which has the highest calculated Q-factor, as it was presented in detail in chapter 2. Special care has to be taken with respect to the wavelength of the "second" mode, i.e. the first anti-symmetric mode, also of theoretical Q>500000, in order to prevent multi-mode operation. Indeed, with sufficient gain, this second mode may also lase, although with a different threshold power. With QWs, mode competition between the first and the second lasing modes can occur, leading to dynamical instabilities. For this reason, multimode operation would constitute a serious drawback to the device and is therefore not desired in this context. Usually, the first anti-symmetric mode is red-shifted of $\approx$ 25 nm with the main mode, and can potentially feel enough gain to lase, even sometimes for lower pump power than that of the main mode if the latter "feels" less gain. To prevent this, it is important to position the main mode close to the maximum of gain or even slightly red-shifted so that the first anti-symmetric mode will never have enough gain to perturb the main mode laser emission.

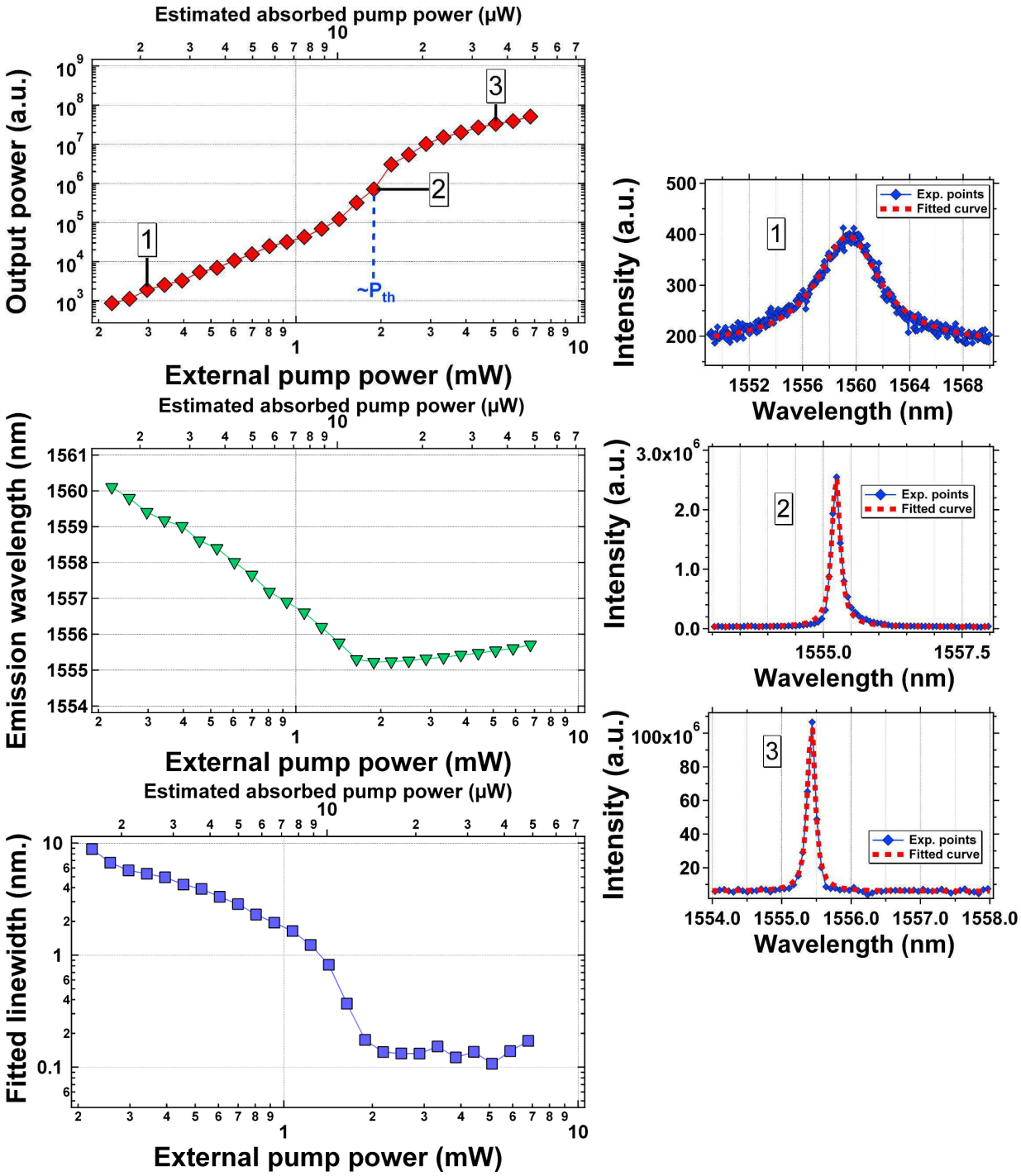

Figure 4.14: *Experimental data from the study of a hybrid III-V PhC Wire cavity laser/SOI waveguide. Left column: characteristics curves of the laser. The plotted graphs correspond to the output power (top), wavelength (middle) and linewidth (bottom) of the laser as a function of the injection pump power. Right column: Spectrum of the emission taken below (1), close to (2) and above (3) the estimated threshold pump power. The threshold corresponds to approximately 2 mW of external power and 15 μW of absorbed pump power.*

Figure 4.14 shows data resulting from the optical pumping at 1180nm of the PhC apodised Wire Cavity - embedding 4 InGaAsP/InGaAsP QWs - coupled to 500nm-wide SOI waveguide. Here the laser is operated in the CW regime. The PhC wire cavity was designed using a targeted FWHM equal to 2.64 μm, a central period a_0= 350 nm, a radius r= 110 nm and a wire width W= 525 nm, the two latter values being the ones written on the mask GDS file, slightly different from the ones effectively fabricated. In fact, one sees that these values take into account a calibrated 10 nm over-etching value. The bonding layer is assumed to be composed of 80 nm of BCB above the SOI waveguide, plus 300 nm of SiO_2. The top cladding is 1 μm of SiO_2. Note that we had to leave around 30 nm of HSQ above the wire, but this has little effect on the laser. The cavities were also surface passivated chemically so that they operate in CW regime (again, the process is described in the last part of this chapter). With passivated surfaces, the non-radiative carrier lifetime we measured is around 2 ns.

To retrieve the characteristic emission properties of the PhC laser under investigation, we measured many spectra of the laser coupled to the SOI waveguide as a function of the injection power, in order to reconstruct the expected S-shaped curve. Each spectrum is normalised with respect to its exposure time set on the spectrometer array detectors. Examples of the emission spectra are represented in the right column of graphs of the figure 4.14 showing three spectra (blue trace) taken below, close to, and above the threshold of the laser, with their Lorentzian fits superimposed (red dashes trace).

We used a Lorentzian function $\mathfrak{L}(\lambda)$ to fit each spectrum. It is written as

$$\mathfrak{L}(\lambda) = I_0 + \frac{2A}{\pi}\frac{\Delta\lambda}{4(\lambda - \lambda_{peak})^2 + (\Delta\lambda)^2}$$

where I_0 is the background noise level, A is the total area under the fitted curve, $\Delta\lambda$ is the linewidth[5] and λ_{peak} is the emission peak wavelength.

Well below the threshold, the emission spectrum (see the top spectrum noted (1)) is wide due to the absorption of the wells and fits perfectly with $\mathfrak{L}(\lambda)$. The S-curve of the PhC laser is constructed by plotting in log-log scale the values of A found for each spectrum versus the pumping power. We also extract from the fitted spectra the dependence of the emission wavelength λ_{peak} and the linewidth $\Delta\lambda$. In our experimental set-up, both of these measurements are limited by the spectral resolution of the spectrometer. Indeed, the separation between two pixels of the array detectors corresponds to a wavelength shift of 0.06nm, which means that it is not possible to resolve the emission wavelength for lower variations. Besides, above the threshold, the

[5] $\Delta\lambda$ is here the Full Width Half Max of the spectrum

measured spectrum is usually constituted of only 3 pixels because the linewidth pass beyond the resolution. As a consequence, it is not possible to retrieve the real linewidth from a Lorentzian fit of the emission above the threshold. This is illustrated in fig. 4.14 by the noisy plateau of the linewidth versus power graph.

The emission wavelength is, for the studied PhC wire cavity, close to 1.55 μm. As expected, the more carriers are injected in the laser, the more it blue-shifts and, around threshold, λ_{tr} is close to 1555 nm. Above the threshold, we observe that the emission wavelength is almost clamped around 1555 nm and even red-shifts moderately ($\delta\lambda=(\lambda-\lambda_{tr})<0.7$ nm at 3 times the laser threshold). This abrupt change in the slope of the wavelength shift versus the pump power is also a very good way of determining the laser threshold as it occurs because of the carrier density clamping at the laser threshold. The red-shift was not predicted by our model (see eq.(4.21) and fig. 4.7) but it is simply due to a slight heating of the sample. Indeed, a small variation of the heterostructure average RI n when the temperature is changed, can shift significantly the cavity resonance. In order to give an idea of the amplitude of this thermal shift, let's consider a regular Fabry-Perot cavity whose fundamental wavelength mode λ_0 is determined by the cavity length L and verifies the constructive interferences condition given by $L=\lambda_0/(2n)$. Under the reasonable assumption that the cavity length L does not vary with temperature, i.e. if we neglect material expansion/contraction effects, a variation of the RI will have to be compensated by a variation of the resonant wavelength λ_0, which is given by $\Delta\lambda_0=(\lambda_0/n)\Delta n$, in order to keep the constructive interference condition. Now, for InP, $\partial n/\partial T$ is around $2\times10^{-4}\ K^{-1}$ [207]. With this value, the wavelength shift for an elevation of the temperature equal to 1 °C is close to 0.1 nm/K in InP ($n_{InP}\approx3.17$). As a consequence of this dependence, the wavelength shift of the cavity resonance constitutes a very interesting probing parameter to measure the temperature inside the cavity, and is the basis of the experimental thermal study of the next part of this chapter. Of course, the sensitivity of the emission wavelength with temperature usually constitutes a serious drawback for a device as this induces some changes in the laser behaviour when the pump power is varied. These effects can be minimized by engineering the thermal environment of the structure as it is presented in the next part of this chapter, but also by engineering the III-V heterostructures emission[208].

Note that to prevent any degradation of the emission in the CW operation, we usually work with pump powers up to 10 times the laser threshold where no thermal roll-over was observed.

4.3.2.2 Impact of the mode FWHM on the laser threshold

We showed in chapter 2 that the value of the targeted FWHM of our design significantly modifies the photon lifetime in the cavity. This was illustrated in figure 2.35 which shows the obtained Q factors as a function of the FWHM of the mode. In order to measure the quality of our fabrication process, directly linked to the photon lifetime of the cavities, we fabricated a sample of PhC wire cavities whose FWHM, central period a_0 and radius r were varied. This sample was made by bonding the III-V epitaxial layer, sputtered with a 400 nm thick SiO_2 layer, on a silicon substrate also coated with a 1 μm thick SiO_2 layer, this to prevent evanescent coupling of the cavity with the substrate modes. The patterned mask contained several blocks of cavities, each one corresponding to a value of the FWHM, varied from 2.1 to 3.9 μm. Inside each blocks, a_0 and r were varied to be able to find an emission wavelength common to all the tested FWHM. This method holds as we showed that our optical design is very weakly affected in terms of Q-factor by variations of the central period or the holes radius.

Figure 4.15 shows the measured threshold pump powers when the FWHM of PhC Wire Cavities, here lasing around 1565 nm, is varied. The expected variation of the theoretical threshold power $(P_{inj})_{th}$, derived with the steady-state rate equations analysis, is also shown in fig. 4.16 for comparison. We also plot in this figure the Q-factors calculated with the FDTD simulations in chapter 2.

First of all, it is quite striking that the values of the laser threshold experimentally determined are of the same of order of magnitude than that of the model, i.e. around 10 μW. As it was previously shown, the theoretical variations of the threshold are expected to be extremely small above a certain value of Q, here close to few 10^4. Experimentally, the plot of the measured thresholds does not exactly reproduce a plateau. We attribute the variations in the plot to the presence of two unexpected values at the FWHM equal to 3.3 and 3.6 μm. The S-curve shapes of these cavities were however significantly different from the others and it could be that these cavities were not processed in the same way than the others. It is also possible that the focusing of the pump was not the same on all cavities, leading to different effective injection powers from one cavity to the other and could explain the observed variations. We can however remark that these discrepancies between the experiment and the model are small, though non negligible, for FWHM above 2.4 μm. The threshold for the smaller cavity (FWHM=1.8 μm) could not be measured as the cavity did not lase for the range of powers we used. This increase in the threshold seems in agreement with the numerical results. However, while the steady-state analysis predicted a change in the threshold by a factor 2 between the smaller and the larger tested cavities, here we could not observe the laser transition even after increasing the pump by a factor 7. Several parameters entered in the model could explain this differences such as additional losses due to the imperfect cavity fabrication, i.e. a change in the Q factor, or the gain value.

In conclusion, we see then that it is difficult to correlate the threshold values with the Q-factors, especially when we expect very high Q. An alternative solution, much more efficient, is to fit the entire S-curves with the rate equations. In [122], we showed how the Q-factors extracted

from such fit where close with the one found by 3D simulations of the TD PhC Wire Cavities, with Q below 20000. However, this method is in general very dependant on the precision of the numerous parameters involved and the number of variable to determine. In order to optimise it, we rewrote the rate equations, in the form presented in the first part of this chapter, with a smaller number of parameters. With this updated model, we will present in the next chapter the result of such fit, used to determine the cavity-waveguide coupling efficiency [117], and the estimated error bars associated with the method.

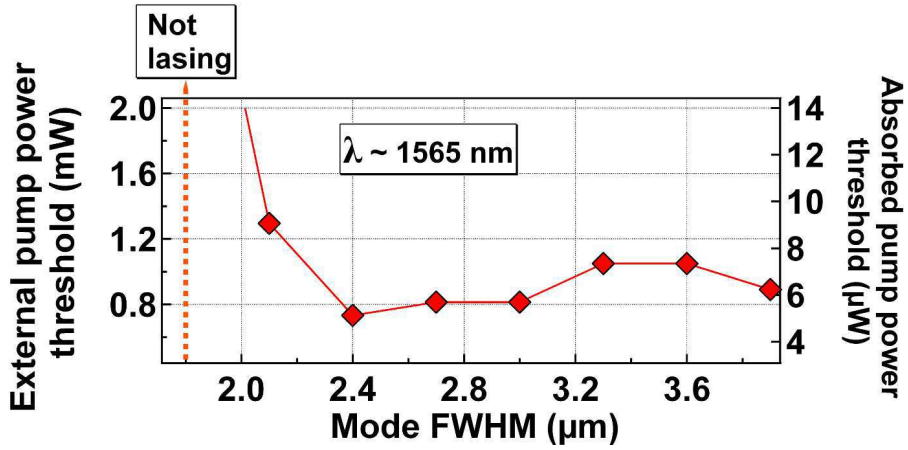

Figure 4.15: *Measured threshold pump powers of PhC Wire Cavities as a function of the targeted FWHM of the mode. The right axis shows the estimated absorbed pump power.*

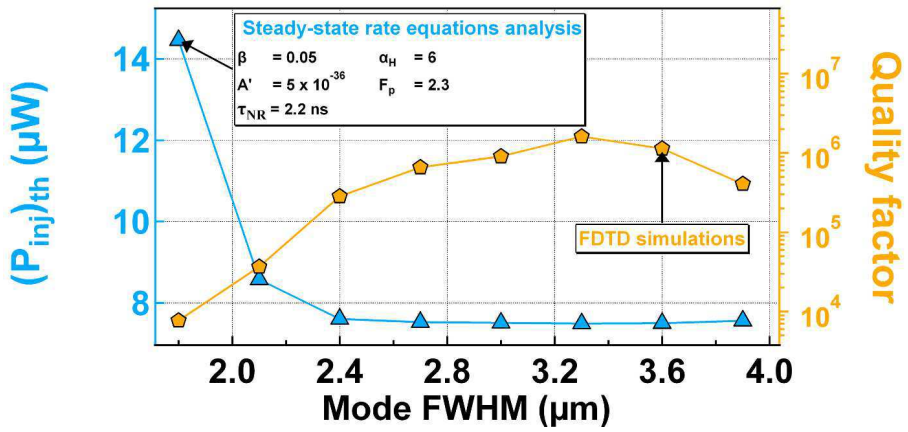

Figure 4.16: *Numerically found values of the threshold injection power $(P_{inj})_{th}$ as a function of the targeted FWHM of the cavity mode. The right axis plots the expected Q factors, extracted from fig. 2.35 .*

The achievement of stable CW laser operation of our PhCs embedding QWs was a major

challenge of this PhD. With this goal in mind, after conducting a thorough analysis of the different problems hindering this regime of operation, an extensive effort has been devoted in order to achieve it. Two specific issues emerged from this analysis: the heat sinking and the non-radiative surface recombinations. We will now detail the study of both issues which allowed to obtained the long desired CW operation with QWs structures.

To start, the following section will show how the optimisation of the heat spreading by an appropriate thermal management can improve the robustness of the laser.

4.4 Heat sinking engineering

The motivations of this study are multiple. The principal aim is to manage the heat sinking in the hybrid structures in order to potentially preclude damaging during CW pumping. Secondarily, good thermal management is necessary to maximize the temperature range of operation of lasers.

More generally, heat management is a critical aspect of the integration of nano-components, such as PhCs, in order to meet the requirements of applications in Si photonics.

4.4.1 PhCs issues

Bi-dimensional PhC lasers using QWs produce an important release of energy in the material through phonons. If the heat sink that constitutes the environment of the cavity is inefficient, the increase of temperature can be high and can have dramatic consequences for the structure. Indeed, an excess of heat can diminish the laser performances, in terms of output power and stability, and, in the worst case, totally and irreversibly kill the laser emission. Because of this reason, there exist only few demonstrations [159, 160] of CW lasing in 2D-PhCs air-bridge membrane embedding III-V QWs, but are however based on fairly sophisticated process. The fraction of the pump power that is lost in heat, the *thermal power*, does not get evacuated easily from the III-V suspended membrane. Therefore, the poor sinking leads to an accumulation of heat causing irreversible damages on the active material. Another difficulty that arises from the use of QWs is the creation of surface defects by the etching of the wells. This adds traps for carriers that shorten the carrier lifetime compared to the unpatterned case. As we saw in section 4.2.2, for a given set of parameters describing the laser, the decrease of the carrier lifetime leads naturally to an increased threshold, which in turn also increases the thermal power in the structure.

The origin of heat in the PhC is due to carriers, injected in the barriers by absorption of the pump, that relax non-radiatively by emission of phonons. We will see in the last part of this chapter what are the mechanisms of non-radiative recombinations and how it is possible to limit their effects. We have already seen in section 4.3.1.1 how it is possible to considerably diminish the generated heat by using a pumping wavelength very close to the gap energy E^B_{gap} of the barriers. In this way, the heat generated until the capture of carriers into the QWs, the *thermalisation process*, is minimized. Additional thermalisation of carriers occurs once in the well releasing an unavoidable amount of heat in the structure. Finally, a part of the produced

heat comes from non-radiative recombinations of carriers in the well, due, for instance, to surface defects.

Heat sinking in bi-dimensional PhC is not an easy task. The reason for this is that most environments that provide good optical confinement usually go hand-in-hand with a poor thermal spreading. This is the case of air-bridged PhCs where most of the heat generated in the membrane spreads in the semiconductor slab because the air cladding acts like a thermal insulator [209]. Several teams working on 2D-PhCs QWs laser[54, 210, 211] have however demonstrated the possibility of achieving CW lasing near $1.55\mu m$ by bonding the III-V layer on an appropriate heat sinking material such as sapphire, AlO_x or gold. The benefit in terms of heat spreading of using such stacks with InP-based PhCs containing QWs was experimentally characterised in [209]. Such study confirmed the importance of having specific heat dissipating paths for these nanolasers.

In the case of the hybrid structures, the poor heat dissipation of heat is mainly due to the presence of three thermal insulators around the cavity: the BCB bonding layer which has an extremely low thermal conductivity $\kappa_{BCB} = 0.29\ W/(K.m)$, the 2-$\mu m$ thick buried oxide layer ($\kappa_{SiO_2} = 1.4\ W/(K.m)$) and the air top-cladding. The purpose of this work was to develop an efficient stack of materials around the PhC that preserves the exceptional optical confinement but increases the heat sinking over the structure. Optical confinement considerations render impractical the use of sapphire or AlO_x (n≈1.7) on the III-V, while the presence of gold in the bonding layer must simply be forgotten for obvious reasons of transparency and absorption between the two optical levels.

From the point of view of thermal management, the use of PhC wire is not ideal as, against a membrane, the wire is surrounded by a cladding in 2 directions of the space, the worst case being, of course, the suspended wire. This can be seen as a drawback to the use of PhC wire cavity in the hybrid structure instead of "regular" bi-dimensional PhC membrane.

Hence, it is primordial to tackle the heat management issue in order to get the hybrid structure to the fore. Therefore, in order to find a solution to the heat sinking in the hybrid structures, we carried out numerical analysis to begin with and then tested experimentally hybrid structures with different spreading stacks around the cavities.

Several configurations were analysed:

- the suspended wire above the SOI (air cladding all around the PhC)
- the PhC wire with a BCB bonding layer and an air top cladding
- the PhC wire with a BCB+SiO_2 bonding layer and
  - ⟶ an air top cladding
  - ⟶ an SiO_2 top cladding
  - ⟶ an MgF_2 top cladding

The properties of those materials are summarized in table 4.2.

Material	Index	Thermal conductivity κ $(W/(K.m))$	Specific heat capacity C $(J/(kg.K))$
Si	3.46	130	700
InP	3.17	68	310
$InGaAsP$	5.25	5.25	331
BCB	1.54	0.31	21
SiO_2	1.46	1.4	730
MgF_2	1.38	14	1056

Table 4.2: *Thermal conductivities and specific heat capacities of different materials used in hybrid structures.*

4.4.2 FEM numerical analysis

At first, thermal properties of our structures were studied numerically using the Finite Element Method (FEM) tool COMSOL. The latter is a commercial software that allows to simulate the behaviour of a system through many physical aspects (mechanical, electrical, thermal, etc). Besides, it contains a pretty exhaustive material library with their associated properties. Of course, it is also possible to enter material parameters taken elsewhere, in literature or from other experimental calibrations.

In this study, FEM is used to determine the temperature distribution $T(x, y, z)$ in 3D inside a PhC wire cavity during laser emission.

Figures 4.17 show two views of a typical simulated hybrid structure. The simulated region is 14 μm in height and 40 μm × 20 μm laterally. The cavity is placed at 1 μm from the top of the simulated region because, *a posteriori*, most of the heat dissipates through the substrate and not through the top-cladding above the cavity. We take into account the presence of the SOI waveguide and, more importantly, the 2μm-thick oxide layer which acts as a major thermal insulator in the structure. The SOI waveguide is surrounded by a 300nm BCB layer and the total thickness of the bonding layer (i.e. the distance between the BOx and the III-V) is kept (in all simulations) to a value of 750 nm which is a typical value in real fabricated structures.

The PhC cavity is modelled as an InGaAsP PhC wire (505×285nm, r=120nm, a=350nm) because InGaAsP material represents more than 2/3 of the thickness of our III-V layer. The InGaAsP thermal conductivity used is $\kappa_{InGaAsP}$ =5.25 $W/(K.m)$. Inside the wire, the source of heat, a central volume 5μm-long (in red in fig. 4.17), produces a thermal power P_{therm}, thus imitating the cavity volume where heat is produced.

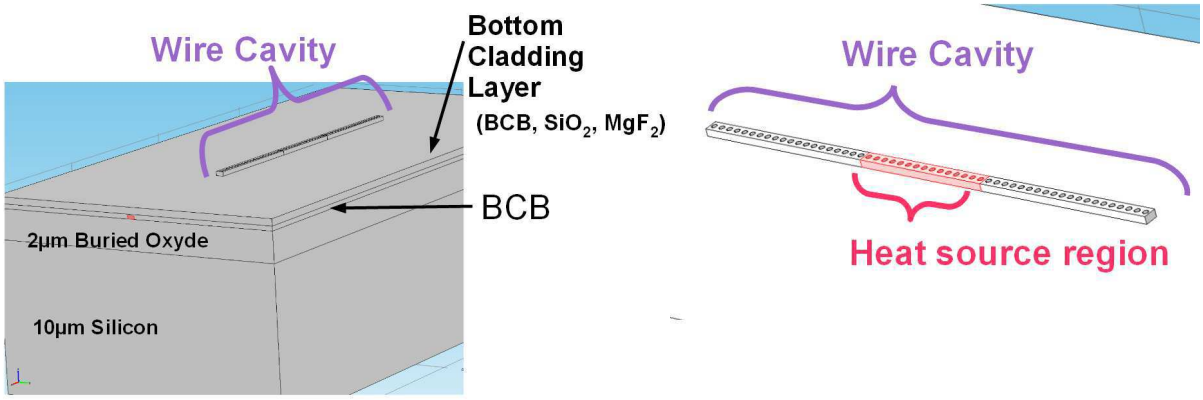

Figure 4.17: *COMSOL 3D representation of the hybrid structure. Left) . Right).*

The thermal power inside the cavity was taken between 100 and 900 μW, which is around one order of magnitude higher than the usual actual absorbed power by the active material around threshold. Thus, we simulate a laser operating much above threshold.

Numerical boundary conditions were set as follow:

- the thermal boundary conditions on the lateral edges were taken as thermally insulating. Indeed, several preliminary tests have shown that a very large fraction of the heat flow is passing through the Si substrate due to a very low thermal conductivity of the other surrounding materials composing the hybrid structure.
- the thermal boundary condition at the bottom of the simulation region (i.e. in the silicon substrate) was set to be a fixed temperature (room-temperature).
- the thermal boundary condition at the top of the simulation region (i.e. in the top cladding layer) was also taken as insulating[6].

4.4.2.1 Case of the suspended PhC nanobeam

Because many 2D-PhC structures are suspended membranes, it is interesting to analyse the behaviour of a PhC wire cavity suspended in the air, forming a so-called *nanobeam*. Figures 4.18 show two cross-sections (top view and transverse cross-section view, both passing through the middle of the cavity) of the temperature distributions calculated in the steady state regime in the case of P_{therm} =100 μW.

For this power, we observe that the elevation of temperature ΔT at the centre of the cavity is around 100 K. We observe on the top view that the zone where the temperature elevation is visible is almost the same as the zone where the heat is produced. On the other hand, the cross-sectional view shows that the increase of temperature is quite important above the cavity.

[6]Tests with a convective air model gave similar results.

Such distribution appears because heat flows mainly along the wire but not efficiently enough to diffuse in the region around the cavity. Note that the distribution of temperature is not symmetric in the vertical direction which means that a significant fraction of heat flows through the 450nm-thick layer of air below the cavity and through the BCB layer. However, this heat spreading is quite inefficient and does not prevent the important observed heat rise.

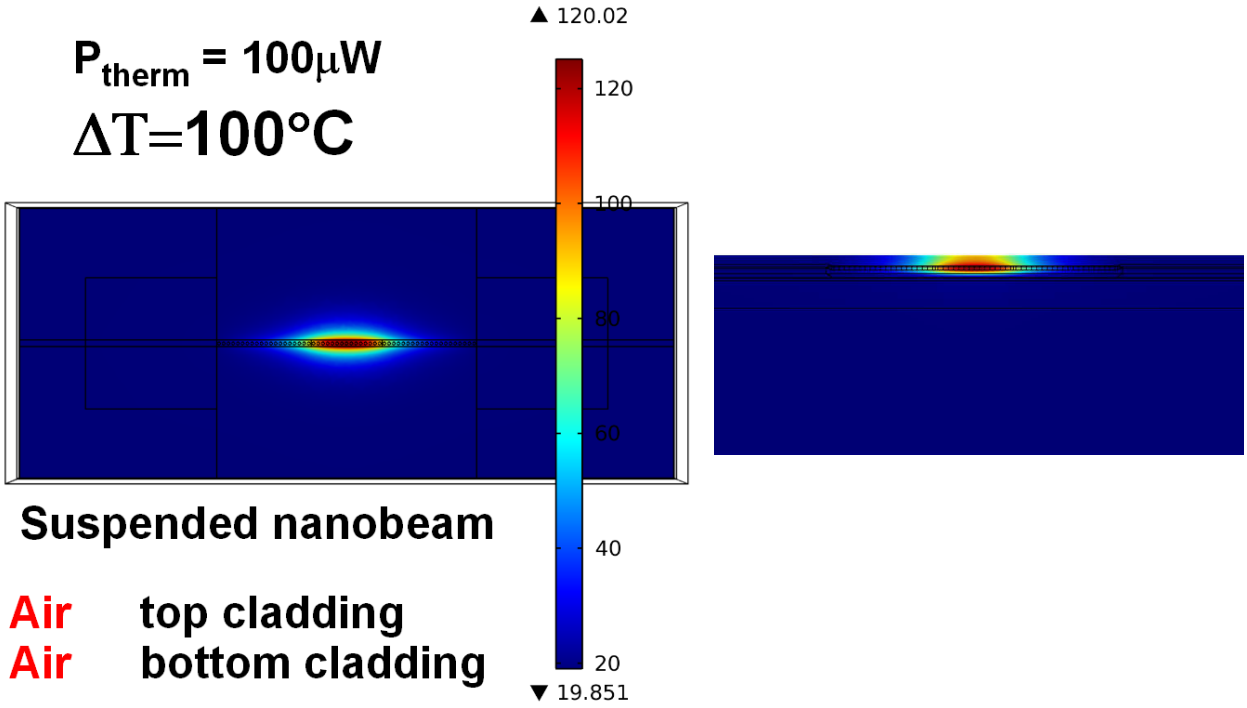

Figure 4.18: *Temperature distributions view in the case of a PhC nanobeam suspended in air. Left) Top view of the distribution in a plane passing*

4.4.2.2 Bottom cladding layer optimisation

We will now investigate the behaviour of a PhC wire cavity in a hybrid structure, therefore bonded with a BCB polymer layer above a SOI waveguide. This case is obviously more favourable to the spreading of the heat although the thermal conductivity of BCB is very low ($\kappa_{BCB} = 0.29$ $W/(K.m)$).

Figures 4.19 show the temperature distributions for different bottom cladding. The two top pictures show the case of a 750 nm-thick BCB bonding layer. The elevation of temperature is 30 K, much lower than in the suspended case.

Here we investigate the possibility of improving the heat evacuation through the bottom-cladding [7], hence keeping air above. Therefore, we introduce into the bottom-cladding a layer of silica to replace as much as BCB as possible above the waveguide. Experimentally, we are able to spin-coat ≈300nm of BCB on the 220nm-high Si waveguide so only ≈80nm separates

[7] which we have been referring as the the bonding layer until now.

the III-V from the rest of the cladding layer. In consequence, we chose to insert numerically 450nm of SiO_2 and to compare the thermal behavior with the bottom cladding of same thickness composed only of BCB.

The result of this structure is shown in the same scale in fig. 4.20. Again, the increase of temperature is smaller compared to the full BCB case, being only 11 K.

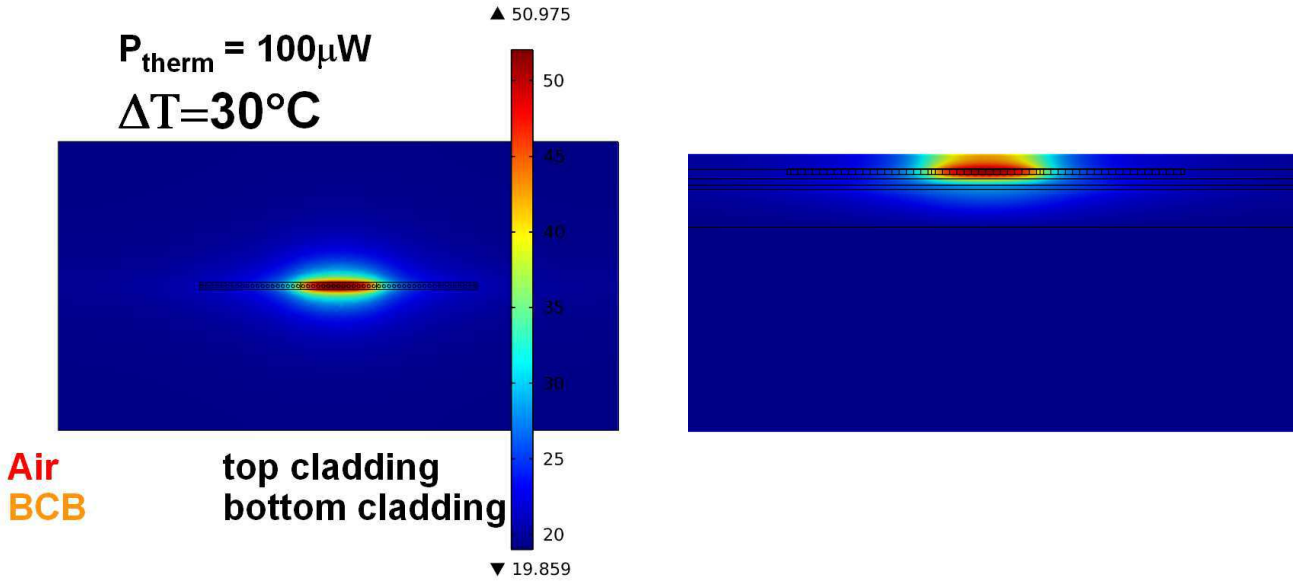

Figure 4.19: *Temperature distribution in the hybrid structure with a BCB bottom-cladding layer.*

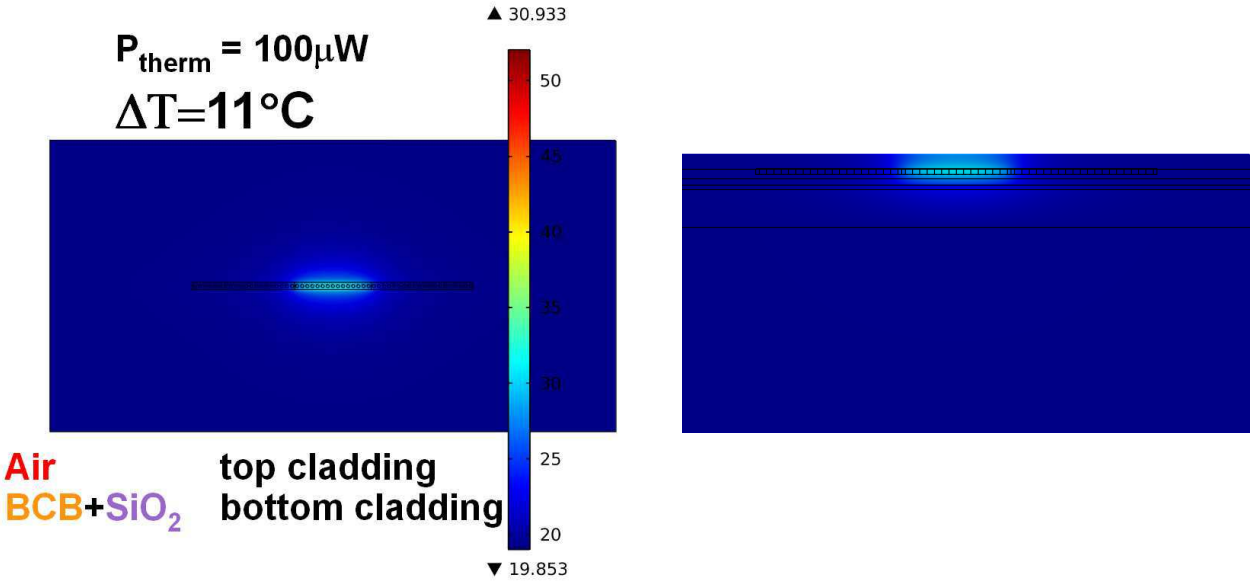

Figure 4.20: *Temperature distribution in the hybrid structure with BCB and silica bottom-cladding layers*

With this result we went on to improve the heat sinking by evaluating numerically the effect of a top-cladding.

4.4.2.3 Top cladding layer optimisation

In order to increase the heat sinking, one way is to replace the air surrounding the upper and the side part of the cavity by a material with higher thermal conductivity.

Encouraged by the positive result of the improvement obtained by the bottom-cladding using SiO_2, we encapsulated the cavity either with SiO_2 or better still with a material of higher thermal conductivity and lower RI: MgF_2. Figures 4.21 and 4.22 show the result of the simulation. The improvement is clear in both cases as the temperature elevation are equal to 6 K with SiO_2 and only 2 K with MgF_2.

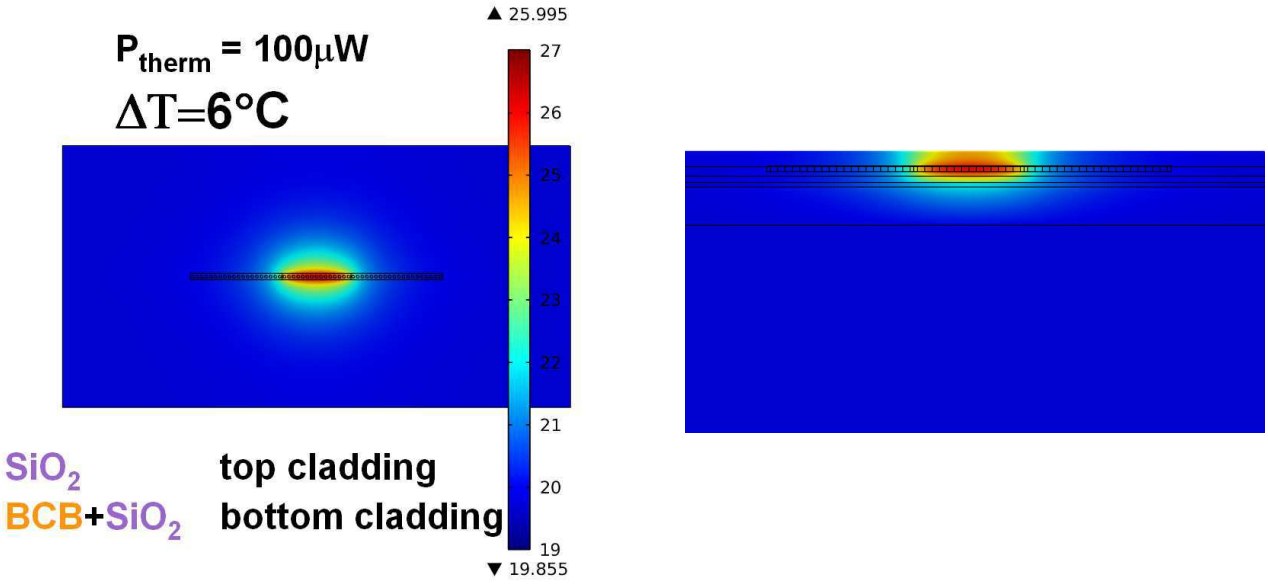

Figure 4.21: *Temperature distribution in the hybrid structure with BCB and silica bottom-cladding layers, and 1µm-thick silica top-cladding layer.*

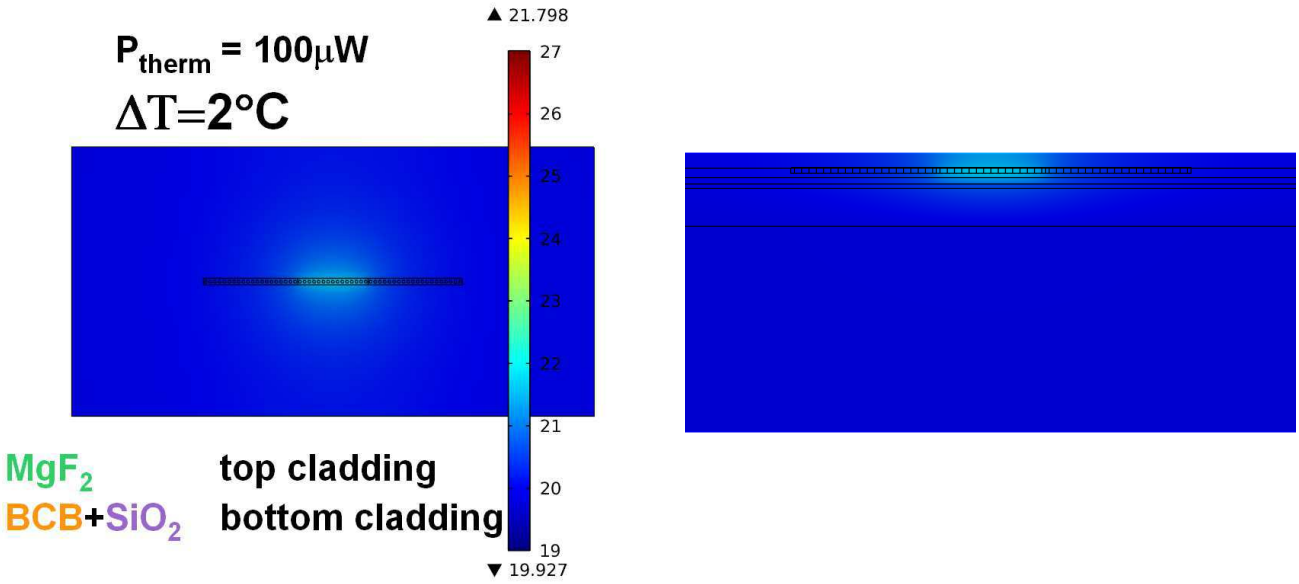

Figure 4.22: *Temperature distribution in the hybrid structure with BCB and silica bottom-cladding layers, and 1µm-thick MgF_2 top-cladding layer.*

4.4.2.4 Thermal resistivity

In order to compare all the stacks which were designed, it is useful to retrieve the thermal resistivity (or impedance) R_{th} for each configuration. The thermal resistivity R_{th} is the variation of the temperature as a function of the variation of the thermal power inside the system. It is then expressed as:

$$R_{th} = \frac{\partial T}{\partial P_{therm}} \qquad \text{in } K/mW$$

To retrieve its value for every case, we repeated the simulations in the steady-state for the thermal power ranging from 100 μW to 900 μW. Figure 4.23 shows the linear dependences of the elevations of temperature ΔT as a function of the thermal power P_{therm}. The slopes give directly the thermal resistivities. We see that the worst case is logically the suspended wire which shows R_{th} =720 K/mW. The addition of a BCB substrate below the cavity decreases the thermal resistivity of the structure by more than a factor of 2 as R_{th} = 304 K/mW. The effect of the replacement of 450 nm of BCB by SiO_2 in the bottom-cladding is also quite impressive as R_{th} is now only 110 K/mW. Finally, we arrive at values of 61.5 and 19.5 K/mW for cavities encapsulated respectively by SiO_2 and MgF_2.

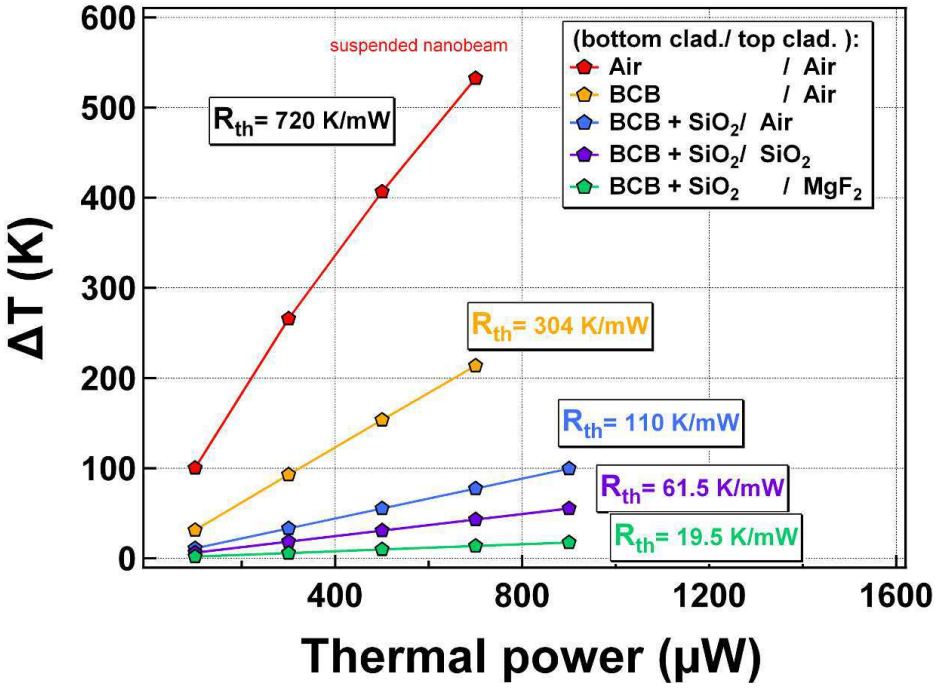

Figure 4.23: *Simulated elevations of the temperature, for all the considered stack of materials surrounding the cavity, as a function of the thermal power injected in the center of the cavity*

All in all, we've seen that by modifying the environment of a PhC wire cavity with materials compatible with strong optical confinement, it is possible to reduce the thermal resistive by a factor of 35!

In the next section, we describe in detail the experiment used to retrieve the variations of the thermal resistivities from one structure to the other.

4.4.3 Thermal resistivity measurements

4.4.3.1 Principle

The principle of the experiment is to optically probe the temperature elevation in the PhC wire cavity laser by monitoring the emission wavelength as a function of the pump power P, the goal of this experiment being of course to retrieve the apparent thermal resistivity $\tilde{R_{th}}$. The emission frequency is simply given by

$$\omega(N,T) = \omega_{tr}(T) + \frac{1}{2}\alpha_H G_0(T) \ln\left(\frac{N}{N_{tr}}\right) \tag{4.21}$$

where N is the carrier density and T is the temperature of the cavity.

Figure 4.24 illustrates the direction of the shift in the emission wavelength depending on the increase or decrease of the RI. RI variations are due to variations of the carrier density and of the temperature. If the carrier density increases or if the temperature decreases, the RI is diminished and the resonant wavelength "blue-shifts" towards the shorter wavelength. On the contrary, if the carrier density decreases or the temperature increases, the RI is increased and the resonant wavelength "red-shifts" towards the longer wavelength.

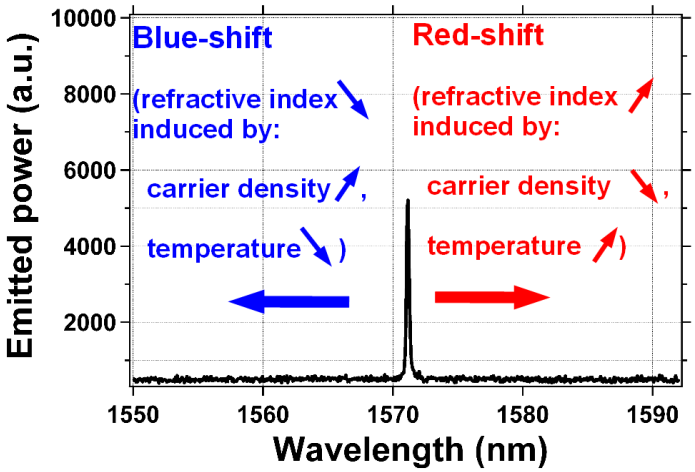

Figure 4.24: *Basic rules for the cavity wavelength shifts.*

Now, in this experiment, the variation of temperature ΔT as a function of the pump power P is achieved by measuring the emission wavelength above the laser threshold. Indeed, as we saw when we solved the laser rate equations (section 4.2.2), the carrier density is almost clamped for carrier injection rate higher than the threshold. So in this situation, the variation in the emission wavelength will be induced almost solely by the sample temperature

Two steps are necessary for each measurement: firstly, a calibration step carried out in an operating regime where the cavity does not heat under the influence of the pump and links the emission wavelength to the sample temperature. Secondly, the emission wavelength is measured as a function of the pump power in a regime where the cavity heats. The combination of the two dependences enables the measurement of ΔT versus P.

4.4.3.2 Set-up

Figure 4.25 shows the μPL set-up used to control the pumping power and the temperature of the sample. The pumping method is the usual pumping scheme described previously. However, here the laser is pumped only by short optical pulses with different duty-cycles that modify the amount of heat released in the structure.

The temperature is controlled by a Peltier cell that is biased positively or negatively in order to heat or cool the sample. The copper holder insures that the variation of temperature is accurately transferred to the sample. A platinum temperature sensor is used to read-out the temperature of the copper holder.

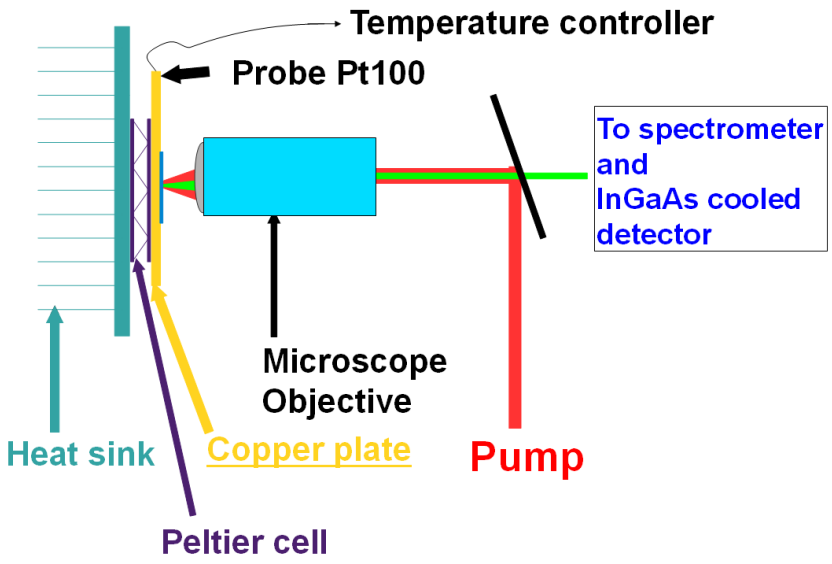

Figure 4.25: *Experimental set-up for the temperature elevation probing.*

The first step is to calibrate the emission wavelength as a function of the temperature of the sample. During the calibration, we assume that the pumping induces negligible heating in the sample and the emission wavelength shifts are solely induced by the temperature variations of the environment. This change is induced when we pump the cavity with square pump pulses of 40 ns duration every 4 μs which is a longer time than the usual thermal diffusion time in III-V PhCs [209], even in the case of a suspended membrane. This pumping scheme with a low-duty cycle is illustrated in fig. 4.26.

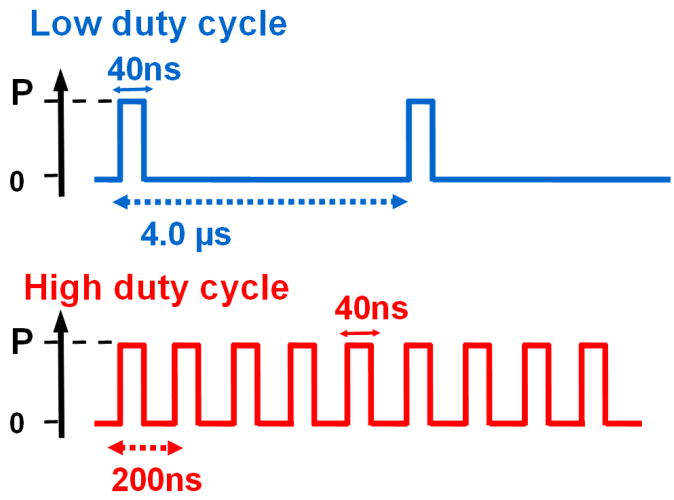

Figure 4.26: *Experimental pumping duty-cycles. The elevation of the average temperature of the sample may be neglected in the low duty-cycle scheme.*

The laser must be pumped above threshold for any temperature we choose. When the temperature increases, the differential gain decreases and, to a lesser extent, the transparency density increases. The consequence of these effects is the increase of the laser threshold at higher temperature. The requirement of the method is to operate the laser at the same carrier density so that the wavelength variations reflects effectively variations of temperature in the cavity through the RI and not a variation of the carrier density induced by less gain. Thus, we start by setting the experiment at the highest temperature of the explored range. A characteristic L-L curve is measured and an injection level above the threshold is set. Then, the temperature is decreased which has for consequence the increase of the differential gain and reduction of the laser threshold. To keep the same carrier density set for the initial temperature, the pumping level is adjusted (decreased) to obtain the same emitted light level. Then, for each temperature, we measure the emission wavelength and plot it like in figure 4.27. We see that $\lambda(T)$ varies linearly with T. The measurements show that $\frac{\partial \lambda}{\partial T}$ is always close to $0.1nm/K$.

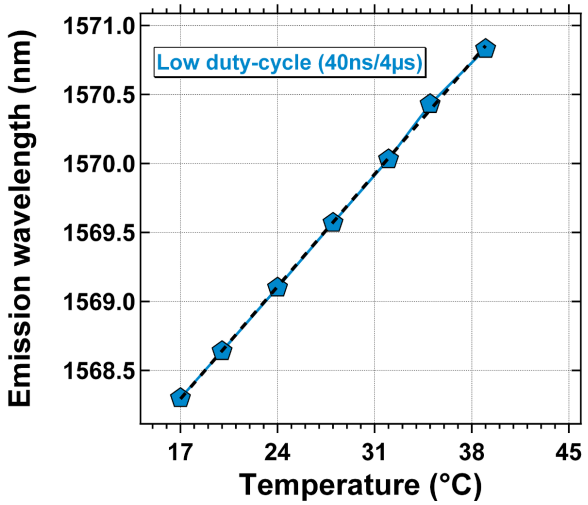

Figure 4.27: *Calibration step: plot of the emission wavelength of a PhC laser above threshold as a function of the temperature. A linear fit gives* $\frac{\partial\lambda}{\partial T} \approx 0.1nm/K$.

Once the calibration done, we set the temperature of the sample in the range where we calibrate the shift with temperature. At this temperature, two light-light curves are taken: one in the low duty-cycle and one in the high duty-cycle, like in fig. 4.28 (measurements from the structure with a MgF_2 top-cladding). The two slopes $\left(\frac{\partial\lambda}{\partial P}\right)_L$ and $\left(\frac{\partial\lambda}{\partial P}\right)_H$ are respectively the slopes in the low and high duty-cycle above the threshold. Then, the apparent thermal resistivity is the given by:

$$\left(\frac{\partial T}{\partial P}\right) = \frac{\left(\frac{\partial\lambda}{\partial T}\right)_L - \left(\frac{\partial\lambda}{\partial P}\right)_H}{\left(\frac{\partial\lambda}{\partial P}\right)_L} \tag{4.26}$$

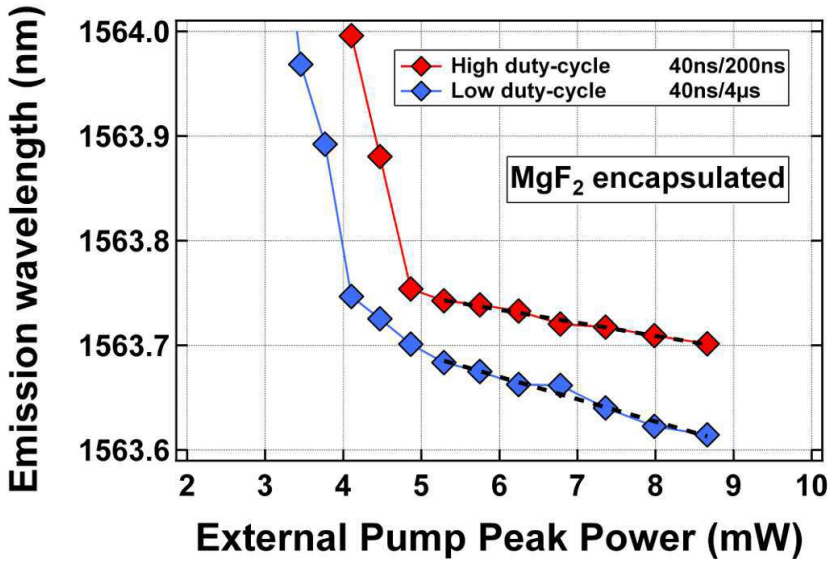

Figure 4.28: *Second step: plot of the emission wavelength above threshold as a function of the pump power. In the case of the MgF_2 top-cladding, the linear fit of the two curves give* $\left(\frac{\partial\lambda}{\partial T}\right)_L$*=-0.0031 nm/mW and* $\left(\frac{\partial\lambda}{\partial T}\right)_H$*=-0.0018 nm/mW*

It is important to realize that the thermal resistivity measured through this method is only the *apparent* thermal resistivity as the pump power P considered is usually very different from the actual thermal power that is generated in the structure after absorption. Here, the mW unity correspond to the external pump power P. To compare those numbers with the FEM simulations, instead of the measured values of thermal resistivities, we will compare the ratio of thermal resistivities in both cases (instead of trying to estimate the real thermal power generated in the material).

4.4.3.3 Results for different heat spreading stacks

Measurements, corresponding to all the cases which were simulated, were carried out on 4 kinds of heat spreading stacks in hybrid structures:

- structures with a BCB bonding layer and an air top cladding
- structures with a BCB+SiO_2 bonding layer and an air top cladding
- structures with a BCB+SiO_2 bonding layer and an SiO_2 top cladding
- structures with a BCB+SiO_2 bonding layer and an MgF_2 top cladding

4.4.3.3.a Bottom-cladding layer

Figure 4.29 shows the elevation of temperature plotted as a function of the external pump peak power for PhC cavities bonded on SOI with two differents bottom-cladding layers: one consisting

of ≈ 750nm of spin-coated BCB and the other consisting of 300nm of BCB (i.e. 80nm above Si waveguide) plus 450nm of SiO_2. We observe experimentally that the temperature shifts is higher in the case where only BCB is used. The apparent thermal resistivities that we found are 1.55 K/mW for the BCB only stack and 0.56 K/mW in the case of a BCB+SiO_2 bottom-cladding.

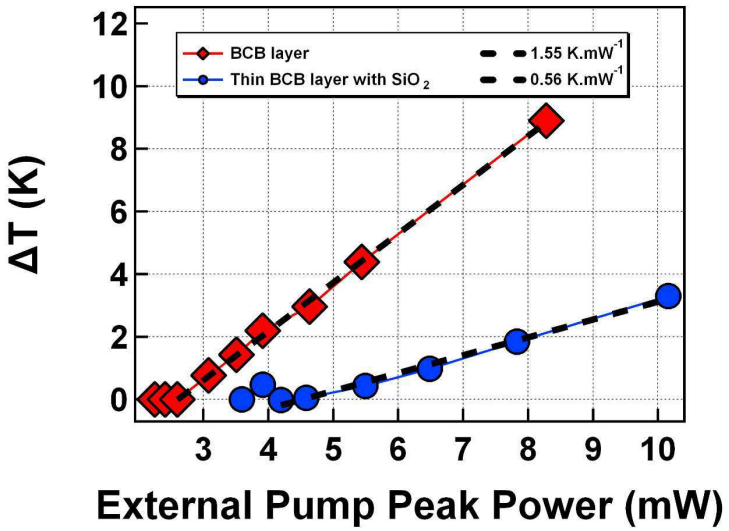

Figure 4.29: *Experimental value of temperature elevation as a function of the external peak pump power in the case of a PhC wire cavity with an air top-cladding and with a bottom-cladding of BCB-only or of BCB and SiO_2.*

Experimentally, the ratio of the thermal resistivities of BCB-only over the optimized BCB+SiO_2 bottom-cladding is 1.55/0.56 ≈ 2.8. This is in total agreement with our numerical simulation results where the ratio 304/110 gives also a result of ≈ 2.8.

4.4.3.3.b Top-cladding layer

Next, we fabricated hybrid structures using the BCB+SiO_2 bottom-cladding and added to this a top-cladding to the cavity instead of air. Here, we used the PhC cavities with gaussian field profiles presented in chapter 3. Remark that in those designs we took into account the cladding of the III-V cavity made of low-RI material like SiO_2.

Figure 4.30 shows the rise of temperature in the case of a cavity with and without encapsulation in a SiO_2 matrix. The improvement in thermal sinking is clear and the resistivities ratio is here of 1.54. This is to be compared to numbers shown in figure 4.23 which give a ratio of 110/61.5 ≈ 1.8. This is again in agreement with the numerical simulations, though the difference between experimental and numerical study are much more significant than for the cases presented previously. A similar result appears in the case of a cladding with MgF_2 cladding as shown in figure 4.31. The apparent thermal resistivities for the MgF_2 encapsulation is R_{th}= $0.15K/mW$, giving a ratio of 3.6 which is a bit lower than the expected ratio found numerically. We explain this difference by two uncertainties concerning the MgF_2 layer. One has to do with

the extent of the PhC hole filling by MgF_2 during the evaporation. Indeed, if MgF_2 does not fill completely the holes, the heat sinking through the hole's edges will be less efficient and lead to a greater overall thermal resistivity. The other unknown in this material is its porosity, which can affect significantly the thermal conductivity, like it was seen in SiO_2 layers obtained by different processing techniques (PECVD, sputtering, oxidation).

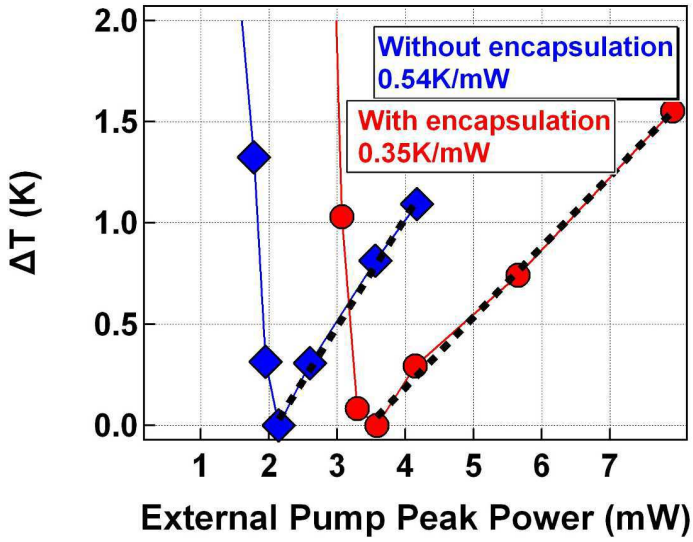

Figure 4.30: *Increase of temperature ΔT in the cavity as a function of the external pump power in the case of a PhC Wire Cavity with and without the 1 μm thick SiO_2 top cladding layer.*

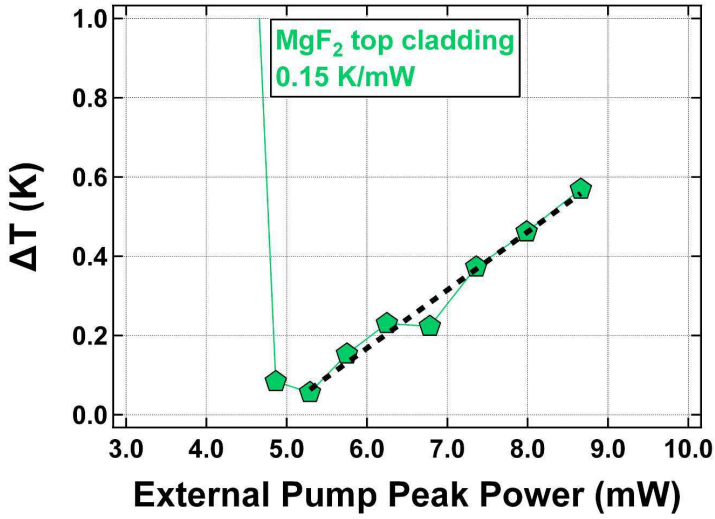

Figure 4.31: *Increase of temperature ΔT in the cavity as a function of the external pump power in the case of a PhC Wire Cavity with a 1 μm thick MgF_2 top cladding layer.*

4.4.4 Test in continuous-wave operation

The outstanding thermal behaviour of the heat sinking stack studied in this work led us to test CW operation by pumping at 1180 nm a PhC wire cavity encapsulated with 1 μm-thick MgF_2 top-cladding layer. One important point is that the QWs were not passivated in this sample. Below the laser threshold, we noticed that the emission intensity increased when the pump was increased, and did not diminish quickly as it in the case in other non-encapsulated structures. By increasing more the pump power, we observed all the characteristic variations which usually accompany the laser emission (non-linear increase of the emission, decrease of the linewidth, etc) as it is illustrated in fig. 4.32.

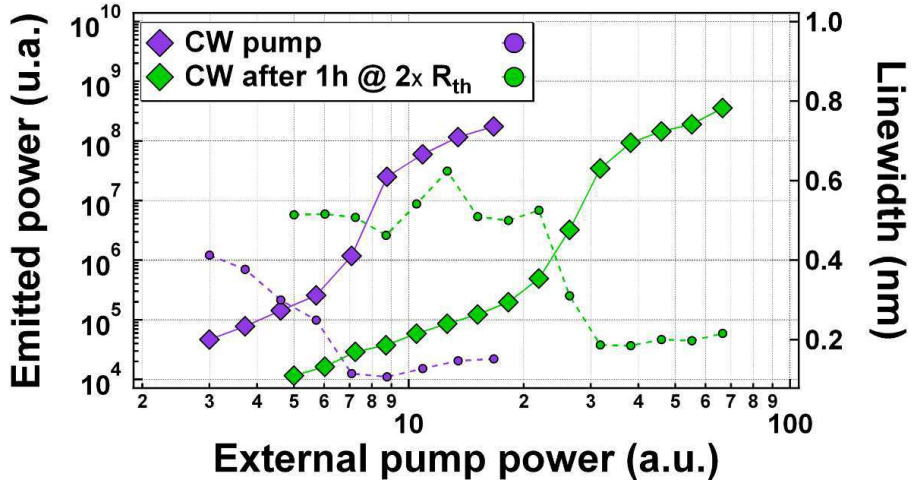

Figure 4.32: *S-curves from a hybrid structure with a top-cladding of MgF_2. The purple data points are taken in CW pumping. A second measurement is taken after the PhC laser is pumped continuously for a duration of one hour at twice the threshold power.*

Despite this other proof of the excellent thermal sinking, the behaviour of these PhC lasers has not proven to be stable with time. Indeed, we observed that the emission slowly but surely decreases after a few tens of minutes. Figure 4.32 shows the modification of the S-curve after letting the cavity operate in CW at twice the threshold for one hour. Despite the laser still works, its threshold was multiplied by more than a factor 3 and would have kept on increasing if we let the CW pump switched-on. Eventually, we observed that the emission almost completely vanished by pumping for an even longer time. Note that this is due to a real damaging of the sample as it is not reversible, and that the laser emission is impacted even when we go back to a low-duty cycle pumping scheme. Kim et al. in [212] also observed slow damaging of InGaAsP QWs-PhC band-edge laser surrounded by MgF_2 layers above a highly thermal conductive CVD diamond layer. By pumping their laser close to the threshold, they showed that their laser emission diminished by a factor 2 after 8 hours but eventually disappeared completely after

18h. They also claim that their damaging process is not completely irreversible as they observed laser emission on the same sample a few days later. In comparison our damaging at twice the threshold was much faster and irreversible.

The mechanism of damaging has not been investigated during this PhD, but we suspect the apparition of localised hot-spots at the surface of the III-V structures. Indeed, this would be compatible with the results of our other study using surface passivation of the QWs to obtain stable CW laser emission.

4.5 Surface passivation for CW operation

4.5.1 Non-radiative carrier recombination process

Non-radiative carrier recombinations are an important source of heat in III-V semiconductor nanostructures and therefore imply a decrease of the radiative efficiency. They result from three recombination processes [180]: *defect recombination*, *surface/interface recombinations* and *Auger recombination*.

Auger recombination arise from carrier-to-carrier collisions: one carrier recombines non-radiatively and the other gains the energy given by the other. The recombination rate varies in

$$R_{Auger} = CN^3$$

where C is the *Auger coefficient*.

This process can play a dreadful role in laser applications, leading sometimes to irreversible damage of the laser. Fortunately, in InGaAs(P) materials and for wavelength around 1.55 μm, C is low (typically 10^{-29} cm^6/s [213]). For instance, at a transparency carrier density of 10^{18} cm^{-3}, the Auger recombination lifetime $\tau_{Auger}(N_{tr}) = (CN_{tr})^{-1}$ is then higher than 10ns. Because the carrier density at the laser threshold has a value almost constant regardless of the pump power, this lifetime value stays for our cavities of the order of its transparency density value. For these reasons, Auger recombination can be neglected compared to the others processes.

Defect recombination refers to non-radiative recombination on deep defect and impurities in the crystalline structure of the semiconductor. The lifetime associated with defect recombination is independant of the carrier concentration. In the case of III-V PhC, this mechanism is also very weak compared to surface recombination.

Surface recombination is the major source of non-radiative carrier recombination inside the III-V QWs. This is particularly true in PhC where holes etched in the slab increase the surface-

volume ratio compared to a classic ridge structure. Moreover, the typical dimension associated to the PhC structuration (100nm) is well below the diffusion length of the carriers during their lifetime (for instance, considering a surface recombination velocity $v_{SR} = 1,2 \times 10^4 cm/s$ [214] and a carrier lifetime of $5ns$ gives a diffusion length $L_D \approx 600nm$). The increased amount of QWs surface exposed to the environment contains usually a large density of surface defects composed of dangling bonds of the etched materials. The effects of the increased surface and the λ-scale structuration on surface recombination rate has been investigated at LPN by measuring carrier lifetime (see fig.4.33) on InP-based mesas containing 4 InGaAsP/InGaAs QWs that we also used as active material for PhC lasers. Those measurements have shown that the carrier lifetime goes from around 1ns for mesas of diameter 10 μm down to a lifetime around 200 ps for mesas of diameter 400nm. These results illustrate the effect of the increased surface-volume ratio as it happens in PhC where holes diameter are typically 250nm.

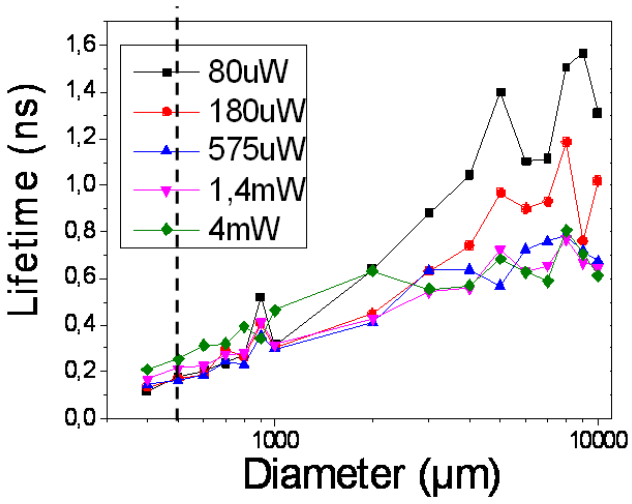

Figure 4.33: *Carrier lifetime as a function of the mesas diameter, for several pump powers. Measurements carried-out at LPN, by Virginie Moreau and David Elvira.*

Other measurements using a different technique were already carried out on InGaAs mesas more than 10 years ago by Boroditsky et al.[215]. Similarly to the recent LPN measurements, the non-radiative recombination rate increased as a function of the exposed surface, and was very dependant on the surface state (see fig.4.34). Different etching process as well as surface passivation proved to significantly modifies these rates.

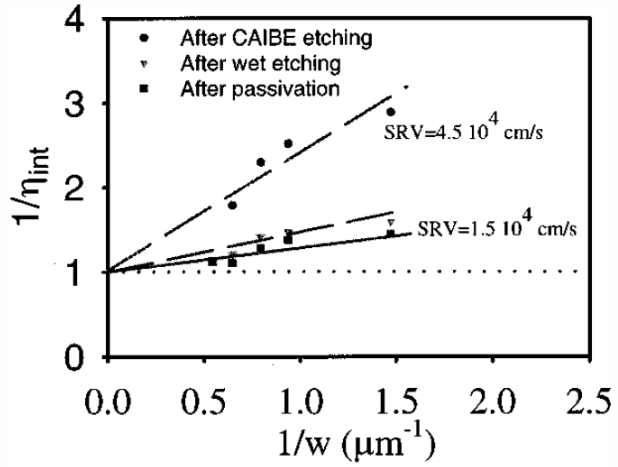

Figure 4.34: *Inverse of the radiative quantum efficiency η_{int} as a function of the inverse width of a rectangular InGaAs mesas. The surface recombination velocity (SRV) depends on the surface states. A low non-radiative recombination rate can be achieved through "gentle cleaning" and surface passivation. From 4.34.*

4.5.2 Principle

Surface passivation refers to the removal of the surface defects, accountable for a large part of non-radiative carrier recombinations, followed by their covering. Indeed, once removed, surface defects, present as dangling bonds, are usually replaced by another species to avoid the return of carrier traps. This effect is called *surface passivation*.

Surface recombination activation often occurs during the plasma etching process due to specy or by-product implantation on the etched sidewalls.

The main steps of the passivation process were developped [216, 217] in 1987 at Bell Communications Research for passivation purpose of GaAs. First, $H_2SO_4 : H_2O_2 : H_2O$ at a ratio 1:8:500 was used as a chemical etchant to remove the surface defects. Then a solution of ammonium sulfide $(NH_4)_2S$ solution was used to create the passivation layer on top of GaAs. The passivation layer is in fact created by the sulfur atoms in the $(NH_4)_2S$ solution that recover the bonds and fill the defects. Oigawa et al. [218] showed that, in addition to the passivation layer formation, the $(NH_4)_2S$ solution begins its effect by etching a bit of the III-V surface. For instance, for InP, at 45°C, the etching rate that is given is around 20 nm/h.

For our InP-based PhCs embeding InGaAsP/InGaAs QWs, we used datas from [215] that specifically examined the passivation effect on InGaAs. The process we used is presented in figure 4.35. Before encapsulating the cavities, we first etched the PhCs with a $H_2SO_4 : H_2O_2 : H_2O$ solution at a ratio 1:8:5000 for 10". Then, the sample is put in a bath of $(NH_4)_2S$ solution at 45°C

for 10'. To prevent further reoxydation of the passivated layer, the sample is then spin-coated with a BCB:Mesitylene solution (1:10) that was calibrated to fill completely the PhC holes. In this way, we ensure the stabilisation of the passivated surface. Finally, an encapsulation top-cladding is deposited to enable the increased heat spreading described in the previous part of this chapter.

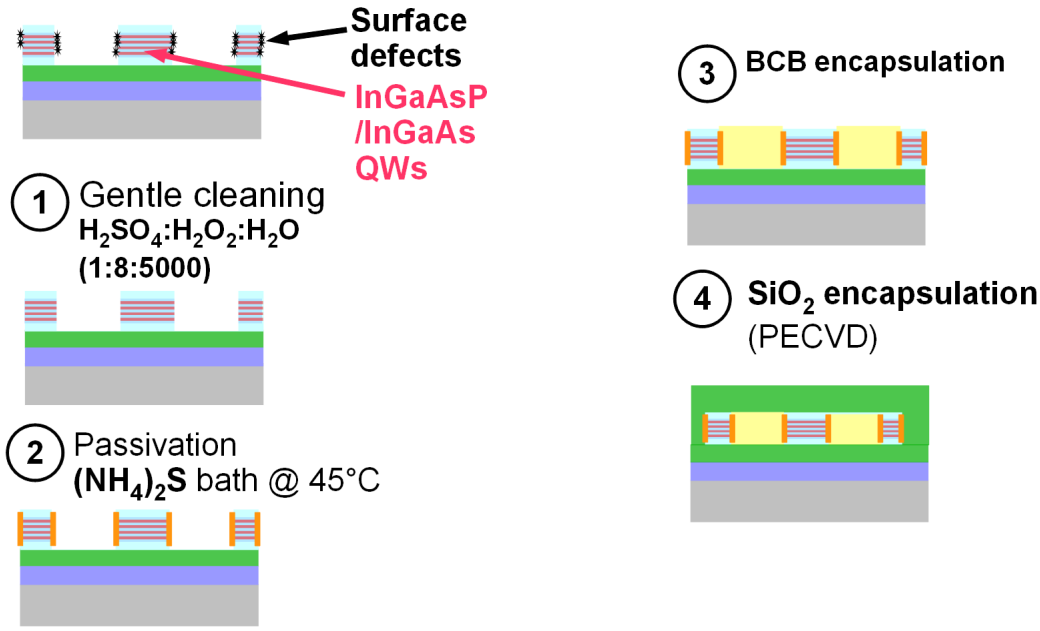

Figure 4.35: *Process steps for the surface passivation of our InP-based PhCs.*

4.5.3 Results

4.5.3.1 Impact on the resonant wavelength

To calibrate the etching rate of the solutions used for passivation, we compared the shift on the resonant wavelengths before and after passivation, whithout any filling nor encapsulation. Figure 4.36 shows the emission wavelengths of the two first modes of a PhC wire cavity which original target radius was 105 nm. The blue arrow indicates the blue shifts ($\approx$ 13nm) that both modes follow after the passivation. By averaging more measurements, this shift gets closer to $\approx$ 15nm. We see that the result of the two solutions bath is an increased of the effective hole diameter (as well as the width of the waveguide, but with a weaker effect on the resonant wavelengths).

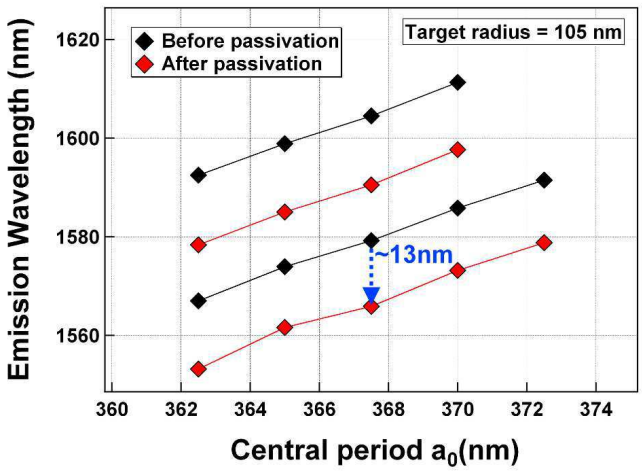

Figure 4.36: *Resonant wavelengths of a group of PhC wire cavities as a function of the central period a_0 before and after the passivation procedure. Here, the target wire width is 505nm and the target radius is 105 nm.*

As we have seen in the previous chapter, the shift of λ as a function of the radius r is approximately equal to 4 nm per nm of radius. Thus, the etched layer by passivating is estimate around 4 nm.

4.5.3.2 Impact on carrier lifetime

In order to retrieve the carrier lifetime, we build a pump-probe experiment where the pump is a 800nm fs-pulse focused at the cavity surface and where the probe is a resonant fs-pulse injected in the SOI waveguide beneath the cavity. The optical pulses employed in this experiment were obtained by a Ti:sapphire laser for the 800 nm pulses ($\approx$ 100 fs long) and by an OPO tunable around 1550 nm ($\approx$ 150 fs long). The pump is absorbed by the III-V and provides a fast increase in the carrier density of the wells. The probe is transmitted through the hybrid structure showing a dip at the cavity wavelength which depends on the carrier density. The principle of the pump-probe experiment consists in measuring this dip as a function of the pump-probe delay.

Using this technique, we carried out measurements on a passivated sample, encapsulated by BCB and SiO_2 as described in fig. 4.35. The pump is maintained well below the pumping intensities necessary to reach the laser threshold, allowing to neglect the stimulated emission. The measured wavelength dependence with the delay is plotted in fig. 4.37. We see that the cavity resonance blueshifts rapidly at first with the carrier capture in the wells and then slowly red-shifts due to carrier recombination either radiatively (bimolecular recombination) or non-radiatively. Taking account of both of these effects, we fitted the data points and found a

non-radiative carrier lifetime of approximately 2.2 ns. This lifetime is an order of magnitude higher than the carrier lifetimes measured previously in non-passivated InP-based 2D-PhC with QWs.

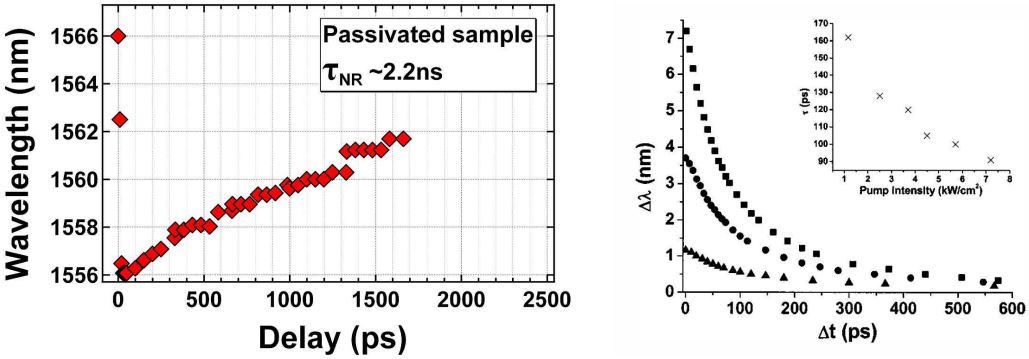

Figure 4.37: *Left: Measured wavelength shift of the cavity resonance as a function of the pump-probe delay. We extracted $\tau_{NR} \approx$ 2.2 ns from these data. Right: Measurement from [219] showing blueshifts of the resonance of a InP-based 2D-PhC slab embedding QWs as a function of the pumpprobe time delay for several pump intensities. The inset shows the shift of the decay times as a function of the pump intensity giving τ_{NR} close to 200 ps.*

4.5.3.3 Impact on the laser emission and threshold

As we have seen in the first part of this chapter, the non-radiative carrier lifetime can have a major impact on the laser threshold level (see fig. 4.3). For this reason, we fabricated a hybrid sample that we characterised before and after the passivation process. To prevent the lasers we studied from "burning" during the characterisation, we worked in pulsed regime with a 40 ns long pulses and a repetition rate of 300 kHz. The cavities are chosen so that their resonances are at the same wavelength and thus have the same material gain. Two typical S-curves of these situations are plotted in fig. 4.38. For experimental reasons, the lower part of each S-curve could not be properly measured. However, their thresholds were measurable and the observed difference of threshold with and without the passivation is significant. Because of the longer non-radiative carrier lifetime, the threshold is reduced by a factor 2.5, in average over more cavity characterisations. This reduction is in agreement with the numerical results in fig. 4.3 for β=0.01.

Most importantly, we demonstrate with this processing technique stable CW emission of passivated PhC wire cavities without any top-cladding. Contrarily to what we observed with MgF_2 cladded samples, we do not observe any degradation nor damaging of the emission during many weeks of actual work with them. Of course, for the latest generation of hybrid PhC laser/SOI produced in this work, we preferred to keep the improved heat spreading with the top-cladding addition, but it is worth to insist than the effect of passivation is so strong that the laser emission is reliable even with air top-cladded structures.

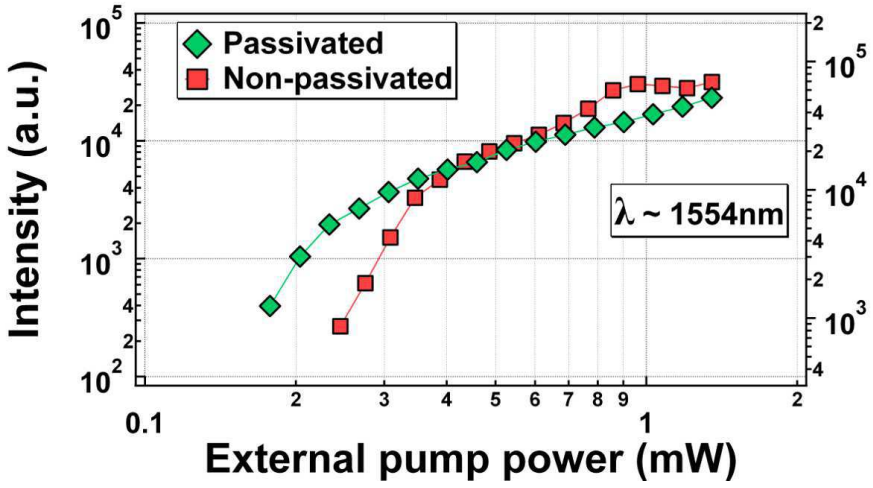

Figure 4.38: *S-curves of PhC Wire Cavity lasers emitting at the same wavelength with and without the passivation process.*

4.6 Conclusion

In conclusion, after a brief description of some of the properties peculiar to PhC nanolasers such as the modification of the spontaneous emission factor β, we set out to construct a dedicated QW laser model. From this, I could extract and highlight the influence of the β factor, the quality factor Q and the non-radiative lifetime τ_{NR} on the laser characteristics with a particular emphasis on the laser threshold.

The heat management was dealt through FEM simulations and precise measurements of the thermal resistance. We showed that substantial increase of the heat sinking can be obtained in the PhC wire cavity lasers by replacing, as much as possible, the BCB of the bonding layer by SiO_2, and by encapsulating them with SiO_2 or MgF_2.

The adverse effect of the augmented non-radiative recombination rate was countered by developing an effective passivation procedure adapted to these hybrid structures, which led to the attainment of the challenging CW operation in Quantum Well PhC structures.

Overall, the studies devoted to each aspect specifically resulted in a method of fabrication of a robust nanolaser with tailor made physical characteristics. The effort spent towards the conception and automation of the entire characterisation of the laser properties bore its fruit in that exhaustive studies, of the myriad of structures which were designed and fabricated, could be carried out with ease with a specifically built experimental set-up dedicated to the exploration of hybrid structures.

The results attest to the effort to optimise the different parameters impacting the laser performances. Reliable CW operation with micro Watt threshold power levels was obtained at 1554 nm.

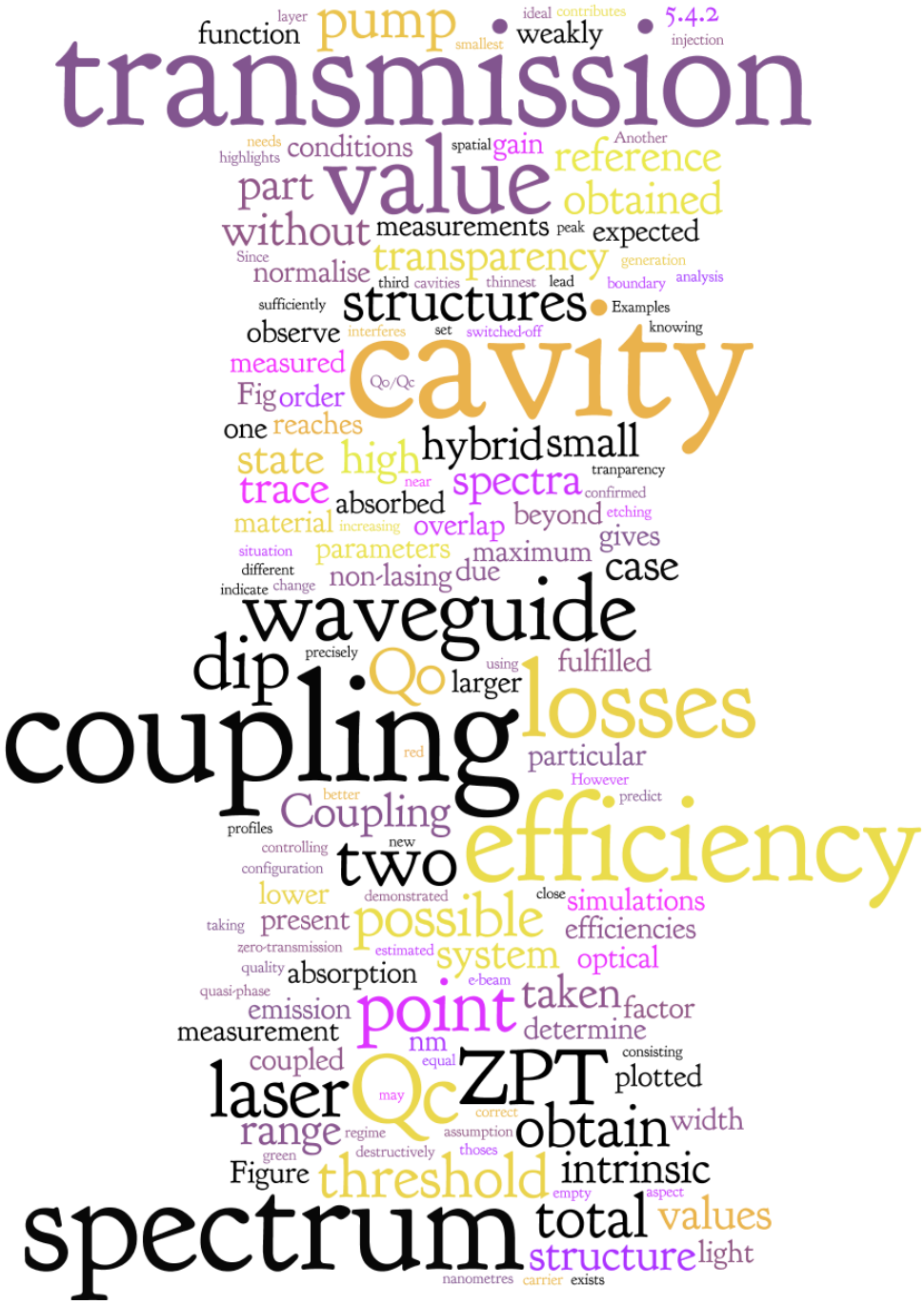
transmission
value
cavity
coupling
waveguide
spectrum
efficiency
losses
structures
transparency
reference
obtained
measurements
expected
pump
function
weakly
5.4.2
injection
conditions
gain
part
without
normalise
hybrid
small
state
high
spectra
trace
absorbed
material
overlap
beyond
gives
parameters
maximum
case
non-lasing
due
dip
Qo
larger
fulfilled
particular
Coupling
two
lower
possible
simulations
efficiencies
present
system
optical
absorption
point
taken
factor
emission
measurement
determine
coupled
laser
Qc
ZPT
plotted
range
obtain
width
Figure
threshold
intrinsic
total
values
structure
light
order
measured
Fig
one
reaches
observe
switched-off
Examples
knowing
boundary
analysis
generation
thinnest
lead
third
cavities
sufficiently
Another
spatial
peak
Since
normalise
Qo/Qc
near
tranparency
confirmed
etching
increasing
situation
different
indicate
change
precisely
using
red
However
predict
better
profiles
new
controlling
configuration
demonstrated
close
taking
zero-transmission
estimated
quality
e-beam
quasi-phase
nm
equal
consisting
may
correct
assumption
regime
destructively
thoses
green
empty
aspect
nanometres
carrier
exists

Chapter 5

Coupling efficiency in the hybrid platform: model and measurements

As we stated on several occasions in this manuscript, the interfacing of a PhC cavity with the outside world has been for a long time a real challenge, particularly when the PhC cavity is made of active material, absorbing, and hence, not suited for routing optical signals -in and -out from the cavity. While the routing of light finds a solution in the use of a SOI waveguide, the coupling between the two levels has to be carefully examined in order to optimise the energy consumption of the final device.

In the case of the coupling of a III-V PhC cavity with a SOI waveguide, the mechanism of coupling is based on side-evanescent coupling. In this mechanism, the mode of each of the two levels is weakly perturbed by the presence of the other level, positioned nearby. For instance, if we considered a typical apodised PhC wire cavity mode profile, the field envelope in the direction perpendicular to the Si substrate (see fig. 5.1) decays exponentially from the border of the III-V with a decay length σ around 60 nm. Roughly, it is the overlap of the exponentially decaying part of the field, the *evanescent tail*, with the field in the core of the other level structure which determines the coupling strength [220]. This coupling mechanism can be very efficient and is commonly used in waveguide couplers [221, 222] as passive power splitters.

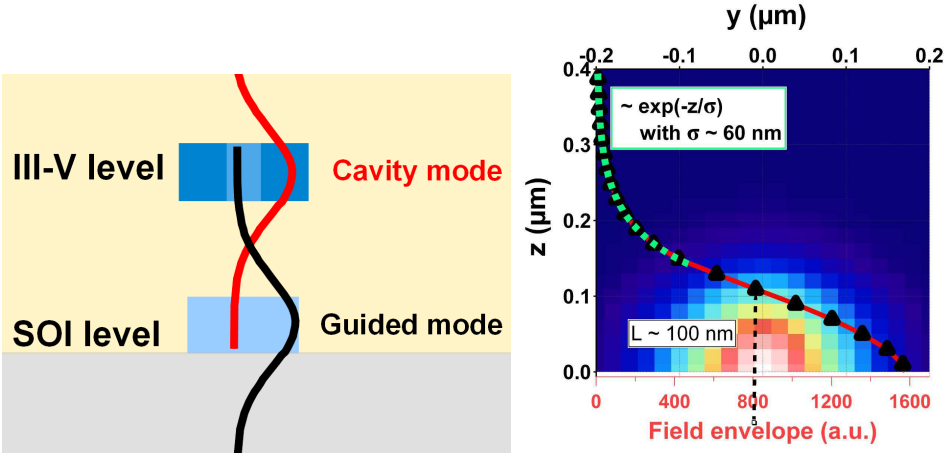

Figure 5.1: *Left: Transverse scheme of the hybrid structure in the coupling region, with the intensity profiles of each mode, overlapping with each other. Right: in the background, transverse intensity profile of the main mode of a PhC apodised cavity, taken at its centre (x=0) and in the z> 0. In red, the trace of the field envelope in the z-direction and in green, its exponential fitted curve outside the III-V, of characteristic length* $\sigma \approx 60$ *nm.*

5.1 Coupling efficiency η

The coupling efficiency between the PhC cavity and the SOI waveguide is a figure of primary importance to determine in order to prove the quality of the PhC interfacing in the hybrid structure. Indeed, one can wonder how much of the laser light produced in the cavity is effectively channelled through the waveguide instead of being lost by coupling to radiative modes. Equivalently, one can also wonder how much of a propagating signal in the waveguide is coupled inside the cavity.

The coupling efficiency, that we note η, is defined as follows:

$$\eta = \frac{\text{Rate of optical losses from the PhC into the SOI waveguide}}{\text{Total rate of optical losses}} \tag{5.1}$$

Mathematically, it is also given by:

$$\eta = \frac{\frac{1}{\tau_c}}{\frac{1}{\tau_c} + \frac{1}{\tau_0}} = \frac{\frac{Q_0}{Q_c}}{1 + \frac{Q_0}{Q_c}} = \frac{Q_0}{Q_0 + Q_c} \tag{5.2}$$

where Q_c (τ_c) and Q_0 (τ_0) are the quality factors (field decay times) respectively associated with the coupling to the waveguide mode and to the radiative modes. Here we make the assumption that the perturbation induced by the SOI wire on the cavity is small enough so that Q_0 can be considered constant. Of course, this is true only when the distance between the cavity and the SOI is large enough so that the coupling remains "weak", i.e. evanescent.

Figure 5.2 shows a plot of the relation (5.2) as a function of Q_0/Q_c (red trace). A legitimate

expectation for an efficient coupling scheme could be to obtain a coupling efficiency above 90 %. This is the case when Q_0 is superior to $9 \times Q_c$. However, the ratio between Q_0 and Q_c is not the only parameter to be considered in practice. Indeed, in order to obtain a structure with such a high η value, it is also necessary to work with a cavity whose uncoupled Q-factor is as high as possible. As an example, we observe (see right axis in fig. 5.2) that the Q-factor obtained for such high values of η is slightly below 10^4 for an initial Q_0 of 10^5. We showed in the previous chapter (see fig. 4.6) that the threshold power of a typical PhC nanolaser may increase importantly when the total Q goes below 10^4. Consequently, for a given cavity, there will be a trade-off between the coupling efficiency and the power necessary to reach the laser threshold. Remark in addition that there is a real motivation in the fabrication of high-Q cavities in order to go beyond this trade-off by obtaining very high coupling efficiencies and low laser power threshold values.

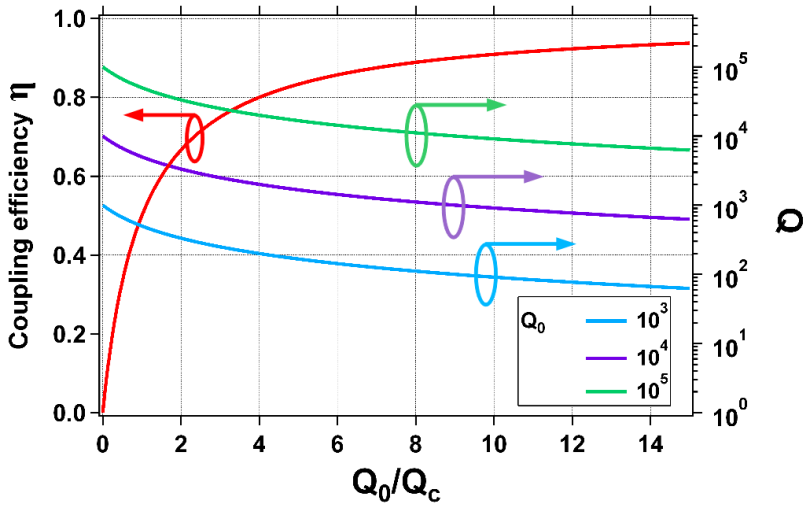

Figure 5.2: *Coupling efficiency η and total Q factor as a function of the ratio Q_0/Q_c and for several values of Q_0.*

In order to maximise η, it is necessary to have a very good overlap in the real space but also in the reciprocal space, as we will show later in the chapter.

The overlap in the real space depends obviously on the geometry of the hybrid structure. If we assume that the two levels have similar transverse mode profiles, the overlap between the two levels will depend on the cavity-waveguide separation distance d but also on the lateral offset between the waveguide and the PhC cavity. The latter issue is not considered in this work due to the demonstration, in a recent study [62] on hybrid samples, of a resolution in the cavity-waveguide alignment better than 30 nm, achieved with the same ebeam lithographic technique presented in chapter 3. In this chapter, we will study the influence of the vertical separation distance experimentally and with FDTD simulations. In order to give a first clue on how the

optical losses vary with d, we present in figure 5.3 the variation of the Q factor of a simulated apodised cavity coupled to a 500 nm waveguide. d is defined as the distance between the top of the SOI waveguide and the bottom of the III-V PhC. Here, the Q of the cavity goes from 10^5 down to 10^3 by varying the d from 600 nm to 225 nm, and passes below 10^4 for $d < 400$ nm. Because Q_0 is close to 10^6, the quality factor associated with coupling Q_c equals the total Q in the considered range of d values. In consequence, the theoretical coupling efficiency η that we found is always superior to 80 %. Of course, in a real sample, Q_0 is usually much lower than the theoretical high-Q predicted by the simulations. This chapter aims at determining experimentally both Q_c and Q_0 values in order to estimate the coupling efficiencies.

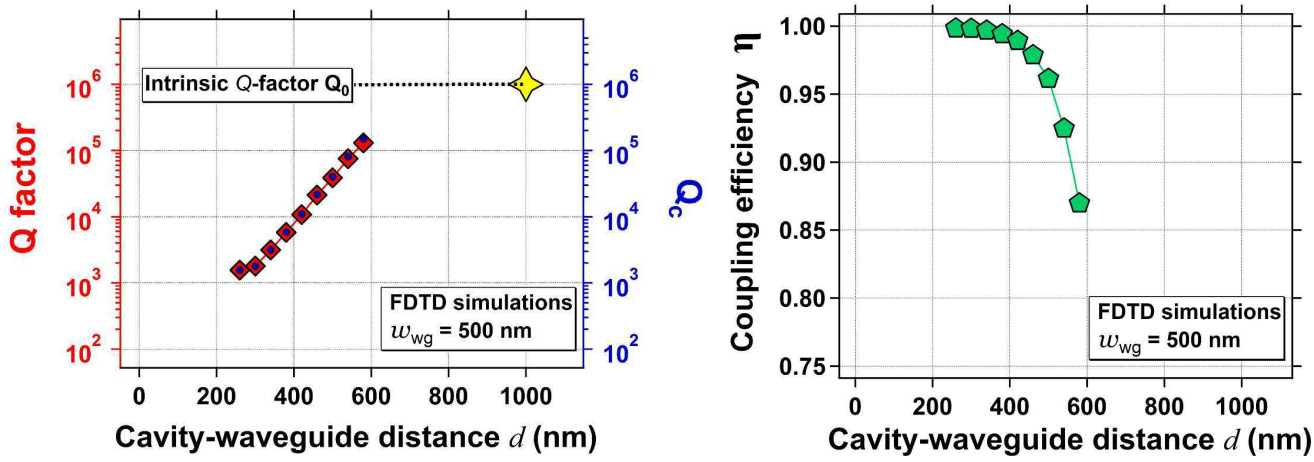

Figure 5.3: *Left: Q-factors and Q_c of the laser mode of a PhC wire cavity, evanescently coupled to a 500 nm wide SOI waveguide, as a function of the cavity-waveguide separation distance d, i.e. the BCB+SiO_2 bonding layer thickness. Right: coupling efficiencies computed with the values of left graph. The parameters of the apodised cavity are a central period a_0= 350 nm, a radius r= 120 nm and a target FWHM= 3 µm. The yellow star indicates the intrinsic Q-factors of the cavity Q_0 reached when the the distance is above ≈ 1µm.*

In the following of this chapter, we first analyse the cavity-waveguide side-evanescent coupling with Temporal Coupled Mode Theory (TCMT), in the specific case of a cavity containing an active material.

In a second step, we will present in detail the transmission measurements of the hybrid structure which allows us to accurately measure the field decay time τ_c associated with the coupling. We then combine these experimental results with a fitting procedure of the characteristic laser curve which permit us to estimate the value of τ_0, β and therefore the coupling efficiency η.

Finally, we will present experiments and simulations on how the coupling efficiency is impacted by the variations of the opto-geometrical parameters of the structure.

5.2 Temporal Coupled-Mode Analysis

In this work, the mechanism of coupling is analysed through the Temporal Coupled-Mode Theory (TCMT) [220, 223]. It is formally very similar to the regular Coupled-Mode Theory (CMT) [224] used in the analysis of coupled waveguides for instance, but, instead of analysing the spatial coupling evolution, it focuses on the time evolution of the resonator modes. TMCT is a simple and powerful analysis method for studying many coupled resonator systems. In this model, a resonator is interfaced with the outside world by multiple ports supporting incoming and outgoing waves with respect to the resonator (see Fig. 5.4). The resonator itself can sustain multiple optical modes and the dynamical equations of each mode take into account the part of each incoming wave which couples to the resonator. In the following, I will briefly present the TMCT as developed in [223], before applying it to our hybrid PhC laser/waveguide system.

Let us consider the most general case described by figure 5.4.a. The cavity state is represented by the n-vector $\overrightarrow{a} = (a_1, a_2, ..., a_n)$ where a_i are electric fields associated with each eigen cavity mode and normalised so that $|a_i|^2$ is the energy of the i^{th} mode. The resonator is coupled to m ports in which the incoming wave s_{j+} and the outgoing wave s_{j-} of the j^{th} port with normalised power ($|s_{j\pm}|^2 = 1$) can propagate.

In the TCMT formalism, the dynamical evolution of the cavity is described by the dynamical equation of the cavity fields and by the expression linking the outgoing waves to the incoming waves and to the cavity fields:

$$\frac{d\overrightarrow{a}}{dt} = (j\Omega_0 - \Gamma)\overrightarrow{a} + K^t |s_+\rangle \tag{5.3}$$

$$|s_-\rangle = C |s_+\rangle + D\overrightarrow{a} \tag{5.4}$$

where the resonant frequencies are arranged in the $n \times n$ matrix Ω and the photon lifetimes of each mode in the $n \times n$ matrix Γ. K^t is a $n \times m$ coupling matrix between the incoming waves and the resonator modes. $|s_\pm\rangle$ is the column vector containing the incoming/outgoing waves $s_{j\pm}$ where j is the related port number. C is the $m \times m$ scattering matrix taking into account the different pathways for $s_{j\pm}$ waves. D is the $m \times n$ coupling matrix between the outgoing waves and the resonator modes. It is assumed that the n eigen-values of $j\Omega - \Gamma$ are real which shows that each resonator mode can escape through a port.

Within the framework of this theory, Suh et al. [223] demonstrated the next relations:

$$D^\dagger D = 2\Gamma \tag{5.5}$$

$$K = D \tag{5.6}$$

$$CD^* = -D \tag{5.7}$$

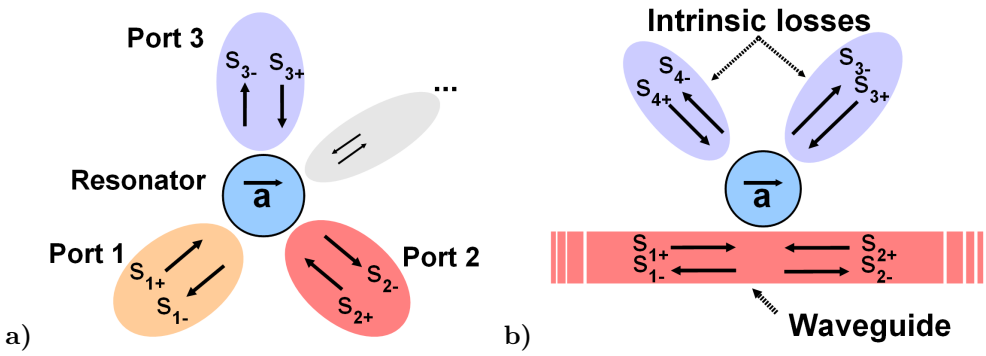

Figure 5.4: *Scheme of a resonator coupled to multiple ports a) General case b) Case of a cavity coupled to a waveguide. Ports 3 and 4 are the channels accounting for intrinsic losses, i.e. without coupling to the waveguide.*

5.2.1 Single-mode laser evanescently coupled to a waveguide

The case of coupling a PhC single-mode cavity with a waveguide is described in Fig. 5.4.b. In TCMT, the cavity optical losses are determined by two independent terms, one related to the intrinsic losses of the cavity, i.e. the losses in absence of the waveguide, and one related to the coupling to the SOI waveguide mode. The waveguide itself is modelled as two ports (ports 1 and 2) linked together. Two more ports are added to take into account optical losses due, on the one hand, to coupling with radiative modes and the other hand, to material losses or material gain inside the cavity. The latter contribution comes from the presence of active material inside the cavity. Depending on the carrier injection in the material, the cavity will present absorption or gain which we mathematically translate by adding an effective photon decay rate $1/\tau_{abs/gain}$ whose sign will depend on which regime, either absorption or gain, is considered. Thus, the decay rate is a tunable parameter that can easily be varied by changing the optical pump power impinging on the cavity. We write

$$\Gamma = \frac{1}{\tau_0} + \frac{1}{\tau_c} - \frac{1}{\tau_g} \tag{5.8}$$

where $\frac{1}{\tau_0}$ and $\frac{1}{\tau_c}$ are the decay rates associated with the intrinsic losses and the coupling to the waveguide losses respectively. We adopt a simplified notation for material losses/gain: $\tau^{-1}_{abs/gain} \hat{=} \tau_g^{-1}$. Therefore, the material state regime is determined by the sign of τ_g^{-1} and is summarised in what follows:

$$\begin{aligned} \tau_g^{-1} > 0 \quad &\Longleftrightarrow \quad \text{gain regime} \\ \tau_g^{-1} = 0 \quad &\Longleftrightarrow \quad \text{transparency} \\ \tau_g^{-1} < 0 \quad &\Longleftrightarrow \quad \text{absorption regime} \end{aligned}$$

In the hybrid structure case, using (5.5), equations (5.3) and (5.4) become:

$$\frac{da}{dt} = (j\omega_0 - \frac{1}{\tau_0} - \frac{1}{\tau_c} + \frac{1}{\tau_g})a + K^t \begin{pmatrix} s_{1+} \\ s_{2+} \\ s_{3+} \\ s_{4+} \end{pmatrix} \tag{5.9}$$

$$\begin{pmatrix} s_{1-} \\ s_{2-} \\ s_{3-} \\ s_{4-} \end{pmatrix} = C \begin{pmatrix} s_{1+} \\ s_{2+} \\ s_{3+} \\ s_{4+} \end{pmatrix} + Ka \tag{5.10}$$

where ω_0 is the scalar resonant frequency of the cavity. K^t takes the form $\begin{pmatrix} \kappa_1, \kappa_2, \kappa_3, \kappa_4 \end{pmatrix}$ where each κ_i is the coupling coefficient between cavity mode and i^{th} port. C is the 4×4 scattering matrix and contains the information describing the waveguide path.

In the case where the incoming waves s_{1+}/s_{2+} are not reflected at the cavity interfaces, the 2 diagonal coefficients of C are zero and C can be written

$$C = \begin{pmatrix} 0 & c_{12} & 0 & 0 \\ c_{21} & 0 & 0 & 0 \\ 0 & 0 & r & t \\ 0 & 0 & t & r \end{pmatrix}$$

We know from (5.6) and (5.7) that

$$CK^* = -K \tag{5.11}$$

hence

$$\begin{cases} 0 + c_{12}\kappa_2^* & = -\kappa_1 \\ c_{21}\kappa_1^* + 0 & = -\kappa_2 \end{cases} \tag{5.12}$$

Here, because a waveguide is formed of ports 1 and 2 that are "stitched" together, ports 1 and 2 are identical (as well as port 3 and 4 for symmetry reasons) so that the system is symmetric. Then $\kappa_1 = \kappa_2 = \kappa$ et $c_{12} = c_{21} = c$ and from (5.7) we have

$$\begin{cases} \kappa^* = -c^*\kappa \\ \kappa = -c\kappa^* \end{cases} \implies \kappa = +|c|^2\kappa \tag{5.13}$$

We deduce that $|c|^2 = 1$, so we can replace c by a pure imaginary complex number $e^{i\phi}$. Because of this, one can reformulate the right hand expression of (5.13)

$$e^{i\phi} = -e^{2i\theta} = -\frac{\kappa^2}{|\kappa|^2} \tag{5.14}$$

Equation (5.14) is a very interesting relation as it highlights the phase relations, specific to the side evanescent coupling, that exist between the incoming field and the coupled field and is fundamentally due to the time reversal symmetry between the loading and unloading processes [223].

Using eq. (5.14), the equation (5.10) simplifies in this case into the following set of equations:

$$s_{1-} = -\frac{\kappa^2}{|\kappa|^2} s_{2+} + \kappa a \tag{5.15}$$

$$s_{2-} = -\frac{\kappa^2}{|\kappa|^2} s_{1+} + \kappa a \tag{5.16}$$

In this model, we assume that we have a coupling scheme spatially very localised so that the value of θ can be fixed to 0. Note that, because eq. (5.14) is a phase relation between two fields, another value for θ would not change the value of the intensity transmission of s_{2-} through the coupled system but would merely complicate the mathematical expressions to calculate it. Using θ=0 and the fact that the units of the squared magnitude of κa must be homogeneous with the units of $|s_{1-}|^2$, we write κ as $1/\sqrt{\tau_c}$.

Finally, eq. (5.15) and (5.16) are again simplified into:

$$s_{1-} = -s_{2+} + \frac{1}{\sqrt{\tau_c}} a \tag{5.17}$$

$$s_{2-} = -s_{1+} + \frac{1}{\sqrt{\tau_c}} a \tag{5.18}$$

5.2.2 Transmission spectrum of the active hybrid structure

In order to evaluate the waveguide transmission of the hybrid structure in the steady state regime, we must find the solutions of eq. (5.9) in the form of $a(t) = \hat{a}(t)e^{i\omega t}$ where ω is an arbitrary excitation frequency of the cavity field. We note that we implicitly assume that temporal dependence of incoming waves s_{i+} is also in $e^{i\omega t}$.

In the steady-state regime, eq. (5.9) gives

$$\left(j(\omega_0-\omega)-\frac{1}{\tau_0}-\frac{1}{\tau_c}+\frac{1}{\tau_g}\right)\hat{a}+\kappa_1 s_{1+}+\kappa_2 s_{2+}+\kappa_3 s_{3+}+\kappa_4 s_{4+}=0 \tag{5.19}$$

Then, the solution for the amplitude $\hat{a}$ is

$$\hat{a}=\frac{\kappa s_{1+}+\kappa s_{2+}+\tilde{\kappa} s_{3+}+\tilde{\kappa} s_{4+}}{\left(j(\omega-\omega_0)+\frac{1}{\tau_0}+\frac{1}{\tau_c}-\frac{1}{\tau_g}\right)} \tag{5.20}$$

where $\tilde{\kappa}=\kappa_3=\kappa_4$. In what follows, we replace $\hat{a}$ by a to alleviate notations.

If we only inject the waveguide with the optical wave s_{1+}, so that we have $s_{2+}=s_{3+}=s_{4+}=0$, the intensity transmission coefficient T of s_{1+} is given by

$$T = \left|\frac{s_{2-}}{s_{1+}}\right|^2 \tag{5.21}$$

In that case, we also have:

$$s_{2-} = -s_{1+}+\frac{1}{\sqrt{\tau_c}}a \tag{5.22}$$

$$= -s_{1+}+\frac{\frac{1}{\tau_c}s_{1+}}{(j(\omega-\omega_0)+\frac{1}{\tau_0}+\frac{1}{\tau_c}-\frac{1}{\tau_g})} \tag{5.23}$$

Including this last equation into eq. (5.21) gives:

$$\begin{aligned} T(\omega) &= \left|-1+\frac{\frac{1}{\tau_c}}{\left(j\left(\omega-\omega_0\right)+\frac{1}{\tau_0}+\frac{1}{\tau_c}-\frac{1}{\tau_g}\right)}\right|^2 \\ &= \frac{\left(\omega-\omega_0\right)^2+\left(\frac{1}{\tau_0}-\frac{1}{\tau_g}\right)^2}{\left(\omega-\omega_0\right)^2+\left(\frac{1}{\tau_0}+\frac{1}{\tau_c}-\frac{1}{\tau_g}\right)^2} \\ &= \frac{\left(\left(\omega-\omega_0\right)\tau_c\right)^2+\left(\frac{\tau_c}{\tau_0}\left(1-\frac{\tau_0}{\tau_g}\right)\right)^2}{\left(\left(\omega-\omega_0\right)\tau_c\right)^2+\left(\frac{\tau_c}{\tau_0}\left(1-\frac{\tau_0}{\tau_g}\right)+1\right)^2} \end{aligned} \tag{5.24}$$

Figure 5.5 illustrates, in the case where the intrinsic losses equal the coupling losses, how the transmission spectrum evolves when we change the material state below the laser threshold. Each value of $(\tau_g)^{-1}$, that we normalise with $(\tau_0)^{-1}$, determines the material state (absorption, transparency, gain).

In the *absorption* regime ($\tau_0/\tau_g < 0$), the transmission spectra shows a dip at the resonant wavelength. The minimum value of the transmission firstly decreases for increasing τ_0/τ_g (negative values), up to a point where the dip reaches 0, before going up again. Note that, at the transparency point ($\tau_0/\tau_g = 0$), $T(\omega_0)$ reaches 0.25, in the particular case where $Q_c = Q_0$. Because it is not possible to predict this values without knowing Q_0 and Q_c, it is not possible in general to determine the transparency point. However, there exists a state above transparency when the gain exactly compensates the intrinsic optical losses of the cavity, i.e. when $\tau_0/\tau_g = 1$, where the value of the transmission dip reaches a zero-transmission point (ZPT). At this point, the amplified part of the field that has coupled to the cavity interferes destructively with the uncoupled part that travels through the waveguide. The total losses of the cavity are then equal to the coupling losses $1/\tau_c$ and

$$\Delta\omega_c = \frac{2}{\tau_c} \tag{5.25}$$

By measuring the width of this particular dip, it is possible to retrieve the quality factor of coupling Q_c equal to $\omega/\Delta\omega_c$.

When the gain continues to increase, the depth of the transmission dip begins to lessen until the spectrum becomes a transmission peak which is an evidence of net gain in the system. At the laser threshold, when gain compensates all optical losses $\frac{1}{\tau_g} = \frac{1}{\tau_0} + \frac{1}{\tau_c}$, the transmission peak diverges.

More generally, when the transmission spectrum presents a dip (peak), the full-width half minimum (maximum) of the spectrum, i.e. the width when the dip (peak) equals $\frac{(1+T(\omega_0))}{2}$, is given by

$$F\left(\frac{1}{\tau_g}\right) = 2\left(\frac{1}{\tau_0} - \frac{1}{\tau_g} + \frac{1}{\tau_c}\right) \tag{5.26}$$

and the transmission value at resonance $T(\omega_0)$ is

$$T\left(\frac{1}{\tau_g}\right) = \frac{\left(\frac{1}{\tau_0} - \frac{1}{\tau_g}\right)^2}{\left(\frac{1}{\tau_0} - \frac{1}{\tau_g} + \frac{1}{\tau_c}\right)^2} \tag{5.27}$$

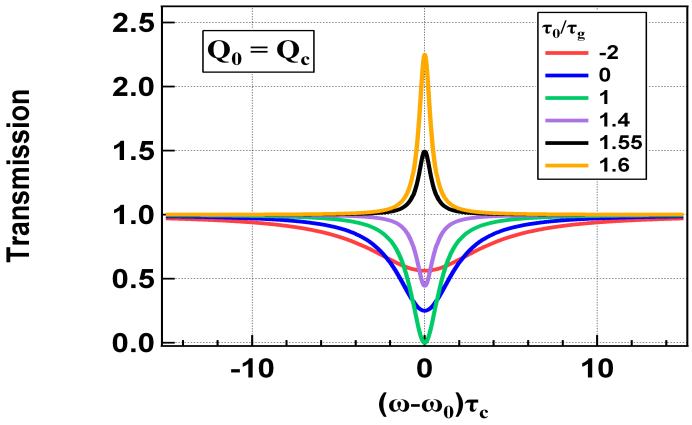

Figure 5.5: *Transmission spectra of an optical signal through the waveguide coupled to the cavity as a function of the normalised frequency* $(\omega - \omega_0)\tau_c$ *and for several values of the ratio* τ_0/τ_g. *Note that the transmission at resonance is exactly 0 only when* τ_0/τ_g=1.

In figures 5.6 are plotted, in linear and log scales, the variations of $T(\omega_0)$ as a function of τ_0/τ_g for 3 values of the ratio τ_0/τ_c. Here, we can assume that τ_0 is a fixed time and that we vary the ratio τ_0/τ_c by varying τ_c. The blue shaded zones of both graphs indicate the absorption regime while the red shaded zones the gain regime. At the transition from this two material states, i.e. at transparency, it is clear that the value of $T(\omega_0)$ is dependent of the value of the ratio between the losses to the radiative modes and the coupling losses. On the contrary, the ZPT is observed at the same material state, when gain compensates the intrinsic losses of the cavity. Remark, as it is obvious in the log-scale plot, that the distance between the ZPT and the laser threshold logically increases with the coupling losses which depend on $(\tau_c)^{-1}$.

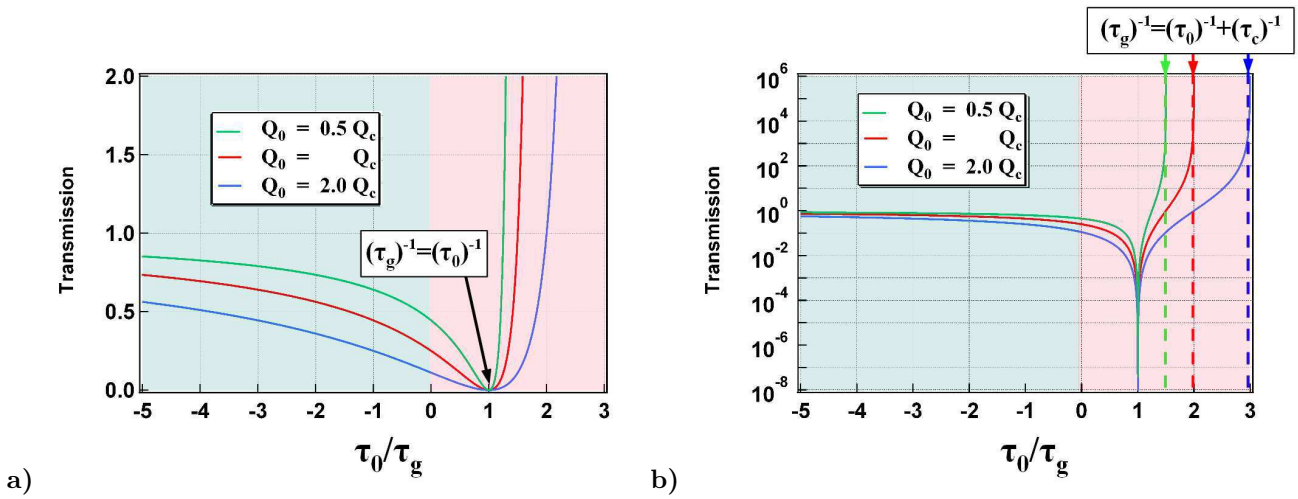

Figure 5.6: *Values of the intensity transmission* T *at the cavity resonance of an injected field in a waveguide evanescently coupled to a PhC laser. The axis of the* T *values is plotted in linear-scale in a) and in log-scale in b).*

From any point of the curves in figure 5.6, it is possible to retrieve the value of the inverse of the coupling time τ_c as a function of F and T. Indeed,

$$\frac{1}{\tau_c} = \begin{cases} \dfrac{F\left(\dfrac{1}{\tau_g}\right)}{2}\left(1-\sqrt{T\left(\dfrac{1}{\tau_g}\right)}\right) & \text{below the ZPT} \\ \dfrac{F\left(\dfrac{1}{\tau_g}\right)}{2}\left(1+\sqrt{T\left(\dfrac{1}{\tau_g}\right)}\right) & \text{above the ZPT} \end{cases} \tag{5.28}$$

and, specially at the ZPT, there is:

$$\frac{1}{\tau_c} = \frac{F\left(\dfrac{1}{\tau_g}=\dfrac{1}{\tau_0}\right)}{2} \qquad \text{at the ZPT} \tag{5.29}$$

The next section presents the experimental procedure used to measure the transmission spectra as a function of the pump power on the cavity.

5.3 Transmission spectrum measurements

The goal of the experiment is to obtain the transmission spectra as a function of the pump power focused on the PhC laser. While pumping the cavity, the SOI waveguide is injected with a Tunable Laser Source (TLS) around 1.55 μm. The next section details the homodyne detection technique used to measure the transmission of the injected light at the SOI output.

5.3.1 Transmission set-up

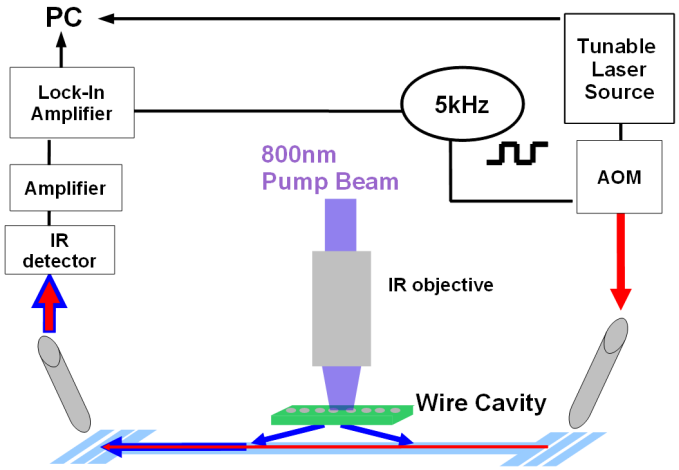

Figure 5.7: *Scheme of the experimental set-up used to obtain transmission spectra of a hybrid structure whose cavity is here optically pumped by a 800 nm laser diode. The emitted light of the PhC coupled to the waveguide is added to the injected light.*

Figure 5.7 shows the experimental set-up using homodyne detection to detect and reconstruct the transmission spectra. First, the PhC laser is surface pumped with the 0.8 μm LD with a fairly low duty-cycle (40 ns long pulses at a 300 kHz repetition rate) to prevent any heating effect but also because those samples could not lase in CW regime neither with the 0.8 μm pump nor with the 1.18 μm pump. Here the pump controls the gain of the active material. In order to measure the transmission values corresponding to a precise carrier injection rate, i.e. to the same cavity material state, it is necessary to time-gate the injection optical signal to obtain pulses synchronized and overlapped with the pump pulses. The pump pulses are generated by directly modulating the pump LD. Because of the limited dynamics of the LD, it is, in fact, difficult to obtain a constant carrier injection rate during the whole duration of the pump pulse. Hence, the TLS pulses were chosen short with respect to the pump pulse length and their relative time delay with the pump pulse was adjusted with a resolution below 2 ns. In practice, the injected TLS pulses were obtained by using an Gouch&Housego Acousto-Optic Modulator (AOM) providing 2 electronic channels for the optical amplitude modulation. The gating modulation was set to produce 13 ns pulses at the same repetition rate as the pump laser.

To separate the PhC laser signal from the TLS one, an extra 5kHz modulation was applied (see fig. 5.8). The light at the output of the SOI waveguide was sent in an infrared fast photodetector, and amplified using a low-noise electronic amplifier. The amplified signal was then sent to a Lock-In Amplifier demodulating the signal at the slow modulation frequency. Finally, for each TLS injected wavelength, the Lock-In output value was retrieved. This experiment including the change in the pump power was controlled by a LabView *.vi program, realising the measurements and plotting the different spectra.

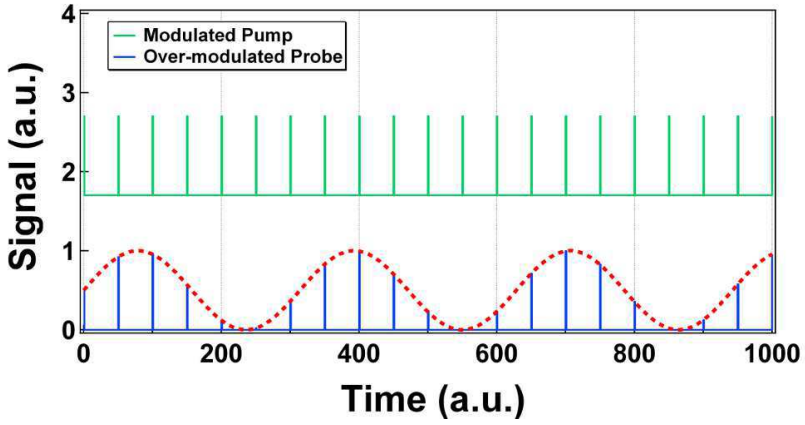

Figure 5.8: *Scheme of the over-modulation of the transmission probe.*

5.3.2 Typical results

Measurements [117] were performed on hybrid structures containing TD PhC Wire Cavity lasers coupled to SOI waveguides. The cavity is formed by separating two high-reflectivity mirrors with a distance of 450 nm. The hole radius r (mask value) and the pitch a of the 550 nm wide 1D lattice were fixed to be respectively at 88.75 nm and 370 nm. A SEM picture of the sample is shown in fig. 5.9. Note that this sample was neither encapsulated nor passivated, and so could not operate in CW regime.

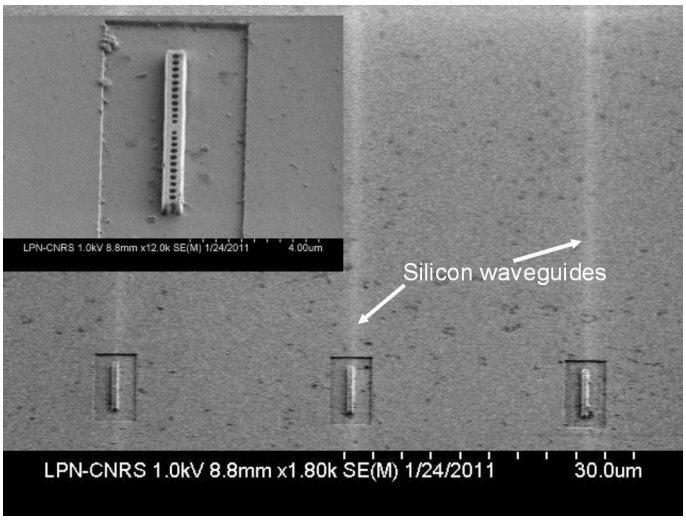

Figure 5.9: *SEM images of the fabricated sample. The SOI waveguides can be seen through the bonding layer aligned with the cavities. Inset: SEM image close-up of a TD PhC Wire Cavity.*

In order to obtain the transmission spectrum, one needs to normalise the spectrum obtained when pumping the cavity by a *reference* spectrum that ideally would be measured without the presence of the cavity above the waveguide. Such measurement requires to precisely reproduce

the positioning of the SMF above the grating couplers of an empty waveguide which is a difficult task in our system. We overcome this issue by using as a reference spectrum, the transmission spectrum taken with the pump switched-off. When the pump power is switched off, the obtained transmission spectrum shows a dip but very shallow because the absorption of the QWs is high. In practice this spectrum is very flat and can be considered as a reference. Moreover the cavity resonance shifts by several nanometres when the pump is increased. Therefore, the value of the reference spectrum taken at the ZPT wavelength is very weakly affected by the cavity and is close to the value that would be found without a cavity. In fact, in the very latest transmission experiments, we adopted a procedure consisting in normalising the transmission spectrum, not by a spectrum taken with no pump, but by a reference spectrum build by sticking parts of spectra where the resonance was shifted away by taking advantage of the dependance of the refractive index on the carrier injection.

Examples of measured transmission spectra are plotted in fig. 5.10 as a function of the absorbed pump power. Each transmission highlights the three typical behaviour expected from TCMT analysis: the dip below ZPT (red trace), the ZPT (blue trace) and the peak near laser threshold (green trace).

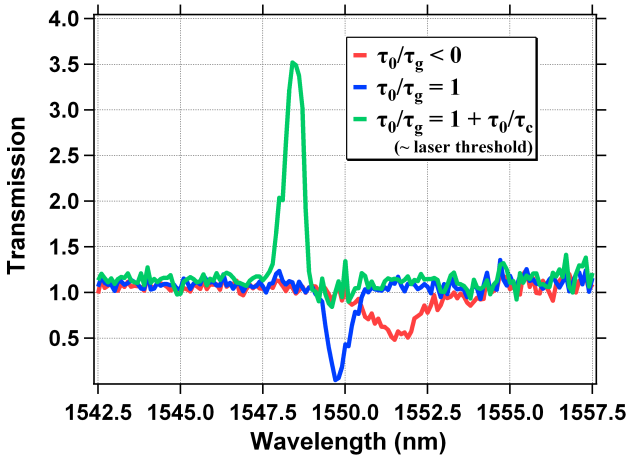

Figure 5.10: *Typical measured transmission spectra below ZPT (red), at ZPT (blue), after ZPT (green).*

The ensemble of measured spectra are surface plotted in fig. 5.11. Transmission shows a dip at resonance which deepens with increasing pump power reaching a minimum at $\lambda = 1550$ nm when $P_{pump} = 12.4$ μW. Net amplification is then observed before attaining the laser emission at a threshold of 29.6 μW for this particular sample. As the material RI is dependent on the carrier density, the change in amplitude is also accompanied by a blue-shift of the resonant wavelength. This is nominally clamped when the laser threshold is reached. The good qualitative agreement of these measurements with modelling can be appreciated in the bottom graph of fig. 5.11, where the transmission at resonance is plotted as a function of the absorbed pump power. The half-width of the resonance is measured to be 0.83 nm when $\tau_0/\tau_g = 1$ giving $Q_c = 1800$ and

$\tau_c \approx 3$ ps (see fig. 5.12).

In the experiment, we vary the value of the gain parameter $1/\tau_g$ by varying the injection rate R_{inj} or equivalently the pump power on the PhC cavity. Note that, because the gain and the injection rate are not linearly dependent, figure 5.11 is not exactly comparable with the theoretical transmission curve given in fig. 5.6.a.

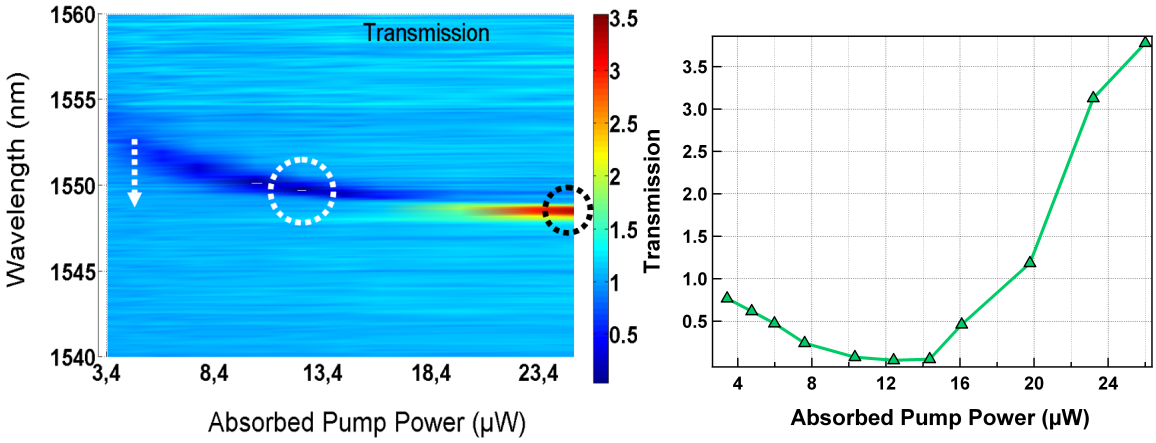

Figure 5.11: *Left: Transmission spectra profile as a function of the estimated absorbed pump power in the cavity. Here the cavity is a TD PhC Wire Cavity, 450 nm-long, and coupled to a 350 nm Si wide waveguide. Right: Transmission value at cavity resonance.*

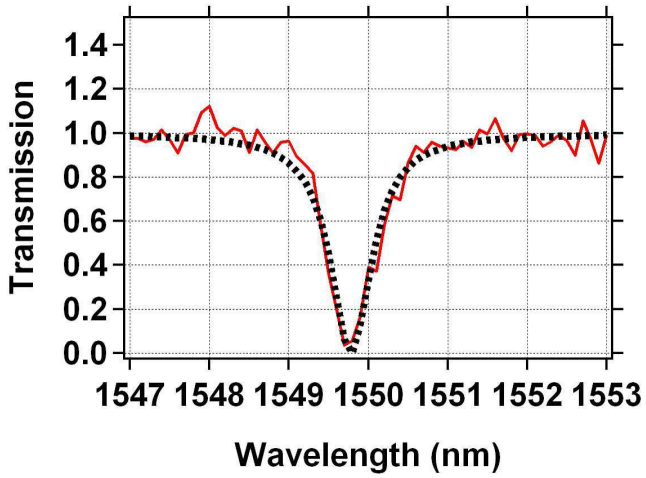

Figure 5.12: *Transmission spectrum at ZPT (solid line) and fit (dashed) giving a FWHM of 0.83nm*

We see how this probing technique allows to measure with a very good precision the quality factor of coupling of any system, as long as the gain is large enough to compensate the intrinsic

losses, i.e. that the uncoupled cavity lase, and as long as the perturbation of the cavity on the waveguide is weak enough so that the TCMT is valid.

The purpose of this work is to retrieve the coupling efficiency between the cavity and the waveguide. In order to compare the amount of optical losses channelling through the waveguide ($\propto 1/\tau_c$) to the total ones ($\propto (1/\tau_c) + (1/\tau_0)$), we need both value of τ_0 and τ_c. Unfortunately, the value of τ_0 cannot be derived from the transmission measurements as simply as for τ_c. The solution opted in this work is to estimate it through a fitting procedure of the experimental S-curves with the steady-state solutions of the laser rate equations and also with the use of the transmission results.

Before describing the fitting procedure and results, we show in the following section how it is possible to use some data of the transmission measurement to improve the accuracy of the fitted curves. Indeed, by expressing the gain parameter $1/\tau_g$ as a function of the power, we can derive a relation linking the gain coefficient G_0 (see gain definition in eq. (4.11)) to $1/\tau_0$ as a function of quantifiable values retrieved from the transmission measurements.

5.3.3 Derivation of a useful relation between G_0 and τ_0

We start by expressing τ_g as a function of the carrier density N. Instead of the logarithmic gain given by eq. (4.11), we choose to use a linear gain which constitutes an usual approximation of the logarithmic gain over a small range of variation of the carrier density. The relation between τ_g and the approximated gain expression is written:

$$\begin{aligned} -\frac{2}{\tau_{abs}} = +\frac{2}{\tau_g} &= G(N) \\ &\approx V_a \frac{G_0}{N_{tr}}(N - N_{tr}) \end{aligned} \tag{5.30}$$

In this case, the linear approximation is valid in our analysis because we restrict the range of interest of material states between the transparency and the threshold, where the carrier density varies little with the usual parameters describing our system (see fig. 4.1).

Experimentally, we do not access the value of the carrier density but only measure the pump power focused on the PhC cavity. As we saw in the steady-state analysis of the laser rate equations, the injection rate - and consequently the input power, either the external or the absorbed one - is not linearly dependent on the carrier density. In the range of powers between the transparency and the threshold, it is possible to approximate the dependence of N with, for instance, the measured external pump power P by a quadratic relation:

$$N = K_0 P + K_1 P^2$$

This is illustrated in fig. 5.13 where we plot the calculated carrier density dependence of nanolasers of different Q factors as function of the carrier injection rate, between the transparency and the threshold. The Q factor are chosen to illustrate two typical case observed in this work:

the uncoupled III-V semiconductor PhC nanolaser with a realistic Q equal to 10000 and the coupled one with Q=2000, the latter decrease corresponding to 75% of coupling efficiency. As we can observe, the same quadratic curve fits accurately the change in carrier density in both lasers, even though not perfectly for the one with largest losses when the laser is biased close to the threshold.

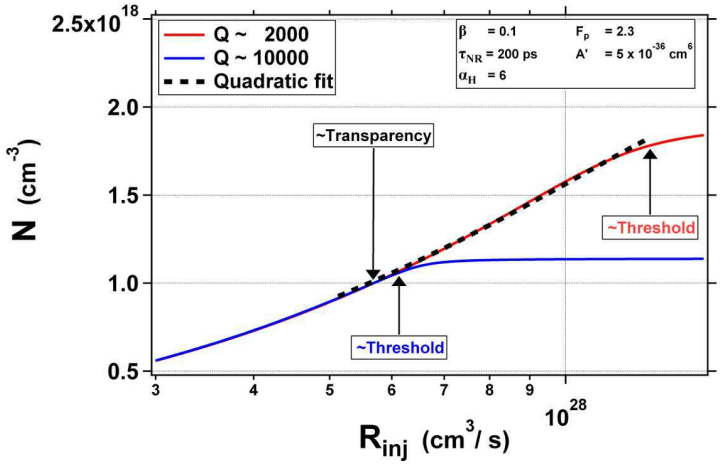

Figure 5.13: *Justification of the quadratic approximation linking the injected power to the carrier density in the range of power between transparency and the threshold for two PhC lasers of Q factor 2000 and 10000.*

With the quadratic relation between N and the pump power P (which can be the external or the absorbed pump power), we rewrite (5.30) as:

$$\begin{aligned} \frac{V_a G_0}{N_{tr}}(K_0 P + K_1 P^2 - N_{tr}) &= \frac{2}{\tau_g} \\ &= F\left(\frac{1}{\tau_g}\right) - 2\left(\frac{1}{\tau_0} + \frac{1}{\tau_c}\right) \end{aligned} \tag{5.31}$$

We apply this relation for three particular power P_0, P_1 and P_2 corresponding respectively to the ZPT, to T=1 in the gain regime, and to the threshold.

Mathematically, this gives a set of 3 equations:

$$\frac{V_a G_0}{N_{tr}}(K_0 P_0 + K_1 P_0^2 - N_{tr}) = \frac{2}{\tau_0} \tag{5.32}$$

$$\frac{V_a G_0}{N_{tr}}(K_0 P_1 + K_1 P_1^2 - N_{tr}) = \frac{2}{\tau_0} + \frac{1}{\tau_c} \tag{5.33}$$

$$\frac{V_a G_0}{N_{tr}}(K_0 P_2 + K_1 P_2^2 - N_{tr}) = \frac{2}{\tau_0} + \frac{2}{\tau_c} \tag{5.34}$$

If we define a third variable $K_2 = 1/G_0$, the set of equations can be rewritten:

$$P_0 K_0 + P_0^2 K_1 \quad - \left(\frac{2}{\tau_0}\right) \frac{N_{tr}}{V_a} K_2 \quad = N_{tr} \tag{5.35}$$

$$P_1 K_0 + P_1^2 K_1 \quad - \left(\frac{2}{\tau_0} + \frac{1}{\tau_c}\right) \frac{N_{tr}}{V_a} K_2 \quad = N_{tr} \tag{5.36}$$

$$P_2 K_0 + P_2^2 K_1 \quad - \left(\frac{2}{\tau_0} + \frac{2}{\tau_c}\right) \frac{N_{tr}}{V_a} K_2 \quad = N_{tr} \tag{5.37}$$

Here, we obtain a set of 3 equations of 3 variables K_0, K_1 and K_2, which can be solved by the Gaussian elimination procedure. Therefore, the 3 solutions can be expressed as a function of the P_0, P_1, P_2 and τ_0, while the value of V_a and τ_c are supposed known. Because the Gaussian elimination is rather tedious, we leave to the reader to assess its dullness rather than its difficulty.

In the end, the solution for G_0 is written as follows

$$\begin{aligned} G_0 \quad = \quad & \frac{1}{V_a} \frac{1}{(P_2 - P_0)(P_1 - P_2)(P_1 - P_0)} \\ & \left\{ \frac{1}{\tau_c} (P_2 P_0 (P_0 - P_2) + P_0 P_1 (P_1 - P_0)) \right. \\ & \left. + \frac{2}{\tau_0} (P_1 (P_1 - P_0)(P_2 + P_0) + P_0 (P_0 - P_2)(P_1 + P_0)) \right\} \end{aligned} \tag{5.38}$$

Finally, it is also possible to retrieve the value of P_2 expressed as a function of P_0 and P_1. Indeed, if an S-curve is not measured together with the transmission spectra, the criteria to define the laser threshold is not very clear. Indeed, we reach here the limit of our model which states that the probe should be, at threshold, infinitely amplified and sharpened to a 0 spectral width. However, the assumption of the probe not perturbing the laser becomes inaccurate very close to the threshold. Hence, it is often easier to replace P_2 by the value of P_0 and P_1. In the case of a quadratic dependence of N with P, the calculus is also quite long and is spared to the reader but we can remark that, if N would have varied linearly with P, P_2 would have simply be equal to $2P_1 - P_0$.

I might add a little aside that the relation giving G_0 is slightly different from the relation given in our publication [117] where we used a laser model expressed with the differential gain σ, and the mode group velocity v_g. The relation between N and P was also assumed linear instead of quadratic which simplified the analysis. Here, we make use of an updated laser model (the one presented in the previous chapter), which does not use v_g nor σ. However, this does not change much the final values of the coupling efficiency which are given with significantly large uncertainty values.

We now understand how the values of P_0, P_1, P_2 and τ_c extracted from transmission measurements allow us to give an expression for G_0 as a function of τ_0. This last expression can be used to restrain the number of parameters used in the fitting procedure of the S-curves of the waveguide-coupled PhC laser.

5.3.4 Determination of the total Q and β by fitting the S-curve

The experimental points constituting the S-curves are used to retrieve an estimation of the τ_0 value. Here, we make use of the steady-state model presented in Section 4.2.2. Let's recall that, in this regime, the steady-state solutions of the photon number S and of the carrier injection rate R_{inj} are written:

$$R_{inj}(N) = \left(F_pBN + \frac{1}{\tau_{NR}}\right)N + \frac{\beta F_pB}{A'}\left(\frac{N-N_{tr}}{N_{tr}}\right)s(N) \tag{5.39}$$

$$s(N) = \frac{V_a\beta F_pBN^2}{\frac{1}{\tau_{ph}} - \frac{V_a\beta F_pB}{A'}\left(\frac{N-N_{tr}}{N_{tr}}\right)} \tag{5.40}$$

where the logarithmic gain is approximated by a linear function as in (5.30). Using the relation between G_0 and A' given by eq. (4.14) as well as equation (5.38), one can rewrite the previous set of equations as:

$$R_{inj}(N) = \left(F_pBN + \frac{1}{\tau_{NR}}\right)N + G_0\left(\tau_{ph},\beta\right)\left(\frac{N-N_{tr}}{N_{tr}}\right)s(N) \tag{5.41}$$

$$s(N) = \frac{V_a\beta F_pBN^2}{\frac{1}{\tau_{ph}} - V_aG_0\left(\tau_{ph},\beta\right)\left(\frac{N-N_{tr}}{N_{tr}}\right)} \tag{5.42}$$

where we replaced τ_0 by its expression as a function of the total photon lifetime τ_{ph} which is $\frac{1}{\tau_{ph}} = \frac{2}{\tau_0} + \frac{2}{\tau_c}$.

In practice, we do not measure R_{inj} nor s, but the input and output powers P_{in} and P_{out}, measured in arbitrary units. Proportionality coefficients X_0 and Y_0 are attached to P_{in} and P_{out} so that $R_{inj} = X_0P_{in}$ and $s = Y_0P_{out}$. Thus, we can finally rewrite:

$$P_{in}(N) = X_0\left\{\left(F_pBN + \frac{1}{\tau_{NR}}\right)N + G_0\left(\tau_{ph},\beta\right)\left(\frac{N}{N_{tr}} - 1\right)\frac{1}{Y_0}P_{out}\right\} \tag{5.43}$$

$$P_{out}(N) = Y_0\frac{V_a\beta F_pBN^2}{\frac{1}{\tau_{ph}} - V_aG_0\left(\tau_{ph},\beta\right)\left(\frac{N}{N_{tr}} - 1\right)} \tag{5.44}$$

where most parameters (F_p, B,...) are supposed known except the 4 unique unknowns: τ_{ph}, β, X_0 and Y_0.

In order to fit our model with our experimental data, we generate a numerical solution of this set of equations for carrier densities varying from $N_{tr}/100$ up to the a few N_{tr}. Our data is a table of m experimental measurements $[P_{in}^{exp}(k); P_{out}^{exp}(k)]$ that we compare to a table containing a sampling of m couples $[P_{in}^{model}(k); P_{out}^{model}(k)]$ from the generated solution. Then we define a residual Res that is

$$Res = \sum_{k=1}^{m} |log(P_{out}^{exp}(k)) - log(P_{out}^{model}(k))|^2 \tag{5.45}$$

Best solutions are found by minimizing this residual when the fitting parameters are varied. Obviously, if the number of fitting parameters is important, many solutions might appear with residual close to each other. This is generally the major drawback of this method, as one can find several solutions with parameters varying by several orders of magnitude. Here, we prevent the risk of inconsistent solutions by limiting our number of free variable to the β factor and the normalizing parameters X_0, Y_0. The fixed parameter values are summarized in Table 4.1. except for V_a which was determined using 3D FDTD calculations [122]. From literature [225], we take $N_{tr} = 10^{18} cm^{-3}$ and $B = 3.10^{10}\ cm^3.s^{-1}$, τ_{NR} is measured to be 200 ps [219]. For each fit, the intrinsic cavity decay time τ_0 is fixed, hence also τ_{ph} as τ_c is determined in the transmission measurements. We proceed in that way because we noticed that the range of suitable solutions, i.e. with minimal residuals, goes across a large range of possible values of τ_0. This means that the values of τ_0 are found with a quite large uncertainty.

A typical result of the fit using this model is plotted on Fig. 5.14 together with the measurements. The collected data are plotted using a custom MATLAB© interface that we used to roughly find the initial fit free variables values. Then a given range of possible τ_0 factor is entered and a MATLAB© built-in function minimises the residual. Even though it is not possible to determine τ_0 precisely, this method gives the range where the residual is minimal, and so, an estimated range for Q_0.

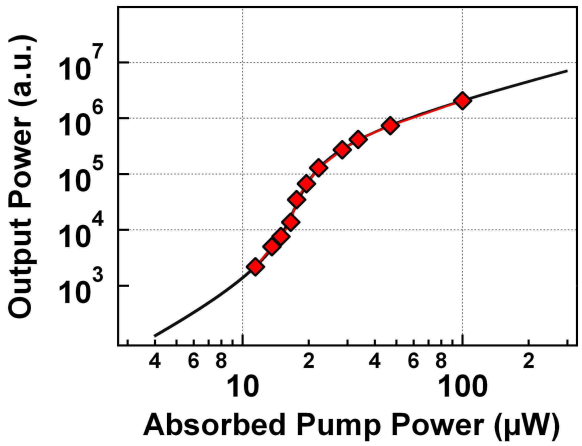

Figure 5.14: *Typical experimental characteristic laser curve (red rhumbus) in log-log scale and a fitted theoretical curve (in black).*

Now we have presented the procedure, we will focus on the proper study and its results in terms of coupling efficiency.

5.4 Coupling efficiency as a function of the opto-geometric parameters

In order to evaluate in detail the impact of the opto-geometrical parameters of the hybrid structure, we fabricated samples with hybrid structures with low-RI (BCB+SiO_2) intermediate layers of different thicknesses.

Three hybrid samples were fabricated with TD PhC Wire Cavities with intermediate SiO_2 layer thicknesses of 200, 300 and 400 nm, in addition to an approximately 80 nm thick BCB layer. Indeed, as it was illustrated in fig. 5.3, it is in that range of thicknesses that the coupling decay time τ_c will become shorter than the intrinsic decay time τ_0, here corresponding to Q_0 of the order of few 10000's [122]. This was expected to result in strong variations of the coupling efficiency. In addition to the separation distance d, the coupling efficiency was also studied as a function of the width w of the underlying SOI waveguide. In our SOI layer, Si waveguides of widths w varying from 250 nm to 550 nm are present. Such a variation has an impact on the real and on the reciprocal space overlaps of the two level modes which is also expected to strongly affect the coupling efficiency level.

Transmission measurements were carried out on the three samples together with the laser characterisation when it was possible. Figure 5.15 shows the measured quality factor of coupling Q_c as a function of the SOI waveguide widths and for the different SiO_2 thicknesses.

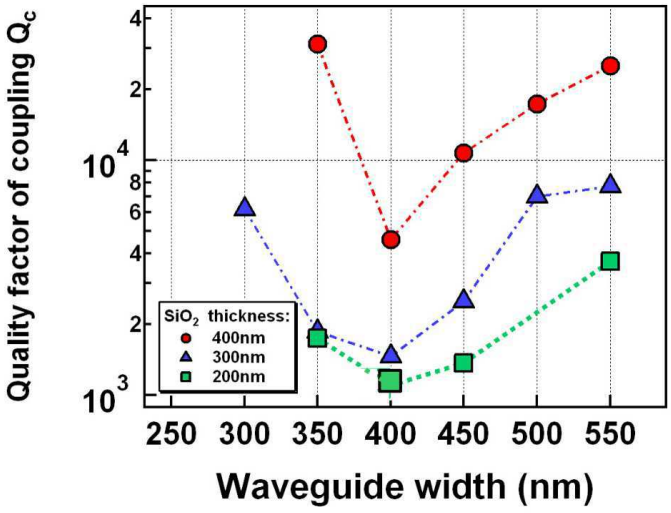

Figure 5.15: *Measured coupling quality factors Q_c as a function of the SOI waveguide width (220 nm high) plotted for three different thicknesses of the SiO_2 intermediate layer (200, 300 and 400 nm). The missing values are due to previously damaged cavities.*

The most striking feature of these measurements is that the traces possess similar shapes with an apparent minimum close to the width $w = 400$ nm. This minimum corresponds to the situation where the field distribution in the k-space of the cavity overlaps the most that of the

SOI waveguide mode as it will be explained a little bit ahead thanks to FDTD simulations. The other important feature is the strong variation of Q_c with the waveguide width. For instance, when $z = 400$ nm, Q_c varies from 5000 to 32000. Note that this graph shows some "missing" points due to previously damaged cavities on the studied samples.

For the sample with $z = 200$ nm, the value at $w = 400$ nm was not extracted from the ZTP value. Indeed, in this case, the coupling losses were so high that the cavity did not have enough gain to compensate the total optical losses and no lasing could be observed. In the end, we used relation (5.28) to determine τ_c. In the latest transmission measurements campaign, we systematically measure τ_c in the whole range of pump powers with relations (5.28).

For most of the waveguide widths, Q_c strongly increases when d increases.This is in agreement with the image of the evanescent transverse tails of each modes, rapidly decaying with the distance, leading to a lower overlap between each evanescent field.

5.4.1 Fitting procedure results and coupling efficiencies values

First, excellent fits of the measurements were obtained for τ_0 ranging from 10 ps to 83 ps ($6000<Q_0<50000$) and $0.16 < \beta < 0.35$. In order to improve these estimations, these values were cross-checked with the results of the fit of an S-curve for the same cavity but coupled to a waveguide of different width. Then, we obtained 16.5 ps $< \tau_0 <$ 49.5 ps ($10000<Q_0<30000$) and $0.2 < \beta < 0.3$ which are typical for this type of nanolasers allowing low laser threshold and ultra-fast dynamics [226]. Those values satisfied us at the time as they were in agreement with the one found in [122]. However, recently, we improved the fitting procedure by adding to the input/output powers data the linewidth below threshold $\Delta\omega(N)$. This gives us a supplementary constraint on β or β/A' if we cannot measure P_0 and P_1. We believe that, in the future, with such considerations we will further improve the accuracy of the τ_0 and β values.

The coupling efficiency η of the emitted light into the Si wires is plotted for the different studied structures in fig. 5.16. Each segment represents the possible range of values for η taking into account the uncertainties on Q_0. By adjusting the parameters of the structures we demonstrate it is possible to vary the efficiency at will from around 20 % to more than 90 % by controlling the evanescent wave coupling strength, i.e. Q_c. The maximum of efficiency is obtained for the thinnest low-RI layer and for $w = 400$ nm which gives the smallest value of Q_c. Yet, the cases corresponding to the highest η do not necessarily correspond to the ideal configuration as it also gives the largest optical losses in the system which may result in an increase of the laser threshold or even worse in a non-lasing situation (like in the case of w= 375 nm and z= 200 nm). The transition from lasing to non-lasing structures is observed to occur when the coupling efficiency goes beyond around 90 %, when the total Q factor of the system is lower than 2000. This estimated boundary between the two regimes is indicated by the dotted line on Fig. 5.16.

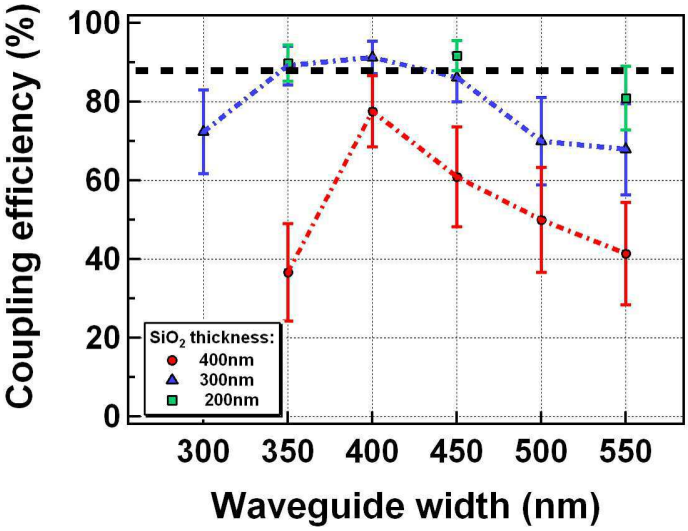

Figure 5.16: *Coupling efficiency η as a function of the waveguide width. The dots indicate the center of the range of Q_0.*

As demonstrated, Q_c can be adjusted by changing the structure parameters in order to obtain optimal coupling of laser emission to the SOI waveguide which can lead to coupling efficiencies well beyond 90 %.

Since those measurements, progress in the cavity fabrication (high resolution e-beam lithography, better dry etching anisotropy) has allowed us to improve the intrinsic quality factor of the cavities and obtain lower threshold. With this new generation of hybrid structures, we obtain larger Q_0/Q_c ratios (see Section 5.4.3), i.e. higher coupling efficiencies while maintaining sufficiently small total losses to observe laser emission.

In the last part of this chapter, we present the result of coupling simulations realised on apodised cavities coupled to SOI waveguides. We choose to perform the simulations on this type of cavity instead of TD PhC Wire Cavities for two reasons. The first is that because of their theoretical high-Q values they are very promising object in terms of laser behaviour and coupling efficiency. The second is that the centre of the cavity mode in the k-space is very close to $\frac{\pi}{a_0}$ with a_0 the central period of the structure. With this design, the k-space overlap is rendered much easier to achieve.

5.4.2 FDTD Simulations of the coupling in hybrid structures

By performing 3D FDTD simulations, it is possible to retrieve the Q-factor of a fully encapsulated apodised PhC Wire Cavity coupled to an SOI waveguide of width w. The FDTD simulations of the hybrid structures can be much longer to perform than isolated cavities due to the larger volume to simulate and the lower number of symmetry planes. Besides, because we do not know *a priori* the final order of magnitude of Q (the Q_0 of the uncoupled cavity is around 10^6), the simulation time is hardly adaptable and should be long enough to preserve the accuracy on the

Q values extracted with harmonic inversion (see Section 2.1.4.2).

Figure 5.17 shows how the Q-factor of the hybrid cavity and the associated coupling efficiency vary with w and d[1]. The range of the variations of d and w were chosen to include the parameters of three fabricated samples. One can clearly see that the Q factor and the coupling efficiency are, as expected, strongly affected by d and w due to the induced modification of the coupling conditions. For certain dimensions of the waveguide, the total Q even drops from 2, 3 or 4 orders of magnitude giving coupling efficiency very close to 1. This high coupling efficiency that results from the total Q alteration can be achieved in the hybrid structure when two conditions are fulfilled: a high spatial overlap between the two individual mode profiles and a high overlap in the k-space, i.e. a good phase-matching.

The spatial overlap depends on both d and w. As can be seen on the figure, the total Q decreases as d decreases for all w values which can be simply explained by the enhanced penetration of the evanescent tail of the field within the other waveguide. However, the impact of d on Q is different for different w's. Indeed, for waveguides with $w < 350$ nm, the variation of Q with d is smaller than in the case of the larger waveguides. In these waveguides, the guided mode is much less confined giving broader transverse mode profiles with longer evanescent tails than that of larger waveguides explaining thereby the poorer sensitivity of Q with d.

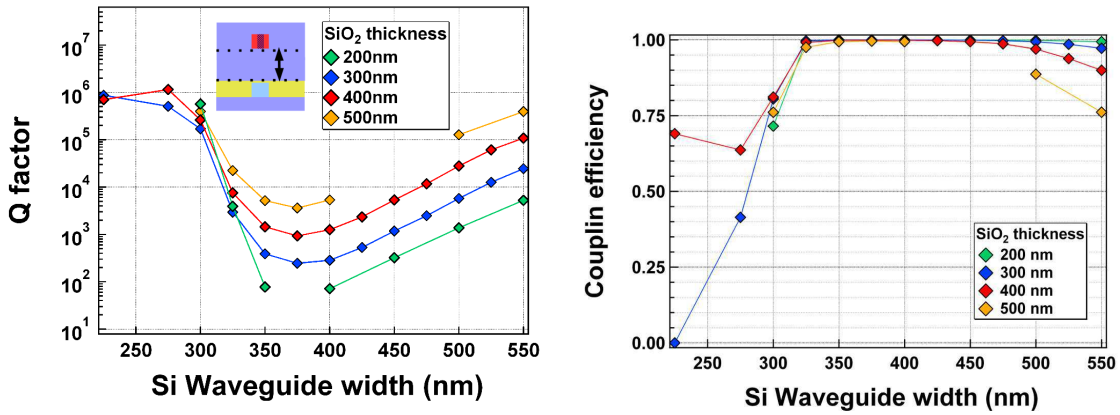

Figure 5.17: *Simulation results: Q factors and coupling efficiencies of the coupled cavities as a function of the SOI waveguide width and for SiO_2 intermediate layer thicknesses going from 225 to 550 nm.*

The k-space overlap or the phase-matching condition explains the strong variations of Q with w for each d and the experimental observation of an optimum of coupling, also corresponding to a minimum of Q_c.

In order to give a good description of what happens when the width w is varied, it is interesting to first analyse the variations of λ (or ω) with w. Indeed, the plot of λ as a function of w, for several values of d (see fig. 5.18), results in Fano-shaped curves, centred on a waveguide width equal to 375 nm. Remark that the "amplitude" of these Fano-shapes increases when the d is

[1]We recall that d is the sum of the BCB thickness above the top of the waveguide, which is estimated to be 80 nm, and the SiO_2 layer sputtered below the III-V.

decreased, i.e. when the coupling efficiency increases.

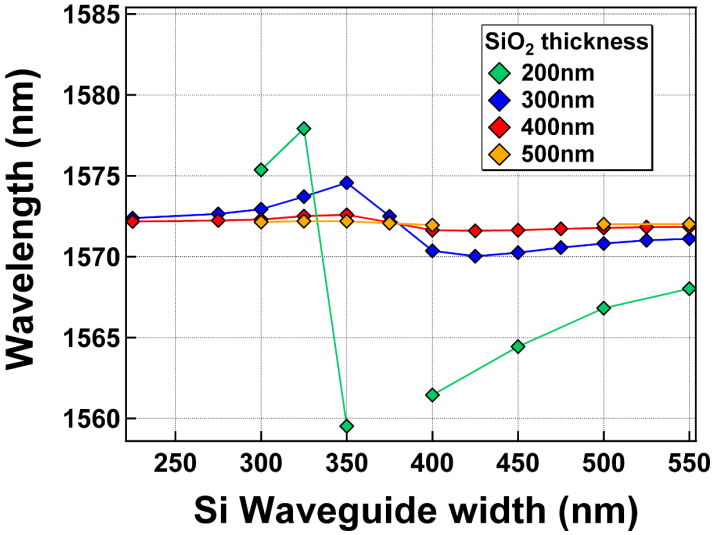

Figure 5.18: *Resonant wavelength λ of the cavities as a function of the SOI waveguide width and for SiO_2 intermediate layer thicknesses going from 225 to 550 nm.*

Similarly to what happens in a system made of two evanescently coupled waveguides, our system dispersion curves are a mix of the SOI waveguide mode dispersion and the "cavity dispersion" which are represented in figure 5.19 by the dashed red and blue lines for the waveguides and the green line for the cavity. As represented in the figure, splitting should be observed where the 2 modes cross and should result in modified dispersion relations. These relations form two branches whose modes are sometimes referred as supermodes in the case of coupled waveguides [227].

However, because we deal with a cavity, the cavity dispersion branch does not exist for any wavevector value but has a limited extension around $k_x \approx \frac{\pi}{a_0}$, which corresponds, in the case of our apodised PhC Wire Cavity, to the maximum of the field distribution in the k-space. The reason why the cavity frequency describes a Fano shape when the waveguide width varies is the following. At $k_x = \frac{\pi}{a_0}$, the supermode frequency corresponding to the case where the field is mostly in the cavity is the one the closest to the uncoupled cavity frequency ω_0. As it is schematised in fig. 5.19, the cavity resonant frequency always correspond to this cavity-*like* supermode. However, the shift from ω_0 due to the presence of the SOI waveguide is different depending on whether the crossing of the modes occurs at $k_x > \frac{\pi}{a_0}$ or $k_x < \frac{\pi}{a_0}$. When $w<w_{PM}$, which is here around 375 nm, the crossing occurs at $k_x<\frac{\pi}{a_0}$ and the resonant frequency is lowered compared to ω_0 as indicated in the 5.19 by a yellow star. Similarly when $w>w_{PM}$, the crossing occurs at

$k_x > \frac{\pi}{a_0}$ and the resonant frequency is increased. In the optimal coupling case where w=w_{PM}, the resonant frequency appears in the simulations to be very close to ω_0.

We see that the frequency shift of the coupled-cavity mode depends on the detuning $\left|\frac{\pi}{a_0} - \beta_g\right|$ between the uncoupled cavity mode centre ($\approx \frac{\pi}{a_0}$) and the SOI waveguide mode propagation constant β_g. When this detuning equals zero, the overlap between the two k-space mode distributions is large. In this condition of phase-matching, for a given cavity-waveguide distance d, the coupling efficiency is maximum.

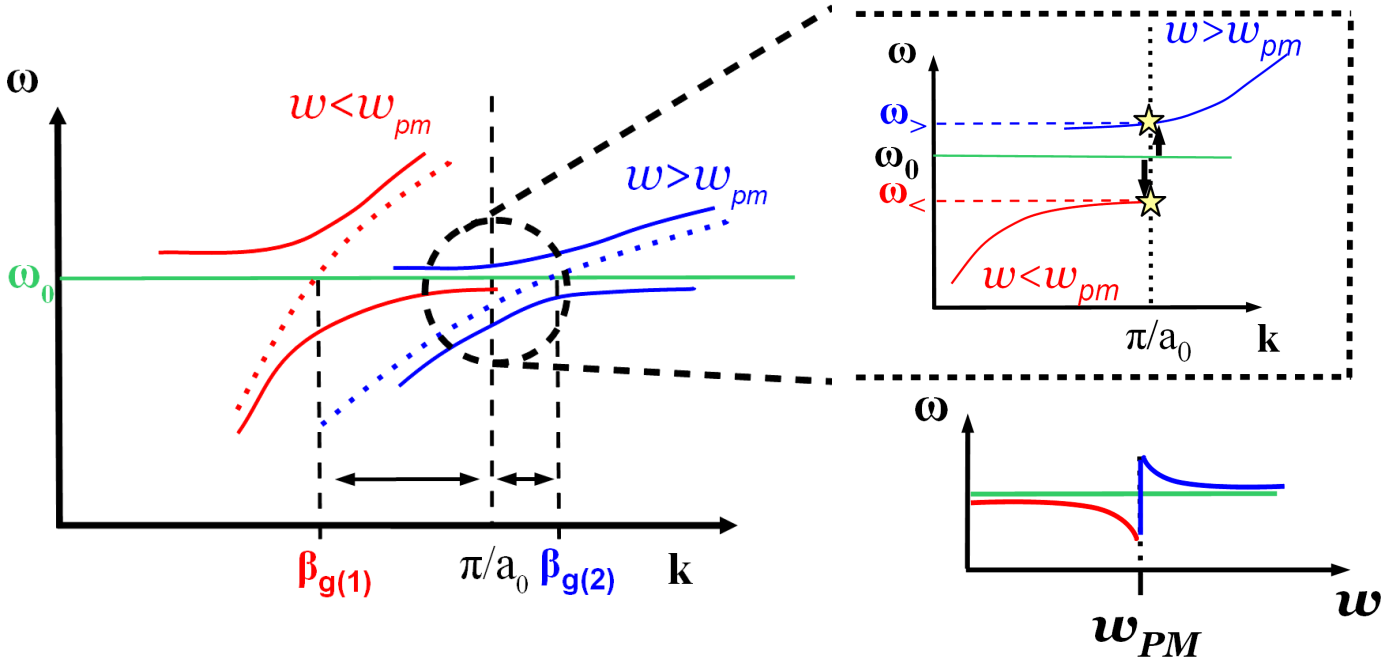

Figure 5.19: *Schematised dispersion diagrams for the cavity-waveguide coupled system and frequency variations of the cavity as a function of the waveguide width.*

In order to prove the veracity of this mechanism, it is useful to define a value for the k-space overlap, that we note Θ, which verifies:

$$\Theta \propto \int dk_x \delta(k_x - \beta_g(w)(\lambda_{w,d}))FFT(E_y)(k_x) \tag{5.46}$$

where we restrain the integral to the k_x direction of the k-space. $\lambda_{w,d}$ is the PhC cavity resonant wavelength which depends on w and d, $\beta_g(w)(\lambda_{w,d})$ is the propagation constant of the SOI waveguide at the wavelength $\lambda_{w,d}$ and $FFT(E_y)(k_x)$ is the Fourier Transform of the uncoupled cavity mode.

Figure 5.20 shows the distribution of an uncoupled apodised PhC Wire Cavity mode in the k-space around π/a_0. Superimposed, the red sticks indicate the position of the propagation constant β_g at the cavity mode wavelength for waveguide widths between 250 and 550 nm. These values are calculated with the Lumerical Mode Solver giving the effective index n_{eff} at the given wavelength and using the relation $\beta_g = \frac{2\pi}{\lambda} n_{eff}$. The phase-matching condition, i.e. the maximum of k-space overlap, is achieved for w_{PM}=375 nm. One can note that β_g decreases more and more rapidly as w is diminished. This is the reason why the phase mismatch becomes rapidly large for waveguides with w<375 nm, and why the associated Q-factor rockets. For waveguides larger than w_{PM}, β_g smoothly increases with w which gives the shallow increase of Q (or Q_c) with w and the asymmetric shape of the curve of fig. 5.17. With these data, from relation (5.46), it is possible to retrieve, to within a scalar factor, the integral in the k_x-direction. Because the guided mode is described by a Dirac function, these integrals are simply equal to the value of the cavity mode distribution at β_g.

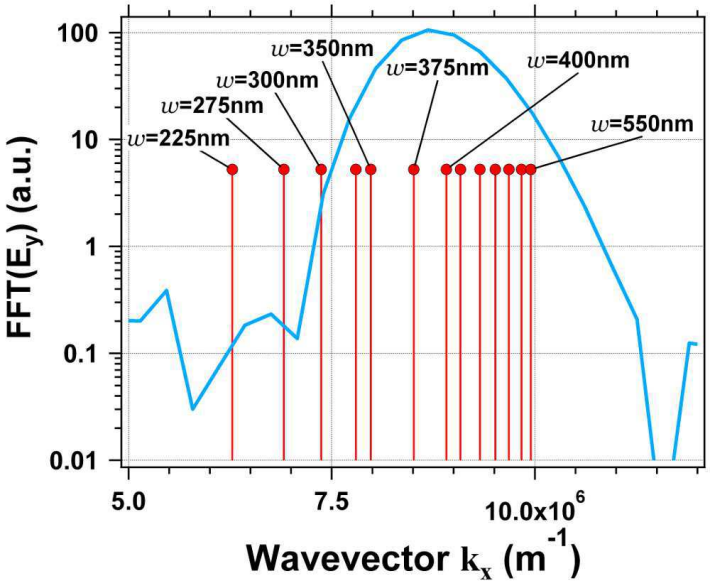

Figure 5.20: *Fourier Transform of the cavity mode as a function of the wavevector k_x, for a SiO_2 thickness of 300 nm. The red sticks indicates the propagation constant β_g, at the wavelength of the cavity, for each SOI waveguide width.*

Figure 5.21 now compares, as a function of w, the overlap in the k_x direction with the inverse of the coupling Q-factor Q_c, both normalised to their maximum values. The y-axis range of the plot is the same (40 dB) for the two normalised variables. As expected, they behave almost identically when w is varied. We believe that the small remaining discrepancies come from the fact the transverse spatial overlap is not taken into account.

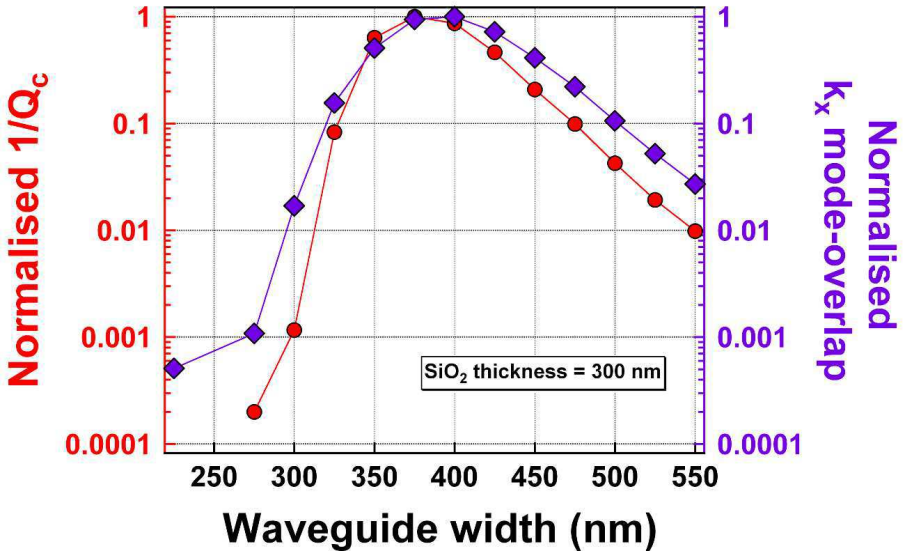

Figure 5.21: *Values of $1/Q_c$ (left axis) and of the k_x mode-overlap (right axis), normalised to their maximum, as a function of the width of the SOI waveguide.*

5.4.3 Comparison with measurement on apodised PhC Wire Cavity

We performed measurements of coupling efficiency on a sample of hybrid structures containing apodised cavities. The thickness of the SiO_2 intermediate layer is 300 nm. These measurements consisted in transmission measurements in order to obtain the coupling quality factor Q_c as a function of w, similarly to the previous study on the TD PhC Wire Cavities. Note that the cavities were pumped in CW regime.

In figure 5.22 are plotted the experimental results together with the simulated values of Q_c. We measured that Q_c varied from 22000 for $w = 550$ nm to less than 600 for $w = 450$ nm. On this particular sample, it was not possible to measure precisely Q_c for waveguide widths smaller than 400nm, however we can surely affirm that Q_c is much greater than 22000 for $w < 400$ nm. These results are in good agreement with the values of Q_c predicted by the simulations. The only difference seems to be that the minimum measured Q_c corresponds to a slightly larger waveguide ($w = 400$ nm instead of $w = 375$ nm). Two effects could explain this: 1) the central period a_0 of the fabricated apodised cavity is larger than expected and/or 2) the fabricated SOI waveguides widths are smaller than expected. The former assumption seems unlikely to happen as the central period of the structure is defined by the ebeam system with a sub-nanometric with precision. The second effect is more realistic as we know that there exists differences of the SOI wire width from one die to the other on the 200 mm SOI wafer.

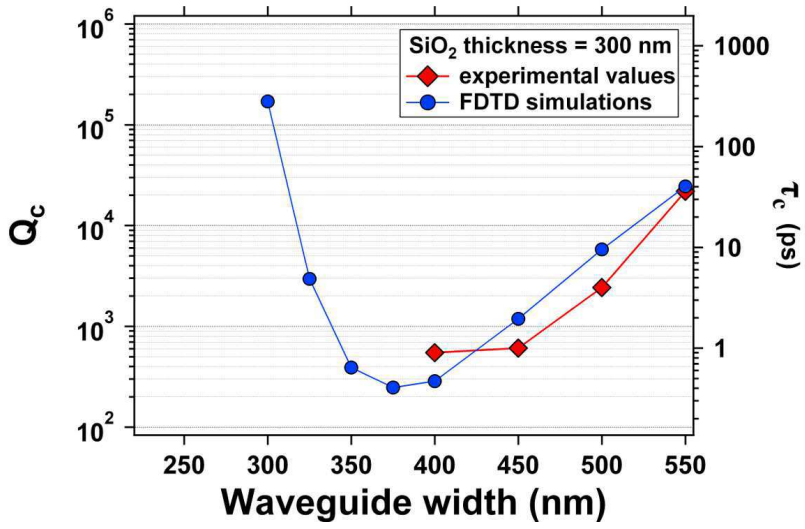

Figure 5.22: *Comparison between Q_c found in simulations and in transmission measurements.*

The intrinsic quality factor Q_0 was retrieved through a laser rate equations fit procedure. The fit procedure gives value of Q_0 around 35000 and a spontaneous emission factor β around 0.05. The coupling efficiency is deduced and plotted on fig. 5.23. This shows that the coupling efficiency can be precisely controlled from 98% to 60% playing on w.

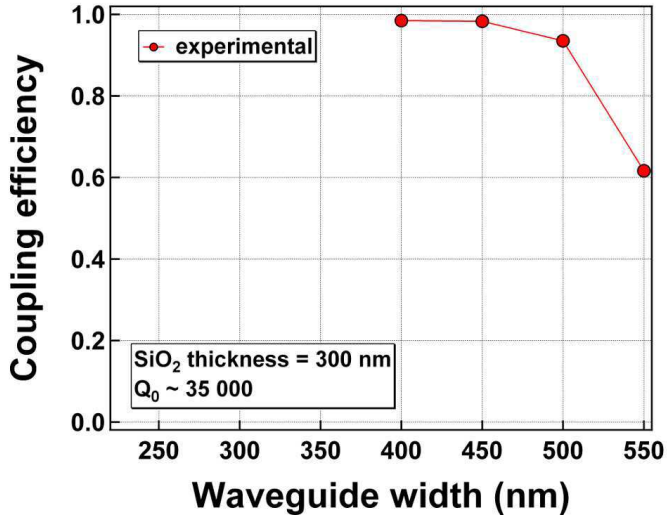

Figure 5.23: *Estimated coupling efficiency versus the SOI waveguide width.*

5.5 Conclusion

The evanescent wave coupling occurring in our hybrid structure between a PhC Cavity laser and a SOI waveguide was minutely studied in this chapter theoretically, numerically and experimentally. We demonstrated that the coupling is governed by the overlap of the cavity mode with the SOI wire mode both in the direct space and the reciprocal space. The spatial overlap is under control by adjusting the vertical separation of the cavity with the SOI wire and the lateral offset of the 2 levels. We demonstrated that these parameters can be accurately fixed by using the technological procedure shown in chapter 3.

Even though we deal with a stationary mode with our PhC cavity, it is also very convenient to analyse the coupling using the reciprocal space as, in this space, the electromagnetic field distribution of these optimised cavities exhibit a very narrow extension around a certain wavevector (around $\frac{\pi}{a_0}$ for the apodised wire cavity). The overlap in the $k-space$ can be almost tuned at will by adjusting the opto-geometrical features of the cavity and the SOI wire giving a handle on the coupling efficiency. Indeed, the beauty of our hybrid III-V/SOI structure is that, by using these two materials which possess almost identical RI, it is possible to control the coupling strength just by changing the design of the III-V or the SOI level. This type of control, for example, is not possible using an optical fibre instead of the SOI wire as the silica refractive is half that of the III-V.

This dependence of the coupling efficiency on the $k-space$ overlap was demonstrated numerically and experimentally by coupling the same PhC cavity laser to SOI waveguides of different widths. The coupling efficiency was retrieved using an original experimental method relying on pump-probe measurements of the transmission of the structure which were analysed using the temporal coupled theory. This method enables the direct measurement of the coupling constant of the system. These measurements associated with the laser light-light characteristics allow us to fully characterise the coupling efficiency of our hybrid PhC laser. The estimated experimental values of the coupling efficiency can be higher than 90% depending on the waveguide width and the vertical separation of the 2 levels which was confirmed by FDTD numerical simulations.

I believe that our hybrid platform offers an elegant and efficient way to interface active PhCs cavities within an optical circuitry by enabling the passive/active integration together with a remarkable control over the coupling efficiency. In this chapter, we used this scheme of integration to collect the laser emission. Of course, this is only one side of the benefit that it brings. In the next chapter, we will show that it is possible to efficiently inject light within our PhC cavity laser and demonstrate low power bistable switching.


high
identified
mechanism
tens
increases
vapour
absorptive
excellent
power
bulk
augment
filled
slow
structures
slightly
good
medium
use
operation
heat
optical
consequently
feedback
generation
non-linear
PhC
change
thereby
gain
linearly
devices
including
turn
intracavity
isolated
resonator
close
ios
two
challenge
PhCs
material
effects
injected
non-linearly
higher
based
point
different
optimal
input
thanks
type
consumption
stays
intensities
factor
efficient
result
fact
ends
next
materials
resonant
resonances
absorption
Nevertheless
occurring
system
compared
resonators
saturation
RI
due
thermo-optical
powers
wavelength
absorber
dispersive
planar
phenomenon
al
right
vastly
bistability
microcavities
stimulated
absorbing
also
dynamics
bistable
time
firstly
order
low
non-linearity
heterostructure
reaches
faster
shows
Bistability
studied
decrease
effect
biased
switching
Szöke
recently
value
decreased
However
semiconductor
off-resonance
resonance
starts
electronic
lasers
Fabry-Perot
using
systems
achieving
cavity
Optical
injection
structure
ns
hybrid
increasing
et certain
compete
allow
obtain
demonstrated
loaded
obtained
takes
sensitivity
hundreds
ps
dependent
light
intensity
optically
taking
either
laser
explained
diminishes

Chapter 6

Optical bistability of injected PhC laser in a hybrid III-V/SOI structure

Optical bistability, as its name indicates, refers to a situation in which an optical system can generate two different stable output powers from a single ensemble of input parameters. This phenomenon is often characterised by the observation of an hysteresis cycle in the graph depicting the output power versus the input power as shown in figure 6.1. For a given input, either the upper or the lower branch output values are obtained, depending on how the system is prepared. This cycle may be clockwise or anticlockwise which indicates the way of acting on the system in order to switch from one state to the other.

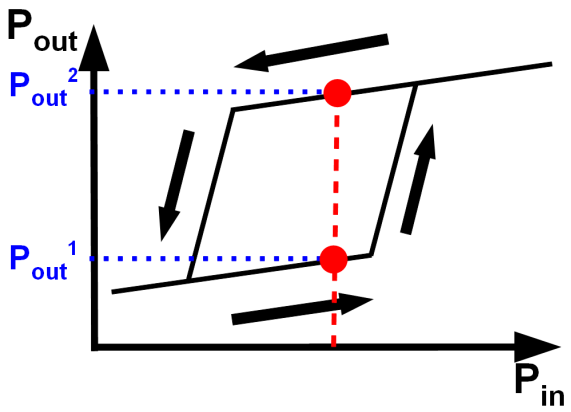

Figure 6.1: *Example of a hysteresis cycle. Two paths for the output power are possible*

Optical bistability is of great importance for applications as it is a simple and robust paradigm for the realization of optical transistors and memories. These bistable devices enable indeed nec-

essary functionalities for all-optical logical data processing such as signal regeneration [228] or optical demultiplexing [229].

During my PhD, I explored optical bistability in the hybrid III-V/SOI PhC lasers with the view to showing that these "nano" devices are endowed with exceptional performance in terms of footprint, power consumption and speed.

In this chapter, I firstly review rapidly the way to achieve optical bistability with semiconductor PhCs resonators. Then, I analyse the theory of bistability based on the injection-locking mechanism obtained with PhC lasers before detailing the experimental studies on the bistable behaviour of the fabricated samples.

6.1 Optical bistability in semiconductor PhCs resonators

Bistability requires both a non-linear medium and a feedback mechanism. One way to obtain such a phenomenon with an optical system is to use an optical resonator filled with an optically non-linear material. The association of an optical resonance with a material showing an intensity dependent RI or absorption (or gain), allows indeed to have two different output powers for the same input power. Saturation of absorption was the first non-linear effect exploited to end up with a bistable behaviour. Bistability based on this non-linear effect was firstly proposed in 1964 [230] and demonstrated in 1965 [231] using a semiconductor Fabry-Perot laser diode which included two electrically isolated portions, one biased to obtain gain the other biased to have a saturable absorber. In 1969, Szöke et al. [232] implemented this concept in a passive Fabry-Perot etalon filled with an absorbing vapour of SF_6. In these systems, bistability is explained by the fact that the same input power (electrical for [231] and optical [232]) can result in 2 different intracavity intensities at resonance. Indeed, at low input powers, absorption of the material is high and almost constant so that the intracavity intensity increases linearly with the input power. For increasing input powers, the absorption begins to decrease, augmenting the loaded Q factor of the resonator and, consequently, the intracavity intensity, which causes in turn a further decrease of the absorption. The intracavity intensity grows very non-linearly with the input power up to certain point for which the absorption is completely bleached. For higher input powers, the intracavity intensity increases again linearly with the input power. Now, when the input power is decreased, the intracavity intensity diminishes linearly as the material absorption weakly changes. It stays higher than its previous level for the same input power until it reaches a value where the saturation of absorption ends.

Bistability based on an intensity dependent RI was demonstrated in 1976 [233] using a Fabry-Perot cavity filled with Na atom vapour. Similarly to the saturation of absorption case, bistability is obtained because a single input power can result in 2 different intracavity intensities. This time, light is injected at a wavelength slightly detuned from the resonant wavelength. As the input power is increased, the cavity resonant wavelength is pulled towards the injection wavelength due to the change of RI, increasing thereby the intracavity intensity which in turn augments the pulling effect. This gives again a very non-linear increase of the intracavity intensity with the input power up to a certain point. When the input power is decreased, the intracavity intensity

takes a different path until it reaches a value where the injection becomes off-resonante. Semiconductor materials (bulk or including quantum confined structures) were identified as excellent materials to achieve bistability right from the early stage of research on this topic [231, 234] as these materials enable very efficient absorptive (or gain) and dispersive non-linearity when they are used close to their electronic resonances [235]. But, they also allow the fabrication of very good optical resonators by taking advantage of the growth or the patterning of high reflectivity mirrors, which is crucial in the quest of achieving power efficient devices. Optical bistability was widely studied in semiconductor planar microcavities [236, 237, 238] and was, more recently demonstrated using semiconductor based PhC resonators in order to further reduce the power consumption and the device footprint. In most of the studies related to PhCs, bistability was demonstrated using a dispersive non-linearity. The non-linearity was either induced by thermo-optical effects [239, 240, 241] or by an optically stimulated change of carrier density in the semiconductor [242, 243], the second type of effect enabling a much faster dynamics (of the order of few hundreds of ps compared to few hundreds of ns for thermal effects). PhCs allow bistable switching with powers as low as few tens of nW [244] thanks to the strong light localisation occurring in these structures.

However, the achievement of continuous operation of these bistable devices remains a challenge mainly due to the poor heat evacuation in the structure and the extreme sensitivity of its optical properties to the environment. Only one recent work by Nozaki et al. [244] shows a stable bistable operation over 10s. This was achieved thanks to a fine optimisation of the structure material (use of burried heterostructure) which facilitates very low operating powers reducing thereby heat generation. Nevertheless, this system is still not optimal as the measured memory dynamics, characterised by a switching time of 44 ps and a recovery time of about 7 ns, is rather slow and should be improved to compete with electronic devices.

During my PhD, I focused my attention on the bistable operation that can be obtained with our hybrid PhCs operated in the laser regime. This type of bistability, which is described in the next section, based on the injection locking mechanism, was of course studied in other types of semiconductor lasers such as edge emitters [245, 246] and VCSELs [247], but also very recently in InP-based PhC lasers [248]. It should allow both low power consumption and fast dynamics.

6.2 Injection-locking based bistability analysis

6.2.1 Rate equations model

Let's consider a single mode laser injected at ω_{ext} by an external laser of electrical field E_{ext}. The field E_{ext} is written as

$$E_{ext} = E_{ext}^{0} e^{j(\omega_{ext} t + \phi_{ext})} \tag{6.1}$$

where E_{ext} is power normalized so that $|E_{ext}|^2 = P_{ext}/(\hbar\omega_{ext})$. For simplicity, the phase of this field ϕ_{ext} is taken to be fixed and equal to 0.

The intracavity field of the laser when it is injected writes [249, 250, 251]

$$\frac{dE}{dt} = \left(\frac{1}{2}V_a G(N) - \frac{1}{2\tau_{ph}} + j\omega(N)\right) E + \kappa E_{ext} \tag{6.2}$$

where

$$G(N) = G_0 \ln\left(\frac{N}{N_{tr}}\right) \qquad \text{with } G_0 = \frac{\beta F_p B}{A'} \tag{6.3}$$

and

$$\begin{aligned} \omega(N) &= \omega_{tr} + \frac{1}{2}\alpha_H V_a G(N) \\ &= \omega_{tr} + \frac{1}{2}\alpha_H V_a G_0 \ln\left(\frac{N}{N_{tr}}\right) \qquad (6.4) \\ &= \omega_{th} + \frac{1}{2}\alpha_H V_a G_0 \ln\left(\frac{N}{N_{th}}\right) \qquad (6.5) \end{aligned}$$

where τ_{ph}, G_0, α_H, β, F_p, B, and V_a are the same parameters introduced in the previous chapter. N_{tr} and N_{th} are the carrier densities respectively at transparency and at the laser threshold in the free-running laser case, i.e. with no external optical injection. $\omega_{tr} = \omega(N_{tr})$ is the frequency of the cavity at transparency and $\omega_{th} = \omega(N_{th})$ is the free-running laser frequency at threshold. The coefficient κ is the coupling factor of the light incident on the laser. If the injection is made through the Si waveguide, this coefficient is equal to $1/\sqrt{\tau_c}$ as it was calculated in the previous chapter (Section 5.2).

Let's write the field as $E(t) = E_0(t)e^{j(\omega_{th}t+\phi_0(t))}$ with $\phi_0(t)$ the temporally varying phase accounting for the change of frequency and for the dephasing due to the injection.

We insert the new expression for the field into eq.6.2 and obtain

$$\frac{dE}{dt} = \frac{dE_0}{dt}e^{j\,(\omega_{th}t+\phi_0(t))} + E_0(t) \times j\left(\omega_{th} + \frac{d\phi_0}{dt}\right)e^{j\,(\omega_{th}t+\phi_0(t))} \tag{6.6}$$

which now becomes,

$$\frac{dE}{dt} = \left(\frac{1}{2}V_a G(N) - \frac{1}{2\tau_{ph}} + j\omega(N)\right) E_0 e^{j(\omega_{th}t+\phi_0(t))} + \kappa E^0_{ext} e^{j\omega_{ext}t} \tag{6.7}$$

By separating real and imaginary parts, we get:

$$\begin{aligned} \frac{dE_0}{dt} &= \frac{1}{2}\left(V_a \frac{\beta F_p B}{A'} \ln\left(\frac{N}{N_{tr}}\right) - \frac{1}{\tau_{ph}}\right) E_0 + \kappa E^0_{ext} cos\,(\Delta\omega t - \phi_0(t)) \qquad (6.8) \\ \frac{d\phi_0}{dt} &= \omega(N) - \omega_{th} + \kappa \frac{E^0_{ext}}{E_0(t)} sin\,(\Delta\omega t - \phi_0(t)) \qquad (6.9) \end{aligned}$$

where we introduced the frequency detuning to the frequency at threshold as $\Delta\omega = \omega_{ext} - \omega_{th}$.

Equation 6.8 does not take into account the part of the emission which is not locked to the injection, i.e. whose frequency is at $\omega(N)$.This part of the emission is taken into account by going back to the standard relation of the rate equation 4.16 linking the emitted photon number s to the carrier density N:

$$\frac{ds}{dt} = -\frac{s}{\tau_{ph}} + V_a \beta F_p B \left(N^2 + \frac{1}{A'} \ln\left(\frac{N}{N_{tr}}\right) s \right) \tag{4.16}$$

Now, the equation for the carrier density variation is a modified version of eq. 4.15 and is given by

$$\frac{dN}{dt} = R_{inj} - R_{sp} - R_{NR} - \frac{\beta F_p B}{A'} \ln\left(\frac{N}{N_{tr}}\right) \left(s + |E_0|^2\right) \tag{6.10}$$

The phase difference between the internal and the external field is put as

$$\varphi(t) = \phi_0(t) - \Delta\omega t \tag{6.11}$$

Then, eq. 6.9 becomes

$$\frac{d\varphi}{dt} = \frac{1}{2}\alpha_H V_a \frac{\beta F_p B}{A'} \ln\left(\frac{N}{N_{th}}\right) - \Delta\omega - \kappa \frac{E^0_{ext}}{E_0(t)} sin\left(\varphi(t)\right) \tag{6.12}$$

and eq. 6.8 becomes

$$\frac{dE_0}{dt} = \frac{1}{2}\left(V_a \frac{\beta F_p B}{A'} \ln\left(\frac{N}{N_{tr}}\right) - \frac{1}{\tau_{ph}} \right) E_0 + \kappa E^0_{ext} cos\left(\varphi(t)\right) \tag{6.13}$$

To summarize, the coupled equations for the injected laser are

$$\begin{aligned}
\frac{dE_0}{dt} &= \frac{1}{2}\left(V_a \frac{\beta F_p B}{A'} \ln\left(\frac{N}{N_{tr}}\right) - \frac{1}{\tau_{ph}} \right) E_0 + \kappa E^0_{ext} cos\left(\varphi(t)\right) && (6.14)\\
\frac{d\varphi}{dt} &= \frac{1}{2}\alpha_H V_a \frac{\beta F_p B}{A'} \ln\left(\frac{N}{N_{th}}\right) - \Delta\omega - \kappa \frac{E^0_{ext}}{E_0(t)} sin\left(\varphi(t)\right) && (6.15)\\
\frac{dN}{dt} &= R_{inj} - R_{sp} - R_{NR} - \frac{\beta F_p B}{A'} \ln\left(\frac{N}{N_{tr}}\right) \left(s + |E_0|^2\right) && (6.16)\\
\frac{ds}{dt} &= -\frac{s}{\tau_{ph}} + V_a \beta F_p B \left(N^2 + \frac{1}{A'} \ln\left(\frac{N}{N_{tr}}\right) s \right) && (6.17)
\end{aligned}$$

6.2.2 Stationary regime

In the stationary regime ($\frac{d}{dt} = 0$), the coupled equations become

$$0 = \frac{1}{2}\left(V_a \frac{\beta F_p B}{A'} \ln\left(\frac{N}{N_{tr}}\right) - \frac{1}{\tau_{ph}}\right) E_0 + \kappa E^0_{ext} cos\left(\varphi(t)\right) \tag{6.18}$$

$$0 = \frac{1}{2}\alpha_H V_a \frac{\beta F_p B}{A'} \ln\left(\frac{N}{N_{th}}\right) - \Delta\omega - \kappa \frac{E^0_{ext}}{E_0(t)} sin\left(\varphi(t)\right) \tag{6.19}$$

$$0 = R_{inj} - R_{sp} - R_{NR} - \frac{\beta F_p B}{A'} \ln\left(\frac{N}{N_{tr}}\right)\left(s + |E_0|^2\right) \tag{6.20}$$

$$s = \frac{V_a \beta F_p B N^2}{\dfrac{1}{\tau_{ph}} - V_a \dfrac{\beta F_p B}{A'} \ln\left(\dfrac{N}{N_{tr}}\right)} \tag{6.21}$$

Note that the denomination of injection locking takes all its sense considering the meaning of the equality $d\phi/dt = 0$ that is that the injected laser frequency is locked to injection frequency ω_{ext} which is most of the time different from the cavity resonant frequency $\omega(N)$. It is useful to express each of the variables (E^0_{ext},φ,s) with N as it was done for the laser rate equations to obtain the steady states characteristics. After some mathematical operations, we can finally write

$$\varphi = atan\left\{\frac{\dfrac{1}{2}\alpha_H V_a \dfrac{\beta F_p B}{A'} \ln\left(\dfrac{N}{N_{th}}\right) - \Delta\omega}{\dfrac{1}{2}\left(\dfrac{1}{\tau_{ph}} - V_a \dfrac{\beta F_p B}{A'} \ln\left(\dfrac{N}{N_{tr}}\right)\right)}\right\} \tag{6.22}$$

$$s = \frac{V_a \beta F_p B N^2}{\dfrac{1}{\tau_{ph}} - V_a \dfrac{\beta F_p B}{A'} \ln\left(\dfrac{N}{N_{tr}}\right)} \tag{6.23}$$

$$|E_0|^2 = \frac{\left(R_{inj} - F_p B N^2 - \frac{N}{\tau_{NR}}\right)}{\dfrac{\beta F_p B}{A'} \ln\left(\dfrac{N}{N_{tr}}\right)} - s \tag{6.24}$$

$$|\kappa E^0_{ext}|^2 = |E_0|^2 \times \frac{1}{4} \frac{\dfrac{1}{\tau_{ph}} - V_a \dfrac{\beta F_p B}{A'} \ln\left(\dfrac{N}{N_{tr}}\right)}{cos^2\left(\varphi\right)} \tag{6.25}$$

where $|E_0|^2$ is the intracavity photon number at the injection frequency ω_{ext} and $|\kappa E^0_{ext}|^2$ is the rate of external photons coupled into the cavity.

6.2.3 Numerical solving of an injected PhC laser

The set of equations (6.22) to (6.25) allows us to characterise the static behaviour of an injected PhC laser in the hybrid structure. They form a parametric set of equations of parameter N, the carrier density . For a given external injection frequency ω_{ext} and a fixed pump power R_{inj} above threshold, we vary N over a large range of values and calculate for each value in the following order:

- the photon number s at the cavity resonance frequency $\omega(N)$
- the phase difference between the intracavity and external fields ϕ
- the photon number $|E_0|^2$ at the injection frequency ω_{ext}
- the injection power given by $|\kappa E^0_{ext}|^2$ (under the assumption of a coupling coefficient κ)

6.2.3.1 Distorted resonances with the wavelength detuning

To start our analysis, we decide to simulate the case of a cavity pumped above the laser threshold, at $1.5 \times R_{th}$ (arbitrary choice). When the PhC laser is freely running, the carrier density at this pump power can be considered as clamped at N_{th}. We note the free-running emission wavelength λ_f. Now, let's fix the external injection power P_{ext} at 0.2 μW and the coupling factor κ such that the coupling efficiency is 70%. Using the parameters given in table 6.1, we start by calculating and plotting in figure 6.2 the number of photons $|E_0|^2$, to which we will refer to as the "locked" photons at the injection wavelength λ_{ext}, and the number of photons s at the cavity resonance frequency $\lambda(N)$ ("unlocked"), both numbers are given as a function of the wavelength detuning of the injection from λ_f.

λ_{tr} =1550 nm	$P_{ext} = 0.2\ \mu W$
$Q = 20000$	$A' = 5 \times 10^{-36}$
$\beta = 0.1$	F_p=2.3
$N_{tr} = 10^{18}\ cm^{-3}$	V_a=6.8 $\times 10^{-14}\ cm^3$
B= 3 $\times 10^{-10}\ cm^3/s$	$\alpha_H = 6$

Table 6.1: *Numerical parameters used in the injection-locking based bistability analysis.*

We observe that the graph of the locked photon number versus detuning shows a distorted resonant peak in comparison to a regular Lorentzian lineshape. This distortion is directed towards the higher wavelengths due to the positive Henry factor α_H. Because of this particular lineshape, we observe a range of detuning for which three solutions exist at each detuning. As an example, we indicate by red circles those solutions for a fixed detuning of 0.2nm. In the upper solutions branch, the number of locked photon at the injected wavelength is high. For the same steady-state carrier density, the corresponding number of unlocked photons (in blue) becomes small. This means that, in this state, most of the stimulated emission is redirected towards the injected wavelength mode instead of the free-running laser mode. For this reason, we shall call this state of emission the *locked state*. On the contrary, the lower circle indicates a solution of $|E_0|^2$ for which it is much smaller than the number of unlocked photons s which are close to their free-running number (here, ≈ 400). This state, weakly perturbed by the injection, is referred as the *unlocked state*. In addition, we note the presence of an intermediate solution for the lock/unlocked photon numbers but it is a dynamically unstable solution[1], inaccessible

[1]The demonstration of the stability of this solutions can be found in literature and is outside the concerns of this work.

experimentally.

This bistable behaviour is obtained for a particular range of wavelengths that varies, among other parameters, with the injection power.

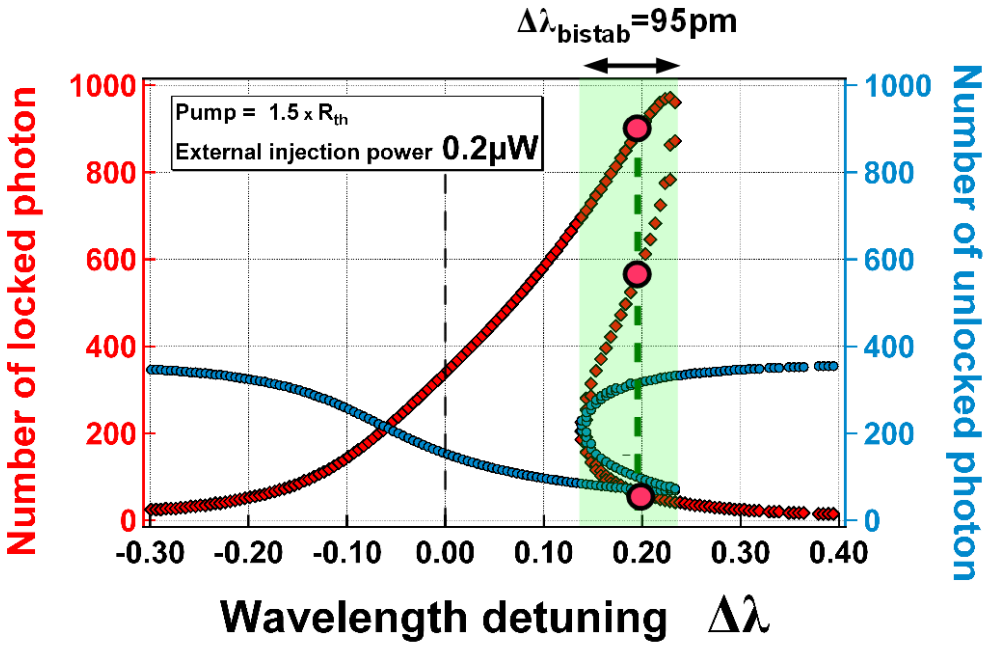

Figure 6.2: *Static solutions for the injected PhC laser. Photon number at λ_{ext} (red dots) and at $\lambda(N)$ (blue dots) versus the wavelength detuning between the injection and the free-running emission wavelength. The green shaded area indicates the range of detuning where bistability can be observed (here $\Delta\lambda_{bistab}$=95pm). The red circles indicate the 3 static solutions of the locked photon number for a detuning $\Delta\lambda = 0.2nm$. The upper and lower solutions are stables whereas the middle one is unstable*

Figures 6.3 shows how the bistable range shifts with the injection power. The higher P_{ext} , the larger is the minimum detuning to obtain bistability. Below this detuning, the PhC laser is however locked by the injection: the locked and unlocked photon numbers respectively increases and decreases for increasing P_{ext}. Note also that, in this case, by varying the injection power from 1 to 10 μW, the detuning range for which bistability is obtained, increases slowly.

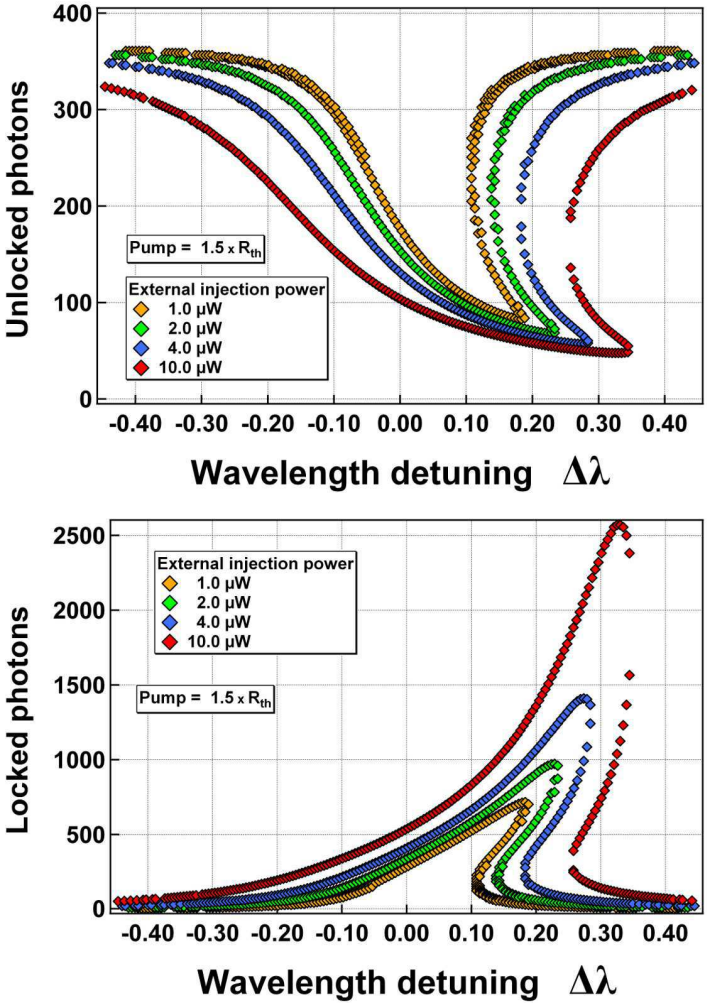

Figure 6.3: *Photon numbers in the unlocked (left graph) and locked (right graph) state as a function of the wavelength detuning from the free-running emission wavelength for injection powers going from 1 to 10 µW and at a pumping level of 1.5 times the laser threshold.*

6.2.3.2 Bistable range versus the injection power

Bistability is often represented by hysteresis cycles where the path of exploration of the states is restrained to clockwise or counter-clockwise direction. To do so, we represent in figures 6.4 the case where we set to +0.2nm the injection detuning, i.e. $\lambda_{ext} = \lambda_f + 0.2$nm. We then calculate the above mentioned variables and plot them as a function of the injection power. Hysteresis cycles are obtained in the different graphs.

The stable solutions are plotted in solid lines while the unstable ones are plotted in dashed lines. For a certain range of injection powers, we notice that the plot is divided in two branches where two stable solutions exist for each injection power. Two solid lines with arrows are added to indicate the directions of the steep transitions that occur between the two branches. The physical interpretation of what happens is the following: for low injection powers, the carrier

density is close to N_{th} and the cavity resonant wavelength to λ_f so that the injection is very inefficient. Indeed, here, the detuning is around 3 times greater than the loaded cavity linewidth giving injection efficiencies 30 times lower compared to a resonant injection. When the injection power increases, stimulated recombination of carriers increases giving thereby a lower carriers density. As a consequence, the cavity resonance is pulled towards the injection wavelength, rendering the injection more and more efficient which explains the very non-linear increase of the locked photons around $P_{lock} \approx 5.2\ \mu W$ and decrease of carriers density. Beyond this power, the system is in the locked state. In order to come back to the unlocked state, the injected power has to be decreased to a level P_{unlock} smaller than P_{lock} to obtain intracavity intensities sufficiently low to retrieve the initial carriers density.

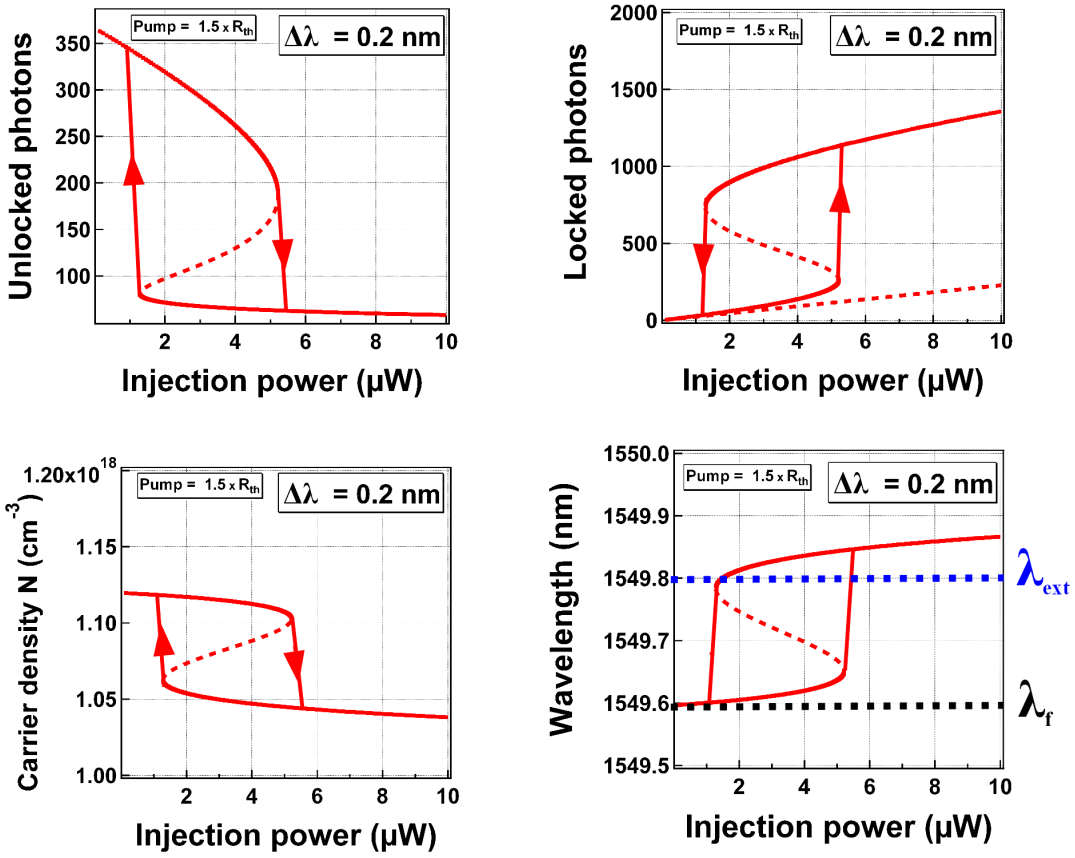

Figure 6.4: *Hysteresis cycles obtained for an injected PhC laser with parameters given by table 6.1. Upper graphs show the locked and unlocked photon numbers as a function of the injection level. Note that the hysteresis direction is clock-wise for the unlocked photons and counter-clock-wise for the locked photons. Lower graphs show the carrier density N (left) and the cavity wavelength $\lambda(N)$ (right) as a function of the injection. The black dashed line indicates the free-running laser wavelength, and the blue line the injection wavelength. Note that even after locking, the cavity wavelength continue to red-shift.*

In figure 6.5, we plot the unlocked photon number as a function of the injection level for several detunings. As we could have guessed by looking at the distorted resonances in fig. 6.2-6.3, the injection power P_{lock} necessary to lock the system increases with the detuning. Indeed, the farther the injection wavelength is from the free-running wavelength, the lower is the injection efficiency and consequently the power necessary to pull the system towards the injection wavelength is increased.

At this pumping bias ($1.5\times R_{th}$), the total bistable range of injection powers also increases with the detuning. Remark that, at first, P_{lock} increases faster than P_{unlock}, but for higher detunings it is not the case anymore. As a consequence, for a fixed pump power, there exists, when the detuning is varied, an optimum of achievable hysteresis cycle opening, i.e. the range between P_{lock} and P_{unlock}. Such opening can be expressed as $(P_{lock} - P_{unlock})/(P_{lock} + P_{unlock})$. A large opening can play an important role for switching applications as it can ensure stability even though some fluctuations may occur due to thermal effects and instabilities in the injection or in the pump powers.

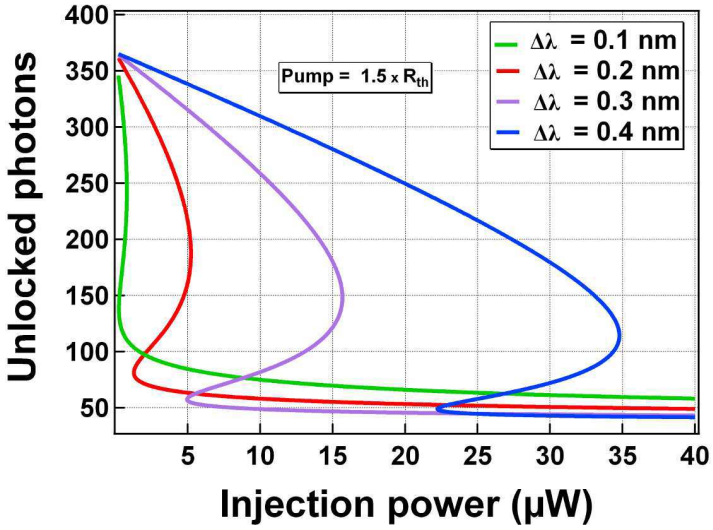

Figure 6.5: *Unlocked photon numbers as a function of the injection power for different detunings.*

In conclusion, these numerical simulations have been used to determine the expected behaviour of an injected PhC laser. Using the specific parameters of a hybrid PhC nanolaser/SOI waveguide, we are able to determine the necessary power and the wavelength detuning to lock a PhC laser and to obtain a bistable system. In order to put our ideas into practice, we considered a system with a coupling efficiency of 70% and injected with an injection detuning of 0.2nm at 1.5 times the laser threshold. In this case, we observed bistability for powers as low as a few μW's. We will now discuss the experimental part of this study and compared the obtained values with the latter values.

6.2.4 Experimental demonstration in the hybrid structures

In order to observe the bistable behaviour predicted by the previously presented analysis of an optically injected laser, we experimentally inject our integrated PhC nanolaser with an external laser light, brought in through the SOI waveguide, and whose frequency is detuned with respect to the laser emission. As it was demonstrated in the previous chapter, our hybrid structure offers one of the most elegant and efficient way to couple PhC lasers to the external world. This, of course, can be advantageously exploited to inject efficiently ($\approx$ 70% as previously assumed) the external laser to obtain bistability with very low power levels. In what follows, I start by describing the studied samples and the implemented experimental set-up before showing and commenting the results.

6.2.4.1 Studied samples

During my PhD, bistability was demonstrated in two different types of samples. It was first investigated on the same samples which were used for the coupling efficiency measurements. They constitute of TD-PhC Wire Cavities (cavity length 400 to 650 nm) without encapsulation nor surface passivation. For this reason, these measurements were done in ns-pulsed regime, to prevent the degradation of the cavities observed under pumping with longer pulses.

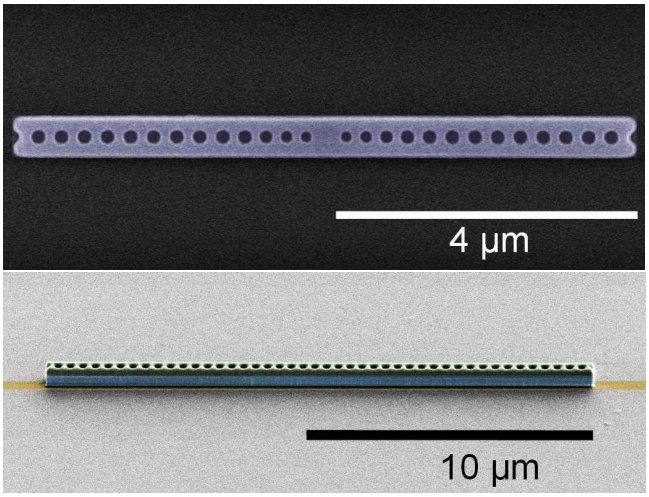

Figure 6.6: *Colored SEM picture of a TD PhC wire cavity (top) and an apodised PhC Wire Cavity (bottom) above a SOI waveguide (in yellow).*

In a second step, bistability was studied in samples containing apodised PhC Wire Cavities which were surface passivated and SiO_2 encapsulated. In this case, the demonstrations were achieved in the CW regime. Most of the results presented here were obtained for a cavity with central period of 340 nm, hole radius of 90 nm and a wire width of 505 nm. The target FWHM of the field was set at 2.6 μm. SEM pictures of the studied samples are shown in figure 6.6.

6.2.4.2 Experimental set-up and measurement principle

The schematic of the experiment is depicted in figure 6.7. The demonstration of bistability is performed by injecting a tunable CW laser slightly detuned (red-shifted as predicted by theory) from the laser emission wavelength reinforced by a picosecond (or femtosecond) mode-locked laser pulse centred at the same wavelength than the injection. The role of the CW external injection is to maintain a constant light injection bias while the short pulse gives the necessary "kick" in the power to switch (if the required conditions are met) the laser emission from the unlocked state to the locked state. Of course, this happens only if 1) the energy of the pulses that couples to the cavity is high enough to let the system reach the locked state 2) if the CW bias level is in the range of bistable operation.

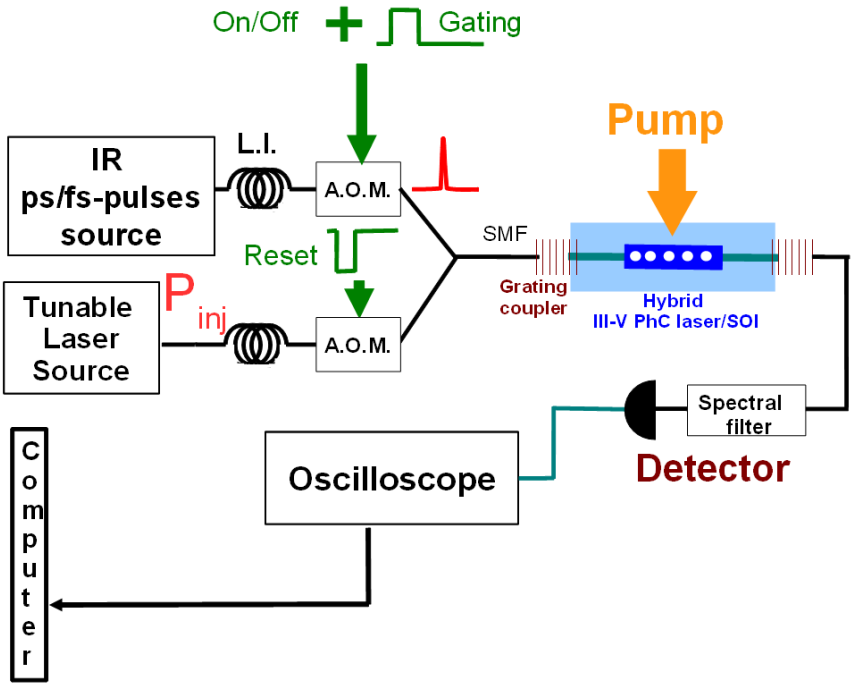

Figure 6.7: *Experimental set-up for optical bistability measurements. The injected optical signal is the addition of tunable laser light, slightly detuned from free-running laser wavelength, and a fs/ps-pulse.*

A more usual experimental approach consists in slowly increasing and decreasing the injection level to form a triangular ramp signal. In this method, an hysteresis cycle attesting for the bistability appears by plotting the output signal time trace versus the injection signal time trace. This method can easily be used when the PhC lasers are pumped in the CW regime or with sufficiently long pulses. However it becomes more difficult to implement when the lasers must be pumped with pulses of duration of the order of few 10's of ns as it was the case for our first generation samples which could not bear a CW operation. Further, such a measurement necessitates both fast enough modulators and detectors to read the signal temporal variation with a

good precision inside the ramp duration. Also, contrary to the method we eventually decided to use, this method does not allow the measurement of the time during which the system stays stable after switching from one state to the other, which is an important characteristic of the system if we want to use it as an optical memory.

The bistable states can be assessed by monitoring, for instance, the locked or the unlocked photon numbers that escape the cavity. This can be achieved by spectrally filtering the output signal of the cavity around either the locked or the unlocked wavelength. However, the monitoring of the locked photon number is experimentally quite inconvenient compared to the monitoring of the unlocked photon number in that, most of the time, these photons cannot be detected in transmission separately from the part of the injected signal which is not coupled to the active cavity, thereby degrading significantly, the achievable contrast between the two stable states. Of course, this could be avoided by collecting and filtering the part of the signal propagating in the opposite direction of the injection (reflected signal) or the part escaping the cavity by its surface (i.e. a part not coupled to the waveguide).

In the reflective configuration, as the injection and the collection of the light is achieved in our set-up by using cleaved optical fibres, a reflectivity measurement necessitates, at the output of the input fibre, an AR coating on the cleaved facets or the use of index matching gel in order to avoid the detection of the signal reflected. However, both of these possible solutions are quite complex to implement and use in a day-to-day basis. Hence, we did not go further in that direction.

In the case of the surface out-coupling, as we took care that most of the signal does not take this path by optimising the coupling efficiency, its detection can be rather tricky.

For all these reasons, we choose to monitor the emission of the system around the free-running laser wavelength which is actually a little different from detecting the unlocked number of photons.

As can be seen in figure 6.3, when the system is in the unlocked state, the corresponding photons are emitted close to λ_f so that the measured signal filtered around λ_f is directly proportional to the unlocked photon number. When the system is in the locked state, the unlocked photons number becomes very small and the emission wavelength of these photons gets red shifted with respect to λ_f. The measured filtered signal is, in consequence, expected to be extremely weak which should give very large contrast between the locked and unlocked states.

Thus, the emission is collected at the end of the SOI waveguide by a SMF fibre connected to a Yenista WS160 tunable spectral filter whose bandwidth is set to 0.3 nm before being sent to a detector. To detect the signals, we use either a *Hamamatsu* InGaAsP-based PhotoMultiplier (H10330A-75) or a *New Focus* Nanosecond InGaAs photodetector (1623) whose signal is amplified by a large bandwidth *Edmund Optics* amplifier. Figure 6.8 summarizes the experimental configuration by showing the measured spectra of the free-running laser emission and of an injected signal slightly detuned, as well as the filtering range (shaded zone).

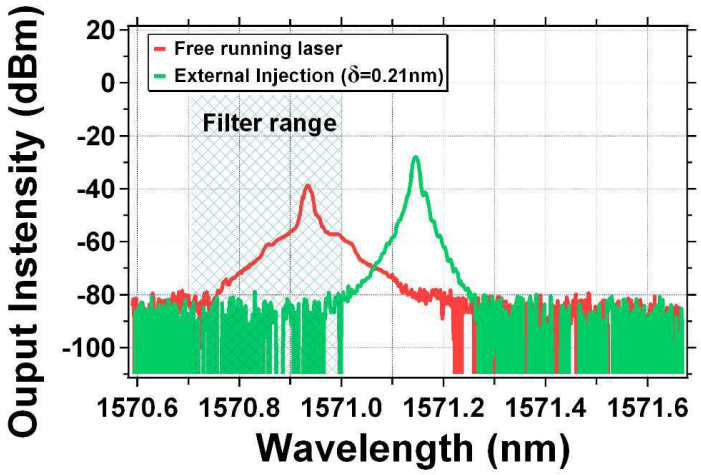

Figure 6.8: *Spectra of the laser emission and the CW external injection sent through an Optical Spectrum Analyser. The shaded zone denotes the range of the spectral filter.*

6.2.4.3 Bistable switching and hysteresis cycle construction

The S-curve of the studied apodised PhC nanolaser is shown on Figure 6.9. The cavity is here coupled to a 400 nm wide Si waveguide and the laser wavelength is 1571.2 nm at threshold.

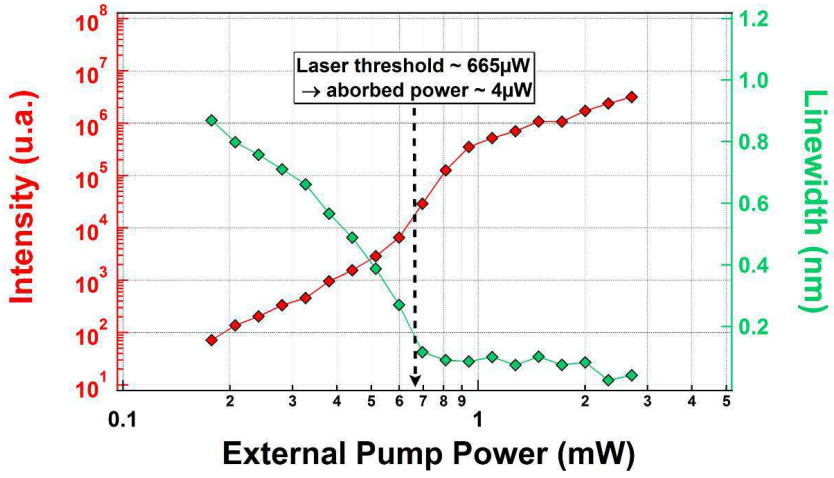

Figure 6.9: *S-curve (in red) of the studied cavity as a function of the external pump power (CW). The green markers indicate the evolution of the linewidth with pumping. The threshold is close to 665 μW corresponding to approximately 4 μW of effective absorbed pump power.*

In order to demonstrate that our system is bistable, we set the CW injection input power and measure the filtered emission intensity before and after the switching pulse arrival to observe the switching from the unlocked to the locked state. Here, the switching pulses are provided at

a repetition rate of 80 MHz by a tunable Optical Parametric Oscillator (OPO). Their duration is 150 fs. When the injection power is set to a value in the bistable range of the sample, the situation illustrated by fig. 6.10 occurs. The filtered emission (black trace) rapidly switches from the unlocked state (up state) to the locked state (down state) and stays locked after the "Set" pulse arrival (red trace). The blue trace shows the injection power which is periodically briefly turned off ("reset") with an A.O. modulator to let the PhC laser return to its free-running state and be able to restart the bistability experiment. Here, the experiments are performed at a 0.5 Hz repetition rate which allowed us to demonstrate that the system stays in the stable locked state for at least 2s! This clearly shows that our surface passivated encapsulated hybrid PhC lasers may be used as an optical memory with extremely long memory time. Actually, we were not able to measure the upper limit of the memory time which shows the very good stability of our system.

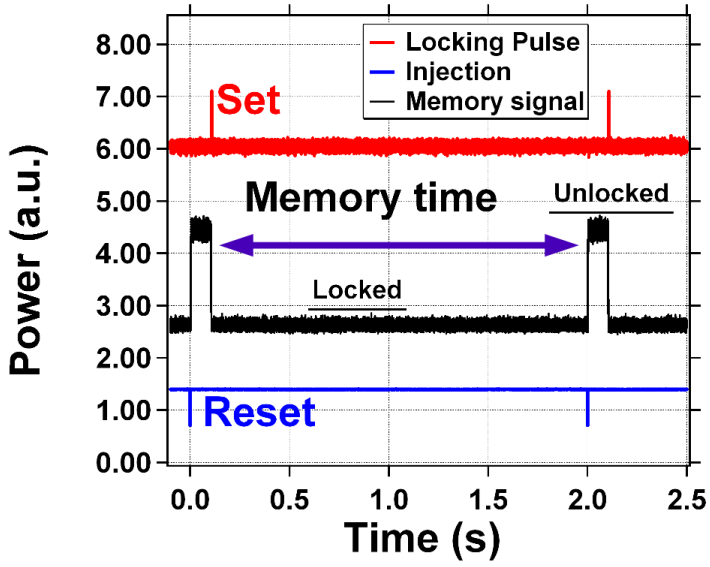

Figure 6.10: *Optical memory demonstration using bistable injected PhC nanolaser in a hybrid structure. A fs-pulse (red trace) is used to switch the laser emission (black trace) from the unlocked state to the locked state. In this scheme, the laser emission is put back to the unlocked state by briefly turning off the injection bias (blue trace).*

These measurements are repeated as a function of the injected power. We plot, in figure 6.11, the filtered emission levels before and after the "Set" pulse arrival when the PhC laser is pumped at 1.4 times its threshold and injected by the CW external laser detuned at 0.21 nm from the free-running laser wavelength.

When the injection power is less than 8 μW (*bistable threshold*), the emission levels before and after the "Set" pulse are measured to be identical showing that the system is not operated in its bistability range and stays unlocked. In fact, the system output may rapidly switch to an other value due to the arrival of the "Set pulse" but recovers rapidly to its initial stage. When the injection power is between 8 μW and 18 μW, the system is operated in its bistability range

as 2 different values are obtained for the output (case of fig. 6.10). When the injection power is greater than 18 μW, the system is locked, its output is not impacted by the arrival of the "Set" pulse any more. We are out of the bistability range. Thus, by looking at figure 6.11, we clearly obtain a clockwise hysteresis cycle in the system response which is a typical feature of such bistable system as expected from the theory. Bistability is observed for weak injected powers of few μW injection power right beneath the cavity) with a bistability range of about of 10 μW (width of the hysteresis cycle) which shows how power efficient these devices can be. These values corresponds nicely to that of the modelling section figures 6.4 where the parameters of the PhC lasers were plugged-in, showing the hybrid structure allows us to obtain sufficient coupling efficiencies to observe the bistable operation at such low powers.

The contrast obtained between the 2 states is also measured to be extremely good as the filtered signal drops almost to 0 in the locked state. The contrast can be estimated by analysing the total optical signal with and without injection. This is done in fig. 6.11 where we can appreciate the contrast level by looking at the ratio between the peak level of the free-running laser emission and the level of emission at the same wavelength when the laser is locked to the injection. We see that the contrast obtained in the filter window is as high as 40 dB!

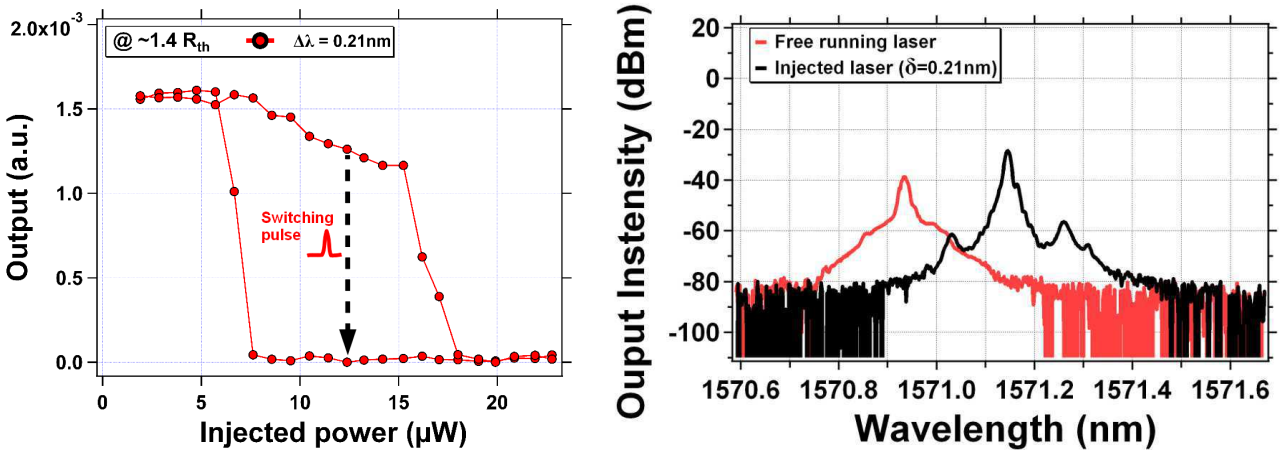

Figure 6.11: *Output power of the filtered emission as a function of the injection power. The laser is pumped at 1.4 times its threshold power and the detuning of the injected signal from the free-running laser wavelength is 0.2 nm. In this experiment, a 150 fs-pulse spectrally centred around the CW injection wavelength allows to switch from the unlocked state to the locked state.*

6.2.4.4 Impact of the detuning and the pump power on the bistable range

The hysteresis cycles were measured at different values of the detuning of the injected laser.

Figure 6.12 shows the various hysteresis cycles obtained when the pump power is fixed at 1.4 times the laser threshold. The traces are offsetted in the y direction for an improved visibility of the cycles. Highly contrasted bistable ranges are obtained for detunings going from 0.26 nm to 0.41 nm, the lower bound value of the detuning being determined by the edge sharpness of our spectral filter. As expected, when the detuning increases, the bistable threshold as well as the

width of the hysteresis cycle increase. The intensity of the output before locking also diminishes slowly, very similar to the cycles of fig. 6.5.

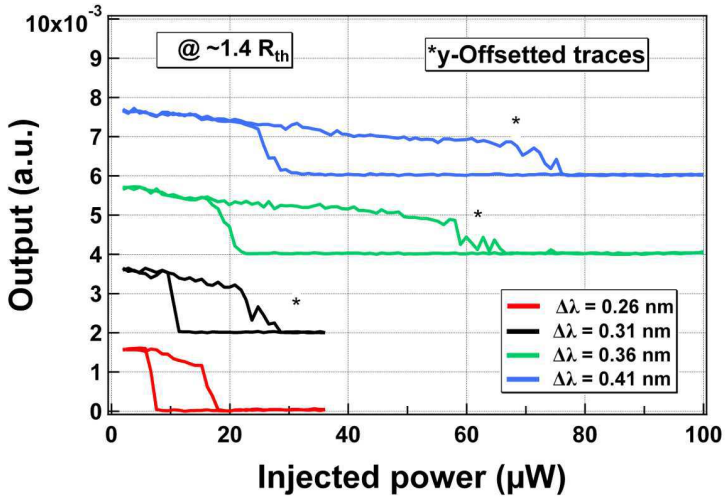

Figure 6.12: *Hysteresis cycles obtained by plotting the emission filtered around the free-running laser wavelength of a PhC wire cavity laser pumped at 1.4 times the laser threshold as a function of the power injected in the 400nm wide SOI waveguide and for various wavelength detunings. The hysteresis are offsetted in the y direction for clarity.*

We repeated these measurements for different pump powers going from 1.4 to 2.7 times the laser threshold. The corresponding bistable ranges are plotted as a function of the detunings in fig. 6.13 and as function of the pumping powers in fig. 6.14. We notice in fig. 6.13 that, for most of the pump powers, the bistable range zone enlarges when the detuning is increased, the bistable threshold increasing slower (for example from 8 μW to 22 μW at $P_{pump} = 1.4P_{th}$) than the upper limit of the hysteresis cycle in injected power (from 18 μW to 75 μW). Some irregular points are however visible. Their presence may most certainly be due to slight variations in the pumping conditions. The same kind of observations can be made by looking at the bistable ranges at fixed detunings as a function of the pump power. The bistable range zone also enlarges when the pump power is increased with the bistable threshold increasing slower (from 8 μW to 24 μW at $\Delta\lambda = 0.26$ nm than the upper limit of the hysteresis cycle in injected power (from 18 μW to 85 μW).

A key point with these results resides in the order of magnitude of injection power necessary to obtain the bistable regime which should ideally be of the order the available power emitted by a PhC laser coupled to a waveguide. As a consequence, in a PIC constituted of PhC lasers, it is then possible to envisage replacing the injection laser we use by a second PhC laser (*master*) in order to inject the first PhC laser (*slave*). Of course, this future work needs to be analysed in detail as two lasers coupled to the same waveguide are most likely to inject into each other.

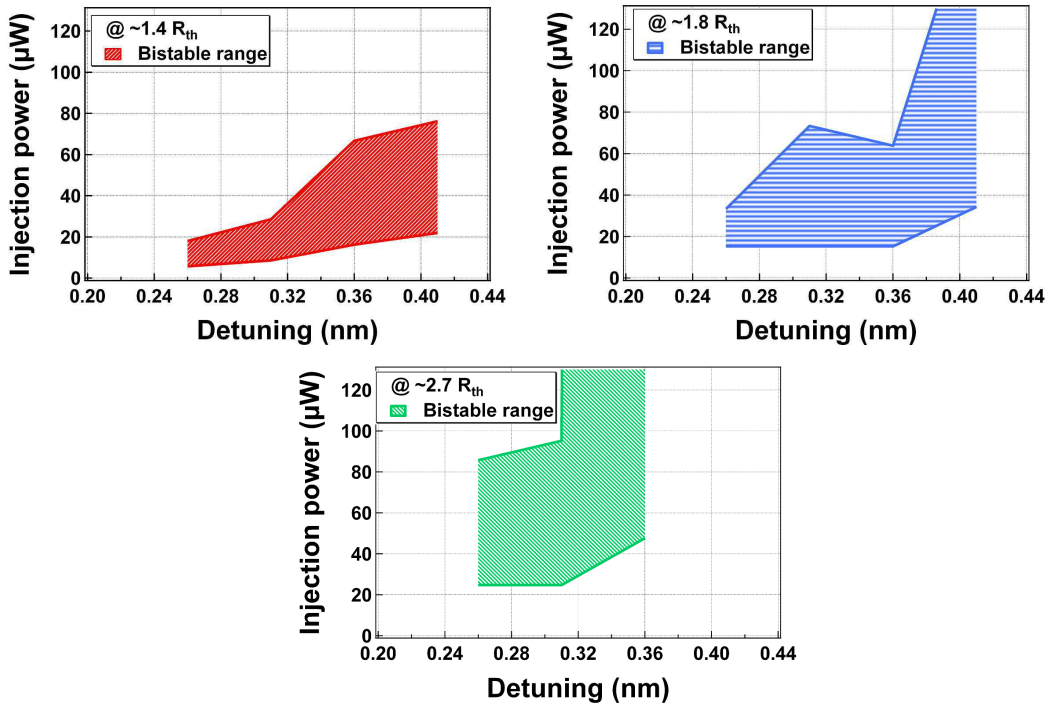

Figure 6.13: *Bistable range as a function of the wavelength detuning measured at 3 different pump powers above the laser threshold. In the case of a pump power at 2.7 × R_{th}, our external injection source could not provide enough power to measure the upper limit of the bistable range for detunings above 0.32nm.*

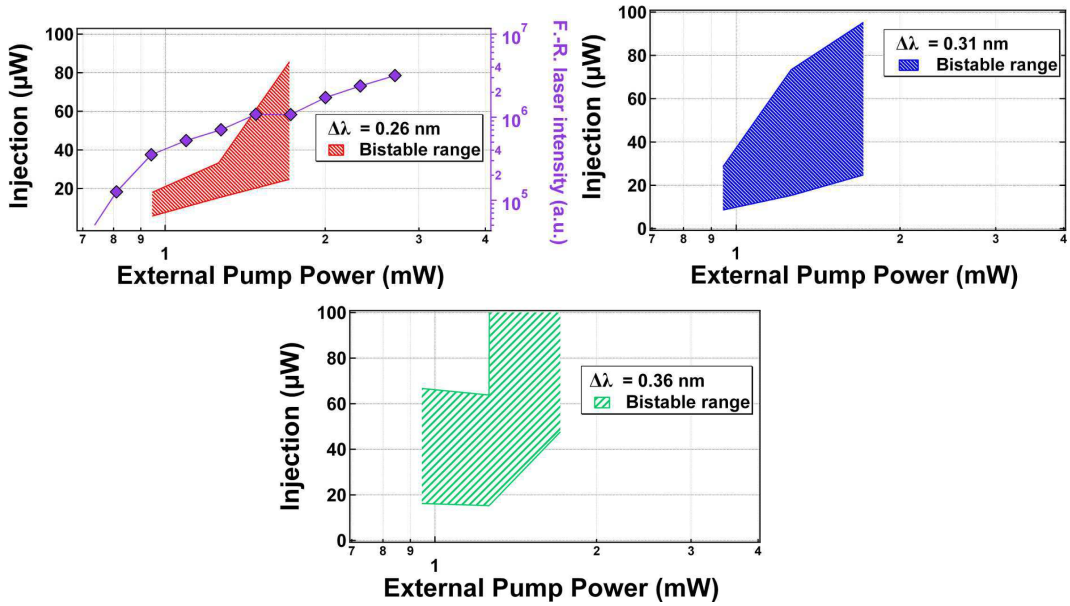

Figure 6.14: *Bistable ranges as a function of the pump power for three detunings. In the top graph, we add the intensity of the free-running laser as a function of the pump.*

Our measurements also show that it is possible to return to the unlocked state by playing on the pump power. As previously described, the system may be put back to the unlocked state by switching off the injection briefly. This means that 3 logical levels on the injection laser are necessary to achieve a set and a reset of the bistable memory. This may cause some problems especially when a fast reset is necessary as it is not so easy to switch off and switch on again a laser rapidly. As an alternative, a short pulse could be sent into the laser pump in order to switch back to the unlocked state. Indeed, looking at the curve showing the bistable range versus the pump power when the detuning is fixed at 0.26 nm (fig. 6.14), one can see that the bistable range obtained when the pump power is equal to 0.95 mW falls completely outside the bistable range obtained when the pump power is equal to 2.5 mW. This clearly shows that the system will return to its unlock state by briefly pumping harder the laser. This is also confirmed by preliminary results from the numerical solving of the injected rate-equations of our nanolaser, giving the dynamic of the system. With the "good" power levels for the "reset" pump power pulses, we observed return to the initial unlocked state. However, these results are still under investigation and will be detailed elsewhere, together with an experimental proof.

6.2.4.5 Ultra-low energy switching demonstration

Up to now, the bistable behaviour was described in terms of average powers of the injection laser. The switching from the unlocked state to the locked state is induced by a short optical pulse which briefly reinforces the injection. Of course, this switching can only be triggered by the pulse if its energy is sufficiently high. What is the necessary energy to switch the system? This question has been the subject of many studies on different types of bistable systems, such as electronic systems [252], microwave systems [253], Fabry-Perot resonator filled with vapour atoms [252], semiconductor laser diodes [254] or semiconductor micro-resonators [255]. The answer is not trivial at all and its theoretical treatment can only be done through a numerical analysis.

In summary, the energy required to switch from the unlocked to the locked state depends, not only on the power difference ΔP between the injected CW beam and the upper limit of the hysteresis cycle P_{lock}, but also on the dynamics of the transition between the 2 states induced by a short optical pulse. At a first glance it should write $E = \tau \Delta P$ with τ the time constant associated to the switching dynamics. However, the value of τ is dependant on the time constant linked to the physical effects inducing the switching which is here supposed to be very fast as we deal with stimulated emission. In addition, an increased level of complexity of the problem arises from the fact that, as shown in [252, 253, 256, 257], τ also varies with the excess of power

above P_{lock}, noted ΔP_S, brought by the switching pulse. Hence, depending on the value of ΔP_S, two types of dynamical regime can be obtained.

The first one is the *critical slowing down regime* which occurs when the switching pulse has a peak power which puts the system right above P_{lock}. In this case, it was demonstrated that $\tau \propto (1/\Delta P_S)^{1/2}$ [258] giving the switching energy E:

$$E \propto (\Delta P + \Delta P_S)/(\Delta P_S)^{1/2},$$

showing that the switching time and the switching energy become infinitely large for $\Delta P_S = 0$.

The second dynamical regime is obtained when ΔP_S is increased. In this regime [256], we have $\tau \propto (\Delta P + \Delta P_S)^{-1}$ and $E = cste$, the determination of the constant being only possible numerically. Our experiments were performed in the latter regime as it enables fast switching and a more stable operation.

Now, in order to quantify experimentally the switching energy, the experiments were carried out using a mode-locked fibre laser emitting 10 ps long pulses around 1.55 μm in order to avoid as much as possible the spectral filtering occurring because of the narrow spectral linewidth of the cavity resonance under optical pumping. This experiment was here performed on a TD PhC cavity coupled to a 450 nm wide SOI waveguide which was neither passivated nor encapsulating so that pulsed optical pumping (40 ns at a 250 kHz repetition rate) was compulsory to obtain laser emission.

The laser characteristic curve and the hysteresis cycles due to the injection-locking bistability are represented in fig. 6.15-6.16. For these measurements, the pump peak power is fixed at 1.4 times the laser threshold.

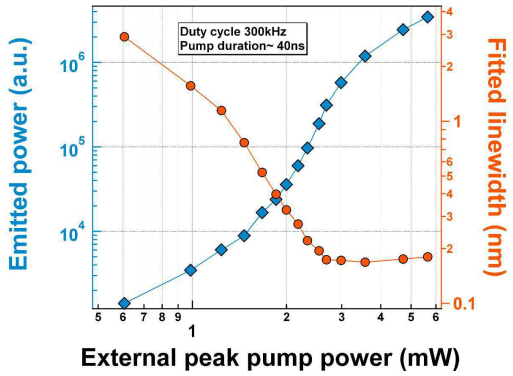

Figure 6.15: *Characteristic S-curve of a TD PhC wire cavity laser coupled to a 450 nm wide SOI waveguide. In addition, we plotted the fitted linewidth that goes below the spectrometer resolution around the threshold.*

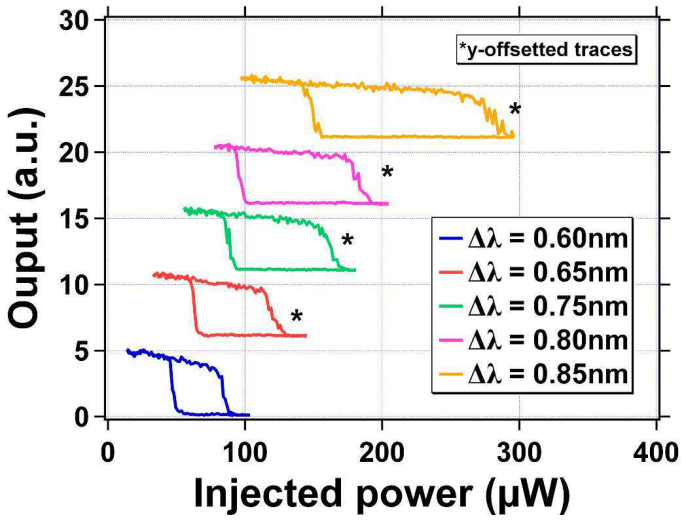

Figure 6.16: *Hysteresis cycles of the filtered emission as a function of the injected power, for several detunings. The pump here is close to 1.4 times the threshold.*

To sum up, similarly to the previously shown results with apodised cavities, the lower and upper limits of the hysteresis cycles in injected powers are plot on fig. 6.17 as a function of the injected wavelength to define the bistable range.

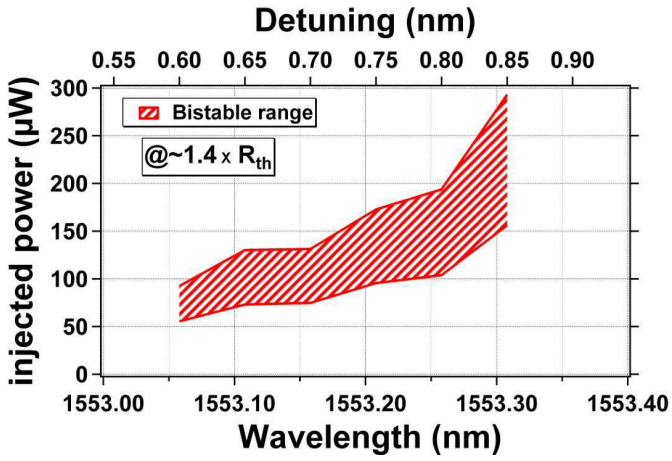

Figure 6.17: *Bistable ranges as a function of the wavelength detuning measured at 1.4 times he laser threshold.*

Here, because the "kick" pulses are much longer than before ($\gtrsim$ 5-10 ps, hence $\gg$ 150 fs), the energy which effectively loads the cavity is enhanced. This allows to "use" much more efficiently the pulse energy to switch the laser. For example, when the system is injected at 0.6 nm detuning and the injection power is set to 75 μW, stable switching operation is obtained with pulses of energy (evaluated inside the SOI wire, right under the cavity) as low as 0.4 fJ !

This ultra-low switching energy is comparable to the best energies so far obtained in other

PhC-based switching devices [259].

In the end, in order to fully evaluate the possibility of such devices for high-bit rate operation, system measurement (including Bit-Error-Rate measurements) are essential. Again, we plan to realise them and expect the outcome of this future measurement will be presented as soon as possible.

6.2.5 Conclusion

In this chapter, PhC nanolasers were investigated as switching elements and as a memory device. Unlike most studies in literature, our PhC lasers were integrated onto SOI. This allows us to envisage the fabrication of much more complex photonic integrated circuits (PICs) than is has been so far possible. Further, the footprint of the optical switch based on hybrid PhC-lasers/SOI structures is here divided by a factor 10 compared to the best previously reported study [259] using a PhC architecture. The smaller dimensions of the nanolasers, of course, imply lower power consumption, smaller footprint and lower switching energies.

By carrying out an injection-locking-based bistability analysis theoretically, I was able to express the most pertinent quantities (E^0_{ext},φ,s) with N in terms of the carrier density intimately linked to the input power. This gave the handle to numerically simulate the bistable behaviour using the characteristics of a real fabricated structure such as the wavelength of resonance, Q factor, β factor, etc.

Armed with all this knowledge, I set up a tailor made experiment to explore bistability in these structures. A thorough mapping of the bistable regime was carried out: injection bias power for a range of external pump powers required for different detuning values, from a different perspective, the range of detuning over which bistable operation is possible was traced, for different pump powers. I could show large openings for the hysteresis cycle which can play an important role for switching applications as it can ensure stability even though fluctuations due to thermal effects or due to instabilities in the injection or the pump powers may occur.

Finally, I was able to show in this chapter that it is possible to obtain in $\approx$10 μm^2 nanolaser bistable switching in the injection locking configuration. The bistable behaviour was studied as a function of different parameters such as the pump power, the wavelength detuning and the injection power. We show that when the laser was biased around 1.5 times its threshold (6 μW of absorbed power), bistability occurred for injected powers below 10 μW. The bistability energy necessary to switch the system was estimated to be as low as 0.4 fJ !

Importantly, a memory holding time of 2 s was observed which in principle can be as long as desired given the extreme stability of the system. For this performance a switching contrast of 40 dB is obtained, to be compared with best reported in o-RAM system [259] where the authors obtained 12 dB.

Chapter 7

Conclusion and perspectives

Silicon photonics constitutes an ideal platform for conveying and routing optical signals, within a chip, and this, over mm long distances with very low losses. Despite the unsurpassed assets of the silicon-on-insulator platform in terms of *passive* functionalities, the lack of *active* functionalities and, above all, the lack of efficient light sources within this platform have been a crucial disadvantage. The integration of III-V semiconductors onto silicon photonic circuits is an exciting but challenging task, which we took-up by combining the best of both III-V optoelectronic and Silicon photonic technologies. In order to be able to use optical interconnects as a replacement technology of current metallic interconnects, we strove for the smallest footprint and lowest energy consuming objects which can potentially be Photonic Crystal nanocavities embedding III-V active material. It is my belief that the present work constitutes a pioneering approach to bring Nanophotonics from lab work to actual on-chip photonic integrated circuits.

In this thesis, we aimed at demonstrating the potential of a hybrid III-V PhC/SOI waveguide platform in terms of footprint, energy consumption, fabrication robustness, control of its optical characteristics and active functionalities. This was done by approaching the different problems that can be encountered while working with such structures and proposing some solutions which can solve them all at the same time. Indeed, most of the studies found in the literature only partially demonstrate the potential of PhC devices. For example, a power efficient emitting device won't be fast, and vice-versa, or won't work in the high bit rate conditions, etc... Here, the work in the design, the fabrication and the experiment was achieved by trying to keep in mind all the constraints for obtaining proper devices.

In chapter two, we presented an analytical method of the hole's positioning in a single-mode wire in order to build $(\lambda/n)^3$ volume nanocavities of high quality factor. After presenting the assets and drawbacks of the *Gaussian* apodisation method, we concluded our analysis by emphasizing the excellent tunability of this procedure while maintaining a Q-factor around 10^6, modal volumes below $(\lambda/n)^3$ and footprints below 20 μm^2. In addition, in order to decrease the

thermal resistivity of the structure as well as to protect it, the design was implemented in a PhC structure fully encapsulated in a material of refractive index close to 1.5 (like SiO_2) instead of air. This analytical method is very general and may be extended to obtain cavity mode profiles of various functional forms other than the Gaussian one, for example similar to those applied for Fourier Transform filtering (Hanning, Nutall,...).

Many key processes inherent to the fabrication of the hybrid structures were better understood and improved. The adhesive bonding of cm² III-V dies upon a patterned SOI chip has benefited from the use of a mechanical press in a vacuum environment. The control of the thickness of the intermediate layer between the III-V and the SOI is now mostly transferred to that of SiO_2 deposition process on the III-V, executed before bonding, which was initially used to improve the bonding yield efficiency. The entire lithographic process (exposure+etching) was rethought and the use of an HSQ mask has allowed us not only to reduce the number of electron beam exposures to just one, but also to improve significantly the surface roughness and the verticality of the III-V plasma-etched holes. Obviously, our whole cavity design which is based on unique variations of the lattice constant, instead of the radius or the wire's width, benefits here from the sub-nanometric precision on the position of the electron beam lithography system. Efforts are still ongoing to improve the III-V ICP etching which lacks of maturity compared to the SOI etching process. The measurement of the PhC etching quality will also be inspected on the optical table through sophisticated dynamical measurement (in order to retrieve the quality factor Q for instance). In addition, the passivation process, which allowed us to lase in the CW regime with a QW's based PhCs cavity, will also be investigated in more detail.

The laser emission of our PhC nanolaser was studied in chapter 4, in three parts. While the first focused on the laser behaviour, numerically and experimentally, the two others dealt with the decrease of the thermal resistivity of the hybrid structure and the surface passivation of the active material. Hence, we started by presenting a carrier density-photon number rate equations model and we went on to extracting the influence on the laser threshold of three important parameters in PhC nanolasers: the quality factor Q, the spontaneous emission factor β and the non-radiative lifetime τ_{NR}. We emphasised that high Q and β are beneficial to obtain low threshold powers. However, we also showed the value of the threshold is rapidly clamped for Q beyond 10^4. Experimental measurements of the threshold were performed, giving an estimation of the absorbed pump power in the order of the μW in order to observe laser emission. We also showed that it is very unlikely that these measurements allow to deduce the Q and β factors of our lasers, due to the expected high values of both these parameters. However, the fit of the light-in-light-out characteristic curve with our model allows to estimate Q-factors of our unloaded fabricated PhC cavities to be around a few 10^4. We firmly think that this number can be increased to, at least, 10^5 by further improvement in the fabrication process.

We demonstrated that a reduction of the thermal resistivity of the cavity could be obtained

by encapsulating the cavity in SiO_2 or MgF_2. Through an optical probing of the temperature elevation, we experimentally proved that an encapsulated PhC cavity could have a thermal resistivity decreased by a factor 1.5 when a SiO_2 top cladding was added and 3.6 when MgF_2 was used. MgF_2 is of great interest due to its very low refractive index (1.38) but its use as a cladding material will strongly depend on the development of etching techniques, probably dry-ones, to pattern it at will. Indeed, until now it has been exploited as an excellent AR coating material, extremely resistant to many kinds of attacks. Despite the excellent thermal properties of our encapsulated cavities, CW operation could not be sustained over more than a few hours at most.

However, we tackled the CW operation from another front by decreasing strongly the non-radiative carrier recombination at the surface. Through chemical etching and passivation processes, we succeeded in increasing by a factor 10 the non-radiative carrier lifetime. Obviously, this had a spectacular effect on the laser operation allowing stable CW operation.

The coupling efficiency between the PhC Wire Cavity and the SOI waveguide was thoroughly analysed in this thesis. Through the TCMT analysis, we highlighted the very interesting features observed in the transmission of the system when the cavity embeds an active material able to provide gain. We were able to reproduce the expected behaviours in transmission measurements, showing a transmission dip to 0 when the optical losses of the cavity corresponded to the loss rate into the waveguide solely. In addition, an estimation of the coupling efficiency could be given after extracting from the laser curves the total Q factor of the cavity coupled to the waveguide. We found that a maximum coupling efficiency around 90% could be reached when the k-space overlap between the guided mode and the cavity mode was optimised. In my opinion, the beauty of the system is that this almost perfect control of the coupling losses is obtained through simple geometrical considerations, such as the cavity-waveguide distance, the SOI waveguide width or the central lattice constant a_0 of the apodised PhC cavity. The pursuit of high (uncoupled) quality factor Q_0 is also motivated by the perspective to obtain a cavity highly coupled to a waveguide together with a low laser threshold which requires a fairly high total (coupled) quality factor Q ($\gtrsim 10^4$).

In the final chapter, we used the injection-locking mechanism of one laser to another to demonstrate an optical memory integrated into the silicon platform. After solving in the stationary regime the rate equations system governing our injected system, we retrieved the basic conditions to obtain optical bistability. We reconstructed the hysteresis patterns that can be seen by plotting, for example, the cavity resonant wavelength or the number of photons which become locked (in phase) with the external laser injected through the waveguide as a function of the input power. Using fs-long pulses, we demonstrated a highly efficient functionality within the hybrid structure: an optical memory. We also showed that this memory was stable (at the second scale) and demonstrated the switching of the cavity state with a sub-fJ energy optical pulse.

During the last year of this thesis, a lot of effort was devoted to build a heterodyne detection set-up in order to measure the dynamics of our lasers and of our memories. This technique allows to perform pump-probe measurements with fs/ps pulses with a much higher sensitivity than with regular homodyne detection. The set-up was finished and tested, but, because rigorous measurements are time-consuming and the analyses of the dynamics is rather complex, we decided to postpone the report of our preliminary results. Among the many dynamical features of our system, the gain recovery time of our injected lasers is definitely a figure we intend to measure in the future. Preliminary measurements show a gain recovery time below 50 ps but, again, only further investigation will confirm it. While additional measurements are being carried out at this moment, high bit-rate optical pumping of our system is considered in order to test the performances of the devices within system experiments.

Despite the improvements on the integration of III-V PhCs above a silicon circuit, a major issue was not addressed during my PhD and remains to be tackled: the electrical pumping of the PhCs within the hybrid platform. Electrical injection of PhC lasers operating at optical wavelengths was successfully achieved, so far, by only 3 groups [260, 261, 262] which shows the complexity to conceive such structures. The recent demonstrations of electrical pumping of PhCs, first at cryogenic temperatures [261, 263] (see fig. 7.1) and then at room-temperature [262], by creating lateral p-i-n junction inside the PhC membrane, are proofs that solutions exist. Indeed, the whole point is to find a solution to efficiently inject the current in such tiny lasers without spoiling the optical properties of the resonators with absorptive metallic electrical contacts or dopants.

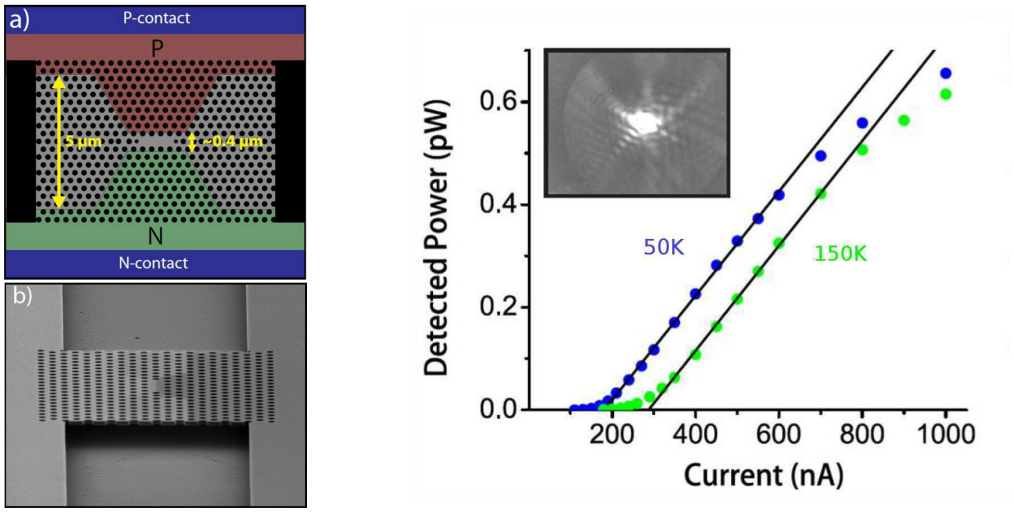

Figure 7.1: *Lateral electrical pumping of 2D PhCs nanolasers. Left: SEM pictures of the fabricated GaAs-based 2D-PhC structures, p-i-n laterally doped. Right: Experimental current-light characteristics for the laser at 50 and 150K. The cavity mode is here close to 1.2 µm. From [263].*

To finish, I would like to mention that, at an early stage of the group's work upon the integration of PhCs above SOI waveguides, it appeared that this platform would be a unique tool to inter-couple active PhC devices. With this active passive integration, it is easy to imagine the cascading of different functionalities along the same waveguide. Even more interesting from the physics point of view, it also provides the potentiality of building unprecedented situations arising from the coupling of two active nanoresonators. For example, new functionalities such as dynamic light trapping or laser without population inversion are possible outcomes of such coupling. During the last year, I fabricated hybrid samples with 2 PhC Wire Cavities, embedding QWs, cascaded on the same waveguide as can be seen in figures 3.18 (chapter 2) and 7.2.

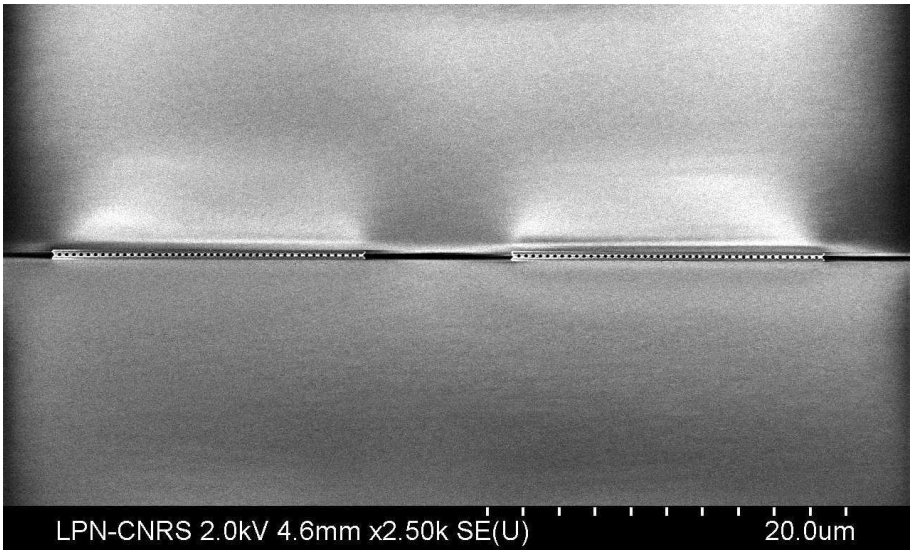

Figure 7.2: *SEM pictures of PhC Wire Cavity coupled through the same SOI waveguide.*

This demanded some important technological efforts as in practice it is difficult to obtain identical structures, a prerequisite for inter-coupling. This was achieved by using our optimised e-beam lithography procedure which allows us, today, to produce devices all emitting at a certain wavelength $\pm$ 0.5 nm. From the application of the TCMT to this system, we already know that very different behaviours will result from the phase difference experienced by the light between the two cavities. As this parameter is simply related by the cavity-to-cavity distance and can be controlled very precisely, we fabricated structures where the phase difference was varied to scan a shift between 0 and π in order to investigate the different inter-coupling configuration. We also implemented a dual optical pumping scheme on our μ-PL set-up which will enable the simultaneous biasing of the two active cavities. This is an other exciting degree of freedom that has already begun to be explored, numerically and experimentally. Systematic measurements will soon be resumed. The results of my thesis, I sincerely hope, will open up new avenues in this exciting field!

List of Figures

List of publications

As a first or second author

Published

- A. Bazin, P. Monnier, X. Lafosse, G. Beaudoin, R. Braive, I. Sagnes, R. Raj, and F. Raineri, "Thermal management in hybrid InP/silicon photonic crystal nanobeam laser," *Opt. Express*, vol. 22, pp. 10570-10578, May 2014.

- A. Bazin, R. Raj, F. Raineri, "Design of silica encapsulated high-Q photonic crystal nanobeam cavity", *Lightwave Technology, Journal of*, vol. 32, pp. 952-958, march 2014.

- A. Bazin, K. Lengle, M. Gay, P. Monnier, L. Bramerie, R. Braive, G. Beaudoin, I. Sagnes, R. Raj and F. Raineri, "Ultrafast All-Optical Switching and Error-free 10 Gbit/s wavelength conversion in Hybrid InP on SOI nanocavities using surface Quantum Wells," *Applied Physics Letters*, vol. 104, pp. 011102-011102-4, jan. 2014.

- Y. Halioua, A. Bazin, P. Monnier, T. J. Karle, G. Roelkens, I. Sagnes, R. Raj, and F. Raineri, "Hybrid III-V semiconductor/silicon nanolaser," *Opt. Express*, vol. 19, pp. 9221-9231, May 2011.

- Y. Halioua, A. Bazin, P. Monnier, T. J. Karle, I. Sagnes, G. Roelkens, D. Van Thourhout, F. Raineri, and R. Raj, "III-V photonic crystal wire cavity laser on silicon wafer," *J. Opt. Soc. Am. B*, vol. 27, pp. 2146-2150, Oct 2010.

In preparation

- A. Bazin, Y. Halioua, D. Chastanet, P. Monnier, T. J. Karle, G. Roelkens, I. Sagnes, R. Raj, and F. Raineri, "Injection-locking-based optical bistability in hybrid III-V photonic crystal laser/SOI waveguide with sub femto-joule swith energies," 2014.

Book Chapter

F. Raineri, A. Bazin, R. Raj, "Optically Pumped Semiconductor Photonic Crystal Lasers," in *Compact Semiconductor Lasers*, First Edition, edited by Richard De La Rue, Siyuan Yu et Jean-Michel Lourtioz. Wiley-VCH Verlag GmbH Co. KGaA, 2014.

Other published

- K. Lengle, T. Nguyen, M. Gay, L. Bramerie, J.-C. Simon, A. Bazin, F. Raineri and R. Raj, "Modulation contrast optimization for wavelength conversion of a 20Gbit/s data in hybrid InP/SOI photonic crystal nanocavity," *Opt. Lett.*, vol. 39, pp. 2298-2301, apr. 2014).

- Y. de Koninck, F. Raineri, A. Bazin, R. Raj, G. Roelkens, and R. Baets, "Experimental demonstration of a hybrid III-V-on-silicon microlaser based on resonant grating cavity mirrors," *Opt. Lett.*, vol. 38, No. 14, 2014.

- S. Haddadi, L. Le-Gratiet, I. Sagnes, F. Raineri, A. Bazin, K. Bencheikh, J. A. Levenson, and A. M. Yacomotti, "High quality beaming and efficient free-space coupling in L3 photonic crystal active nanocavities," *Opt. Express*, vol. 20, pp. 18876-18886, Aug 2012.

- P. Mechet, F. Raineri, A. Bazin, Y. Halioua, T. Spuesens, T. J. Karle, P. Regreny, P. Monnier, D. Van Thourhout, I. Sagnes, R. Raj, G. Roelkens, and G. Morthier, "Uniformity of the lasing wavelength of heterogeneously integrated InP microdisk lasers on SOI," *Opt. Express*, vol. 21, pp. 10622-10631, 2013.

- H. Kataria, C. Junesand, Z. Wang, W. Metaferia, Y.-T. Sun, S. Lourdudoss, G. Patriarche, A. Bazin, F. Raineri, P. A. Mages, N. Julian, J. E. Bowers, "Towards a monolithically integrated III-V laser on silicon: optimization of multi-quantum well growth on InP on Si", *Semicond. Sci. Technol.*, vol. 28, 094008, 2013.

Bibliography

[1] G. E. Moore, "Cramming more components onto integrated circuits," *Electronics*, vol. 38, 1965.

[2] ITRS, *International Technology Roadmap for Semiconductors: Interconnect*. 2011.

[3] R. Beausoleil, P. Kuekes, G. S. Snider, S.-Y. Wang, and R. S. Williams, "Nanoelectronic and Nanophotonic Interconnect," *Proceedings of the IEEE*, vol. 96, no. 2, pp. 230–247, 2008.

[4] W. Steinhögl, G. Schindler, G. Steinlesberger, and M. Engelhardt, "Size-dependent resistivity of metallic wires in the mesoscopic range," *Phys. Rev. B*, vol. 66, p. 075414, Aug 2002.

[5] D. A. B. Miller, "Device Requirements for Optical Interconnects to Silicon Chips," *Proceedings of the IEEE*, vol. 97, no. 7, pp. 1166–1185, 2009.

[6] A. Naeemi and J. Meindl, "Design and performance modeling for single-walled carbon nanotubes as local, semiglobal, and global interconnects in gigascale integrated systems," *Electron Devices, IEEE Transactions on*, vol. 54, no. 1, pp. 26–37, 2007.

[7] X. Chen, K.-J. Lee, D. Akinwande, G. Close, S. Yasuda, B. Paul, S. Fujita, J. Kong, and H.-S. Wong, "High-speed graphene interconnects monolithically integrated with CMOS ring oscillators operating at 1.3Ghz," in *Electron Devices Meeting (IEDM), 2009 IEEE International*, pp. 1–4, 2009.

[8] J. W. Goodman, F. Leonberger, S.-Y. Kung, and R. Athale, "Optical interconnections for VLSI systems," *Proceedings of the IEEE*, vol. 72, no. 7, pp. 850–866, 1984.

[9] D. A. B. Miller, "Optics for low-energy communication inside digital processors: quantum detectors, sources, and modulators as efficient impedance converters," *Opt. Lett.*, vol. 14, pp. 146–148, Jan 1989.

[10] D. Miller and H. Ozaktas, "Limit to the Bit-Rate Capacity of Electrical Interconnects from the Aspect Ratio of the System Architecture," *Journal of Parallel and Distributed Computing*, vol. 41, no. 1, pp. 42 – 52, 1997.

[11] D. A. B. Miller, "Rationale and challenges for optical interconnects to electronic chips," *Proceedings of the IEEE*, vol. 88, no. 6, pp. 728–749, 2000.

[12] S. Assefa, F. Xia, W. M. J. Green, C. Schow, A. Rylyakov, and Y. Vlasov, "CMOS-Integrated Optical Receivers for On-Chip Interconnects," *Selected Topics in Quantum Electronics, IEEE Journal of*, vol. 16, no. 5, pp. 1376–1385, 2010.

[13] M. Taubenblatt, "Optical interconnects for high-performance computing," *Lightwave Technology, Journal of*, vol. 30, no. 4, pp. 448–457, 2012.

[14] S. Manipatruni, M. Lipson, and I. Young, "Device Scaling Considerations for Nanophotonic CMOS Global Interconnects," *Selected Topics in Quantum Electronics, IEEE Journal of*, vol. 19, no. 2, pp. 8200109–8200109, 2013.

[15] A. Naeemi, J. Xu, A. Mule', T. Gaylord, and J. Meindl, "Optical and electrical interconnect partition length based on chip-to-chip bandwidth maximization," *Photonics Technology Letters, IEEE*, vol. 16, no. 4, pp. 1221–1223, 2004.

[16] W. Stutius and W. Streifer, "Silicon nitride films on silicon for optical waveguides," *Appl. Opt.*, vol. 16, pp. 3218–3222, Dec 1977.

[17] J. F. Bauters, M. J. R. Heck, D. John, D. Dai, M.-C. Tien, J. S. Barton, A. Leinse, R. G. Heideman, D. J. Blumenthal, and J. E. Bowers, "Ultra-low-loss high-aspect-ratio Si_3N_4 waveguides," *Opt. Express*, vol. 19, pp. 3163–3174, Feb 2011.

[18] N. Daldosso, M. Melchiorri, F. Riboli, M. Girardini, G. Pucker, M. Crivellari, P. Bellutti, A. Lui, and L. Pavesi, "Comparison among various Si_3N_4 waveguide geometries grown within a CMOS fabrication pilot line," *Lightwave Technology, Journal of*, vol. 22, no. 7, pp. 1734–1740, 2004.

[19] R. Soref and J. Lorenzo, "Single-crystal silicon: a new material for 1.3 and 1.6 μm integrated-optical components," *Electronics Letters*, vol. 21, no. 21, pp. 953–954, 1985.

[20] P. Dumon, W. Bogaerts, V. Wiaux, J. Wouters, S. Beckx, J. Van Campenhout, D. Taillaert, B. Luyssaert, P. Bienstman, D. Van Thourhout, and R. Baets, "Low-loss SOI photonic wires and ring resonators fabricated with deep UV lithography," *Photonics Technology Letters, IEEE*, vol. 16, pp. 1328 –1330, may 2004.

[21] H. Rong, A. Liu, R. Jones, O. Cohen, D. Hak, R. Nicolaescu, A. Fang, and M. Paniccia, "An all-silicon Raman laser," *Nature*, vol. 433, pp. 292–294, Jan. 2005.

[22] T. J. Kippenberg, J. Kalkman, A. Polman, and K. J. Vahala, "Demonstration of an erbium-doped microdisk laser on a silicon chip," *Phys. Rev. A*, vol. 74, p. 051802, Nov 2006.

[23] R. N. Hall, G. E. Fenner, J. D. Kingsley, T. J. Soltys, and R. O. Carlson, "Coherent Light Emission From GaAs Junctions," *Phys. Rev. Lett.*, vol. 9, pp. 366–368, Nov 1962.

[24] S. Franssila, *Introduction to Microfabrication*. John Wiley & Sons, 2004.

[25] D. L. Mathine, "The integration of III-V optoelectronics with silicon circuitry," *Selected Topics in Quantum Electronics, IEEE Journal of*, vol. 3, no. 3, pp. 952–959, 1997.

[26] D. A. B. Miller, "Dense two-dimensional integration of optoelectronics and electronics for interconnections," in *Heterogeneous Integration: Systems on a Chip*, pp. 80–109, Eds. Bellingham, WA, 1998.

[27] G. Roelkens, L. Liu, D. Liang, R. Jones, A. Fang, B. Koch, and J. Bowers, "III-V/silicon photonics for on-chip and intra-chip optical interconnects," *Laser & Photonics Reviews*, vol. 4, no. 6, pp. 751–779, 2010.

[28] K. Goossen, J. Walker, L. D'Asaro, S. P. Hui, B. Tseng, R. Leibenguth, D. Kossives, D. D. Bacon, D. Dahringer, L. M. F. Chirovsky, A. Lentine, and D. Miller, "GaAs MQW modulators integrated with silicon CMOS," *Photonics Technology Letters, IEEE*, vol. 7, no. 4, pp. 360–362, 1995.

[29] A. Krishnamoorthy, L. M. F. Chirovsky, W. Hobson, R. Leibengath, S. P. Hui, G. Zydzik, K. Goossen, J. Wynn, B. J. Tseng, J. Lopata, J. Walker, J. Cunningham, and L. D'Asaro, "Vertical-cavity surface-emitting lasers flip-chip bonded to gigabit-per-second CMOS circuits," *Photonics Technology Letters, IEEE*, vol. 11, no. 1, pp. 128–130, 1999.

[30] T. Pinguet, B. Analui, E. Balmater, D. Guckenberger, M. Harrison, R. Koumans, D. Kucharski, Y. Liang, G. Masini, A. Mekis, S. Mirsaidi, A. Narasimha, M. Peterson, D. Rines, V. Sadagopan, S. Sahni, T. Sleboda, D. Song, Y. Wang, B. Welch, J. Witzens, J. Yao, S. Abdalla, S. Gloeckner, P. de Dobbelaere, and G. Capellini, "Monolithically integrated high-speed CMOS photonic transceivers," in *Group IV Photonics, 2008 5th IEEE International Conference on*, pp. 362–364, 2008.

[31] A. Krishnamoorthy and K. Goossen, "Optoelectronic-VLSI: photonics integrated with VLSI circuits," *Selected Topics in Quantum Electronics, IEEE Journal of*, vol. 4, no. 6, pp. 899–912, 1998.

[32] R. Chen, T.-T. D. Tran, K. W. Ng, W. S. Ko, L. C. Chuang, F. G. Sedgwick, and C. Chang-Hasnain, "Nanolasers grown on silicon," *Nat Photon*, vol. 5, pp. 170–175, Mar. 2011.

[33] D. G. Deppe, J. N. Holonyak, D. W. Nam, K. C. Hsieh, G. S. Jackson, R. J. Matyi, H. Shichijo, J. E. Epler, and H. F. Chung, "Room-temperature continuous operation of p-n $Al_xGa_{1-x}As$-GaAs quantum well heterostructure lasers grown on Si," *Applied Physics Letters*, vol. 51, no. 9, pp. 637–639, 1987.

[34] Y. Chriqui, G. Saint-Girons, S. Bouchoule, J.-M. Moison, G. Isella, H. Von Kaenel, and I. Sagnes, "Room temperature laser operation of strained InGaAs/GaAs QW structure monolithically grown by MOCVD on LE-PECVD Ge/Si virtual substrate," *Electronics Letters*, vol. 39, no. 23, pp. 1658–1660, 2003.

[35] Y. Chriqui, L. Largeau, G. Patriarche, G. Saint-Girons, S. Bouchoule, I. Sagnes, D. Bensahel, Y. Campidelli, and O. Kermarrec, "Direct growth of GaAs-based structures on exactly (001)-oriented Ge/Si virtual substrates: reduction of the structural defect density and observation of electroluminescence at room temperature under CW electrical injection," *Journal of Crystal Growth*, vol. 265, no. 12, pp. 53 – 59, 2004.

[36] O. Kwon, J. J. Boeckl, M. L. Lee, A. J. Pitera, E. A. Fitzgerald, and S. A. Ringel, "Monolithic integration of AlGaInP laser diodes on SiGe/Si substrates by molecular beam epitaxy," *Journal of Applied Physics*, vol. 100, no. 1, p. 013103, 2006.

[37] G. Saint-Girons, P. Regreny, L. Largeau, G. Patriarche, and G. Hollinger, "Monolithic integration of InP based heterostructures on silicon using crystalline Gd_2O_3 buffers," *Applied Physics Letters*, vol. 91, no. 24, p. 241912, 2007.

[38] B. Gobaut, J. Penuelas, J. Cheng, A. Chettaoui, L. Largeau, G. Hollinger, and G. Saint-Girons, "Direct growth of InAsP/InP quantum well heterostructures on Si using crystalline $SrTiO_3$/Si templates," *Applied Physics Letters*, vol. 97, no. 20, p. 201908, 2010.

[39] Y. Ujiie and T. Nishinaga, "Epitaxial Lateral Overgrowth of GaAs on a Si Substrate," *Japanese Journal of Applied Physics*, vol. 28, no. Part 2, No. 3, pp. L337–L339, 1989.

[40] F. Olsson, M. Xie, S. Lourdudoss, I. Prieto, and P. A. Postigo, "Epitaxial lateral overgrowth of InP on Si from nano-openings: Theoretical and experimental indication for defect filtering throughout the grown layer," *Journal of Applied Physics*, vol. 104, no. 9, p. 093112, 2008.

[41] G. Wang, M. R. Leys, R. Loo, O. Richard, H. Bender, N. Waldron, G. Brammertz, J. Dekoster, W. Wang, M. Seefeldt, M. Caymax, and M. M. Heyns, "Selective area growth of high quality InP on Si (001) substrates," *Applied Physics Letters*, vol. 97, no. 12, p. 121913, 2010.

[42] H. Kataria, C. Junesand, Z. Wang, W. Metaferia, Y.-T. Sun, S. Lourdudoss, G. Patriarche, A. Bazin, F. Raineri, P. A. Mages, N. Julian, and J. E. Bowers, "Towards a monolithically integrated III-V laser on silicon: optimization of multi-quantum well growth on InP on Si," *IOP Journal of Semiconductor Science and Technology*, 2013 (accepted).

[43] J. Liu, X. Sun, R. Camacho-Aguilera, L. C. Kimerling, and J. Michel, "Ge-on-Si laser operating at room temperature," *Opt. Lett.*, vol. 35, pp. 679–681, Mar 2010.

[44] J. Liu, L. C. Kimerling, and J. Michel, "Monolithic Ge-on-Si lasers for large-scale electronicphotonic integration," *Semiconductor Science and Technology*, vol. 27, no. 9, p. 094006, 2012.

[45] S. Koester, J. Schaub, G. Dehlinger, and J. Chu, "Germanium-on-SOI Infrared Detectors for Integrated Photonic Applications," *Selected Topics in Quantum Electronics, IEEE Journal of*, vol. 12, no. 6, pp. 1489–1502, 2006.

[46] L. Chen, P. Dong, and M. Lipson, "High performance germanium photodetectors integrated on submicron silicon waveguides by low temperature wafer bonding," *Opt. Express*, vol. 16, pp. 11513–11518, Jul 2008.

[47] J. Michel, J. Liu, and L. C. Kimerling, "High-performance Ge-on-Si photodetectors," *Nat Photon*, vol. 4, pp. 527–534, Aug. 2010.

[48] D. Feng, S. Liao, H. Liang, J. Fong, B. Bijlani, R. Shafiiha, B. J. Luff, Y. Luo, J. Cunningham, A. V. Krishnamoorthy, and M. Asghari, "High speed gesi electro-absorption modulator at 1550 nm wavelength on soi waveguide," *Opt. Express*, vol. 20, pp. 22224–22232, Sep 2012.

[49] A. R. Hawkins, T. E. Reynolds, D. R. England, D. I. Babic, M. J. Mondry, K. Streubel, and J. E. Bowers, "Silicon heterointerface photodetector," *Applied Physics Letters*, vol. 68, no. 26, pp. 3692–3694, 1996.

[50] A. Black, A. Hawkins, N. Margalit, D. Babic, J. Holmes, A.L., Y.-L. Chang, P. Abraham, J. Bowers, and E. Hu, "Wafer fusion: materials issues and device results," *Selected Topics in Quantum Electronics, IEEE Journal of*, vol. 3, no. 3, pp. 943–951, 1997.

[51] K. Tanabe, K. Watanabe, and Y. Arakawa, "III-V/Si hybrid photonic devices by direct fusion bonding," *Sci. Rep.*, vol. 2, Apr. 2012.

[52] R. Venkatasubramanian, M. L. Timmons, T. P. Humphreys, B. M. Keyes, and R. K. Ahrenkiel, "High-quality eutectic-metal-bonded AlGaAs-GaAs thin films on Si substrates," *Applied Physics Letters*, vol. 60, no. 7, pp. 886–888, 1992.

[53] C. Symonds, J. Dion, I. Sagnes, M. Dainese, M. Strassner, L. Leroy, and J.-L. Oudar, "High performance 1.55 μm vertical external cavity surface emitting laser with broadband integrated dielectric-metal mirror," *Electronics Letters*, vol. 40, pp. 734–735(1), June 2004.

[54] G. Vecchi, F. Raineri, I. Sagnes, A. Yacomotti, P. Monnier, T. J. Karle, K.-H. Lee, R. Braive, L. Le Gratiet, S. Guilet, G. Beaudoin, A. Taneau, S. Bouchoule, A. Levenson, and R. Raj, "Continuous-wave operation of photonic band-edge laser near 1.55 μm on silicon wafer," *Opt. Express*, vol. 15, pp. 7551–7556, Jun 2007.

[55] D. Pasquariello and K. Hjort, "Plasma-assisted InP-to-Si low temperature wafer bonding," *Selected Topics in Quantum Electronics, IEEE Journal of*, vol. 8, no. 1, pp. 118–131, 2002.

[56] A. Fang, H. Park, R. Jones, O. Cohen, M. Paniccia, and J. Bowers, "A continuous-wave hybrid AlGaInAs-silicon evanescent laser," *Photonics Technology Letters, IEEE*, vol. 18, no. 10, pp. 1143–1145, 2006.

[57] A. W. Fang, H. Park, Y. hao Kuo, R. Jones, O. Cohen, D. Liang, O. Raday, M. N. Sysak, M. J. Paniccia, and J. E. Bowers, "Hybrid silicon evanescent devices," *Materials Today*, vol. 10, no. 78, pp. 28 – 35, 2007.

[58] C. Seassal, P. Rojo-Romeo, X. Letartre, P. Viktorovitch, G. Hollinger, E. Jalaguier, S. Pocas, and B. Aspar, "InP microdisk lasers on silicon wafer: CW room temperature operation at 1.6 μm," *Electronics Letters*, vol. 37, pp. 222–223(1), Feb. 2001.

[59] G. Roelkens, D. Van Thourhout, and R. Baets, "Ultra-thin benzocyclobutene bonding of III-V dies onto SOI substrate," *Electronics Letters*, vol. 41, pp. 561–562(1), April 2005.

[60] G. Roelkens, D. Van Thourhout, and R. Baets, "Coupling schemes for heterogeneous integration of III-V membrane devices and silicon-on-insulator waveguides," *Lightwave Technology, Journal of*, vol. 23, no. 11, pp. 3827–3831, 2005.

[61] G. Roelkens, J. Brouckaert, D. Van Thourhout, R. Baets, R. Nötzel, and M. Smit, "Adhesive Bonding of InP/InGaAsP Dies to Processed Silicon-On-Insulator Wafers using DVS-bis-Benzocyclobutene," *Journal of The Electrochemical Society*, vol. 153, no. 12, pp. G1015–G1019, 2006.

[62] T. J. Karle, Y. Halioua, F. Raineri, P. Monnier, R. Braive, L. Le Gratiet, G. Beaudoin, I. Sagnes, G. Roelkens, F. van Laere, D. Van Thourhout, and R. Raj, "Heterogeneous integration and precise alignment of InP-based photonic crystal lasers to complementary metal-oxide semiconductor fabricated silicon-on-insulator wire waveguides," *Journal of Applied Physics*, vol. 107, no. 6, p. 063103, 2010.

[63] K. Tanabe, K. Watanabe, and Y. Arakawa, "1.3 μm InAs/GaAs quantum dot lasers on Si rib structures with current injection across direct-bonded GaAs/Si heterointerfaces," *Opt. Express*, vol. 20, pp. B315–B321, Dec 2012.

[64] H. Park, A. Fang, S. Kodama, and J. Bowers, "Hybrid silicon evanescent laser fabricated with a silicon waveguide and III-V offset quantum wells," *Opt. Express*, vol. 13, pp. 9460–9464, Nov 2005.

[65] A. W. Fang, H. Park, O. Cohen, R. Jones, M. J. Paniccia, and J. E. Bowers, "Electrically pumped hybrid AlGaInAs-silicon evanescent laser," *Opt. Express*, vol. 14, pp. 9203–9210, Oct 2006.

[66] T. Baba, M. Fujita, A. Sakai, M. Kihara, and R. Watanabe, "Lasing characteristics of GaInAsP-InP strained quantum-well microdisk injection lasers with diameter of 2-10 μm," *Photonics Technology Letters, IEEE*, vol. 9, no. 7, pp. 878–880, 1997.

[67] P. Rojo Romeo, J. Van Campenhout, P. Regreny, A. Kazmierczak, C. Seassal, X. Letartre, G. Hollinger, D. Van Thourhout , R. Baets, J. M. Fedeli, and L. Di Cioccio, "Heterogeneous integration of electrically driven microdisk based laser sources for optical interconnects and photonic ICs," *Opt. Express*, vol. 14, pp. 3864–3871, May 2006.

[68] J. Van Campenhout, P. Rojo Romeo, P. Regreny, C. Seassal, D. Van Thourhout, S. Verstuyft, L. Di Cioccio, J.-M. Fedeli, C. Lagahe, and R. Baets, "Electrically pumped InP-based microdisk lasers integrated with a nanophotonic silicon-on-insulator waveguide circuit," *Opt. Express*, vol. 15, pp. 6744–6749, May 2007.

[69] H. M. H. Chong and R. De La Rue, "Tuning of photonic crystal waveguide microcavity by thermooptic effect," *Photonics Technology Letters, IEEE*, vol. 16, no. 6, pp. 1528–1530, 2004.

[70] L. Liu, T. Spuesens, G. Roelkens, D. Van Thourhout, P. Regreny, and P. Rojo-Romeo, "A Thermally Tunable III-V Compound Semiconductor Microdisk Laser Integrated on Silicon-on-Insulator Circuits," *Photonics Technology Letters, IEEE*, vol. 22, no. 17, pp. 1270–1272, 2010.

[71] S. Keyvaninia, G. Roelkens, D. Van Thourhout, C. Jany, M. Lamponi, A. Le Liepvre, F. Lelarge, D. Make, G.-H. Duan, D. Bordel, and J.-M. Fedeli, "Demonstration of a heterogeneously integrated III-V/SOI single wavelength tunable laser," *Opt. Express*, vol. 21, pp. 3784–3792, Feb 2013.

[72] J. M. Fedeli, L. Di Cioccio, D. Marris-Morini, L. Vivien, R. Orobtchouk, P. Rojo-Romeo, C. Seassal, and F. Mandorlo, "Development of Silicon Photonics Devices Using Microelectronic Tools for the Integration on Top of a CMOS Wafer," *Advances in Optical Technologies*, vol. 2008, p. 15, 2008.

[73] T. Dupont, *Réalisation de sources laser III–V sur silicium.* PhD thesis, Ecole Centrale de Lyon, 2011.

[74] M. Notomi, A. Shinya, K. Nozaki, T. Tanabe, S. Matsuo, E. Kuramochi, T. Sato, H. Taniyama, and H. Sumikura, "Low-power nanophotonic devices based on photonic crystals towards dense photonic network on chip," *Circuits, Devices Systems, IET*, vol. 5, no. 2, pp. 84–93, 2011.

[75] D. Pudo, B. Corcoran, C. Monat, M. Pelusi, D. Moss, B. Eggleton, T. White, L. OFaolain, and T. Krauss, "Investigation of slow light enhanced nonlinear transmission for all-optical regeneration in silicon photonic crystal waveguides at 10 gbit/s," *Photonics and Nanostructures - Fundamentals and Applications*, vol. 8, no. 2, pp. 67 – 71, 2010. <ce:title>Special Issue {PECS} 8</ce:title>.

[76] B. Corcoran, C. Monat, M. Pelusi, C. Grillet, T. P. White, L. O'Faolain, T. F. Krauss, B. J. Eggleton, and D. J. Moss, "Optical signal processing on a silicon chip at 640gb/s using slow-light," *Opt. Express*, vol. 18, pp. 7770–7781, Apr 2010.

[77] B. Corcoran, M. D. Pelusi, C. Monat, J. Li, L. O'Faolain, T. F. Krauss, and B. J. Eggleton, "Ultracompact 160 gbaud all-optical demultiplexing exploiting slow light in an engineered silicon photonic crystal waveguide," *Opt. Lett.*, vol. 36, pp. 1728–1730, May 2011.

[78] Y. Halioua, *Study of hybrid III-V/Si photonic crystal lasers*. PhD thesis, Laboratoire de Photonique et de Nanostructures, CNRS, and Ghent University, Belgium, 2011.

[79] Y. Halioua, T. J. Karle, F. Raineri, P. Monnier, I. Sagnes, G. Roelkens, D. Van Thourhout, and R. Raj, "Hybrid InP-based photonic crystal lasers on silicon on insulator wires," *Applied Physics Letters*, vol. 95, no. 20, p. 201119, 2009.

[80] E. Yablonovitch, "Photonic Crystals: What's in a Name?," *Optics & Photonics News*, 2010.

[81] E. Yablonovitch, "Inhibited Spontaneous Emission in Solid-State Physics and Electronics," *Phys. Rev. Lett.*, vol. 58, pp. 2059–2062, May 1987.

[82] S. John, "Strong localization of photons in certain disordered dielectric superlattices," *Phys. Rev. Lett.*, vol. 58, pp. 2486–2489, Jun 1987.

[83] S. Noda, M. Fujita, and T. Asano, "Spontaneous-emission control by photonic crystals and nanocavities," *Nat Photon*, vol. 1, pp. 449–458, Aug. 2007.

[84] S. G. Johnson and J. D. Joannopoulos, "Three-dimensionally periodic dielectric layered structure with omnidirectional photonic band gap," *Applied Physics Letters*, vol. 77, no. 22, pp. 3490–3492, 2000.

[85] J. Joannopoulos, S. G. Johnson, J. N. Winn, and R. D. Meade, *Photonic crystals, Molding the flow of light*. Princeton University Press, 2007.

[86] K. Sakoda, *Optical Properties of Photonic Crystals*. Springer-Verlag, 2005.

[87] M. Notomi, K. Yamada, A. Shinya, J. Takahashi, C. Takahashi, and I. Yokohama, "Extremely Large Group-Velocity Dispersion of Line-Defect Waveguides in Photonic Crystal Slabs," *Phys. Rev. Lett.*, vol. 87, p. 253902, Nov 2001.

[88] A. Sakai, G. Hara, and T. Baba, "Propagation characteristics of ultrahigh-Δ optical waveguide on silicon-on-insulator substrate," *Japanese Journal of Applied Physics*, vol. 40, no. Part 2, No. 4B, pp. L383–L385, 2001.

[89] H. Gersen, T. J. Karle, R. J. P. Engelen, W. Bogaerts, J. P. Korterik, N. F. van Hulst, T. F. Krauss, and L. Kuipers, "Real-Space Observation of Ultraslow Light in Photonic Crystal Waveguides," *Phys. Rev. Lett.*, vol. 94, p. 073903, Feb 2005.

[90] L. O'Faolain, T. P. White, D. O'Brien, X. Yuan, M. D. Settle, and T. F. Krauss, "Dependence of extrinsic loss on group velocity in photonic crystal waveguides," *Opt. Express*, vol. 15, pp. 13129–13138, Oct 2007.

[91] T. Baba, "Slow light in photonic crystals," *Nat Photon*, vol. 2, pp. 465–473, Aug. 2008.

[92] L. O'Faolain, D. Beggs, T. White, T. Kampfrath, K. Kuipers, and T. Krauss, "Compact Optical Switches and Modulators Based on Dispersion Engineered Photonic Crystals," *Photonics Journal, IEEE*, vol. 2, pp. 404 –414, june 2010.

[93] M. Imada, S. Noda, A. Chutinan, T. Tokuda, M. Murata, and G. Sasaki, "Coherent two-dimensional lasing action in surface-emitting laser with triangular-lattice photonic crystal structure," *Applied Physics Letters*, vol. 75, no. 3, pp. 316–318, 1999.

[94] J. Mouette, C. Seassal, X. Letartre, P. Rojo-Romeo, J.-L. Leclereq, P. Regreny, P. Viktorovitch, E. Jalaguier, R. Perreau, and H. Moriceau, "Very low threshold vertical emitting laser operation in InP graphite photonic crystal slab on silicon," *Electronics Letters*, vol. 39, pp. 526 – 528, march 2003.

[95] S.-H. Kwon, H.-Y. Ryu, G.-H. Kim, Y.-H. Lee, and S.-B. Kim, "Photonic bandedge lasers in two-dimensional square-lattice photonic crystal slabs," *Applied Physics Letters*, vol. 83, no. 19, pp. 3870–3872, 2003.

[96] T. F. Krauss, R. M. De La Rue, and S. Brand, "Two-dimensional photonic-bandgap structures operating at near-infrared wavelengths," *Nature*, vol. 383, pp. 699–702, Oct. 1996.

[97] M. V. Kotlyar, T. Karle, M. D. Settle, L. O'Faolain, and T. F. Krauss, "Low-loss photonic crystal defect waveguides in InP," *Applied Physics Letters*, vol. 84, no. 18, pp. 3588–3590, 2004.

[98] S. Y. Lin, J. G. Fleming, D. L. Hetherington, B. K. Smith, R. Biswas, K. M. Ho, M. M. Sigalas, W. Zubrzycki, S. R. Kurtz, and J. Bur, "A three-dimensional photonic crystal operating at infrared wavelengths," *Nature*, vol. 394, pp. 251–253, July 1998.

[99] J. G. Fleming and S.-Y. Lin, "Three-dimensional photonic crystal with a stop band from 1.35 to 1.95 μm," *Opt. Lett.*, vol. 24, pp. 49–51, Jan 1999.

[100] S. Noda, N. Yamamoto, M. Imada, H. Kobayashi, and M. Okano, "Alignment and stacking of semiconductor photonic bandgaps by wafer-fusion," *Lightwave Technology, Journal of*, vol. 17, pp. 1948 –1955, nov 1999.

[101] S. Noda, K. Tomoda, N. Yamamoto, and A. Chutinan, "Full Three-Dimensional Photonic Bandgap Crystals at Near-Infrared Wavelengths," *Science*, vol. 289, no. 5479, pp. 604–606, 2000.

[102] S. G. Johnson, S. Fan, P. R. Villeneuve, J. D. Joannopoulos, and L. A. Kolodziejski, "Guided modes in photonic crystal slabs," *Phys. Rev. B*, vol. 60, pp. 5751–5758, Aug 1999.

[103] M. Lon**c**ar, D. Nedeljković, T. Doll, J. Vu**c**ković, A. Scherer, and T. P. Pearsall, "Waveguiding in planar photonic crystals," *Applied Physics Letters*, vol. 77, no. 13, pp. 1937–1939, 2000.

[104] E. Moreno, F. J. Garcia-Vidal, and L. Martin-Moreno, "Enhanced transmission and beaming of light via photonic crystal surface modes," *Phys. Rev. B*, vol. 69, p. 121402, Mar 2004.

[105] S.-H. Kim, S.-K. Kim, and Y.-H. Lee, "Vertical beaming of wavelength-scale photonic crystal resonators," *Phys. Rev. B*, vol. 73, p. 235117, Jun 2006.

[106] B.-S. Song, T. Asano, Y. Akahane, Y. Tanaka, and S. Noda, "Multichannel Add/Drop Filter Based on In-Plane Hetero Photonic Crystals," *Lightwave Technology, Journal of*, vol. 23, no. 3, pp. 1449–1455, 2005.

[107] R. D. Meade, A. Devenyi, J. D. Joannopoulos, O. L. Alerhand, D. A. Smith, and K. Kash, "Novel applications of photonic band gap materials: Low-loss bends and high Q cavities," *Journal of Applied Physics*, vol. 75, no. 9, pp. 4753–4755, 1994.

[108] F. Raineri, *Optique Non-Linéaire dans les cristaux photoniques en semiconducteur III-V*. PhD thesis, Laboratoire de Photonique et de Nanostructures, CNRS, 2004.

[109] T. Asano, B.-S. Song, Y. Akahane, and S. Noda, "Ultrahigh-Q Nanocavities in Two-Dimensional Photonic Crystal Slabs," *Selected Topics in Quantum Electronics, IEEE Journal of*, vol. 12, no. 6, pp. 1123–1134, 2006.

[110] E. Kuramochi, M. Notomi, S. Mitsugi, A. Shinya, T. Tanabe, and T. Watanabe, "Ultrahigh-Q photonic crystal nanocavities realized by the local width modulation of a line defect," *Applied Physics Letters*, vol. 88, no. 4, p. 041112, 2006.

[111] B.-H. Ahn, J.-H. Kang, M.-K. Kim, J.-H. Song, B. Min, K.-S. Kim, and Y.-H. Lee, "One-dimensional parabolic-beam photonic crystal laser," *Opt. Express*, vol. 18, pp. 5654–5660, Mar 2010.

[112] Q. Quan and M. Loncar, "Deterministic design of wavelength scale, ultra-high Q photonic crystal nanobeam cavities," *Opt. Express*, vol. 19, pp. 18529–18542, Sep 2011.

[113] K. Yee, "Numerical solution of initial boundary value problems involving Maxwell's equations in isotropic media," *Antennas and Propagation, IEEE Transactions on*, vol. 14, pp. 302 –307, may 1966.

[114] A. Taflove and S. Hagness, *Computational electrodynamics : the finite-difference timedomain method*. MA Artech House, 2000.

[115] V. A. Mandelshtam and H. S. Taylor, "Harmonic inversion of time signals and its applications," *The Journal of Chemical Physics*, vol. 107, no. 17, pp. 6756–6769, 1997.

[116] J. S. Foresi, P. R. Villeneuve, J. Ferrera, E. R. Thoen, G. Steinmeyer, S. Fan, J. D. Joannopoulos, L. C. Kimerling, H. I. Smith, and E. P. Ippen, "Photonic-bandgap microcavities in optical waveguides," *Nature*, vol. 390, pp. 143–145, Nov. 1997.

[117] Y. Halioua, A. Bazin, P. Monnier, T. J. Karle, G. Roelkens, I. Sagnes, R. Raj, and F. Raineri, "Hybrid III-V semiconductor/silicon nanolaser," *Opt. Express*, vol. 19, pp. 9221–9231, May 2011.

[118] M. Palamaru and P. Lalanne, "Photonic crystal waveguides: Out-of-plane losses and adiabatic modal conversion," *Applied Physics Letters*, vol. 78, no. 11, pp. 1466–1468, 2001.

[119] P. Lalanne and J. Hugonin, "Bloch-wave engineering for high-Q, small-V microcavities," *Quantum Electronics, IEEE Journal of*, vol. 39, pp. 1430 – 1438, nov. 2003.

[120] C. Sauvan, G. Lecamp, P. Lalanne, and J. Hugonin, "Modal-reflectivity enhancement by geometry tuning in Photonic Crystal microcavities," *Opt. Express*, vol. 13, pp. 245–255, Jan 2005.

[121] P. Velha, E. Picard, T. Charvolin, E. Hadji, J. Rodier, P. Lalanne, and D. Peyrade, "Ultra-high Q/V fabry-perot microcavity on SOI substrate," *Opt. Express*, vol. 15, pp. 16090–16096, Nov 2007.

[122] Y. Halioua, A. Bazin, P. Monnier, T. J. Karle, I. Sagnes, G. Roelkens, D. Van Thourhout , F. Raineri, and R. Raj, "III-V photonic crystal wire cavity laser on silicon wafer," *J. Opt. Soc. Am. B*, vol. 27, pp. 2146–2150, Oct 2010.

[123] M. W. McCutcheon and M. Loncar, "Design of a silicon nitride photonic crystal nanocavity with a Quality factor of one million for coupling to a diamond nanocrystal," *Opt. Express*, vol. 16, pp. 19136–19145, Nov 2008.

[124] Y. Akahane, T. Asano, B. Song, and S. Noda, "High-Q photonic nanocavity in a two-dimensional photonic crystal," *Nature*, vol. 425, pp. 944–947, Oct. 2003.

[125] K. Srinivasan and O. Painter, "Momentum space design of high-Q photonic crystal optical cavities," *Opt. Express*, vol. 10, pp. 670–684, Jul 2002.

[126] Y. Tanaka, T. Asano, and S. Noda, "Design of photonic crystal nanocavity with Q-factor of $\sim 10^9$," *J. Lightwave Technol.*, vol. 26, pp. 1532–1539, Jun 2008.

[127] M. Notomi, E. Kuramochi, and H. Taniyama, "Ultrahigh-Q Nanocavity with 1D Photonic Gap," *Opt. Express*, vol. 16, pp. 11095–11102, Jul 2008.

[128] E. Kuramochi, H. Taniyama, T. Tanabe, K. Kawasaki, Y.-G. Roh, and M. Notomi, "Ultrahigh-Q one-dimensional photonic crystal nanocavities with modulated mode-gap barriers on SiO_2 claddings and on air claddings," *Opt. Express*, vol. 18, pp. 15859–15869, 2010.

[129] Q. Quan, P. B. Deotare, and M. Loncar, "Photonic crystal nanobeam cavity strongly coupled to the feeding waveguide," *Applied Physics Letters*, vol. 96, no. 20, p. 203102, 2010.

[130] F. Römer and B. Witzigmann, "Spectral and spatial properties of the spontaneous emission enhancement in photonic crystal cavities," *J. Opt. Soc. Am. B*, vol. 25, pp. 31–39, Jan 2008.

[131] N.-V.-Q. Tran, S. Combrié, and A. De Rossi, "Directive emission from high-Q photonic crystal cavities through band folding," *Phys. Rev. B*, vol. 79, p. 041101, Jan 2009.

[132] S. L. Portalupi, M. Galli, C. Reardon, T. Krauss, L. O'Faolain, L. C. Andreani, and D. Gerace, "Planar photonic crystal cavities with far-field optimization for high coupling efficiency and quality factor," *Opt. Express*, vol. 18, pp. 16064–16073, Jul 2010.

[133] S. Haddadi, L. Le Gratiet, I. Sagnes, F. Raineri, A. Bazin, K. Bencheikh, J. A. Levenson, and A. M. Yacomotti, "High quality beaming and efficient free-space coupling in L3 photonic crystal active nanocavities," *Opt. Express*, vol. 20, pp. 18876–18886, Aug 2012.

[134] C. J. M. Smith, R. M. De La Rue, M. Rattier, S. Olivier, H. Benisty, C. Weisbuch, T. F. Krauss, R. Houdré, and U. Oesterle, "Coupled guide and cavity in a two-dimensional photonic crystal," *Applied Physics Letters*, vol. 78, no. 11, pp. 1487–1489, 2001.

[135] B.-S. Song, S. Noda, and T. Asano, "Photonic Devices Based on In-Plane Hetero Photonic Crystals," *Science*, vol. 300, no. 5625, p. 1537, 2003.

[136] M. Notomi, A. Shinya, S. Mitsugi, E. Kuramochi, and H. Ryu, "Waveguides, resonators and their coupled elements in photonic crystal slabs," *Opt. Express*, vol. 12, pp. 1551–1561, Apr 2004.

[137] E. Waks and J. Vuckovic, "Coupled mode theory for photonic crystal cavity-waveguide interaction," *Opt. Express*, vol. 13, pp. 5064–5073, Jun 2005.

[138] A. Mekis and J. D. Joannopoulos, "Tapered Couplers for Efficient Interfacing Between Dielectric and Photonic Crystal Waveguides," *J. Lightwave Technol.*, vol. 19, p. 861, Jun 2001.

[139] P. Pottier, M. Gnan, and R. M. D. L. Rue, "Efficient coupling into slow-light photonic crystal channel guides using photonic crystal tapers," *Opt. Express*, vol. 15, pp. 6569–6575, May 2007.

[140] A. Talneau, K. H. Lee, S. Guilet, and I. Sagnes, "Efficient coupling to w1 photonic crystal waveguide on inp membrane through suspended access guides," *Applied Physics Letters*, vol. 92, no. 6, p. 061105, 2008.

[141] K. Nozaki, H. Watanabe, and T. Baba, "Photonic crystal nanolaser monolithically integrated with passive waveguide for effective light extraction," *Applied Physics Letters*, vol. 92, no. 2, p. 021108, 2008.

[142] S. Matsuo, A. Shinya, C.-H. Chen, K. Nozaki, T. Sato, Y. Kawaguchi, H. Taniyama, and M. Notomi, "20-Gbit/s directly modulated photonic crystal nanocavity laser with ultra-low power consumption," *Opt. Express*, vol. 19, pp. 2242–2250, Jan 2011.

[143] P. Barclay, K. Srinivasan, M. Borselli, and O. Painter, "Experimental demonstration of evanescent coupling from optical fibre tapers to photonic crystal waveguides," *Electronics Letters*, vol. 39, pp. 842 – 844, may 2003.

[144] I.-K. Hwang, S.-K. Kim, J.-K. Yang, S.-H. Kim, S. H. Lee, and Y.-H. Lee, "Curved-microfiber photon coupling for photonic crystal light emitter," *Applied Physics Letters*, vol. 87, no. 13, p. 131107, 2005.

[145] C. Grillet, C. Monat, C. L. Smith, B. J. Eggleton, D. J. Moss, S. Frédérick, D. Dalacu, P. J. Poole, J. Lapointe, G. Aers, and R. L. Williams, "Nanowire coupling to photonic crystal nanocavities for single photon sources," *Opt. Express*, vol. 15, pp. 1267–1276, Feb 2007.

[146] M. Brunstein, R. Braive, R. Hostein, A. Beveratos, I. Rober-Philip, I. Sagnes, T. J. Karle, A. M. Yacomotti, J. A. Levenson, V. Moreau, G. Tessier, and Y. De Wilde, "Thermo-optical dynamics in an optically pumped photonic crystal nano-cavity," *Opt. Express*, vol. 17, pp. 17118–17129, Sep 2009.

[147] R. Emmons and D. Hall, "Buried-oxide silicon-on-insulator structures. II. Waveguide grating couplers," *Quantum Electronics, IEEE Journal of*, vol. 28, pp. 164 –175, jan 1992.

[148] D. Taillaert, W. Bogaerts, P. Bienstman, T. Krauss, P. Van Daele, I. Moerman, S. Verstuyft, K. De Mesel, and R. Baets, "An out-of-plane grating coupler for efficient butt-coupling between compact planar waveguides and single-mode fibers," *Quantum Electronics, IEEE Journal of*, vol. 38, pp. 949 –955, jul 2002.

[149] D. Taillaert, F. Van Laere, M. Ayre, W. Bogaerts, D. Van Thourhout, P. Bienstman, and R. Baets, "Grating Couplers for Coupling between Optical Fibers and Nanophotonic Waveguides," *Japanese Journal of Applied Physics*, vol. 45, no. 8A, pp. 6071–6077, 2006.

[150] M. Bruel, "Silicon on insulator material technology," *Electronics Letters*, vol. 31, pp. 1201 –1202, jul 1995.

[151] A. P. K. Graham T. Reed, *Silicon Photonics: The State of the Art*. Wiley, 2004.

[152] S. K. Selvaraja, P. Jaenen, W. Bogaerts, D. Van Thourhout, P. Dumon, and R. Baets, "Fabrication of Photonic Wire and Crystal Circuits in Silicon-on-Insulator Using 193-nm Optical Lithography," *J. Lightwave Technol.*, vol. 27, pp. 4076–4083, Sep 2009.

[153] S. K. Selvaraja, W. Bogaerts, and D. Van Thourhout, "Loss reduction in silicon nanophotonic waveguide micro-bends through etch profile improvement," *Optics Communications*, vol. 284, no. 8, pp. 2141 – 2144, 2011.

[154] T. Yoshie, O. Shchekin, H. Chen, D. Deppe, and A. Scherer, "Quantum dot photonic crystal lasers," *Electronics Letters*, vol. 38, pp. 967 – 968, aug 2002.

[155] S. Strauf, K. Hennessy, M. T. Rakher, Y.-S. Choi, A. Badolato, L. C. Andreani, E. L. Hu, P. M. Petroff, and D. Bouwmeester, "Self-Tuned Quantum Dot Gain in Photonic Crystal Lasers," *Phys. Rev. Lett.*, vol. 96, p. 127404, Mar 2006.

[156] M. Nomura, S. Iwamoto, K. Watanabe, N. Kumagai, Y. Nakata, S. Ishida, and Y. Arakawa, "Room temperature continuous-wave lasing in photonic crystal nanocavity," *Opt. Express*, vol. 14, pp. 6308–6315, Jun 2006.

[157] B. Ellis, I. Fushman, D. Englund, B. Zhang, Y. Yamamoto, and J. Vu**c**ković, "Dynamics of quantum dot photonic crystal lasers," *Applied Physics Letters*, vol. 90, no. 15, p. 151102, 2007.

[158] R. Braive, S. Barbay, I. Sagnes, A. Miard, I. Robert-Philip, and A. Beveratos, "Transient chirp in high-speed photonic-crystal quantum-dot lasers with controlled spontaneous emission," *Opt. Lett.*, vol. 34, pp. 554–556, Mar 2009.

[159] K. Nozaki, S. Kita, and T. Baba, "Room temperature continuous wave operation and controlled spontaneous emission in ultrasmall photonic crystal nanolaser," *Opt. Express*, vol. 15, pp. 7506–7514, Jun 2007.

[160] S. Matsuo, A. Shinya, T. Kakitsuka, K. Nozaki, T. Segawa, T. Sato, Y. Kawaguchi, and M. Notomi, "High-speed ultracompact buried heterostructure photonic-crystal laser with 13 fJ of energy consumed per bit transmitted," *Nat Photon*, vol. 4, pp. 648–654, Sept. 2010.

[161] S. Keyvaninia, M. Muneeb, S. Stanković, P. J. Van Veldhoven , D. Van Thourhout, and G. Roelkens, "Ultra-thin DVS-BCB adhesive bonding of III-V wafers, dies and multiple dies to a patterned silicon-on-insulator substrate," *Opt. Mater. Express*, vol. 3, pp. 35–46, Jan 2013.

[162] F. Niklaus, R. J. Kumar, J. J. McMahon, J. Yu, J.-Q. Lu, T. S. Cale, and R. J. Gutmann, "Adhesive Wafer Bonding Using Partially Cured Benzocyclobutene for Three-Dimensional Integration," *Journal of The Electrochemical Society*, vol. 153, no. 4, pp. G291–G295, 2006.

[163] S. das Neves and M. De Paoli, "A quantitative study of chemical etching of InP," *Journal of The Electrochemical Society*, vol. 140, no. 9, pp. 2599–2603, 1993.

[164] H. Namatsu, Y. Takahashi, K. Yamazaki, T. Yamaguchi, M. Nagase, and K. Kurihara, "Three-dimensional siloxane resist for the formation of nanopatterns with minimum linewidth fluctuations," *Journal of Vacuum Science & Technology B: Microelectronics and Nanometer Structures*, vol. 16, no. 1, pp. 69–76, 1998.

[165] D. L. Olynick, B. Cord, A. Schipotinin, D. F. Ogletree, and P. J. Schuck, "Electron-beam exposure mechanisms in hydrogen silsesquioxane investigated by vibrational spectroscopy and in situ electron-beam-induced desorption," *Journal of Vacuum Science & Technology B: Microelectronics and Nanometer Structures*, vol. 28, no. 3, pp. 581–587, 2010.

[166] S. Assefa, G. S. Petrich, L. A. Kolodziejski, M. K. Mondol, and H. I. Smith, "Fabrication of photonic crystal waveguides composed of a square lattice of dielectric rods," *The 48th*

International Conference on Electron, Ion, and Photon Beam Technology and Nanofabrication, vol. 22, no. 6, pp. 3363–3365, 2004.

[167] S. Guilet, S. Bouchoule, C. Jany, C. S. Corr, and P. Chabert, "Optimization of a Cl_2–H_2 inductively coupled plasma etching process adapted to nonthermalized InP wafers for the realization of deep ridge heterostructures," *Journal of Vacuum Science & Technology B: Microelectronics and Nanometer Structures*, vol. 24, no. 5, pp. 2381–2387, 2006.

[168] S. Bouchoule, G. Patriarche, S. Guilet, L. Gatilova, L. Largeau, and P. Chabert, "Sidewall passivation assisted by a silicon coverplate during Cl_2–H_2 and HBr inductively coupled plasma etching of inp for photonic devices," *Journal of Vacuum Science & Technology B: Microelectronics and Nanometer Structures*, vol. 26, no. 2, pp. 666–674, 2008.

[169] L. Gatilova, S. Bouchoule, S. Guilet, and P. Chabert, "Investigation of inp etching mechanisms in a Cl_2/H_2 inductively coupled plasma by optical emission spectroscopy," *Journal of Vacuum Science & Technology A: Vacuum, Surfaces, and Films*, vol. 27, no. 2, pp. 262–275, 2009.

[170] S. Bouchoule, S. Azouigui, S. Guilet, G. Patriarche, L. Largeau, A. Martinez, L. Le Gratiet, A. Lemaitre, and F. Lelarge, "Anisotropic and Smooth Inductively Coupled Plasma Etching of III-V Laser Waveguides Using HBr-O_2 Chemistry," *Journal of The Electrochemical Society*, vol. 155, no. 10, pp. H778–H785, 2008.

[171] M. Volatier, D. Duchesne, R. Morandotti, R. Ares, and V. Aimez, "Extremely high aspect ratio GaAs and GaAs/AlGaAs nanowaveguides fabricated using chlorine ICP etching with N_2-promoted passivation," *Nanotechnology*, vol. 21, no. 13, p. 134014, 2010.

[172] K. H. Lee, S. Guilet, G. Patriarche, I. Sagnes, and A. Talneau, "Smooth sidewall in InP-based photonic crystal membrane etched by N_2-based inductively coupled plasma," *Journal of Vacuum Science & Technology B: Microelectronics and Nanometer Structures*, vol. 26, no. 4, pp. 1326–1333, 2008.

[173] P. J. Martin, R. P. Netterfield, T. J. Kinder, and V. Stambouli, "In situ stress measurements of ion-assisted MgF_2 and SiO_x thin films," *Applied Physics Letters*, vol. 58, pp. 2497 –2499, jun 1991.

[174] E. M. Purcell, "Proceedings of the American Physical Society," *Phys. Rev.*, vol. 69, pp. 674–674, Jun 1946.

[175] D. Englund, D. Fattal, E. Waks, G. Solomon, B. Zhang, T. Nakaoka, Y. Arakawa, Y. Yamamoto, and J. Vu**c**ković, "Controlling the Spontaneous Emission Rate of Single Quantum Dots in a Two-Dimensional Photonic Crystal," *Phys. Rev. Lett.*, vol. 95, p. 013904, Jul 2005.

[176] T. Kuroda, N. Ikeda, T. Mano, Y. Sugimoto, T. Ochiai, K. Kuroda, S. Ohkouchi, N. Koguchi, K. Sakoda, and K. Asakawa, "Acceleration and suppression of photoemission

of GaAs quantum dots embedded in photonic crystal microcavities," *Applied Physics Letters*, vol. 93, no. 11, p. 111103, 2008.

[177] M. Fujita, S. Takahashi, Y. Tanaka, T. Asano, and S. Noda, "Simultaneous Inhibition and Redistribution of Spontaneous Light Emission in Photonic Crystals," *Science*, vol. 308, no. 5726, pp. 1296–1298, 2005.

[178] S. Laurent, S. Varoutsis, L. Le Gratiet, A. Lemaître, I. Sagnes, F. Raineri, A. Levenson, I. Robert-Philip, and I. Abram, "Indistinguishable single photons from a single-quantum dot in a two-dimensional photonic crystal cavity," *Applied Physics Letters*, vol. 87, no. 16, p. 163107, 2005.

[179] J.-Y. Bigot, M. Portella, R. Schoenlein, C. Shank, and J. Cunningham, "Two-Dimensional CarrierCarrier Screening Studied with Femtosecond Photon Echoes," in *Ultrafast Phenomena VII* (C. B. Harris, E. P. Ippen, G. A. Mourou, and A. H. Zewail, eds.), vol. 53 of *Springer Series in Chemical Physics*, pp. 239–243, Springer Berlin Heidelberg, 1990.

[180] L. A. Coldren and S. W. Corzine, *Diode Lasers and Photonic Integrated Circuits*. John Wiley & Sons, 2012.

[181] F. Koyama, K. Morito, and K. Iga, "Intensity noise and polarization stability of GaAlAs-GaAs surface emitting lasers," *Quantum Electronics, IEEE Journal of*, vol. 27, no. 6, pp. 1410–1416, 1991.

[182] D. V. Kuksenkov, H. Temkin, K. L. Lear, and H. Q. Hou, "Spontaneous emission factor in oxide confined vertical-cavity lasers," *Applied Physics Letters*, vol. 70, no. 1, pp. 13–15, 1997.

[183] J. M. Gérard, B. Sermage, B. Gayral, B. Legrand, E. Costard, and V. Thierry-Mieg, "Enhanced spontaneous emission by quantum boxes in a monolithic optical microcavity," *Phys. Rev. Lett.*, vol. 81, pp. 1110–1113, Aug 1998.

[184] G. Bjork and Y. Yamamoto, "Analysis of semiconductor microcavity lasers using rate equations," *Quantum Electronics, IEEE Journal of*, vol. 27, pp. 2386 –2396, nov 1991.

[185] G. Björk, A. Karlsson, and Y. Yamamoto, "Definition of a laser threshold," *Phys. Rev. A*, vol. 50, pp. 1675–1680, Aug 1994.

[186] F. Raineri, A. M. Yacomotti, T. J. Karle, R. Hostein, R. Braive, A. Beveratos, I. Sagnes, and R. Raj, "Dynamics of band-edge photonic crystal lasers," *Opt. Express*, vol. 17, pp. 3165–3172, Mar 2009.

[187] Y. Zhang, M. Khan, Y. Huang, J. Ryou, P. Deotare, R. Dupuis, and M. Lon**c**ar, "Photonic crystal nanobeam lasers," *Applied Physics Letters*, vol. 97, no. 5, p. 051104, 2010.

[188] T.-W. Lu, L.-H. Chiu, P.-T. Lin, and P.-T. Lee, "One-dimensional photonic crystal nanobeam lasers on a flexible substrate," *Applied Physics Letters*, vol. 99, no. 7, p. 071101, 2011.

[189] Y. Gong, B. Ellis, G. Shambat, T. Sarmiento, J. S. Harris, , and J. Vuckovic, "Nanobeam photonic crystal cavity quantum dot laser," *Opt. Express*, vol. 18, pp. 8781–8789, 2010.

[190] D. Englund, H. Altug, I. Fushman, and J. Vu**c**ković, "Efficient terahertz room-temperature photonic crystal nanocavity laser," *Applied Physics Letters*, vol. 91, no. 7, p. 071126, 2007.

[191] K. J. Vahala and C. E. Zah, "Effect of doping on the optical gain and the spontaneous noise enhancement factor in quantum well amplifiers and lasers studied by simple analytical expressions," *Applied Physics Letters*, vol. 52, no. 23, pp. 1945–1947, 1988.

[192] T. Makino, "Analytical formulas for the optical gain of quantum wells," *Quantum Electronics, IEEE Journal of*, vol. 32, pp. 493 –501, mar 1996.

[193] N. Bouché, *Etude de la dynamique, de l'émission laser, de l'amplification et de la commutation dans les structures laser à cavité verticale à 1,55 μm.* PhD thesis, France TELECOM, Centre National d'Etudes des Télécommunications, Laboratoire de Bagneux, 1998.

[194] R. Braive, *Contrôle de l'émission spontanée dans les cristaux photoniques.* PhD thesis, Laboratoire de Photonique et de Nanostructures, CNRS, 2008.

[195] T. Kobayashi, T. Segawa, A. Morimoto, , and T. Sueta *Technical Digest of 43rd Fall Meeting of Japanese Applied Physics Society*, 1982.

[196] T. Kobayashi, A. Morimoto, and T. Sueta *Technical Digest of 46rd Fall Meeting of Japanese Applied Physics Society*, 1985.

[197] H. Yokoyama and S. D. Brorson, "Rate equation analysis of microcavity lasers," *Journal of Applied Physics*, vol. 66, no. 10, pp. 4801–4805, 1989.

[198] M. Nomura, N. Kumagai, S. Iwamoto, Y. Ota, and Y. Arakawa, "Photonic crystal nanocavity laser with a single quantum dot gain," *Opt. Express*, vol. 17, pp. 15975–15982, Aug 2009.

[199] R. Hostein, R. Braive, L. L. Gratiet, A. Talneau, G. Beaudoin, I. Robert-Philip, I. Sagnes, and A. Beveratos, "Demonstration of coherent emission from high-β photonic crystal nanolasers at room temperature," *Opt. Lett.*, vol. 35, pp. 1154–1156, Apr 2010.

[200] A. Lebreton, I. Abram, R. Braive, I. Sagnes, I. Robert-Philip, and A. Beveratos, "Unequivocal Differentiation of Coherent and Chaotic Light through Interferometric Photon Correlation Measurements," *Phys. Rev. Lett.*, vol. 110, p. 163603, Apr 2013.

[201] E. Rosencher and B. Vinter, *Optoelectronics.* Cambridge University Press, 2002.

[202] C. Henry, "Theory of the linewidth of semiconductor lasers," *Quantum Electronics, IEEE Journal of*, vol. 18, no. 2, pp. 259–264, 1982.

[203] G. Björk, A. Karlsson, and Y. Yamamoto, "On the linewidth of microcavity lasers," *Applied Physics Letters*, vol. 60, no. 3, pp. 304–306, 1992.

[204] Z. Toffano, "Investigation of threshold transition in semiconductor lasers," *Selected Topics in Quantum Electronics, IEEE Journal of*, vol. 3, pp. 485 –490, apr 1997.

[205] W. Bogaerts, R. Baets, P. Dumon, V. Wiaux, S. Beckx, D. Taillaert, B. Luyssaert, J. Van Campenhout, P. Bienstman, and D. Van Thourhout, "Nanophotonic waveguides in silicon-on-insulator fabricated with CMOS technology," *Lightwave Technology, Journal of*, vol. 23, pp. 401 – 412, jan. 2005.

[206] D. Vermeulen, S. Selvaraja, P. Verheyen, G. Lepage, W. Bogaerts, P. Absil, D. Van Thourhout, and G. Roelkens, "High-efficiency fiber-to-chip grating couplers realized using an advanced CMOS-compatible Silicon-On-Insulator platform," *Opt. Express*, vol. 18, pp. 18278–18283, Aug 2010.

[207] E. Gini and H. Melchior, "Thermal dependence of the refractive index of InP measured with integrated optical demultiplexer," *Journal of Applied Physics*, vol. 79, no. 8, pp. 4335–4337, 1996.

[208] J. Piprek, Y. A. Akulova, D. I. Babic, L. A. Coldren, and J. E. Bowers, "Minimum temperature sensitivity of 1.55 μm vertical-cavity lasers at -30 nm gain offset," *Applied Physics Letters*, vol. 72, no. 15, pp. 1814–1816, 1998.

[209] V. Moreau, G. Tessier, F. Raineri, M. Brunstein, A. Yacomotti, R. Raj, I. Sagnes, A. Levenson, and Y. D. Wilde, "Transient thermoreflectance imaging of active photonic crystals," *Applied Physics Letters*, vol. 96, no. 9, p. 091103, 2010.

[210] J. Hwang, H. Ryu, D. Song, I. Han, H. Park, D. Jang, and Y. Lee, "Continuous room-temperature operation of optically pumped two-dimensional photonic crystal lasers at 1.6 μm," *Photonics Technology Letters, IEEE*, vol. 12, pp. 1295 –1297, oct. 2000.

[211] J. Cao, W. Kuang, Z. jian Wei, S.-J. Choi, H. Yu, M. Bagheri, J. O'Brien, and P. Dapkus, "Sapphire-bonded photonic Crystal microcavity lasers and their far-field radiation patterns," *Photonics Technology Letters, IEEE*, vol. 17, pp. 4 –6, jan. 2005.

[212] S. Kim, S. Kim, K. Hwang, H. Jeon, and H. J. Kim, "Operation of Photonic Crystal Laser in Continuous-Wave Mode for 18 Hours," *Applied Physics Express*, vol. 4, no. 12, p. 122101, 2011.

[213] N. F. Massé, A. R. Adams, and S. J. Sweeney, "Experimental determination of the band gap dependence of Auger recombination in InGaAs/InP multiple quantum well lasers at room temperature," *Applied Physics Letters*, vol. 90, no. 16, p. 161113, 2007.

[214] K. Tai, T. R. Hayes, S. L. McCall, and W. T. Tsang, "Optical measurement of surface recombination in InGaAs quantum well mesa structures," *Applied Physics Letters*, vol. 53, no. 4, pp. 302–303, 1988.

[215] M. Boroditsky, I. Gontijo, M. Jackson, R. Vrijen, E. Yablonovitch, T. Krauss, C.-C. Cheng, A. Scherer, R. Bhat, and M. Krames, "Surface recombination measurements on III–V candidate materials for nanostructure light-emitting diodes," *Journal of Applied Physics*, vol. 87, no. 7, pp. 3497–3504, 2000.

[216] C. J. Sandroff, R. N. Nottenburg, J.-C. Bischoff, and R. Bhat, "Dramatic enhancement in the gain of a GaAs/AlGaAs heterostructure bipolar transistor by surface chemical passivation," *Applied Physics Letters*, vol. 51, no. 1, pp. 33–35, 1987.

[217] E. Yablonovitch, H. M. Cox, and T. J. Gmitter, "Nearly ideal electronic surfaces on naked $In_{0.53}Ga_{0.47}$as quantum wells," *Applied Physics Letters*, vol. 52, no. 12, pp. 1002–1004, 1987.

[218] H. Oigawa, J.-F. Fan, Y. Nannichi, H. Sugahara, and M. Oshima, "Universal passivation effect of $(NH_4)_2S_x$ treatment on the surface of III-V compound semiconductors," *Japanese Journal of Applied Physics*, vol. 30, no. Part 2, No. 3A, pp. L322–L325, 1991.

[219] F. Raineri, C. Cojocaru, P. Monnier, A. Levenson, R. Raj, C. Seassal, X. Letartre, and P. Viktorovitch, "Ultrafast dynamics of the third-order nonlinear response in a two-dimensional inp-based photonic crystal," *Applied Physics Letters*, vol. 85, no. 11, pp. 1880–1882, 2004.

[220] H. A. Haus, *Waves and Fields in Optoelectronics*. Prentice-Hall, Englewood Cliffs, N.J., 1984.

[221] E. A. J. Marcatili, "Dielectric Rectangular Waveguide and Directional Coupler for Integrated Optics," *Bell Syst. Tech. J.*, vol. 48, pp. 2071–2102, 1969.

[222] H. F. Taylor, "Optical switching and modulation in parallel dielectric waveguides," *Journal of Applied Physics*, vol. 44, no. 7, pp. 3257–3262, 1973.

[223] W. Suh, Z. Wang, and S. Fan, "Temporal coupled-mode theory and the presence of non-orthogonal modes in lossless multimode cavities," *Quantum Electronics, IEEE Journal of*, vol. 40, pp. 1511 – 1518, oct. 2004.

[224] D. Marcuse, *Theory of Dielectric Optical Waveguides*. Academic Press, Inc., 1973.

[225] H. Kawaguchi, "Optical bistability and chaos in a semiconductor laser with a saturable absorber," *Applied Physics Letters*, vol. 45, no. 12, pp. 1264–1266, 1984.

[226] H. Altug, D. Englund, and J. Vuckovic, "Ultrafast photonic crystal nanocavity laser," *Nat Phys*, vol. 2, pp. 484–488, July 2006.

[227] K. J. Ebeling, *Integrated Opto-electronics*. Springer-Verlag, 1993.

[228] K. Nonaka, Y. Noguchi, H. Tsuda, and T. Kurokawa, "Digital signal regeneration with side-injection-light-controlled bistable laser diode as a wavelength converter," *Photonics Technology Letters, IEEE*, vol. 7, no. 1, pp. 29–31, 1995.

[229] M. Hill, A. Srivatsa, N. Calabretta, Y. Liu, H. D. Waardt, G.-D. Khoe, and H. J. S. Dorren, "1×2 optical packet switch using all-optical header processing," *Electronics Letters*, vol. 37, no. 12, pp. 774–775, 2001.

[230] G. Lasher, "Analysis of a proposed bistable injection laser," *Solid-State Electronics*, vol. 7, no. 10, pp. 707 – 716, 1964.

[231] M. I. Nathan, J. C. Marinace, R. F. Rutz, A. E. Michel, and G. J. Lasher, "GaAs Injection Laser with Novel Mode Control and Switching Properties," *Journal of Applied Physics*, vol. 36, no. 2, pp. 473–480, 1965.

[232] A. Szöke, V. Daneu, J. Goldhar, and N. A. Kurnit, "Bistable optical element and its applications," *Applied Physics Letters*, vol. 15, no. 11, pp. 376–379, 1969.

[233] H. M. Gibbs, S. L. McCall, and T. N. C. Venkatesan, "Differential gain and bistability using a sodium-filled Fabry-Perot interferometer," *Phys. Rev. Lett.*, vol. 36, pp. 1135–1138, May 1976.

[234] H. M. Gibbs, S. L. McCall, T. N. C. Venkatesan, A. C. Gossard, A. Passner, and W. Wiegmann, "Optical bistability in semiconductors," *Applied Physics Letters*, vol. 35, no. 6, pp. 451–453, 1979.

[235] N. Peychambarian and H. M. Gibbs, "Optical nonlinearity, bistability, and signal processing in semiconductors," *J. Opt. Soc. Am. B*, vol. 2, pp. 1215–1227, Jul 1985.

[236] O. Sahlén, U. Olin, E. Masseboeuf, G. Landgren, and M. Rask, "Optical bistability and gating in metalorganic vapor phase epitaxy grown GaAs étalons operating in reflection," *Applied Physics Letters*, vol. 50, no. 22, pp. 1559–1561, 1987.

[237] R. Kuszelewicz, J. L. Oudar, J. C. Michel, and R. Azoulay, "Monolithic GaAs/AlAs optical bistable étalons with improved switching characteristics," *Applied Physics Letters*, vol. 53, no. 22, pp. 2138–2140, 1988.

[238] B. G. Sfez, J. L. Oudar, J. C. Michel, R. Kuszelewicz, and R. Azoulay, "High contrast multiple quantum well optical bistable device with integrated Bragg reflectors," *Applied Physics Letters*, vol. 57, no. 4, pp. 324–326, 1990.

[239] P. Barclay, K. Srinivasan, and O. Painter, "Nonlinear response of silicon photonic crystal microresonators excited via an integrated waveguide and fiber taper," *Opt. Express*, vol. 13, pp. 801–820, Feb 2005.

[240] M. Notomi, A. Shinya, S. Mitsugi, G. Kira, E. Kuramochi, and T. Tanabe, "Optical bistable switching action of Si high-Q photonic-crystal nanocavities," *Opt. Express*, vol. 13, pp. 2678–2687, Apr 2005.

[241] E. Weidner, S. Combrié, A. de Rossi, N.-V.-Q. Tran, and S. Cassette, "Nonlinear and bistable behavior of an ultrahigh-Q GaAs photonic crystal nanocavity," *Applied Physics Letters*, vol. 90, no. 10, p. 101118, 2007.

[242] T. Tanabe, M. Notomi, S. Mitsugi, A. Shinya, and E. Kuramochi, "Fast bistable all-optical switch and memory on a silicon photonic crystal on-chip," *Opt. Lett.*, vol. 30, pp. 2575–2577, Oct 2005.

[243] A. M. Yacomotti, F. Raineri, G. Vecchi, P. Monnier, R. Raj, A. Levenson, B. Ben Bakir, C. Seassal, X. Letartre, P. Viktorovitch, L. Di Cioccio, and J. M. Fedeli, "All-optical bistable band-edge Bloch modes in a two-dimensional photonic crystal," *Applied Physics Letters*, vol. 88, no. 23, p. 231107, 2006.

[244] K. Nozaki, A. Shinya, S. Matsuo, Y. Suzaki, T. Segawa, T. Sato, Y. Kawaguchi, R. Takahashi, and M. Notomi, "Ultralow-power all-optical RAM based on nanocavities," *Nat Photon*, vol. 6, pp. 248–252, Apr. 2012.

[245] K. Kobayashi, H. Nishimoto, and R. Lang, "Experimental observation of asymmetric detuning characteristics in semiconductor laser injection locking," *Electronics Letters*, vol. 18, no. 2, pp. 54–56, 1982.

[246] M. T. Hill, H. J. S. Dorren, T. de Vries, X. J. M. Leijtens, J. H. den Besten, B. Smalbrugge, Y.-S. Oei, H. Binsma, G.-D. Khoe, and M. K. Smit, "A fast low-power optical memory based on coupled micro-ring lasers," *Nature*, vol. 432, pp. 206–209, Nov. 2004.

[247] Y. Hong, P. Spencer, and K. Shore, "Power and frequency dependence of hysteresis in optically bistable injection locked VCSELs," *Electronics Letters*, vol. 37, no. 9, pp. 569–570, 2001.

[248] C.-H. Chen, S. Matsuo, K. Nozaki, A. Shinya, T. Sato, Y. Kawaguchi, H. Sumikura, and M. Notomi, "All-optical memory based on injection-locking bistability in photonic crystal lasers," *Opt. Express*, vol. 19, pp. 3387–3395, Feb 2011.

[249] R. Lang, "Injection locking properties of a semiconductor laser," *Quantum Electronics, IEEE Journal of*, vol. 18, pp. 976 – 983, jun 1982.

[250] F. Mogensen, H. Olesen, and G. Jacobsen, "FM noise suppression and linewidth reduction in an injection-locked semiconductor laser," *Electronics Letters*, vol. 21, pp. 696 –697, 1 1985.

[251] L. Li, "Static and dynamic properties of injection-locked semiconductor lasers," *Quantum Electronics, IEEE Journal of*, vol. 30, pp. 1701 –1708, aug 1994.

[252] F. Mitschke, C. Boden, W. Lange, and P. Mandel, "Exploring the dynamics of the unstable branch of bistable systems," *Optics Communications*, vol. 71, no. 6, pp. 385 – 392, 1989.

[253] B. Segard, J. Zemmouri, and B. Macke, "Noncritical slowing down in optical bistability," *Optics Communications*, vol. 63, no. 5, pp. 339 – 343, 1987.

[254] B. Ghafary, S. Donghui, and M. Okada, "Dynamics of an optically switched bistable semiconductor laser," *Optical Review*, vol. 5, no. 2, pp. 99–104, 1998.

[255] J.-L. Oudar, R. Kuszelewicz, T. Riviera, F. Perez, and R. Raj, "Dynamics of optical switching in bistable microresonators under transient excitation," *Nonlinear Optics*, vol. 11, pp. 229–244, 1998.

[256] F. Hopf and P. Meystre, "Numerical studies of the switching of a bistable optical memory," *Optics Communications*, vol. 29, no. 2, pp. 235 – 238, 1979.

[257] E. Garmire, J. H. Marburger, S. D. Allen, , and H. G. Winful, "Transient response of hybrid bistable optical devices," *Applied Physics Letters*, vol. 34, p. 374, 1979.

[258] G. Grynberg and S. Cribier, "Critical exponents in dispersive optical bistability," *J. Physique Lett.*, vol. 44, no. 12, pp. 449–453, 1983.

[259] K. Nozaki, T. Tanabe, A. Shinya, S. Matsuo, T. Sato, H. Taniyama, and M. Notomi, "Sub-femtojoule all-optical switching using a photonic-crystal nanocavity," *Nat Photon*, vol. 4, pp. 477–483, July 2010.

[260] H.-G. Park, S.-H. Kim, S.-H. Kwon, Y.-G. Ju, J.-K. Yang, J.-H. Baek, S.-B. Kim, and Y.-H. Lee, "Electrically Driven Single-Cell Photonic Crystal Laser," *Science*, vol. 305, no. 5689, pp. 1444–1447, 2004.

[261] B. Ellis, M. A. Mayer, G. Shambat, T. Sarmiento, J. Harris, E. E. Haller, and J. Vuckovic, "Ultralow-threshold electrically pumped quantum-dot photonic-crystal nanocavity laser," *Nat Photon*, vol. 5, pp. 297–300, May 2011.

[262] S. Matsuo, K. Takeda, T. Sato, M. Notomi, A. Shinya, K. Nozaki, H. Taniyama, K. Hasebe, and T. Kakitsuka, "Room-temperature continuous-wave operation of lateral current injection wavelength-scale embedded active-region photonic-crystal laser," *Opt. Express*, vol. 20, pp. 3773–3780, Feb 2012.

[263] G. Shambat, B. Ellis, J. Petykiewicz, M. Mayer, A. Majumdar, T. Sarmiento, J. Harris, E. Haller, and J. Vuckovic, "Electrically driven photonic crystal nanocavity devices," *Selected Topics in Quantum Electronics, IEEE Journal of*, vol. 18, no. 6, pp. 1700–1710, 2012.